INTERNATIONAL DOCTORAL COURSE IN
"EARTH AND MARINE SCIENCES (EMAS)"

CYCLE XXXII

PhD Coordinator: Prof. Coltorti Massimo

The composition of noble gas and CO_2 in the European subcontinental lithospheric mantle

Scientific/Disciplinary Sector (SDS) GEO/07-08

Candidate

Dott. Andrea Luca Rizzo

Supervisors

Prof. Massimo Coltorti

Prof. Luis Carlos Barbero Gonzalez

Years 2016-2019

Table of contents

View of maars formed in Eifel region (Germany)

Abstract

Abstract

The investigation of mantle-derived products coming from Sub Continental Lithospheric Mantle (SCLM) is crucial for constraining its geochemical features and evolution, and for better evaluating the information arising from the study and monitoring of volcanic gases. A significant contribution in the comprehension of the mantle features may come from the study of fluid inclusions (FI) geochemistry in ultramafic xenoliths. Several researches have already demonstrated that noble gases (He, Ne, Ar) and CO_2 systematics in FI represent an useful tool for understanding the main processes that modify in time and space the original features of the mantle (Deines, 2002; Gautheron et al., 2002, 2005, Martelli et al., 2011, 2014, Correale et al., 2012, 2015; Gennaro et al., 2017). However, the contemporarily measurement of helium, neon, argon, and CO_2 concentrations and isotope ratios in mantle xenoliths is limited to a few suites of samples and localities on Earth.

This thesis proposes an update of knowledge on this topic coming from the integrated study of petrography and geochemistry of the minerals with noble gases and CO_2 (when available) in FI from the European lithospheric mantle xenoliths. The aim of the thesis is to show how processes of partial melting, metasomatism, refertilization, magmatic degassing, volatile recycling, and mixing modified the pristine composition of fluids stored in European SCLM and give clues on its geodynamic evolution. Four localities have been chosen: Lower Silesia (Eger Rift in SW Poland), Persani Mts. (Eastern Transylvanian Basin, Romania), Eifel and Siebengebirge (Germany), and French Massif Central. The study of the latter is still ongoing, so I present the results of the other three localities only.

The first part of the thesis focuses on the study of the chemistry and isotope composition (noble gases and CO_2) of fluid inclusions (FI) from selected mantle xenoliths originating from Wilcza Góra (WG), which is located in Lower Silesia (Eger Rift, in southwest Poland), with the aim of integrating their petrography and mineral chemistry. Mantle xenoliths are mostly harzburgites and sometimes bear amphiboles, and are brought to the surface by intraplate alkaline basalts that erupted outside the north-easternmost part of the Eger (Ohře) Rift in Lower Silesia. Olivine (Ol) is classified into two groups based on its forsterite content: (1) $Fo_{88.9–91.5}$, which accounts for a fertile-to-residual mantle, and (2) $Fo_{85.5–88.1}$, which indicates large interactions with circulating (basic) melts. This dichotomy is also related to orthopyroxene (Opx) and clinopyroxene (Cpx), which show two ranges of Mg# values (87–90 and 91–93, respectively) and clear evidence of recrystallization. CO_2 predominates within FI, followed by N_2. We report the first measurements of C isotope composition of CO_2 in FI from European mantle. The $\delta^{13}C$ of mantle CO_2 varies between –4.7‰ and –3.1‰, which mostly spans the MORB range ($-8‰ < \delta^{13}C < -4‰$). The $^3He/^4He$ ratio is 6.7–6.9 Ra in Cpx, 6.3–6.8 Ra in Opx, and 5.9–6.2 Ra in Ol, where Ra is the $^3He/^4He$ ratio of air that is equal to 1.39×10^{-6}. These values

are within the range proposed for European SCLM (6.3±0.3 Ra). The decrease in $^3He/^4He$ from Cpx to Ol is decoupled from the He concentration, and excludes any diffusive fractionation from FI. The chemistry of FI entrapped in Ol indicates that this mineral phase better preserves memory of partial melting history than Opx and Cpx, suggesting that the mantle is strongly depleted by variable extents of partial melting, while that of Opx and Cpx suggests the overprinting of at least one metasomatic event. According to Matusiak-Małek et al. (2017), Cpx, Opx, and amphiboles were added to the original harzburgite by carbonated hydrous silicate melt related to Cenozoic volcanism. This process resulted in entrapment of CO_2-rich inclusions whose chemical and isotope composition resembles that of metasomatizing fluids. I argue that FI data reflect a mixing between two endmembers: (1) the residual mantle, resulting from partial melting of European SCLM, and (2) the metasomatic agent, which is strongly He-depleted and characterized by MORB-like features.

The second part of the thesis focuses on the petrological and noble gases study on a mantle xenolith suite from Perşani Mts. (Eastern Transylvanian Basin, Romania). Eastern Transylvanian Basin in Romania is one of the few places where the alkaline eruptions of Perşani Mts. occurred contemporaneously with the last calc-alkaline activity of the South Harghita volcanic chain. In fact, calc-alkaline and alkaline magmatisms are generally separated in space and/or in time. Based on mineral major and trace element and noble gases in fluid inclusions, two different events left their imprint on the examined lithospheric mantle section: the first is configured as a pervasive, complete re-fertilization of a previously depleted mantle by a calc-alkaline subduction-related melt, causing the restoration of very fertile, amphibole-bearing lithotypes. This is evidenced by the a) modal clinopyroxene up to 21.9 % with Al_2O_3 contents up to 8.16 wt%, higher than what expected for clinopyroxene in a Primordial Mantle; b) $^4He/^{40}Ar^*$ up to 1.2, within the reported range for mantle production; c) $^3He/^4He$ in olivine, opx, and cpx of 5.8±0.2 Ra, among the most radiogenic values of European mantle, below the typical MORB mantle (8±1 Ra), reflecting the recycling of crustal material in the local lithosphere. The second event is related to the interaction with an alkaline metasomatic agent similar to the host basalts that caused a later-stage, slight LREE enrichment in pyroxenes and disseminated amphiboles and the precipitation of vein amphiboles with a composition similar to amphiboles megacrystals also found in Perşani deposits. This is further highlighted by the $^4He/^{40}Ar^*$ and $^3He/^4He$ values found in some opx and cpx, up to 2.5 and 6.6 Ra, respectively, more typical of magmatic fluids.

The third part of the thesis focuses on the study of mantle xenoliths sampled from three localities of the Quaternary West Eifel volcanic field and two localities from the Tertiary Siebengebirge volcanic field (Germany), which track the evolution of the rift system in the last ~30 Ma, aiming at improving the knowledge of the local SCLM. We characterize a large collection of

mantle xenoliths sampled within lava, sills and/or necks (Siebengebirge), as well as within scoria cone and/or pyroclastic deposits (Eifel). A detailed textural and petrological study of the bulk xenoliths and the primary mineral phases was complemented by the determination of the concentration of volatiles (He, Ne, Ar, CO_2) in mineral-hosted Fluid Inclusions (FI) after single-step crushing. A remarkable difference exists between xenoliths erupted from Siebengebirge and Eifel volcanic fields. In the former xenoliths are mostly harzburgitic, while in the latter xenoliths are lherzolitic, harzburgitic, and wehrlitic in composition with the exclusive modal presence of both amphibole and phlogopite. Few ol-clinopyroxenites and one ol-websterite are also present. Texture varies from protogranular, porphyroclastic and equigranular in most of the xenoliths, to cumulitic in some samples. Mg# [$MgO/(MgO+FeO_{tot})$ mol%] varies from 83 to 92 for olivine, from 84 to 92 for orthopyroxene, and from 84 to 94 for clinopyroxene. Al_2O_3 content of orthopyroxene and clinopyroxene ranges from 0.5 to 6.5 wt% and from 0.7 to 8.2 wt%, respectively. Spinel is characterized by Cr# [$Cr_2O_3/(Cr_2O_3+Al_2O_3)$ mol%] ranging between 10 and 82, and by Mg# varying from 40 to 78. Xenoliths from the Siebengebirge localities are characterized by the highest Mg# for clinopyroxene and Cr# for spinel, together with the lowest Al_2O_3 contents for both pyroxenes. Based on these petrographic and geochemical features, we argue that the mantle beneath Siebengebirge experienced higher degree of melt extraction (up to 30% or even more) and that metasomatic/refertilization events were more efficient in the mantle beneath West Eifel and reasonably postponed Siebengebirge magmatism. In terms of CO_2 and noble gas concentration, clinopyroxene and most of the orthopyroxene show the highest gas content, while olivine are gas-poor. Volatiles content in olivine does not vary between Siebengebirge and West Eifel xenoliths, whereas Opx and Cpx in West Eifel are richer in volatiles. This variability in FI concentration seems not related to the variations observed in the He, Ne, and Ar isotopic compositions. In detail, $^3He/^4He$ varies between 5.5 and 6.9 Ra. These values are comparable to previous measures in West Eifel, mostly within the range proposed for European SCLM (6.3±0.4 Ra), and slightly below that of MORB (Mid-Ocean Ridge Basalts; 8±1Ra). The Ne and Ar isotope ratios fall along a binary mixing trend between air and MORB-like mantle. He/Ar* in FI and Mg# and Al_2O_3 content in minerals confirm that variable extents of partial melting occurred in the local SCLM, followed by metasomatic processes. As indicated by the mineral chemistry, the mantle beneath Siebengebirge experienced the highest degree of melting. The different age and erosion between Siebengebirge and Eifel outcrops prevent the univocal link between the mantle geochemical features and magma explosivity. However, the presence of hydrous phases (Phlog and Amph), together with the occurrence of cumulitic xenoliths and the metasomatic/refertilization processes recorded in the West Eifel lead us to speculate that the explosivity could be related the volatile abundance in the mantle introduced by the most

recent metasomatic/refertilization processes. The ongoing carbon isotopic measurements in the most CO_2-rich mantle xenoliths, coupled to the noble gases systematics in FI and mineral chemistry, will help in shedding light on the local mantle composition and the volatile recycling within the European SCLM, adding new clues to the present knowledge. An additional benefit of this type of studies is the possibility of better constraining the composition of fluids rising through the crust and used for volcanic or seismic monitoring.

Introduction

Introduction

This PhD thesis reports an integrated study of petrography and geochemistry of the minerals with noble gases and CO_2 (when available) in fluid inclusions (FI) from selected lithospheric mantle xenoliths erupted in Europe during alkaline magmatism. Indeed, these products represent a unique opportunity for constraining the geochemical features and evolution of the mantle. The aim of the thesis is thus to show how processes of partial melting, metasomatism, refertilization, magmatic degassing, volatile recycling, and mixing may modify the pristine composition of fluids stored in SCLM and give clues on the geodynamic evolution. To address these scientific topics, we focus but not limit on the European area that has experienced extensive volcanic activity related to its complex geodynamic evolution. We selected mantle xenoliths from a few key regions where magmatism occurred in different temporal and geodynamic conditions: Lower Silesia (Eger Rift) in SW Poland, Persani Mts. (Transylvania) in Romania, Eifel and Siebengebirge in Germany, and French Massif Central. The latter study is still ongoing.

The main outcomes of this thesis should help in better comprehend the characterization of fluids circulation and the extent of crustal recycling in these portions of European SCLM, the influence of recent and/or fossil subductions, and the geodynamics of Europe with the occurrence (or not) of a plume as the source of alkaline magmatism,. Finally, this thesis contributes at the comprehension of CO_2 cycle in the European lithospheric mantle, where a few data are nowadays available.

The thesis is developed on the following rationale that sheds light on the geochemical features of the European mantle beneath the selected localities:

Chapter 1: brief summary of the geodynamic and geological framework of the European area, with a description of the selected localities.

Chapter 2: list of the analytical methods, which consist of: i) modal composition of mantle xenoliths under microscope observation; ii) mineral chemistry by major elements analyses (EMP); iii) mineral chemistry by trace elements analyses (LA-ICP-MS); iv) noble gas (He, Ne, and Ar) elemental and isotope composition in fluid inclusions of mineral separates (mass spectrometry); v) CO_2 concentration and C isotope composition in fluid inclusions of mineral separates (IRMS).

Chapter 3: Geochemistry of noble gases and CO_2 in fluid inclusions from lithospheric mantle beneath Lower Silesia (Eger Rift), aimed at defining the main signature of fluids circulating in this portion of European mantle and the processes occurred therein (partial melting, metasomatism, crustal recycling).

Chapter 4: Geochemistry of noble gases and CO_2 in fluid inclusions from lithospheric mantle beneath Persani Mts. (Transylvania), aimed at defining the main signature of fluids circulating in this portion

of European mantle and the processes occurred therein (partial melting, refertilization, crustal recycling due to subduction).

Chapter 5: Geochemistry of noble gases and CO_2 in fluid inclusions from lithospheric mantle beneath Eifel and Siebengebirge (Germany), aimed at defining the main signature of fluids circulating in this portion of European mantle, its temporal and spatial evolution, and the processes occurred therein (partial melting, metasomatism/refertilization, crustal recycling).

Chapter 6: Concluding remarks, with a general overview of the main outcomes of this study.

Chapter – 1 –

Geodynamic and geological setting of Europe

1. Geodynamic and geological setting of Europe

From late Mesozoic to Quaternary times, the geodynamic setting of Europe was complex being characterized by the occurrence of subduction, back-arc extension and lithospheric delamination. These activities were accompanied by widespread magmatism developed in the Mediterranean and surrounding regions to form the Cenozoic central European Volcanic Province (CEVP; Wilson and Downes, 2006; Harangi and Lenkey, 2007; Lustrino and Wilson, 2007) (Fig. 1). This volcanism occurred during the convergence between the African and European plates along with the progressive closure of oceanic basins in the Mediterranean region and the formation of the Alpine orogeny. Consequently, in many areas (e.g., Spain, France, Algeria, Morocco, Sardinia, Carpathian–Pannonian region, Bulgaria, Serbia, Turkey) there is a temporal sequence of two distinct types of igneous activity, with different geochemical and petrographic characteristics, which have been grouped into "orogenic" and "anorogenic" (Harangi and Lenkey, 2007; Lustrino & Wilson, 2007) (Fig. 1). The former is mainly Oligocene-Miocene and is characterized by magmas essentially calc-alkaline to high-K calc-alkaline in composition with subduction-related geochemical fingerprint. The latter is mainly Pliocene-Recent and is characterized by mildly alkaline sodic magmas, with minor tholeiitic reflecting the nature of asthenospheric and lithospheric mantle regions unaffected by any metasomatic agents related to recycling of crustal lithologies (Harangi and Lenkey, 2007; Lustrino & Wilson, 2007).

The alkali basaltic volcanism spreads over a vast region of Western, Central, and Southeastern Europe (Wilson and Bianchini, 1999; Beccaluva et al., 2007). Its westernmost occurrences are confined to the Central, Eastern, and Northeastern part of the Iberian Peninsula, southern France (Massif Central, France), Rhine graben (Eifel, Siebengebirge, Rennes, Gessen, etc.) in Germany, the Eger zone within the Bohemian massif, Silesia (southwestern Poland), Styria and Burgenland in Austria, Pannonian Basin in Hungary, the southern part of Slovakia, the South Carpathians within the territory of Romania, and the Bulgarian Sredna Gora and PreBalkan regions (Fig. 1). In most cases, the basalts brought to the surface mantle xenoliths that represent a unique opportunity for petrological and geochemical studies of the lithosphere beneath the Mediterranean area. A striking character of the anorogenic rocks is that their isotopic compositions converge into a relatively restricted field with similarities to the HIMU (high μ, where $\mu=^{238}U/^{204}Pb$) end-member. Several models, often invoking the presence of one or a multiple plume, have been proposed (Fig. 2). Among the European alkaline mafic volcanic fields, mantle plume activity has been considered beneath the French Massif Central and the Eifel area (Lustrino and Wilson, 2007 and references therein; Ritter, 2007 and references therein). On the contrary, Lustrino and Carminati (2007) pointed out on the presence of phantom plumes in Europe and the circum-Mediterranean region,

suggesting that the existence of large and/or extensive thermal anomalies under Europe is unnecessary, while passive upwelling of asthenospheric mantle could explain the magmatic activity. Thus, the debate on the existence of the plumes and the nature of the processes generating these heterogeneities also remain disputable.
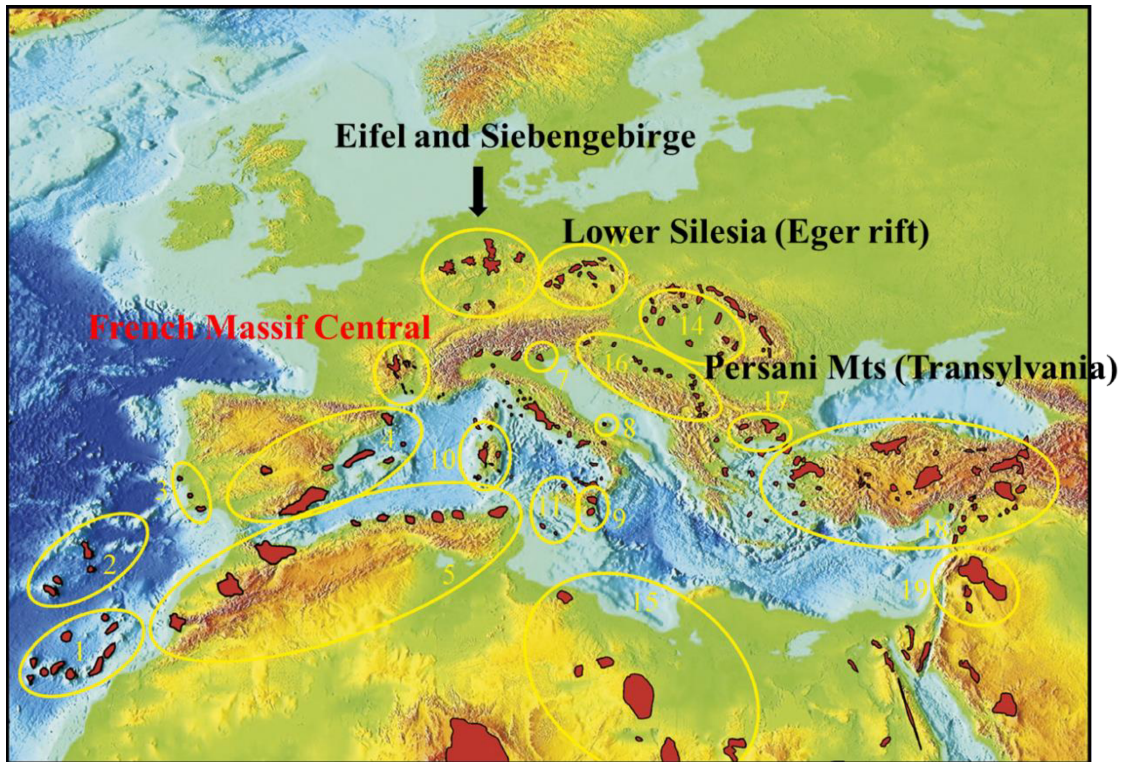
Figure 1. Sketch map showing the locations of studied areas in European Cenozoic igneous provinces (with both anorogenic and orogenic geochemical signatures) in red. Modified from Lustrino and Wilson (2007).

A significant contribution to this debate comes from the isotope systematics of He and other noble gases (Ne, Ar) hosted in the mantle xenoliths from European mantle. The known data indicate that the ^{3}He/^{4}He ratio normalized to the atmosphere (R/Ra) is 6.3±0.4 Ra (Dunai and Baur, 1995; Buikin et al., 2005; Gautheron et al., 2005), which is close to MORB-type mantle but lower than that of typical plume-related OIB (e.g. Hawaii, Iceland) of up to 40 Ra. This evidence contradicts the mantle plume hypothesis. The origin of the radiogenic helium is still debated. It has been attributed to a mantle plume having low ^{3}He/^{4}He ratio, to addition of crustal materials to a MORB source (Dunai and Baur, 1995) or to a feature of the European subcontinental lithospheric mantle (SCLM) itself (Gautheron et al., 2005). On the other hand, neon and argon isotopes performed on xenoliths from Eifel region and Pannonian basin highlight the presence of plume component (Buikin et al., 2005). As a matter of fact, the current measurement of helium, neon, and argon

isotopes in European mantle xenoliths is limited to a few suites of samples, which leaves open the question of the mantle features and the geodynamic implications.

The noble gases measurements performed in free gas exhalations from intra-continental rift areas of the European Cenozoic rift system (ECRS) in the Massif Central, the Eifel, the western Eger Rift, and the Pannonian Basin (Vaselli et al., 2002; Bräuer et al., 2005, 2008, 2011, 2013, 2016; Caracausi et al., 2016; Bekaert et al., 2019; Kis et al., 2019 and references therein), reveal rather high contributions of mantle-derived helium. However, only at a few sites in the European intraplate volcanism do ^{3}He/^{4}He ratios in free volatiles completely overlap the signature typical of mantle xenoliths (e.g. Bräuer et al., 2011, 2013, 2016). All these studies indicate that the ^{3}He/^{4}He ratios of free gases escaping in volcanic zones tend to those of the xenoliths, and that the mantle is the primary source of these gases but crustal fluids also act in lowering these ratios (Vaselli et al., 2002; Bräuer et al., 2016 and references therein).
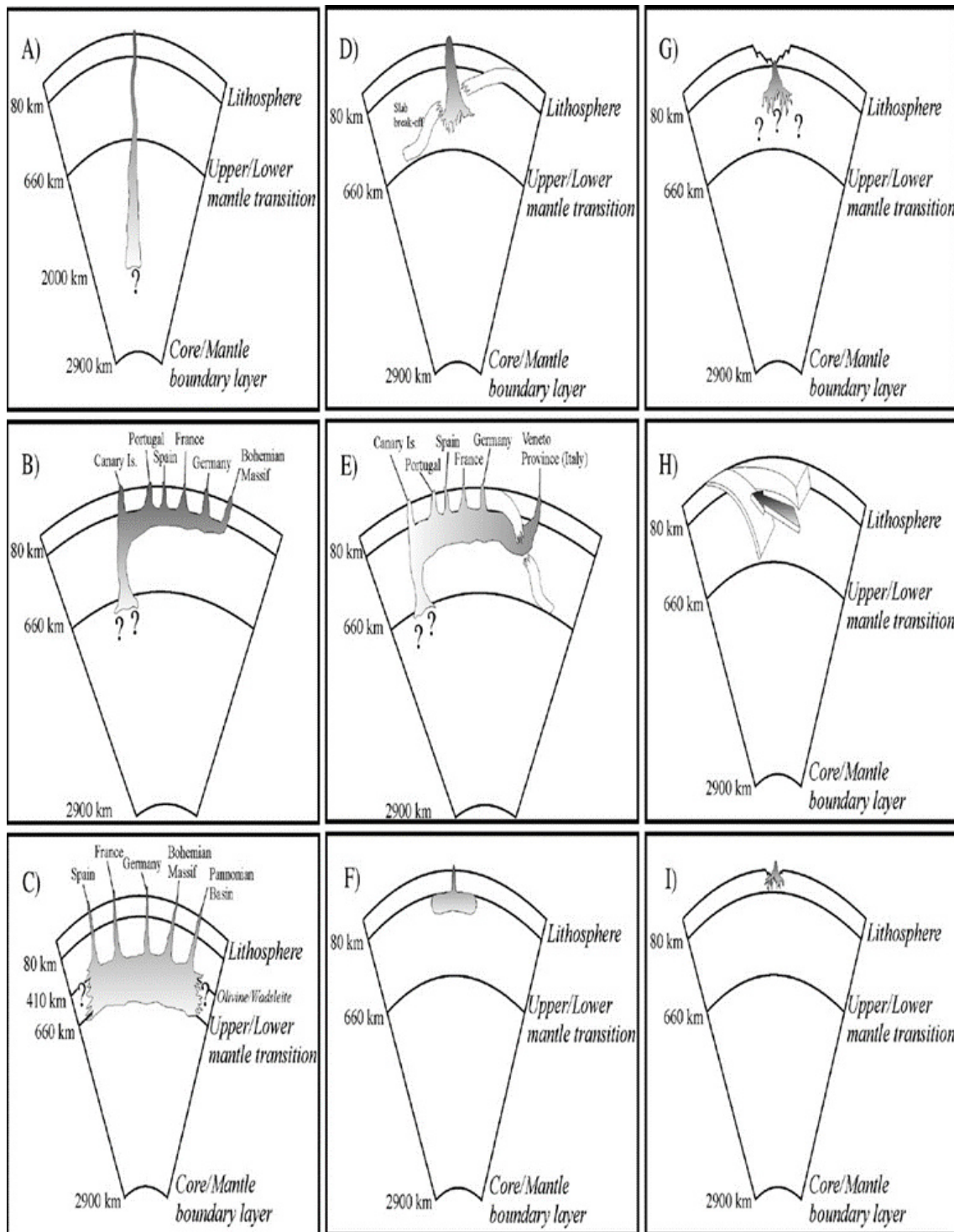
Figure 2. Schematic representation of the various petrological and geodynamic models proposed in the literature to explain the origin of individual igneous districts within the CiMACI province. From Lustrino and Wilson (2007).

1.1 Geodynamic and geological framework of Lower Silesia (Eger Rift)

Within the general compressional regime, an extensional phase triggered the opening of the European Cenozoic Rift System (ECRS) (Dèzes et al., 2004), whose products occur typically in the proximity of graben systems. The north-easternmost part of the CEVP is related to the northeast–southwest

trending Eger (Ohře) Rift in the western part of the Bohemian Massif in the Czech Republic (Fig. 3a). Volcanic rocks occur both along the rift axis and in the off-rift environment in this area (Ulrych et al., 2011). Volcanic rocks located northeast of the rift in southwest Poland follow the northwest–southeast trending Odra fault zone (Fig. 3a). Volcanism in southwest Poland has exhibited three main activity peaks: (1) Eocene-Oligocene (34–26 Ma), (2) Miocene (22–18 Ma), and (3) Pliocene-Pleistocene (5.5–1.0 Ma) (Pécskay and Birkenmajer, 2013). More than 300 outcrops of Cenozoic mafic volcanic rocks have been identified in southwest Poland, and around 3% of them contain xenoliths originating from the upper mantle and lower crust (Matusiak-Małek et al., 2017).

The present thesis investigates mantle xenoliths from Wilcza Góra (WG) basanite rocks (20.07±0.90 Ma) (Birkenmajer et al., 2007) located in the Kaczawskie Mountains around 40 km east of the axis of the Eger Graben. These mountains constitute the western part of the Sudetes mountain range, which constitutes the northern part of the Bohemian Massif and was amalgamated during the Variscan closure of the Rheic Ocean ca. 370 Ma (Mazur et al., 2006 and references therein). The Kaczawskie Mountains comprise a metamorphosed volcano-sedimentary succession from Cambrian to late Devonian/early Carboniferous and Mesozoic clastic sediments (Mazur et al., 2006; Białek et al., 2007).
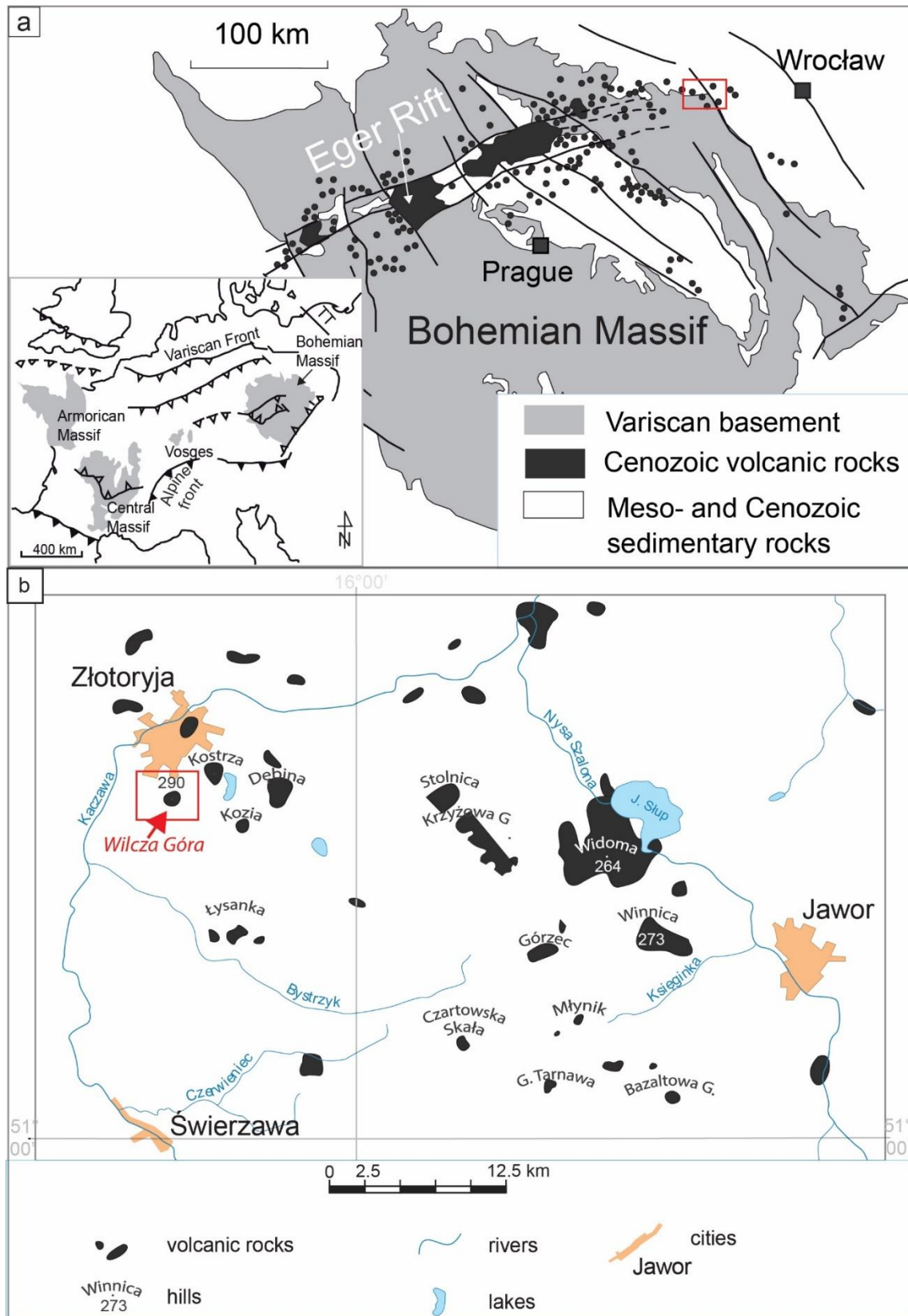
Figure 3. a) Location of Eger Rift in Bohemian Massif (based on Ulrych et al., 2011), inset shows European Variscan Basement and major fault zones (Mazur et al., 2006, modified); b) Outcrops of Cenozoic volcanic rocks in the vicinity of Złotoryja city, location of Wilcza Góra indicated by arrow and red box (based on Sawicki, 1995).

1.2 Geodynamic and geological framework of Persani Mts. (Transylvania)

The Pliocene–Quaternary Perșani Mountains Volcanic 79 Field (PMVF) is located in the internal part of the Carpathian Bend Area, in the south-eastern corner of the Transylvanian Basin (Fig. 4). It represents the youngest and largest monogenetic volcanic fields in south-eastern Europe. This volcanism was coeval with the last peak of crustal deformation in the Carpathian bending zone (Merten et al., 2010) and the generation of the Brașov Basin (Gîrbacea et al., 1998), as well as with the orogenic adakite-like calc-alkaline volcanism of the southernmost Harghita Mountains, and with the emplacement of two K-alkalic bodies, located 40 km to the east (Szakács et al., 1993; Seghedi et al., 2004, 2011). The PMVF is underlain by a relatively thick continental crust (35–40 km), whereas the thickness of the whole lithosphere is interpreted to be relatively thin (60–80 km; Martin et al., 2006; Seghedi et al., 2011).

The volcanic activity occurred in six episodes between 1.2 Ma and 0.6 Ma (Panaiotu et al., 2004, 2013), generating 21 monogenetic volcanic centers (maars, tuff-rings, scoria cones and lava flows) in a 22 km long and 8 km wide area (Seghedi et al., 2016). The three contemporaneous magma sources (Na-, K-alkaline, and adakite-like calc-alkaline) detected in a narrow area have been related to the same regional tectonic event, coeval with the last episode (latest Pliocene onward) of the tectonic inversion in the Southeastern Carpathians, probably linked to the indentation of the Adria micro-plate (Matenco et al., 2007; Seghedi et al., 2011).

The petrological features of the PMVF basalts are similar to those of continental intraplate alkali basalts worldwide (e.g., Lustrino and Wilson, 2007; Harangi et al., 2014), with some subtle differences (e.g. Pb isotopic characteristics, high LILE) resembling those of subduction-related magmas, thus suggesting a generation from a mantle source slightly influenced by subduction components. The frequent occurrence of mantle xenoliths in the PMVF provides evidence for a rapid magma ascent, within only 4-5 days (Harangi et al., 2013). This indicates that the magmas, generated by deep mantle processes, were almost unaffected by interaction with the crust (Vaselli et al., 1995; Downes et al., 1995; Falus et al., 2008; Seghedi et al., 2011; Harangi et al., 2013).
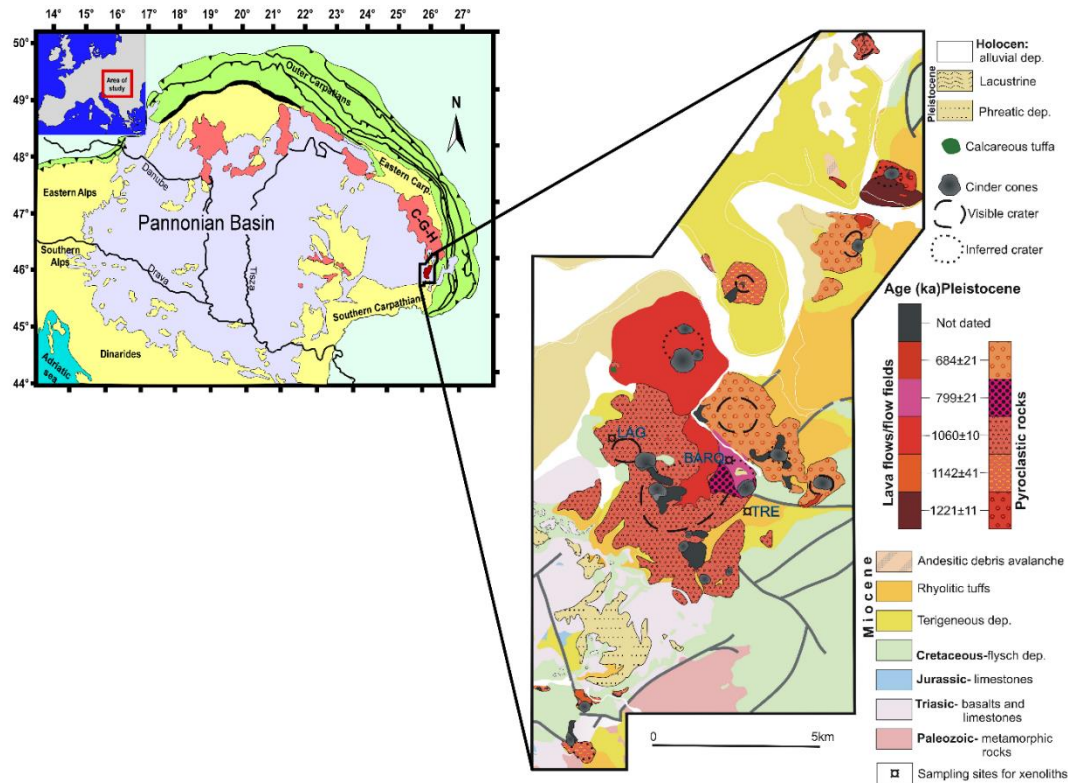
Figure 4. Geological sketch of Pannonian Basin and volcanological map of Perşani Mountains in the Transylvanian Basin. C-G-H indicates the Calimani-Ghiurghiu-Harghita volcanic arc. The mantle xenolith sampling sites (LAG-BARC-TRE) are also indicated, corresponding to loose pyroclastic deposits of La Gruiu volcanic center and along Barc and Trestia creeks, respectively.

1.3 Geodynamic and geological framework of Eifel and Siebengebirge (Germany)

The German volcanic fields are part of the Central European Volcanic Province (CEVP), which results from the development of Tertiary to Quaternary intra-continental rifts (Wilson and Downes, 1991, 2006; Dèzes et al., 2004; Lustrino and Wilson, 2007) (Fig. 5A). The most relevant volcanic areas from W to E are: Hocheifel (~45-24 Ma) and Eifel (~0.5-0.01 Ma), Siebengebirge (~30-6 Ma), Westerwald (~32–0.4 Ma), Vogelsberg (~21–9 Ma), Hessian Depression (~21–8 Ma), Rhön (~26–11 Ma), Heldburg (~42–11 Ma) and Upper Palatinate (~29–19 Ma) (Fig. 5B), whose ages are from Lippolt (1983).

The Tertiary Hocheifel volcanic area represents the western part of the CEVP and overlaps that of the Quaternary East and West Eifel Volcanic Fields (Fig. 5A). Instead, north-eastward of Eifel in Tertiary developed the volcanic field of Siebengebirge (Fig. 5B) that is associated with the middle and upper Rhine rift system. This volcanic field formed during Eocene to Oligocene because of syn- to post-Alpine extension (Ziegler, 1992). Indeed, mafic magmas with variable degrees of SiO_2-undersaturation were erupted from ~30 Ma to 6 Ma (Frechen & Vieten, 1970a, 1970b; Todt &

Lippolt, 1980; Vieten et al., 1988; Kolb et al., 2012). In the Quaternary, the volcanism shifted to the Eifel volcanic fields west of the Rhine, inducing the uplift of the Rhenish Massif since 0.8 Ma; the last known eruption at Eifel is dated 11 ka from the Ulmer Maar in the West Eifel (Zolitschka et al., 1995).

Eifel volcanism comprises 250 eruptive centers that spread over 600 km^2. The Hocheifel lavas mostly intruded weakly metamorphosed Devonian and Carboniferous sediments of the Hercynian Rhenish Massif (e.g., Ernst & Bohaty, 2009). Two distinct areas can be defined: the West and the East Eifel volcanic fields. Each domain was developed on both sides of the zone of maximum uplift. The volcanoes of the West Eifel sit atop the highest parts of the Rhenish Massif and started erupting less than 700 ka ago, while the lavas of the East Eifel were erupted in the Neuwied Basin since about 460 ka ago (Schmincke, 2007). In each area, the early eruptions are characterized by potassic basanites followed by more evolved and sodic lava (Mertes and Schmincke, 1985). Volcanoes are mainly cinder and tuff cones and maars with tuff rings whose formation is partially governed by magma–water interaction resulting in phreatomagmatic eruptions. The emission of CO_2-dominated gases as well as weak volcanic earthquakes show that magmatic activity in Eifel is nowadays dormant, but not ended (e.g., Giggenbach et al., 1991; Griesshaber et al., 1992; Aeschbach-Hertig et al., 1996; Bräuer et al., 2005, 2013; Schmincke, 2007). The West Eifel field shows a clear trend NW–SE in both the distribution of volcanoes and age of volcanism (Schmincke et al., 1983). The volcanic activity of this field started near Ormont, and then volcanism migrated to the SE. The frequency of volcanic eruption has decreased during the last 100,000 years (Nowell et al., 2006).

Tomography studies indicate abnormal seismic velocities between 50–60 km and 410-660 km depth, which have been interpreted to result from a narrow thermal plume in the asthenosphere below the Eifel (Ritter et al., 2001; Keyser et al., 2002; Ritter, 2007 and references therein). Instead, detailed geophysical and geodynamic observations as well as geochemical and petrological studies would exclude the hypothesis of a mantle plume, while proponents for alternative models invoking passive upwelling of the asthenosphere or crustal extension and melting of the lithospheric mantle (Lustrino and Carminati, 2007 and references therein). Since the origin of Eifel magmatism as well as that of CEVP is still a matter of debate, this study aims to give a contribution to this scientific dispute.
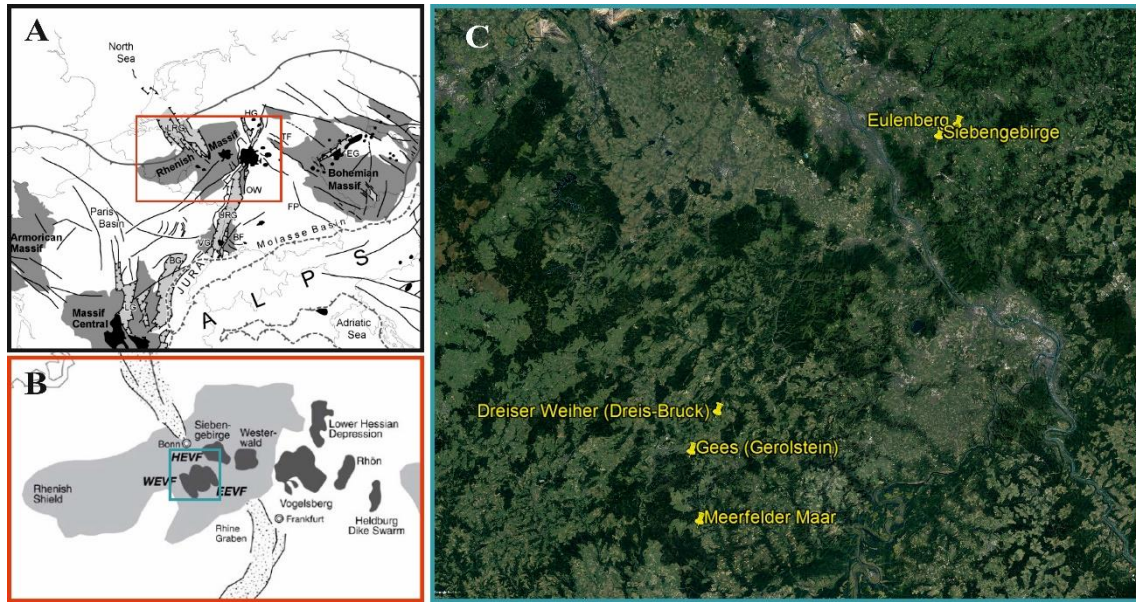
Figure 5. A) Map of Rhine rift system from Ziegler et al. (2004), showing Cenozoic fault systems (black lines), rift-related sedimentary basins (light grey), outcropping parts of the Variscan orogen (dark grey) and Cenozoic volcanic fields (black). B) Enlargement of part of Fig. 5a, modified from Schmincke (1982), showing Cenozoic volcanic fields on the uplifted Rhenish shield and in adjacent areas. The area of the Eocene Hocheifel Volcanic Field (HEVF) overlaps that of the Quaternary West and East Eifel Volcanic Fields (WEVF and EEVF). C) Google Earth map showing the sampling sites location in West Eifel (Dreiser Weiher, Gees and Meerfelder Maar) and Sibengebirge (Sibengebirge and Eulenberg) volcanic fields.

Chapter – 2 –

Methods

2. Methods

2.1 Samples location and preparation

2.1.1 Lower Silesia (Eger Rift, SW Poland)

Ultramafic mantle xenoliths were collected from an active quarry near Złotoryja city (Fig. 3b). They were hosted in basanite lavas, and are relatively scarce and typically less than 5 cm in diameter, although occasionally up to 10 cm. A suite of samples from the WG quarry was studied and well characterized by Matusiak-Małek et al. (2017) for major and trace elements, and for Sr and Nd isotopes. The present samples are appended with the subscript "II" (e.g., $WG1_{II}$) in order to avoid confusion with the nomenclature adopted by Matusiak-Małek et al. (2017).

Seventeen aliquots of pure and unaltered olivine (Ol), orthopyroxene (Opx), and clinopyroxene (Cpx) were separated for analyzing the noble gases and CO_2 in FI from nine mantle xenoliths. The only exception is for sample $WG5_{II}$ that due to the small dimension of the xenolith was only studied for the modal composition, petrography, and mineral chemistry.

2.1.2 Persani Mts. (Eastern Transylvanian Basin, Romania)

PMVF mantle xenoliths were collected from pyroclastic deposits of La Gruiu and Fântana eruptive centers and from lava flows along Bârc and Trestia creeks (Fig. 4). The xenoliths are fresh, with sizes varying from 4 to 12 cm in diameter. Modal estimates were obtained mainly by thin section point counting; if the samples were large enough to allow whole rock analyses, the point counting results were crosschecked with mass balance calculations between whole rock and mineral major element compositions.

2.1.3 Eifel and Siebengebirge (Germany)

Fourteen ultramafic xenoliths were selected from West Eifel (Meerfelder Maar, Gees, Dreis Bruck), while four from Siebengebirge (Eulenberg, Siebengebirge) (Fig. 5C). Most of the xenoliths are hosted within lava, sills and/or necks (Siebengebirge), as well as within scoria cone and/or pyroclastic deposits (West Eifel), and were sampled in active quarries or in fresh surface within maars or compact lavas. Mantle xenoliths are relatively abundant, especially in some locations from West Eifel (e.g., Meerfelder Maar and Dreiser Weiher). They are typically between 5 and 15 cm in diameter, although occasionally up to 20 cm.

2.2 Analytical procedure

2.2.1 Petrographic observation and mineral chemistry analysis

The xenoliths were selected from among the largest unaltered specimens, and then cut, sliced, and polished into 80-μm-thick sections for defining the modal composition, petrography, and mineral

chemistry. The modal proportion of minerals was determined by point counting, averaging two runs with more than 2,000 points for each thin section (2.5 cm × 4.0 cm). The smallness of the xenolith samples (5–10 cm) prevented analyses of the bulk major and trace elements, and so the chemical characterization of this xenolith group was based on a detailed *in-situ* investigation.

The major-elements composition of mineral and glass chemistry was determined by combined microscopic and back-scattered electron (BSE) imaging, followed by analysis using a CAMECA SXFive FE electron microprobe equipped with five wavelength-dispersive spectrometers and one energy-dispersive spectrometer at the Department of Lithospheric Research, University of Vienna, Austria. The operating conditions were an accelerating voltage of 15 kV, a beam current of 20 nA, and a counting time 20 s at the peak position. Natural and synthetic standards were used for calibration and PAP corrections were applied to the intensity data (Pouchou and Pichoir, 1991).Microscopic images allowed the description of fluid inclusions trapped within single minerals.

Trace element concentrations in pyroxenes and amphiboles were obtained by Laser Ablation Microprobe Inductively Coupled Plasma Mass Spectrometry (LAM-ICP-MS) at the IGG (Istituto di Geoscienze e Georisorse) - C.N.R., Pavia (Italy) and at the University of Graz (Austria). The basic set and protocol were described by Tiepolo et al. (2003). A 40–80 μm beam diameter was used, depending on mineral phase. NIST 610

and NIST 612 standard glasses were used to calibrate relative element sensitivity. The precision and accuracy of trace element analyses were assessed by standard sample BCR-2 (reference values from USGS Geochemical Reference Materials Database). Each analysis was corrected with internal standards using CaO for clinopyroxene and amphibole and SiO2 for orthopyroxene. The detection limit is a function of the ablation volume and counting time and was therefore calculated for each analysis; indeed, ablation volume greatly depends on instrument configuration. As a consequence, the detection limit reduces if spot size, beam power and cell gas flow are decreased. Since analyses for clinopyroxenes and amphiboles were carried out using a smaller spot size and lower beam power, the detection limit for some elements was up to two times less than standard analyses. The theoretical detection limit ranges from 10 to 20 ppb for REE, Ba, Th, U and Zr and 2 ppm for Ti.

2.2.2 Analysis of noble gases (He, Ne, and Ar) and CO_2 in fluid inclusions

After lightly crushing and sieving the rocks, crystals without impurities and larger than 0.5 mm were handpicked under a binocular microscope following the laboratory protocol developed at the Istituto Nazionale di Geofisica e Vulcanologia (INGV), Sezione di Palermo, Italy (e.g., Martelli et al., 2014; Rizzo et al., 2015; Gennaro et al., 2017 and references therein). Aliquots of the minerals were then cleaned ultrasonically in 6.5% HNO_3 before being rinsed with deionized water. The samples were

then accurately weighed and loaded into an ultra-high-vacuum crusher for analyses. The amount of loaded sample varied from 0.02 to 1.27 g.

The element and isotope composition of noble gases (He, Ne, and Ar) and CO_2 in FI was determined at the laboratories of INGV-Palermo in Italy. The selected crystals were split into two aliquots: the first was loaded into a stainless-steel crusher capable of holding up to six samples simultaneously for noble-gas analysis, and the second was used for determining the concentration and isotope ratio of CO_2. FI were released by in-vacuo single-step crushing of minerals at about 200 bar applied by a hydraulic press. This conservative procedure was used to minimize the contribution of cosmogenic ^{3}He and radiogenic ^{4}He that could possibly have grown or been trapped in the crystal lattice (Kurz, 1986; Hilton et al., 1993, 2002; Rizzo et al., 2015). However, since our samples were collected in a quarry, and have been shielded from cosmic rays for most of their history, there should have been no cosmogenic effect. The CO_2 measurement was first performed during noble-gas extraction at the time of crushing by quantifying the total gas pressure ($CO_2+N_2+O_2$+noble gases) and subtracting the residual pressure of N_2+O_2+noble gases after removing CO_2 using a "cold finger" immersed in liquid N_2 at –196°C. The noble gases were then cleaned under getters in an ultra-high-vacuum (10^{-9}–10^{-10} mbar) purification line, and all species in the gas mixture except for noble gases were removed. A cold finger with active charcoal immersed in liquid N_2 then removed Ar, while He and Ne were separated by using a cold head cooled at 10°K and then moved at 40 and 80K in order to release He and Ne, respectively.

He isotopes (^{3}He and ^{4}He) and Ne isotopes (^{20}Ne, ^{21}Ne, and ^{22}Ne) were measured separately using two different split-flight-tube mass spectrometers (Helix SFT, Thermo Scientific). The values of the ^{3}He/^{4}He ratio are expressed in units of R/Ra, where Ra is the ^{3}He/^{4}He ratio of air, which is equal to 1.39×10^{-6}. The analytical uncertainty of the He-isotope ratio (1σ) was <3.7%, while this was <2.1% and <4.2% for ^{20}Ne/^{22}Ne and ^{21}Ne/^{22}Ne, respectively. The reported values of both Ne-isotope ratios are corrected for isobaric interferences at m/z values of 20 (^{40}Ar^{2+}) and 22 (^{44}CO$_2^{2+}$). Corrections are generally performed by measuring ^{20}Ne, ^{21}Ne, ^{22}Ne, ^{40}Ar, and ^{44}CO$_2$ during the same analysis, and considering the previously determined ^{40}Ar^{2+}/^{40}Ar$^+$ and ^{44}CO$_2^{2+}$/CO$_2^+$ ratios on the same Helix SFT that run FI samples. Ar isotopes (^{36}Ar, ^{38}Ar, and ^{40}Ar) were analyzed by a multicollector mass spectrometer (Argus, GVI) with an analytical uncertainty (1σ) of <1.5%. For each analytical session we analyzed at least one standard of each of He, Ne, and Ar that had previously been purified from air and stored in tanks. The analytical uncertainty (1σ) values for the ^{3}He/^{4}He, ^{20}Ne/^{22}Ne, ^{21}Ne/^{22}Ne, ^{40}Ar/^{36}Ar, and ^{38}Ar/^{36}Ar ratios were <0.94%, <0.07%, <0.3%, <0.05%, and <0.12%, respectively. The uncertainty in the determinations of the elemental He, Ne, and Ar contents was <5% after considering natural variability and the assumption of residual (not crushed) crystals for weight

normalization of the number of moles of gas; typical blanks for He, Ne, and Ar were $<10^{-15}$, $<10^{-16}$, and $<10^{-14}$ mol, respectively. Further details about the sample preparation and analytical procedures are available in Martelli et al. (2014), Rizzo et al. (2015), and Robidoux et al. (2017).

Our protocol represents the first attempt to estimate the N_2 concentration corrected for atmospheric contamination during the simultaneous extraction of CO_2 and noble gases, which is hereafter reported as N_2*. We did this by first quantifying ^{40}Ar corrected for air contamination (^{40}Ar*) and then calculating the atmospheric ^{40}Ar present in our samples:

$^{40}Ar* = {}^{40}Ar_{sample} - [{}^{36}Ar_{sample} \cdot ({}^{40}Ar/{}^{36}Ar)_{air}]$

$^{40}Ar_{air} = {}^{40}Ar_{sample} - {}^{40}Ar*$

Based on the $O_2/{}^{40}Ar$ and $N_2/{}^{40}Ar$ ratios in the atmosphere, we finally calculated the amounts of O_2 and N_2 pertaining to air and subtracted these values from the number of moles of N_2+O_2 measured during extraction. The only assumption was that mantle gases trapped in FI do not contain O_2.

Based on the $^{20}Ne/{}^{22}Ne$ and $^{21}Ne/{}^{22}Ne$ ratios (see Section 5.4), we corrected ^{21}Ne as follows:

$^{21}Ne* = {}^{21}Ne_{sample} - [{}^{22}Ne_{sample} \cdot ({}^{21}Ne/{}^{22}Ne)_{air}]$

Although most of the samples showed a low atmospheric contamination (air has $^4He/{}^{20}Ne = 0.318$, $^{20}Ne/{}^{22}Ne = 9.8$, $^{21}Ne/{}^{22}Ne = 0.029$, and $^{40}Ar/{}^{36}Ar = 295.5$; Ozima and Podosek, 1983), $^3He/{}^4He$ was corrected for contamination based on the measured $^4He/{}^{20}Ne$ ratio as follows:

Rc/Ra = ((R$_M$/Ra)(He/Ne)$_M$ − (He/Ne)$_A$)/((He/Ne)$_M$ − (He/Ne)$_A$)

where subscripts M and A refer to measured and atmospheric theoretical values, respectively. The corrected $^3He/{}^4He$ ratios are hereafter reported as Rc/Ra values. However, the correction was either small or negligible for most of the samples, with a maximum bias of ~0.06 Ra for Opx WG1$_{II}$ showing the lowest $^4He/{}^{20}Ne$ ratio.

The CO_2 samples used in the analyses of C isotopes were extracted and quantified in a glass line, which avoids the adsorption and fractionation of CO_2 that can occur in powders and upon contact with stainless steel. We found a very good agreement between the number of moles of CO_2 extracted and quantified in the glass line and that measured during the extraction of noble gases (Fig. 6). After purification, CO_2 was trapped in a glass sampler and moved to a stable-isotope laboratory for the isotope measurements. Further details about the extraction and analytical protocol can be found in Gennaro et al. (2017). The $^{13}C/{}^{12}C$ is expressed in delta notation ($\delta^{13}C$) as the difference in parts per mil relative to the V-PDB international standard. The analytical error estimated as 1σ was better than 0.3‰.
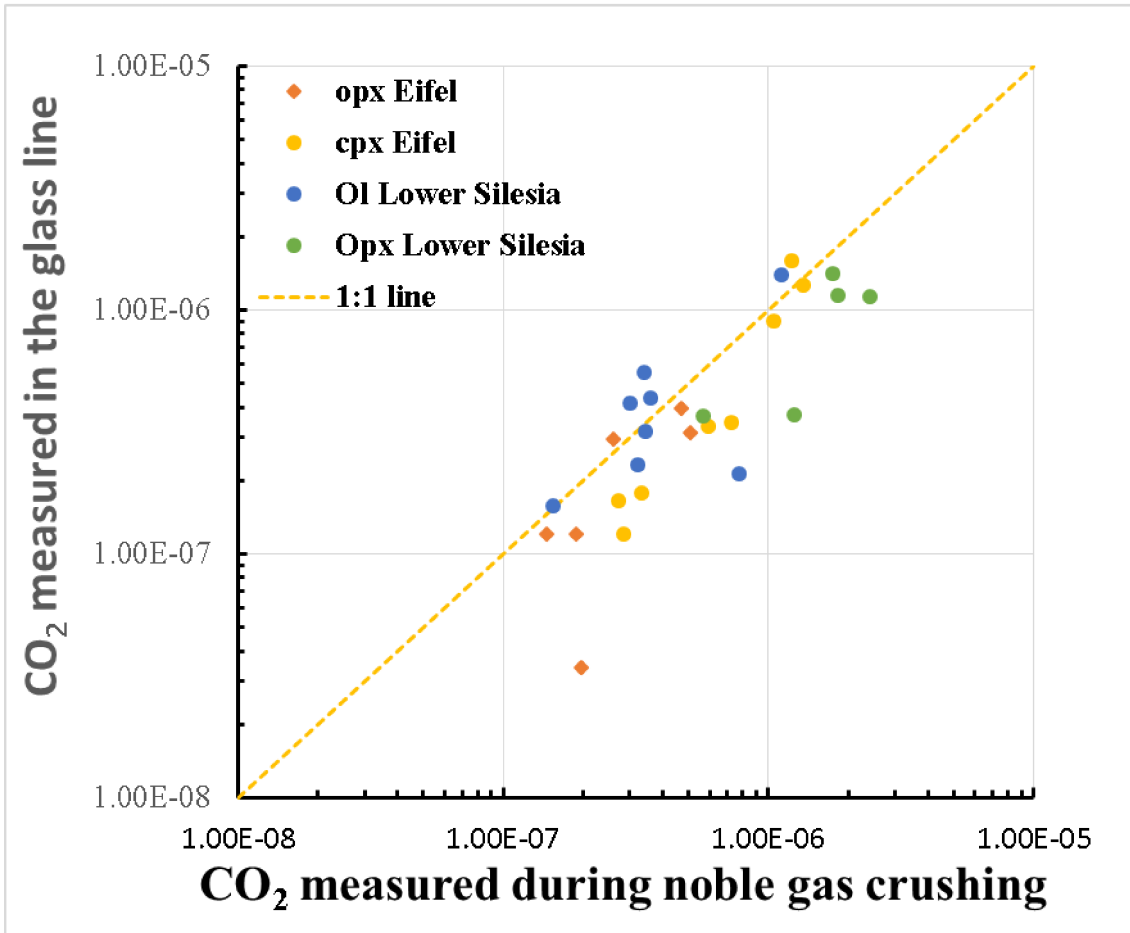
Figure 6. Comparison between CO_2 (mol/g) measured in the extraction system of noble gases crusher and that measured in the system used to extract and purify CO_2. The 1:1 line is also reported (orange dotted line).

Chapter – 3 –

Geochemistry of noble gases and CO₂ in fluid inclusions from lithospheric mantle beneath Lower Silesia

3. Geochemistry of noble gases and CO₂ in fluid inclusions from lithospheric mantle beneath Lower Silesia

3.1 Introduction

During the last 60–70 Myr, Europe and the circum-Mediterranean area have experienced extensive volcanic activity related to their complex geodynamic evolution. The erupted rocks have geochemical characteristics resembling two types of magmatism: (1) orogenic with calc-alkaline magmas, generated in subduction-related settings, and (2) anorogenic with alkaline magmas, generated in intraplate conditions (Lustrino and Wilson, 2007 and references therein). Most cases of anorogenic magmatism started up to 30 Myr later than orogenic magmatism, and brought mantle-derived ultramafic xenoliths to the surface. These xenoliths represent an essential source of information about (1) the nature and evolution of the European lithospheric mantle, (2) the genesis of basic magmas, and (3) magma–mantle geochemical interactions at mantle depth or at the Earth's surface (Downes et al., 2001; Gautheron and Moreira, 2002; Coltorti et al., 2009, 2010; Bonadiman and Coltorti, 2011; Day et al., 2015).

The easternmost major exposure of Cenozoic volcanic activity in Central Europe occurs in the Eger (Ohře) Rift (Bohemian Massif) and its surroundings. The northeastern prolongation of this rift is located in Lower Silesia (southwest Poland) at the margin of the Variscan orogenic belt, where some SiO_2-undersaturated basalts carry mantle xenoliths (Ćwiek et al., 2018 and references therein). Most of these xenoliths are anhydrous spinel-bearing harzburgites and dunites, but there are also some lherzolites. Studies of these xenoliths have shown that the subcontinental lithospheric mantle (SCLM) in this area is strongly depleted (up to 35%), and has been further affected by reactions with CO_2-bearing alkaline silicate metasomatic melt, possibly related to Cenozoic volcanism (e.g., Matusiak-Małek et al., 2014, 2017 and references therein). The amount of percolating metasomatic melt would decrease continuously during this reaction, thereby progressively modifying its chemical composition. Those two factors resulted in the formation of strong heterogeneities that are visible in the modal and chemical compositions of the mantle.

A considerable amount of information about features of the mantle beneath the north-easternmost part of the Eger (Ohře) Rift can be obtained by studying the geochemistry of fluid inclusions (FI) in ultramafic xenoliths. Several studies have already demonstrated that noble gases (He, Ne, and Ar) and CO_2 systematics in FI represent an useful tool for understanding the main processes that modify the original features of the mantle both temporally and spatially (Deines, 2002; Gautheron and Moreira, 2002; Gautheron et al., 2005; Martelli et al., 2011, 2014; Correale et al., 2012, 2016; Day et al., 2015; Gennaro et al., 2017). However, contemporaneous measurements of He, Ne, and Ar isotopes in European mantle xenoliths are limited to a few sample suites. Noble gases and C isotopes

of CO_2 have never been studied in mantle xenoliths from Europe and the circum-Mediterranean area, and hence the features of the mantle and its geodynamic implications remain unclear.

To the best of our knowledge, studies of noble gases from central European mantle xenoliths have only involved the volcanic provinces of the French Massif Central, Eifel, and Pannonian Basin (Dunai et al., 1995; Buikin et al., 2005; Gautheron et al., 2005). These studies suggest that the $^3He/^4He$ ratio normalized to the atmosphere is 6.32±0.39 Ra (mean±SD). This range of values is lower than that MORB mantle (8±1 Ra; Graham, 2002) or plume-related settings (e.g., up to 40 Ra in Hawaii and Iceland; Stuart et al., 2003), and the origin of this radiogenic isotope signature is still debated. It has been attributed to a mantle plume with a low $^3He/^4He$ ratio due to either the addition and recycling of crustal materials to a MORB-like source (Dunai and Baur, 1995), or being an original feature of the European SCLM (Gautheron et al., 2005). On the other hand, Ne and Ar isotopes from selected suites of ultramafic xenoliths from the Eifel and Pannonian Basin have been interpreted based on the presence of a mantle plume beneath these areas (Buikin et al., 2005). However, those authors used a multistep crushing method to extract gases from mineral-hosted FI, and this approach is notably less conservative than the single-step crushing applied by Gautheron et al. (2005) because it can result in the release of radiogenic and cosmogenic noble gases trapped within the crystal lattice. The consequences of this methodological difference need to be carefully evaluated and compared.

The present study is the first to investigate the chemistry and isotope composition of noble gases and CO_2 hosted in FI from mantle xenoliths found in basanite rocks from Wilcza Góra (WG) in Lower Silesia, southwest Poland. These data were integrated with the main information obtained in mineralogical and petrological studies to define the features of the mantle beneath this sector of the European SCLM and interpret the results in the context of other European mantle xenoliths. We also compare the isotope composition of FI with that of surface gases emitted along the Eger (Ohře) Rift.

3.2 Petrological background

Xenoliths from WG basanite have been studied by Smulikowski and Kozłowska-Koch (1984) and Matusiak-Małek et al. (2017). They are spinel-bearing peridotites, mostly harzburgites but also some dunites, wehrlites, and clinopyroxenites (Fig. 7); approximately half of the studied xenoliths contained pargasitic amphibole, but their modal composition and dimensions prevented them from being separated for gas analyses. Xenoliths also contain numerous fine-grained intergranular glassy aggregates (so-called melt pockets). Matusiak-Małek et al. (2017) grouped WG xenoliths based on the chemical composition of Ol into (1) group A, characterized by Ol with $Fo_{89.1-92.5}$, (2) group B, characterized by Ol with $Fo_{85.5-88.1}$, and (3) group C (not described here), characterized by Ol with $Fo_{77.0-82.4}$. The forsterite content of Ol is positively correlated with the Mg# values of pyroxenes (Px)

and amphiboles. The entire xenolith suite is interpreted as resulting from a metasomatic reaction between hydrous, CO_2-bearing alkaline silicate melt and a strongly depleted lithospheric mantle. From this viewpoint, group-C xenoliths represent products of reactions involving very high melt/rock ratios, close to that for an open conduit (hydraulic fracturing) system, while group-B and group-A xenoliths record decreasing amounts of melt percolating through and reacting with the refractory mantle. The metasomatic reaction initially enriched the peridotites located close to the source of the agent in Fe and Ti (group B), and the continuum metasomatic interaction introduced Cpx and amphiboles (and possibly also spinel).
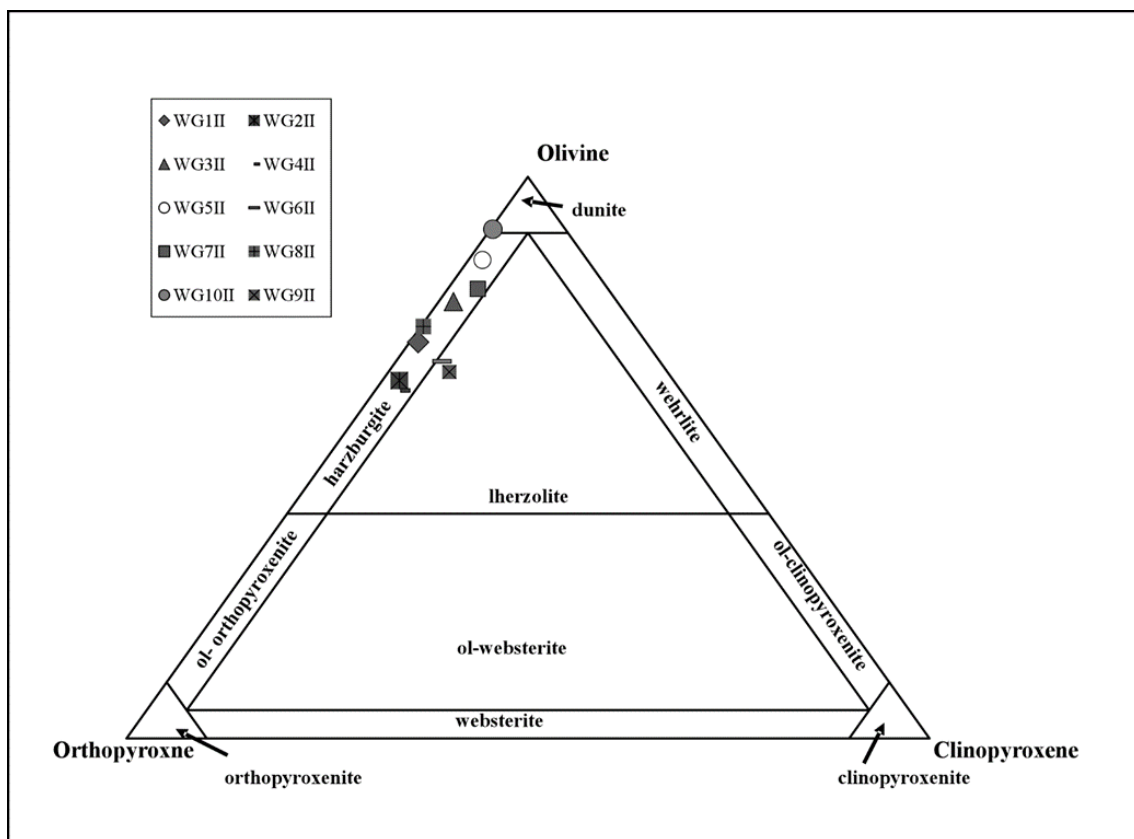
Figure 7. Modal composition of Wilcza Góra xenoliths plotted in the Ol-Opx-Cpx IUGS classification diagram.

3.3 Results

3.3.1 Petrography

The mantle peridotites are fresh and quite homogeneous. The modal proportion of minerals is presented in Figure 7 and Table 1. The studied samples consist of seven harzburgites, two Cpx-poor lherzolites, and one dunite. The harzburgites contain 85–61 vol.% Ol, 34–13 vol.% Opx, <5 vol.% Cpx, and 1–2.3 vol.% spinel, while the two Cpx-poor lherzolites (Cpx <8 vol.%) contain 67–65 vol.% Ol, around 27 vol.% Opx, and <0.5 vol.% spinel. The dunite mainly consists of Ol (>90 vol.%), with a small amount of Opx (<10 vol.%). These rocks common exhibit a protogranular texture; that is,

harzburgites $WG1_{II}$, $WG4_{II}$, and $WG7_{II}$, lherzolite $WG9_{II}$, and dunite $WG10_{II}$. They generally exhibit coarse-grained Opx and Ol (0.6–3 mm; Fig. 8a); Cpx is smaller (typically 0.4–1 mm) than the other phases and it occurs primarily as a protogranular phase or as nearly formed crystals in the reaction zone (Fig. 8b). In a few cases ($WG9_{II}$; Fig. 8c) the Opx core is characterized by Cpx exsolution lamellae. Spinel appears as crystallites associated with a fine-grained reaction zone (Fig. 8b, d).

Lherzolite $WG6_{II}$ and harzburgites $WG5_{II}$ and $WG8_{II}$ exhibit clearly phorphyroclastic (Fig. 8d; $WG5_{II}$) textures and generally contain two generations of both Ol and Opx. The large Ol porphyroclasts were subjected to deformation and developed kink bands, whereas the small neoblasts commonly occur as an embayment and partly replace large Opx and Ol porphyroclasts (Fig. 8d, e).

Harzburgites $WG2_{II}$ and $WG3_{II}$ display a well-developed equigranular/granoblastic texture with Ol arranged with a 120° grain-boundary intersection (Fig. 8f; $WG3_{II}$).

Disseminated amphiboles appear as small anhedral grains that are often associated with the spongy rim of Cpx (Fig. 8g) or clearly enclose Cpx.

orthopyroxene

olivine

a

2 mm

olivine

Reaction zone with clinopyroxene and spinel

spinel

b

2 mm

Clinopyroxene exolution lamellae in orthopyroxene

c

2 mm

Porphyroclastic texture

spinel

d

2 mm

orthopyroxene

e

2 mm

Triple juctions

Olivine

f

2 mm

Amphibole

Olivine

g

2 mm
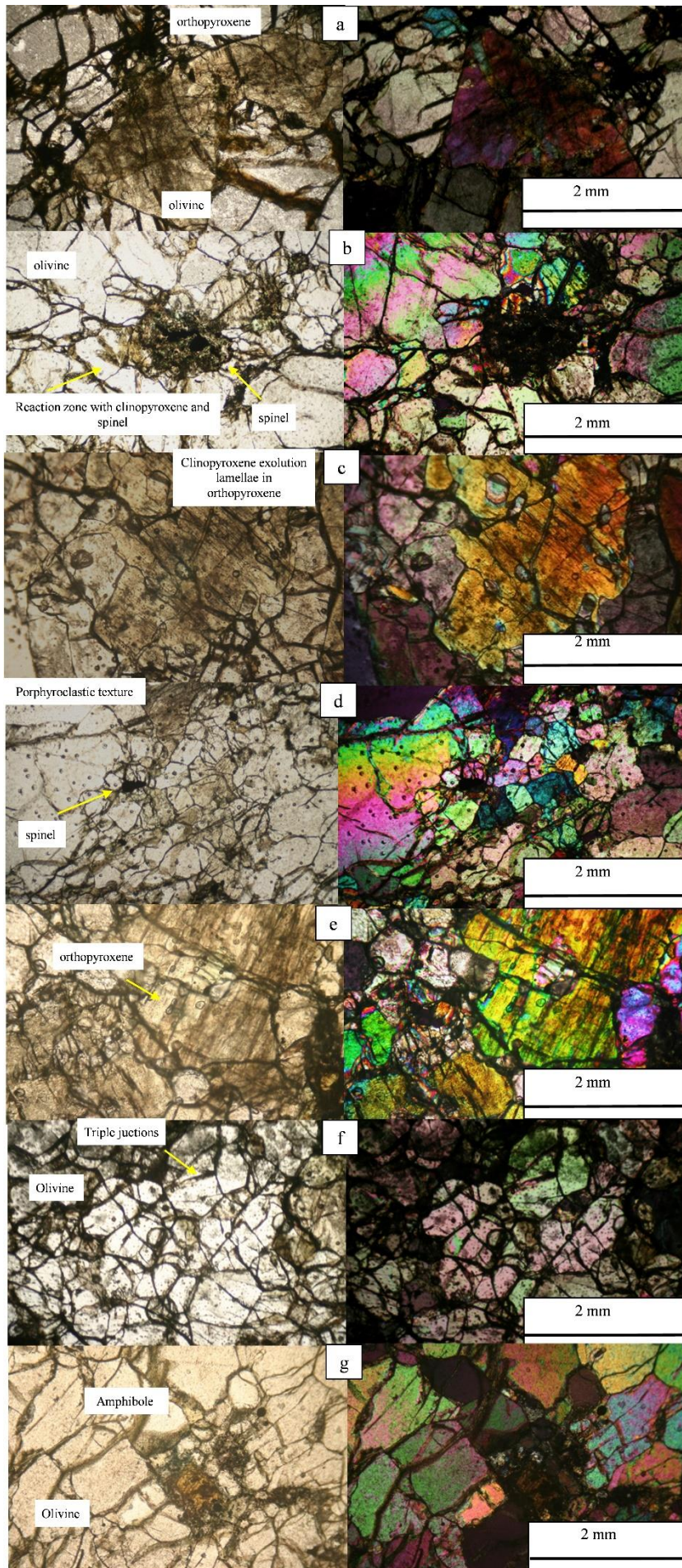
Figure 8. a, b, c, d, e, f, g) Photomicrographs of representative microstructures of WG xenoliths in transmitted plane-polarized light (left) and in cross-polarized light (right). In detail: a and b) images showing protogranular textures with large Opx and Ol grains (WG4$_{II}$); b) a reaction zone with the spongy rims of Cpx and spinel (WG1$_{II}$); c) a protogranular texture with large Opx hosting Cpx exsolution lamellae (WG9$_{II}$); d) examples of porphyroclastic textures with Ol neoblasts slightly oriented and with small Ol replacing large Opx. f) Equigranular texture with Ol converging at 120 degrees. g) Small amphiboles associated with the spongy rim of Cpx. Bubbles are evident in Ol (WG7$_{II}$; d).

Table 1 -Textural features and modal composition of Wilcza Góra xenoliths. Modal content of phases by volume percentages.

	Lithology	Texture	Olivine	Orthopyroxene	Clinopyroxene	Spinel	Amphibole
WG1$_{II}$	Harzburgite	protogranular	69.3	27.9	1.0	1.8	-
WG2$_{II}$	Harzburgite	equigranular	63.0	32.8	3.0	1.0	-
WG3$_{II}$	Harzburgite	equigranular	75.0	20.0	2.0	2.0	trace
WG4$_{II}$	Harzburgite	protogranular	60.6	34.1	3.1	2.2	trace
WG5$_{II}$	Harzburgite	porphyroclastic	84.7	13.0	1.7	0.5	trace
WG6$_{II}$	Lherzolite	porphyroclastic	67.1	27.1	5.7	trace	-
WG7$_{II}$	Harzburgite	protogranular	77.6	15.8	3.6	2.3	-
WG8$_{II}$	Harzburgite	porphyroclastic	71.9	25.8	trace	2.3	-
WG9$_{II}$	Lherzolite	protogranular	64.9	27.0	7.6	0.6	-
WG10$_{II}$	Dunite	protogranular	90.9	9.1	trace	trace	trace

3.3.2 Mineral chemistry

The mineral chemistry data are reported in Table 2. On the basis of Fo [calculated as $Mg/(Mg+Fe_{tot})$ in atoms per formula unit] versus the distribution of NiO contents, Ol could be divided into two distinct groups: group A (Fo = 89.12–91.48 and NiO = 0.31–0.43 wt.%) and group B (Fo = 85.53–88.13 and NiO = 0.25–0.37 wt.%); this categorization is consistent with groups A and B reported by Matusiak-Małek et al. (2017) (Fig. 9a).

The two geochemical groups observed in terms of Fo components in Ol are also observed in Px. Opx (En = 85.14–76.85, Fs = 10.07–21.09, and Wo = 1.77–2.04) exhibits a negative correlation between Al_2O_3 contents (1.27–3.31 wt.%) and Mg# values [$Mg/(Mg+Fe_{tot})$ = 86.65–92.05 mol.%; Fig. 9b], without any significant variation in relation to petrographic features (i.e., Opx in the reaction zone or Opx with exsolution lamellae). Cpx (Wo = 38.52–55.47, En = 52.11–33.91, and Fs = 9.36–10.6) is characterized by a low TiO_2 content (0.02–0.27 wt.%; Fig. 10a). Samples WG7$_{II}$ and WG10$_{II}$ have slightly elevated TiO_2 (0.66 wt.%), whereas a few of the secondary grains in samples WG4$_{II}$ and WG6$_{II}$ have TiO_2 contents ranging from 1 to 1.20 wt.%. In both Opx and Cpx the Al_2O_3 content (1.43–4.24 wt.%) is negatively correlated with Mg# (87.81–90.84) (Fig. 10b). Irrespective of the lithology, spinel has Mg# values within the narrow range of 46.94–55.79, while Cr# [= Cr/(Cr+Al)

mol.%] values span a larger range (38.88–69.46; Fig. 10c). The only exception is for sample WG5$_{II}$ that plots out of the mentioned ranges (Mg#=71.63–71.78; Cr#=27.06–27.58; Fig. 10c).

According to the classification of Leake et al. (1997), the amphiboles are pargasite (samples WG3$_{II}$ and WG4$_{II}$) and ferropargasite (samples WG5$_{II}$ and WG10$_{II}$), whose Mg# values span from 84.63 to 88.88 and their Al$_2$O$_3$ and TiO$_2$ contents are in the ranges of 12.23–13.74 and 0.81–2.85 wt.%, respectively (Fig. 10d, 10e).
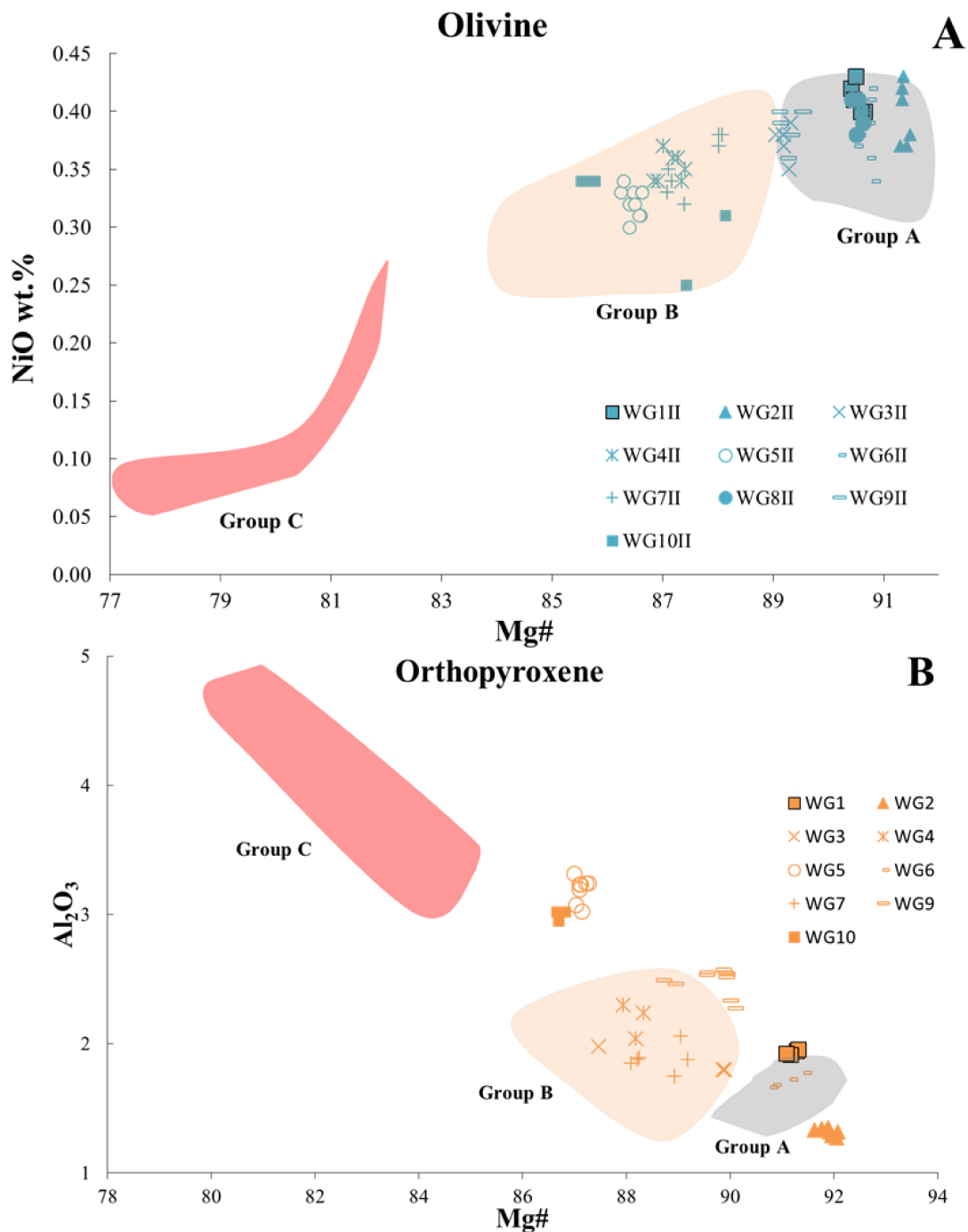
Figure 9. a) Mg# versus NiO concentration in Ol. b) Mg# versus Al$_2$O$_3$ in Opx from WG xenoliths. The indicated areas are for the group data reported by Matusiak-Małek et al. (2017).
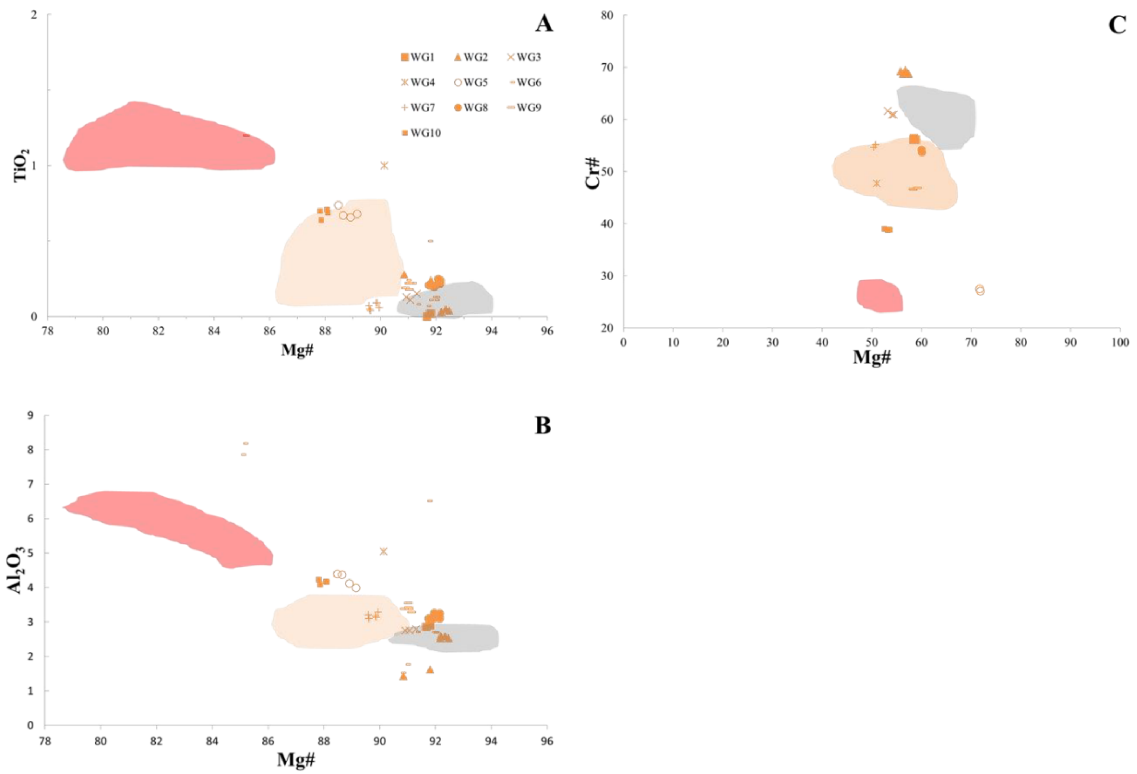
Figure 10. Variation of A) Mg# *vs.* TiO$_2$ wt. % and B) Al$_2$O$_3$ wt. % *vs.* in Cpx in WG xenoliths. C) Variation of Mg# *vs.* Cr# (Cr#= [Cr/(Cr + Al) at%]) in spinel. Fields report data from Matusiak-Małek et al. (2017).

Table 2 - Chemistry of minerals forming Wilcza Góra xenoliths

	olivine									
	$WG1_{II}$	$WG2_{II}$	$WG3_{II}$	$WG4_{II}$	$WG5_{II}$	$WG6_{II}$	$WG7_{II}$	$WG8_{II}$	$WG9_{II}$	$WG10_{II}$
Group	A	A	A	B	B	A	B	A	A	B
n. of analyses	5	6	6	7	10	9	7	4	6	5
SiO_2	40.46	40.71	40.29	39.64	39.81	40.61	40.06	40.46	40.28	39.76
TiO_2	0.00	0.00	0.01	0.00	0.01	0.00	0.00	0.00	0.00	0.02
Al_2O_3	0.01	0.01	0.01	0.01	0.02	0.01	0.01	0.01	0.02	0.02
Fe_2O_3										
FeO	9.25	8.50	10.47	12.33	12.92	9.16	11.98	9.25	10.38	13.00
MnO	0.15	0.14	0.17	0.19	0.19	0.15	0.18	0.14	0.15	0.23
MgO	49.60	50.48	48.53	46.87	46.33	49.83	47.29	49.61	48.73	46.75
CaO	0.05	0.05	0.05	0.06	0.06	0.05	0.05	0.05	0.06	0.11
Na_2O										
K_2O										
Cr_2O3	0.02	0.02	0.02	0.01	0.01	0.02	0.01	0.02	0.02	0.02
NiO	0.41	0.40	0.38	0.35	0.32	0.38	0.35	0.40	0.39	0.32
Total	99.95	100.30	99.91	99.47	99.66	100.21	99.94	99.94	100.02	100.22
FeOtot										
Mg#	90.52	91.37	89.20	87.14	86.47	90.65	87.55	90.53	89.32	86.50
Cr#										
A.f.u.										
Si	0.992	0.991	0.994	0.991	0.995	0.993	0.995	0.992	0.992	0.990
Ti										
Al										0.001
FeIII										
FeII	0.190	0.173	0.216	0.258	0.270	0.187	0.249	0.190	0.214	0.271
Mn	0.003	0.003	0.004	0.004	0.004	0.003	0.004	0.003	0.003	0.005
Mg	1.813	1.832	1.784	1.747	1.726	1.815	1.750	1.813	1.789	1.734
Ca	0.001	0.001	0.001	0.002	0.002	0.001	0.001	0.001	0.002	0.003
Na										
K										
Cr										
Ni	0.008	0.008	0.007	0.007	0.006	0.008	0.007	0.008	0.008	0.006

	orthopyroxene								
	WG1$_{II}$	WG2$_{II}$	WG3$_{II}$	WG4$_{II}$	WG5$_{II}$	WG6$_{II}$	WG7$_{II}$	WG9$_{II}$	WG10$_{II}$
Group	A	A	A	B	B	A	B	A	B
n.of analyses	4	7	3	3	8	4	6	11	3
SiO$_2$	56.66	57.87	56.61	56.23	55.32	57.13	56.45	56.62	55.62
TiO$_2$	0.02	0.02	0.05	0.15	0.22	0.03	0.08	0.07	0.27
Al$_2$O$_3$	1.93	1.32	1.86	2.19	3.19	1.71	1.89	2.48	3.00
Fe$_2$O$_3$	0.12	0.02	0.00	0.00	0.02	0.05	0.02	0.01	0.10
FeO	5.77	5.47	7.16	7.81	8.34	5.94	7.51	6.83	8.61
MnO	0.15	0.14	0.18	0.20	0.19	0.15	0.19	0.16	0.23
MgO	34.28	34.93	32.84	32.59	31.75	34.20	32.88	33.34	31.90
CaO	0.67	0.73	0.73	0.77	0.77	0.74	0.79	0.73	0.84
Na$_2$O	0.05	0.09	0.09	0.05	0.04	0.07	0.06	0.05	0.05
K$_2$O	0.00	0.00	0.00	0.00	0.00	0.00	0.00	0.00	0.00
Cr$_2$O3	0.51	0.51	0.50	0.46	0.48	0.54	0.40	0.54	0.37
NiO									
Total	100.17	101.03	99.39	100.31	100.17	100.34	100.19	100.59	100.96
FeOtot	5.88	5.49	7.16	7.81	8.36	5.99	7.53	6.85	8.71
Mg#	91.22	91.89	89.07	88.15	87.13	91.05	88.62	89.66	86.72
Cr#									
A.f.u.									
Si	1.949	1.970	1.973	1.950	1.926	1.963	1.957	1.948	1.924
Ti	0.000	0.001	0.001	0.004	0.006	0.001	0.002	0.002	0.007
Al	0.078	0.053	0.077	0.090	0.131	0.069	0.077	0.101	0.122
FeIII	0.003	0.000	0.000	0.000	0.000	0.001	0.000	0.000	0.003
FeII	0.166	0.155	0.208	0.226	0.242	0.171	0.218	0.196	0.249
Mn	0.005	0.004	0.005	0.006	0.006	0.004	0.006	0.005	0.007
Mg	1.757	1.772	1.705	1.684	1.648	1.751	1.698	1.709	1.645
Ca	0.025	0.027	0.028	0.029	0.029	0.028	0.030	0.027	0.031
Na	0.003	0.006	0.006	0.003	0.003	0.005	0.004	0.004	0.003
K									
Cr	0.014	0.014	0.014	0.013	0.013	0.014	0.011	0.015	0.010
Ni									

	clinopyroxene									
	WG1$_I$	WG2$_{II}$	WG3$_{II}$	WG4$_{II}$	WG5$_{II}$	WG6$_{II}$	WG7$_{II}$	WG8$_{II}$	WG9$_{II}$	WG10II
Group	A	A	A	B	B	A	B	A	A	B
n.of analyses	3	6	3	1	4	11	6	8	5	4
SiO$_2$	53.48	54.72	53.61	50.64	52.06	52.65	53.31	53.25	53.13	52.29
TiO$_2$	0.01	0.11	0.13	1.21	0.69	0.36	0.07	0.22	0.21	0.69
Al$_2$O$_3$	2.91	2.22	2.77	5.05	4.23	3.85	3.17	3.15	3.40	4.17
Fe$_2$O$_3$	0.29	0.14	0.27	0.21	0.20	0.22	0.33	0.17	0.09	0.25
FeO	2.42	2.67	2.64	3.00	3.42	2.88	3.02	2.41	2.78	3.70
MnO	0.08	0.10	0.11	0.10	0.11	0.10	0.11	0.09	0.10	0.15
MgO	16.73	17.82	16.55	16.36	16.02	16.44	16.27	16.61	16.26	16.07
CaO	21.47	19.96	21.45	20.92	21.90	20.78	21.17	21.75	21.67	21.42
Na$_2$O	1.06	1.25	1.12	0.68	0.71	1.07	1.18	0.95	0.93	0.84
K$_2$O										
Cr$_2$O3	1.28	1.74	1.43	1.45	0.87	1.92	1.51	1.50	1.42	1.05
NiO										
Total	99.74	100.71	100.08	99.62	100.20	100.26	100.12	100.09	99.95	100.61
FeOtot	2.68	2.79	2.88	3.19	3.60	3.07	3.31	2.57	2.86	3.92
Mg#	91.75	91.97	91.10	90.14	88.80	90.38	89.75	92.02	91.02	87.96
Cr#										
A.f.u.										
Si	1.940	1.962	1.942	1.850	1.892	1.906	1.932	1.929	1.930	1.893
Ti	0.001	0.003	0.004	0.033	0.019	0.010	0.002	0.006	0.006	0.019
Al	0.125	0.094	0.118	0.217	0.181	0.165	0.136	0.135	0.146	0.178
FeIII	0.008	0.003	0.008	0.006	0.005	0.006	0.009	0.005	0.002	0.007
FeII	0.073	0.080	0.080	0.092	0.104	0.087	0.091	0.073	0.084	0.112
Mn	0.002	0.003	0.003	0.003	0.004	0.003	0.003	0.003	0.003	0.005
Mg	0.905	0.952	0.893	0.890	0.868	0.886	0.879	0.897	0.880	0.867
Ca	0.835	0.767	0.833	0.819	0.853	0.807	0.822	0.844	0.843	0.831
Na	0.075	0.087	0.079	0.048	0.050	0.075	0.083	0.067	0.065	0.059
K										
Cr	0.037	0.049	0.041	0.042	0.025	0.055	0.043	0.043	0.041	0.030
Ni										

	spinel								
	$WG1_{II}$	$WG2_{II}$	$WG3_{II}$	$WG4_{II}$	$WG5_{II}$	$WG7_{II}$	$WG8_{II}$	$WG9_{II}$	$WG10_{II}$
Group	A	A	A	B	B	B	A	A	B
n.of analyses	3	5	3	1	2	3	2	3	4
SiO_2	0.11	0.02	0.02	0.06	0.05	0.04	0.04	0.03	0.10
TiO_2	0.05	0.07	0.40	0.92	1.01	0.21	0.44	0.34	1.24
Al_2O_3	22.08	15.40	18.83	25.12	40.89	21.87	23.62	27.78	30.68
Fe_2O_3	4.95	4.05	7.20	6.90	6.08	7.36	4.64	4.73	6.17
FeO	12.97	13.79	13.84	15.80	8.38	15.10	12.95	13.69	15.77
MnO	0.33	0.40	0.39	0.10	0.21	0.37	0.34	0.30	0.36
MgO	13.80	12.76	13.32	12.85	19.70	12.49	14.41	14.23	13.57
CaO	0.06	0.01	0.01	0.01	0.27	0.11	0.00	0.04	0.09
Na_2O	0.00	0.00	0.00						
K_2O	0.00	0.00	0.00						
Cr_2O3	42.33	51.28	44.17	34.26	22.92	39.82	41.33	36.32	29.17
NiO	0.17	0.15	0.17	0.24	0.30	0.16	0.17	0.17	0.23
Total	96.85	97.92	98.35	96.26	99.78	97.53	97.92	97.64	97.36
FeOtot	17.42	17.43	20.32	22.01	13.85	21.72	17.13	17.94	21.32
Mg#	58.53	56.61	53.87	51.00	71.71	50.62	59.98	58.57	53.14
Cr#	56.25	69.07	61.14	47.78	27.32	54.97	54.00	46.72	38.93
A.f.u.									
Si	0.004	0.001	0.001	0.002	0.002	0.001	0.001	0.001	0.003
Ti	0.001	0.002	0.009	0.022	0.021	0.005	0.010	0.008	0.028
Al	0.820	0.587	0.702	0.934	1.329	0.816	0.861	0.998	1.097
FeIII	0.120	0.100	0.170	0.164	0.125	0.173	0.105	0.110	0.140
FeII	0.343	0.372	0.367	0.417	0.195	0.397	0.335	0.350	0.400
Mn	0.009	0.011	0.011	0.003	0.005	0.010	0.009	0.008	0.009
Mg	0.648	0.615	0.628	0.604	0.810	0.589	0.664	0.647	0.614
Ca	0.002	0.000	0.000		0.008	0.004	0.000	0.001	0.003
Na	0.000	0.000	0.000		0.000	0.000	0.000	0.000	0.000
K	0.000	0.000	0.000		0.000	0.000	0.000	0.000	0.000
Cr	1.054	1.310	1.106	0.855	0.500	0.996	1.010	0.875	0.700
Ni	0.005	0.004	0.005		0.007	0.004	0.004	0.004	0.006

	amphibole			
	WG3$_{II}$	WG4$_{II}$	WG5$_{II}$	WG10$_{II}$
Group	A	B	B	B
n.of analyses	4	1	5	8
SiO$_2$	44.28	43.13	42.56	42.67
TiO$_2$	0.83	1.90	2.59	2.76
Al$_2$O$_3$	12.25	12.84	13.51	13.19
Fe$_2$O$_3$				
FeO	4.09	4.82	5.02	5.29
MnO	0.08	0.08	0.09	0.10
MgO	18.19	17.30	16.78	16.67
CaO	10.97	11.27	11.50	11.24
Na$_2$O	3.20	3.00	2.77	2.90
K$_2$O	0.83	0.89	0.96	0.98
Cr$_2$O3				
NiO				
Total	94.72	95.23	95.77	95.79
FeOtot				
Mg#	88.79	86.47	85.64	84.89
Cr#				
A.f.u.				
Si	6.47	6.308	6.20	6.23
Ti	0.09	0.209	0.28	0.30
Al	2.11	2.213	2.32	2.27
FeIII	0.00	0.000	0.00	0.00
FeII	0.50	0.590	0.61	0.65
Mn	0.01	0.010	0.01	0.01
Mg	3.96	3.772	3.65	3.63
Ca	1.72	1.766	1.80	1.76
Na	0.91	0.851	0.78	0.82
K	0.15	0.167	0.18	0.18
Cr				
Ni				

3.3.3 Chemistry of FI

The chemistry of FI hosted in WG xenoliths is reported in Table 3 and shown in Figs. 11 and 12. The gas mixture is dominated by CO_2, which ranges from 0.9×10^{-7} to 24×10^{-7} mol/g (Fig. 11a and 11b). N_2 corrected for atmospheric contamination (N_2*) represents the second major species, whose content varies from 0.86×10^{-9} to 42×10^{-9} mol/g (Fig. 11b). The atmospheric component in FI, which here is considered to be N_2+O_2+Ar, varies within the same order of magnitude (1.2×10^{-10} to 1.1×10^{-9} mol/g) and with no systematic differences between mineral phases (Table 3), and represents <0.3% of the total gas mixture. ^{40}Ar* is within the range of 0.53–7.2×10^{-11} mol/g (Fig. 11c and 11d), while ^4He ranges from 0.1×10^{11} to 1.4×10^{11} mol/g (Fig. 11a and 11c). The ^{20}Ne concentration ranges from 0.47×10^{-14} to 7.3×10^{-14} mol/g (Table 3). Finally, ^{21}Ne* varies from 9.3×10^{-19} to 1.1×10^{-17} mol/g (Fig. 12).

The average numbers of moles of CO_2, N_2^*, $^{40}Ar^*$, and $^{21}Ne^*$ are higher in Opx than in Ol, which in turn shows a wider compositional range, while the values in Cpx are intermediate (Figs. 11 and 12). The only exception is for He, whose content is comparable in Ol and Opx, while it is lowest in Cpx (Figs. 11a and 12). Among Ol, samples $WG4_{II}$, $WG7_{II}$, and $WG10_{II}$ (Fo<88) show the highest concentrations of He and CO_2, and among the largest amounts of N_2^*, $^{40}Ar^*$, and $^{21}Ne^*$. CO_2 is positively correlated with N_2^*, $^{40}Ar^*$, $^{21}Ne^*$, and ^4He (Figs. 11a, 11b, 11d, and 12c), indicating that the CO_2-rich FI are also rich in the other gas species.
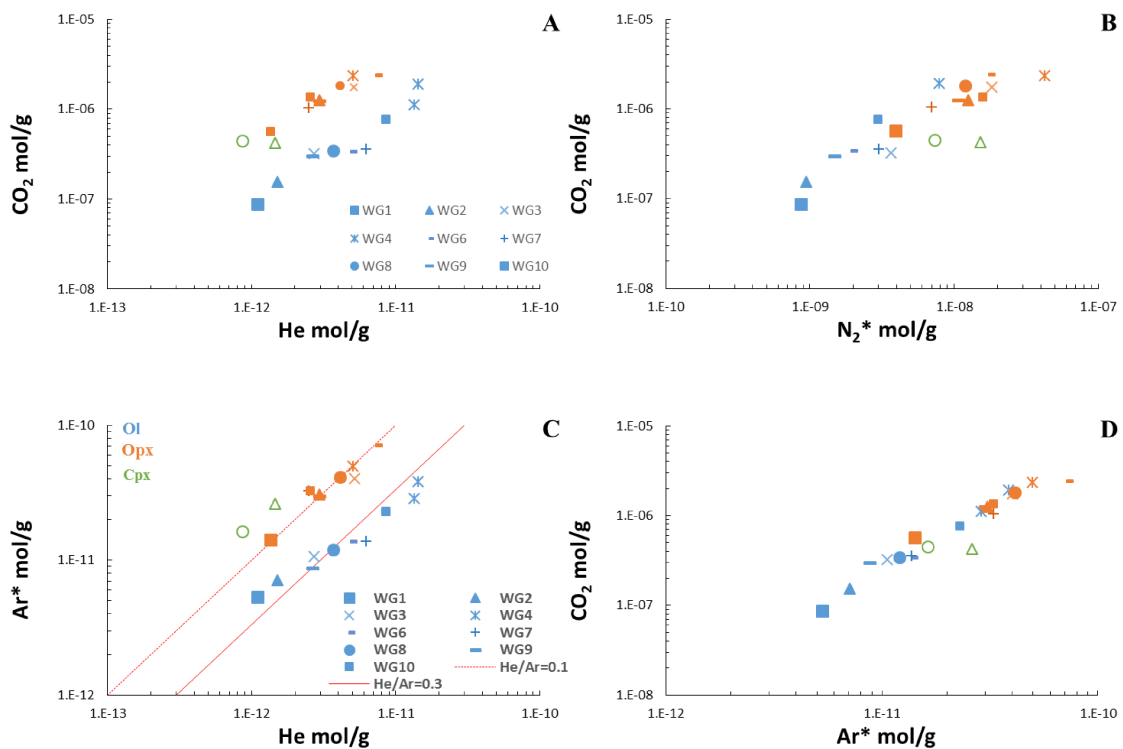
Figure 11. Elemental concentrations measured in FI after single-step crushing of CO_2 versus a) He, b) N_2^*; diagram of concentrations of Ar^* versus c) He and d) CO_2.
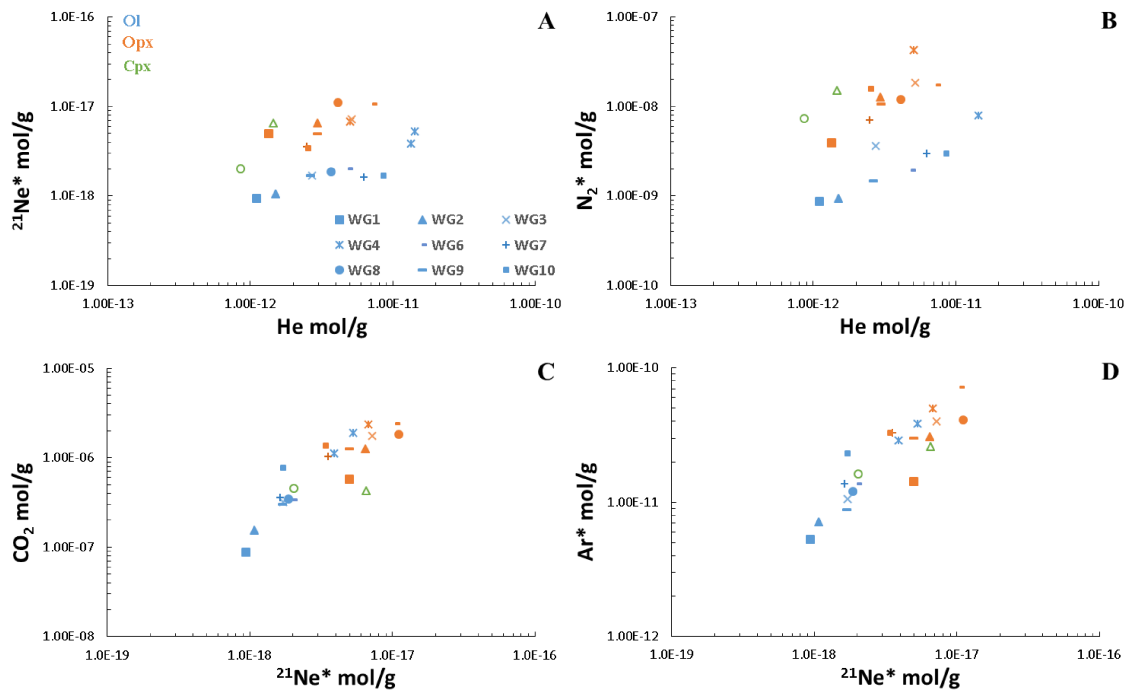
Figure 12. Elemental concentration of He, ^{21}Ne*, CO$_2$, N$_2$*, and Ar* measured in fluid inclusions.

Table 3 - Geochemistry of fluid inclusions hosted in minerals forming mantle xenoliths from Wilcza Góra. Ol stands for olivine, cpx for clinopyroxene, and opx for orthopyroxene. [#]Indicates CO$_2$ measured from glass line. Among these measurements, those reported in italics and underlined are single analysis while the other represent average of two or more replicates

Sample	Mineral	weight (g)	^{4}He mol/g	^{20}Ne mol/g	^{21}Ne mol/g	^{22}Ne mol/g	CO$_2$	N$_2$*	Air mol/g	^{40}Ar mol/g	^{36}Ar mol/g	^{40}Ar* mol/g
WG1$_{II}$	Ol	1.0066	1.10E-12	5.27E-15	1.61E-17	5.26E-16	8.75E-08	8.62E-10	1.26E-10	6.48E-12	3.95E-15	5.31E-12
WG1$_{II}$	Opx	0.30161	1.35E-12	4.26E-14	1.28E-16	4.27E-15	5.69E-07	3.91E-09	3.36E-10	1.73E-11	1.06E-14	1.42E-11
WG2$_{II}$	Ol	1.00371	1.50E-12	9.20E-15	2.81E-17	9.35E-16	1.54E-07	9.38E-10	4.31E-10	1.11E-11	1.36E-14	7.10E-12
WG2$_{II}$	Cpx	0.01834	1.45E-12	3.54E-14	1.08E-16	3.57E-15	4.25E-07	1.52E-08	8.49E-10	3.40E-11	2.67E-14	2.61E-11
WG2$_{II}$	Opx	0.19729	2.96E-12	1.86E-14	5.94E-17	1.85E-15	1.25E-06	1.26E-08	7.83E-10	3.81E-11	2.47E-14	3.08E-11
WG3$_{II}$	Ol	0.52208	2.73E-12	7.05E-15	2.18E-17	6.97E-16	3.21E-07	3.63E-09	3.41E-10	1.38E-11	1.07E-14	1.06E-11
WG3$_{II}$	Opx	0.21646	5.15E-12	1.40E-14	4.69E-17	1.39E-15	1.75E-06	1.84E-08	5.47E-10	4.53E-11	1.72E-14	4.02E-11
WG4$_{II}$	Ol	0.517	1.34E-11	6.29E-15	2.13E-17	6.04E-16	1.12E-06	n.a.	5.71E-10	3.40E-11	1.80E-14	2.87E-11
WG4$_{II}$	Ol	0.12001	2.56E-12	9.69E-15	3.09E-17	9.44E-16	1.36E-06	1.58E-08	3.85E-10	3.64E-11	1.21E-14	3.29E-11
WG4$_{II}$	Opx	0.09876	7.27E-12	7.33E-14	2.20E-16	7.27E-15	2.42E-06	1.75E-08	1.06E-09	8.14E-11	3.33E-14	7.16E-11
WG6$_{II}$	Ol	1.05665	4.89E-12	4.72E-15	1.53E-17	4.59E-16	3.41E-07	1.94E-09	3.54E-10	1.71E-11	1.11E-14	1.38E-11
WG6$_{II}$	Opx	0.05044	3.68E-12	9.28E-15	2.85E-17	9.22E-16	3.44E-07	n.a.	1.30E-10	1.32E-11	4.09E-15	1.20E-11
WG7$_{II}$	Ol	1.01719	6.24E-12	7.65E-15	2.35E-17	7.59E-16	3.60E-07	2.99E-09	3.41E-10	1.69E-11	1.07E-14	1.38E-11
WG7$_{II}$	Opx	0.02895	4.13E-12	3.54E-14	1.11E-16	3.48E-15	1.83E-06	1.19E-08	5.93E-10	4.67E-11	1.87E-14	4.12E-11
WG8$_{II}$	Ol	0.50791	1.43E-11	4.32E-14	1.30E-16	4.34E-15	1.91E-06	7.91E-09	4.66E-10	4.29E-11	1.47E-14	3.85E-11
WG8$_{II}$	Cpx	0.04533	8.60E-13	4.90E-15	1.56E-17	4.78E-16	4.50E-07	7.31E-09	5.61E-10	2.15E-11	1.77E-14	1.63E-11
WG8$_{II}$	Opx	0.103	5.04E-12	3.96E-14	1.20E-16	3.91E-15	2.35E-06	4.24E-08	7.65E-10	5.67E-11	2.41E-14	4.96E-11
WG9$_{II}$	Ol	1.02294	2.65E-12	6.92E-15	2.16E-17	6.88E-16	3.01E-07	1.48E-09	1.98E-10	1.06E-11	6.25E-15	8.79E-12
WG9$_{II}$	Opx	0.28838	2.50E-12	7.03E-15	2.28E-17	6.62E-16	1.04E-06	6.99E-09	5.56E-10	3.79E-11	1.75E-14	3.27E-11
WG10$_{II}$	Ol	0.90088	8.58E-12	6.06E-15	1.86E-17	5.90E-16	7.73E-07	2.96E-09	9.48E-10	3.18E-11	2.99E-14	2.30E-11
WG10$_{II}$	Opx	0.07229	2.97E-12	5.35E-15	1.96E-17	5.12E-16	1.25E-06	1.07E-08	4.83E-10	3.44E-11	1.52E-14	2.99E-11

Sample	Mineral	^{4}He/^{20}Ne	^{4}He/^{40}Ar*	^{4}He/N$_2$*	^{4}He/CO$_2$	CO$_2$/N$_2$*	CO$_2$/Ar*	Ar*/N$_2$*	R/Ra	Rc/Ra	Err Rc/Ra +/-
WG1$_{II}$	Ol	209.1	0.21	1.28E-03	1.26E-05	101.58	1.65E+04	6.16E-03	5.92	5.93	0.06
WG1$_{II}$	Opx	31.7	0.10	3.45E-04	2.38E-06	145.34	4.00E+04	3.63E-03	6.71	6.77	0.08
WG2$_{II}$	Ol	163.4	0.21	1.60E-03	9.78E-06	163.82	2.16E+04	7.57E-03	5.90	5.91	0.06
WG2$_{II}$	Cpx	41.2	0.06	9.59E-05	3.42E-06	28.03	1.63E+04	1.72E-03	6.85	6.90	0.26
WG2$_{II}$	Opx	159.5	0.10	2.35E-04	2.37E-06	99.51	4.07E+04	2.45E-03	6.54	6.55	0.08
WG3$_{II}$	Ol	386.9	0.26	7.52E-04	8.51E-06	88.34	3.02E+04	2.93E-03	6.18	6.18	0.06
WG3$_{II}$	Opx	368.8	0.13	2.81E-04	2.94E-06	95.44	4.35E+04	2.19E-03	6.27	6.28	0.07
WG4$_{II}$	Ol	2125.5	0.47	n.a.	1.20E-05	n.a.	3.90E+04	n.a.	5.95	5.95	0.05
WG4$_{II}$	Ol	264.0	0.08	n.a.	1.89E-06	n.a.	4.13E+04	n.a.	6.11	6.12	0.07
WG4$_{II}$	Opx	99.2	0.10	4.15E-04	3.01E-06	138.19	3.38E+04	4.09E-03	6.30	6.32	0.09
WG6$_{II}$	Ol	1035.5	0.35	2.52E-03	1.43E-05	175.35	2.47E+04	7.09E-03	5.88	5.88	0.06
WG6$_{II}$	Opx	396.3	0.31	n.a.	1.07E-05	n.a.	2.86E+04	n.a.	5.90	5.91	0.06
WG7$_{II}$	Ol	815.4	0.45	2.09E-03	1.73E-05	120.29	2.61E+04	4.61E-03	5.93	5.93	0.05
WG7$_{II}$	Opx	116.7	0.10	3.47E-04	2.25E-06	153.90	4.45E+04	3.46E-03	6.60	6.61	0.09
WG8$_{II}$	Ol	331.5	0.37	1.81E-03	7.50E-06	241.46	4.95E+04	4.87E-03	6.07	6.07	0.06
WG8$_{II}$	Cpx	175.6	0.05	1.18E-04	1.91E-06	61.51	2.76E+04	2.23E-03	6.66	6.67	0.20
WG8$_{II}$	Opx	127.3	0.10	1.19E-04	2.14E-06	55.43	4.74E+04	1.17E-03	6.06	6.08	0.08
WG9$_{II}$	Ol	383.6	0.30	1.79E-03	8.82E-06	203.16	3.42E+04	5.94E-03	5.94	5.94	0.09
WG9$_{II}$	Opx	355.2	0.08	3.57E-04	2.40E-06	149.10	3.18E+04	4.69E-03	6.26	6.26	0.12
WG10$_{II}$	Ol	1416.6	0.37	2.90E-03	1.11E-05	261.65	3.37E+04	7.77E-03	6.08	6.08	0.06
WG10$_{II}$	Opx	555.6	0.10	2.77E-04	2.38E-06	116.24	4.17E+04	2.79E-03	6.39	6.39	0.07

Sample	Mineral	^{40}Ar/^{36}Ar	Err (%)	^{38}Ar/^{36}Ar	Err (%)	^{20}Ne/^{22}Ne	Err 20/22 +/-	^{21}Ne/^{22}Ne	Err 21/22 +/-	^{3}He	CO$_2$/^{3}He	#CO$_2$	δ^{13}C ‰ VPDB
WG1$_{II}$	Ol	1638.8	0.1	0.18630	0.19	10.07	0.02	0.0308	0.0003	9.08E-18	9.64E+09	n.a.	n.a.
WG1$_{II}$	Opx	1639.9	0.1	0.18893	0.19	10.01	0.02	0.0302	0.0002	1.27E-17	4.48E+10	*3.66E-07*	-3.6
WG2$_{II}$	Ol	818.3	0.7	0.18708	0.19	9.87	0.02	0.0301	0.0002	1.24E-17	1.24E+10	1.58E-07	-3.8
WG2$_{II}$	Cpx	1270.5	0.3	0.18697	0.19	10.07	0.09	0.0308	0.0013	1.40E-17	3.05E+10	n.a.	n.a.
WG2$_{II}$	Opx	1543.4	1.1	0.18940	0.19	10.15	0.02	0.0325	0.0005	2.70E-17	4.64E+10	*3.73E-07*	-4.1
WG3$_{II}$	Ol	1283.5	0.0	0.18470	0.18	10.14	0.03	0.0315	0.0004	2.35E-17	1.37E+10	2.33E-07	-4.2
WG3$_{II}$	Opx	2631.3	0.1	0.19146	0.19	10.15	0.03	0.0342	0.0004	4.50E-17	3.89E+10	1.41E-06	-4.7
WG4$_{II}$	Ol	1890.4	0.9	0.18938	0.19	10.47	0.03	0.0354	0.0007	1.11E-16	1.01E+10	1.40E-06	-4.1
WG4$_{II}$	Ol	3007.1	0.2	0.19221	0.19	10.23	0.07	0.0326	0.0014	2.18E-17	6.24E+10	n.a.	n.a.
WG4$_{II}$	Opx	2445.0	0.1	0.18869	0.19	10.14	0.03	0.0305	0.0005	6.39E-17	3.79E+10	1.13E-06	-4.1
WG6$_{II}$	Ol	1532.6	0.8	0.18676	0.19	10.30	0.02	0.0334	0.0005	3.99E-17	8.53E+09	5.55E-07	-3.9
WG6$_{II}$	Opx	3232.4	0.1	0.18852	0.19	10.09	0.02	0.0310	0.0004	3.02E-17	1.14E+10	3.20E-07	-3.8
WG7$_{II}$	Ol	1579.1	0.7	0.18825	0.19	10.12	0.02	0.0311	0.0004	5.14E-17	6.99E+09	4.34E-07	-4.0
WG7$_{II}$	Opx	2500.2	0.1	0.19080	0.19	10.22	0.03	0.0322	0.0004	3.80E-17	4.82E+10	1.15E-06	-4.0
WG8$_{II}$	Ol	2921.4	0.1	0.18788	0.19	10.05	0.02	0.0302	0.0004	1.21E-16	1.58E+10	n.a.	n.a.
WG8$_{II}$	Cpx	1217.1	0.2	0.18589	0.19	10.41	0.22	0.0333	0.0014	7.97E-18	5.64E+10	n.a.	n.a.
WG8$_{II}$	Opx	2354.5	0.1	0.18628	0.19	10.10	0.02	0.0307	0.0005	4.25E-17	5.53E+10	n.a.	n.a.
WG9$_{II}$	Ol	1702.9	1.3	0.18299	0.18	10.08	0.02	0.0315	0.0003	2.19E-17	1.37E+10	*4.17E-07*	-4.0
WG9$_{II}$	Opx	2163.8	0.3	0.18860	0.19	10.58	0.17	0.0344	0.0027	2.17E-17	4.79E+10	n.a.	n.a.
WG10$_{II}$	Ol	1064.8	0.4	0.18335	0.18	10.35	0.01	0.0319	0.0012	7.25E-17	1.07E+10	2.13E-07	-3.1
WG10$_{II}$	Opx	2260.2	1.6	0.18960	0.19	10.52	0.06	0.0387	0.0007	2.64E-17	4.72E+10	n.a.	n.a.

3.3.4 Isotope compositions of He, Ne, Ar, and CO$_2$ in FI

The ^{3}He/^{4}He ratio not corrected for air contamination (R/Ra) is 5.9–6.2 Ra in Ol, 6.1–6.7 Ra in Opx, and 6.7–6.8 Ra in Cpx (Table 3). Ol from samples WG4$_{II}$, WG7$_{II}$, and WG10$_{II}$ (Fo<88) does not show any significant difference in the ^{3}He/^{4}He ratio. The ^{4}He/^{20}Ne ratio is 163–2125 in Ol, 32–556 in Opx, and 41–176 in Cpx (Table 3). The ^{40}Ar/^{36}Ar ratio is 818–3232 in Ol, 1543–3007 in Opx, and 1217–1270 in Cpx (Table 2). The ^{20}Ne/^{22}Ne and ^{21}Ne/^{22}Ne ratios are 9.9–10.5 and 0.0301–0.0354,

respectively, in Ol, 10.0–10.5 and 0.0302–0.0387 in Opx, and 10.1–10.4 and 0.0308–0.333 in Cpx (Table 3 and Fig. 13).

The ^{3}He/^{4}He ratio corrected for air contamination (Rc/Ra values) is 5.9–6.2 Ra in Ol, 6.1–6.8 Ra in Opx, and 6.7–6.9 Ra in Cpx (Table 3 and Fig. 14). It is worth noting that the ^{3}He/^{4}He ratio increases from Ol to Cpx, with Opx displaying intermediate values (Fig. 14). This increase is decoupled from the He concentration, since Ol covers the entire range of He contents at almost constant ^{3}He/^{4}He ratios (6.0±0.1 Ra; Fig. 14a). On the other hand, the ^{3}He/^{4}He ratios are highest in samples showing the lowest He contents and the largest amounts of CO_2 (Fig. 14b), N_2*, ^{40}Ar*, and ^{21}Ne* (Table 3).

The δ^{13}C value of mantle CO_2 was determined in most of the mantle xenoliths according to the concentration of CO_2 and the availability of crystals (Table 3), with the exception of Cpx from WG2$_{II}$ and WG8$_{II}$, which were not sufficiently abundant to allow further measurements after the noble gases had been measured. δ^{13}C ranges between –4.2‰ and –3.1‰ in Ol and between –4.7‰ and –3.6‰ in Opx, without any evidence of a correlation with the CO_2 contents (Fig. 15a). The ratio is slightly less negative for Ol (–3.8±0.4‰) than for Opx (–4.1±0.4‰). δ^{13}C in Ol was the most negative (–4.2‰) in sample WG3$_{II}$, which also showed the most-negative ratio for Opx (–4.7‰), whereas the least-negative δ^{13}C was measured in WG10$_{II}$, which did not contain enough Opx for the analysis (Table 3).
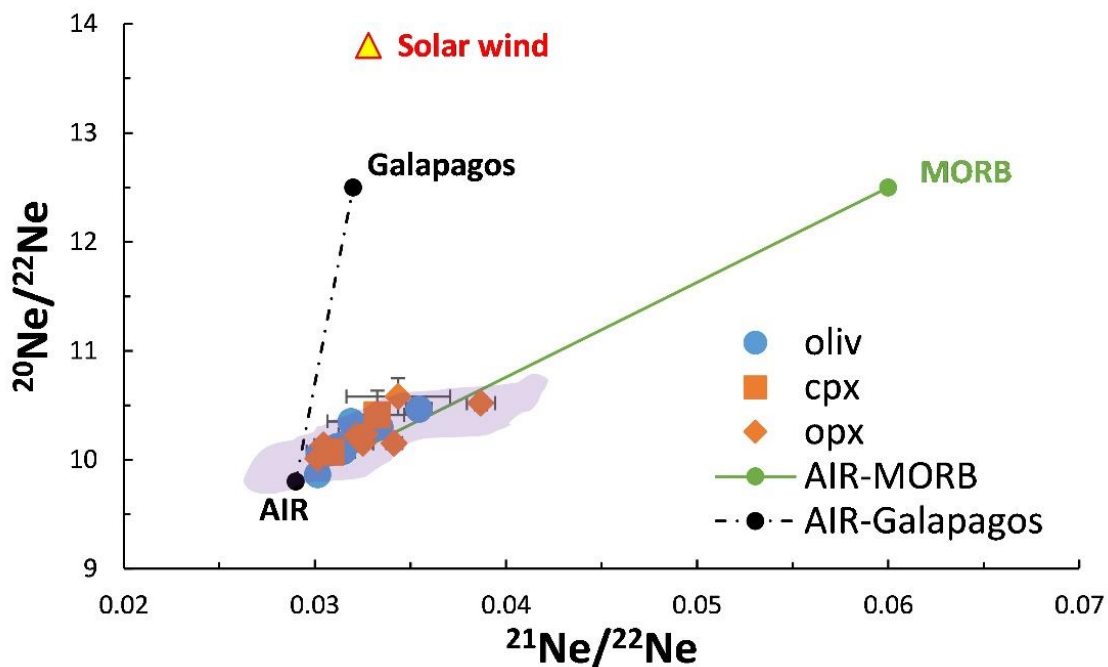
Figure 13. Diagram of ^{21}Ne/^{22}Ne versus ^{20}Ne/^{22}Ne. The green line represents binary mixing between air and a MORB mantle as defined by Sarda et al. (1988) and Moreira et al. (1998) at ^{21}Ne/^{22}Ne = 0.06 and ^{20}Ne/^{22}Ne = 12.5. The black dotted line indicates binary mixing between air and the OIB domain of the Galapagos Islands as determined by Kurz et al. (2009) at ^{21}Ne/^{22}Ne = 0.032 and ^{20}Ne/^{22}Ne = 12.5. The primordial neon composition is also reported as Solar wind

(e.g., Heber et al., 2009), with at $^{21}Ne/^{22}Ne = 0.0328$ and $^{20}Ne/^{22}Ne = 13.8$. The violet area indicates data from other European localities (French Massif Central, Eifel, and Pannonian Basin) measured by Gautheron et al. (2005).
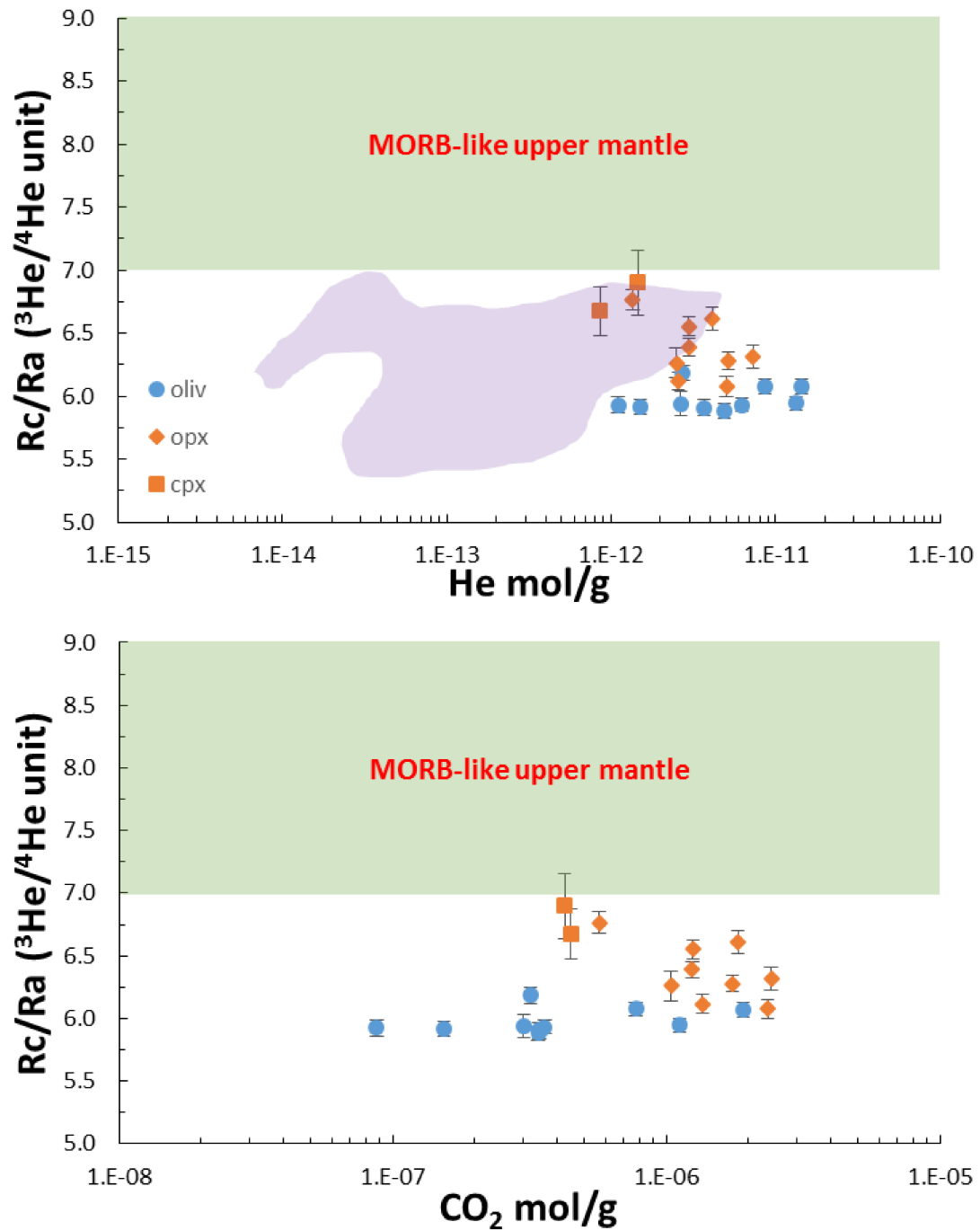
Figure 14. Concentrations of He and CO_2 versus $^3He/^4He$ corrected for air contamination (Rc/Ra values). The green bar indicates the range of $^3He/^4He$ ratios for a MORB-like mantle (8±1 Ra; Graham, 2002). The violet area indicates data from other European localities (French Massif Central, Eifel, and Pannonian Basin) as measured by Gautheron et al. (2005).
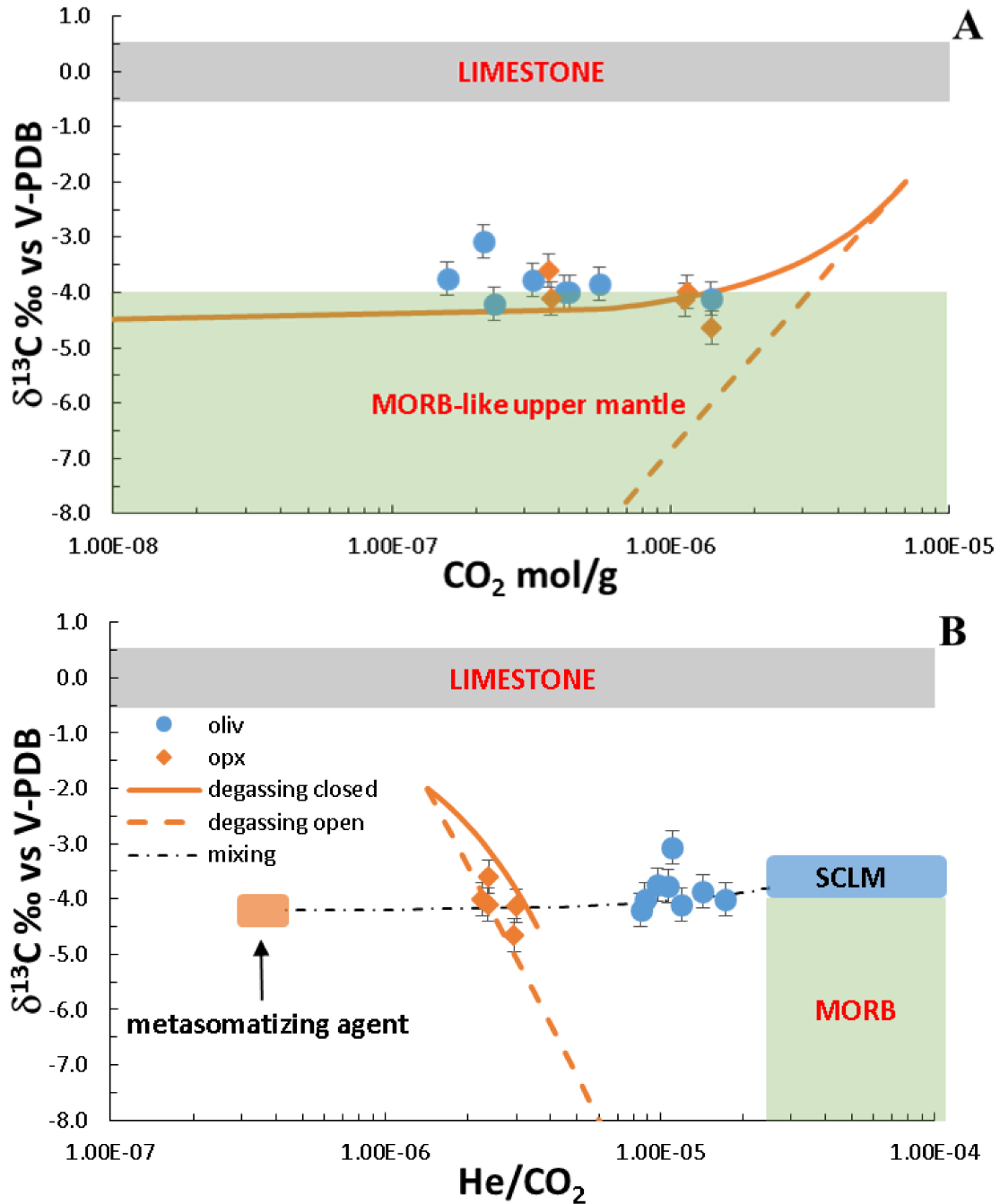
Figure 15. a) CO_2 concentration and b) He/CO_2 versus the C-isotope composition ($\delta^{13}C$ relative to V-PDB) in FI. The green bar (and rectangle in panel b) indicates the range of $\delta^{13}C$ values for a MORB-like mantle ($-8‰ < \delta^{13}C < -4‰$; Sano and Marty, 1995), while the gray bar is for limestone ($-1‰ < \delta^{13}C < +1‰$; Sano and Marty, 1995). The orange solid line indicates a closed-system equilibrium degassing path [equation from Jambon et al. (1986) and Macpherson and Mattey (1994)], while the red dashed line indicates an open-system equilibrium degassing path (equation from Hoefs, 2015). The following starting conditions were assumed for degassing modeling: $CO_2 = 7 \times 10^{-6}$ mol/g, He = 2.5×10^{-11} mol/g, $\delta^{13}C = -4.5‰$, and $\varepsilon_{vap-melt} = 2.5‰$ (Mattey, 1991), solubility of $CO_2 = 7.6 \times 10^{-4}$ cc STP/g/bar (taken from Guillot and Sator, 2011) at 2 GPa and 1673 °K, and solubility of He = 1.9×10^{-3} cc STP/g/bar [assumed considering a He/CO_2 ($\alpha_{He,CO2}$) solubility ratio of 2.5 as indicated by Hilton et al. (1997), Barry et al. (2014), and Gennaro et al. (2017)]. The black dotted line in panel b represents binary mixing between two endmembers: (1) the residual mantle (blue rectangle)

having He/CO$_2$ = 2.5×10^{-5} and δ^{13}C = –3.5‰, and (2) the metasomatic agent (orange rectangle) having He/CO$_2$ = 3.7×10^{-7} and δ^{13}C = –4‰.

3.4 Discussion

3.4.1 Description of FI

The thin section petrographic observations of the WG mantle xenoliths from which Ol, Opx, and Cpx were separated reveal the clear presence of FI within single crystals (Fig. 16A-16D). These FI have variable dimensions, with the smallest ones being few μm in diameter and the biggest reaching some tens of μm (Fig. 16A-16D). We recognized two types of FI, in accordance with the classification made by Roedder (1984): 1) primary inclusions, present as single inclusions or clusters (Figs. 16A and 16B) and/or trails (Fig. 16C) sometimes developed along plans; 2) secondary inclusions that form clusters and/or trails (Fig. 16D) mostly developed along plans. The primary inclusions (Fig 16A-16C) were found always within single coarse grained olivine crystals without continuation to the neighbour grains, an indication that support their primary character (Roedder, 1984); 2) secondary inclusions (Fig. 16D) form clusters or trails that propagate from clinopyroxene (right part of 16D) to the recrystallized fine grained olivine (left part of 16D). We did not observe FI located along healed fractures. We consider secondary inclusions also trails of FI developed within Cpx and Opx, present e.g. as exsolution lamellae (Fig. 16E), because trapped after recrystallization due to metasomatic processes.

A detailed study of FI from WG mantle xenoliths was performed by Ladenberger et al. (2009) with similar findings. For this reason, we did not further investigate the morphology and structure of FI from our samples. Importantly, Ladenberger et al. (2009) inferred that FI were formed under upper-mantle conditions, which supports the reliability of information on mantle features and processes obtained in the present work.
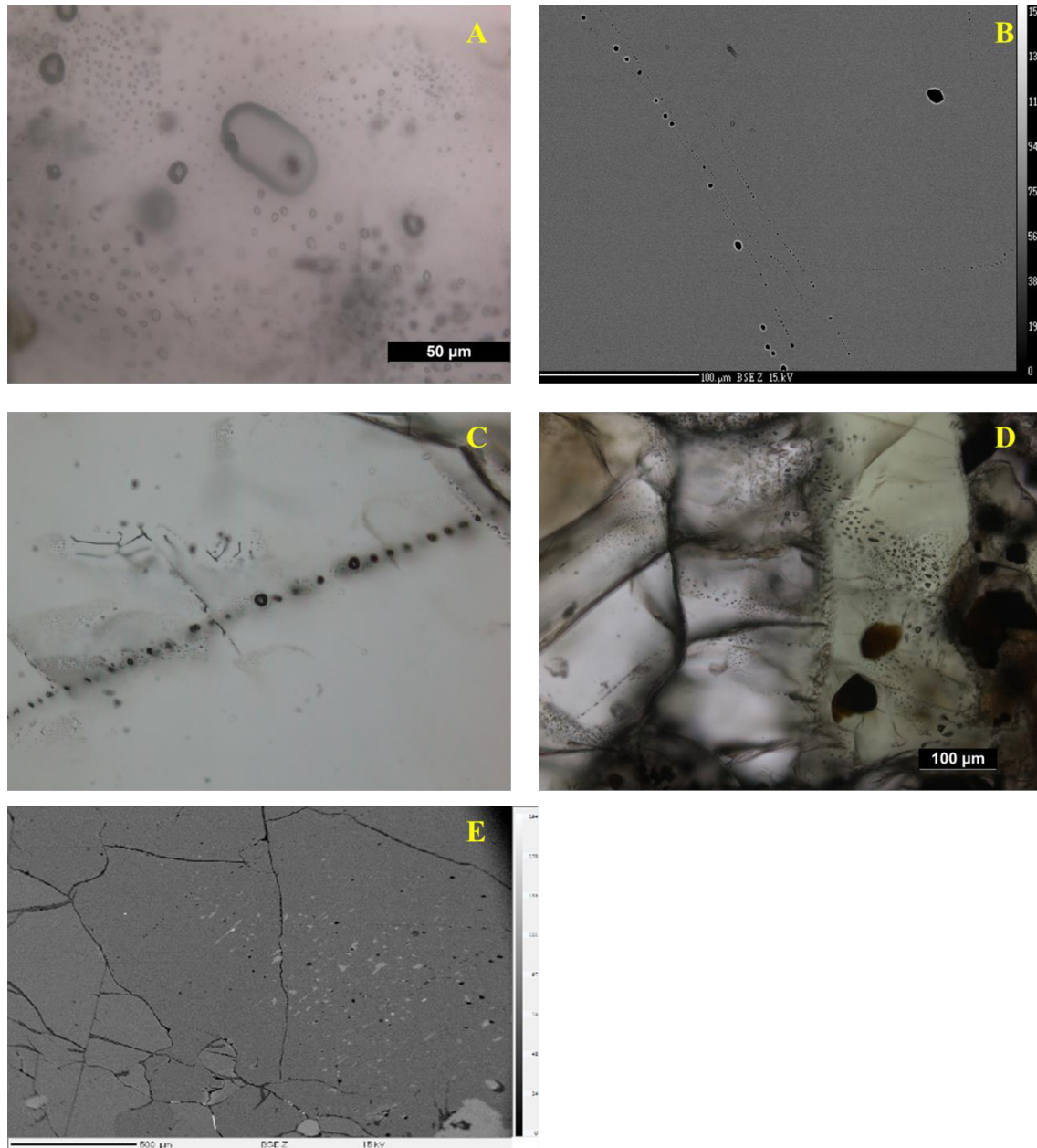
Figure 16. Examples of FI in mantle xenoliths from Wilcza Góra. A-B) Single and isolated primary inclusions in Ol crystals. C) Trail of small primary FI developed along a plan in Ol crystal. D) Clusters of secondary FI in Cpx (in green) that propagate inside a recrystallized olivine (left side of the Cpx). E) Secondary inclusions associated to Cpx exsolution lamellae in a Opx core (WG9$_{II}$).

3.4.2 Petrological evidence of the type and timing of processes modifying local mantle

The textural features and chemistry of major mineral phases of WG mantle xenoliths provide important evidence of the type and timing of processes that acted in modifying the local mantle before the mantle xenoliths were brought to the surface. In a hypothetical melting trend, fusible elements (Ti and Al) tend to decrease with increasing Mg# (Ionov and Hofmann, 2007; Bonadiman and Coltorti, 2011). We estimated the degree of melting of WG mantle based on the contents of Al$_2$O$_3$ versus MgO in primary Opx (Fig. 17) following the model of Upton et al. (2011). Comparing our results with

those of Matusiak-Małek et al. (2017) confirms that WG xenoliths record a residual mantle that is strongly depleted after 25–30% of partial melting (Fig. 17).

The textural characteristics (i.e., secondary Px and the presence of amphiboles; Fig. 9) and geochemical characteristics (i.e., TiO_2 enrichment in Cpx; Fig. 10) of the group-A and group-B xenoliths provide evidence of peridotite–melt interaction. This evidence is in accordance with the findings of Matusiak-Małek et al. (2017), who suggested that Ol from group-A xenoliths represent the residuum after partial melting. Instead, Cpx is clearly metasomatized, and consequently the FI entrapped by this mineral are secondary (Fig. 16D) and inherited by the metasomatic agent. Opx, which exhibits petrographic and mineral chemistry evidence of recrystallization, is at least partially modified by metasomatic interactions. Based on these evidence we argue that the residual mantle was subsequently modified by metasomatic processes.

Finally, the presence of amphiboles, sometimes enclosing Cpx, suggests the introduction of hydrous fluids that could originate from a previous (fossil) subduction, as proposed by the model of Faccenna et al. (2010).
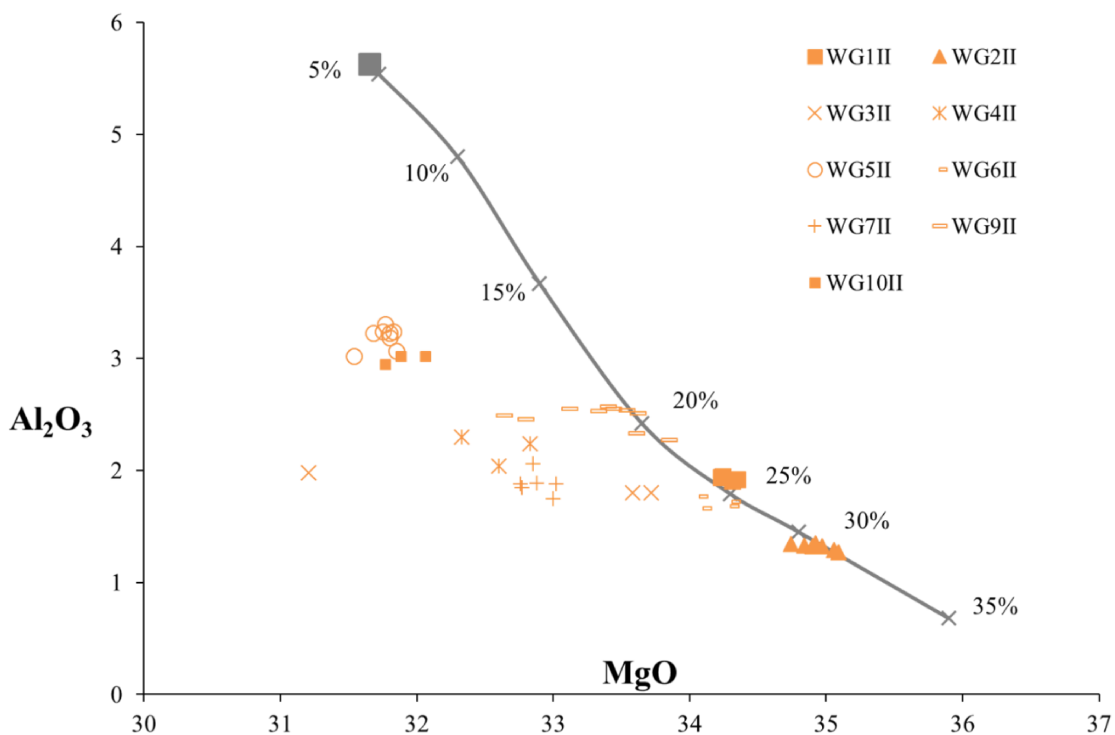
Figure 17. Al_2O_3 vs MgO melting trends (Bonadiman and Coltorti, 2011) for Opx in WG peridotites. The Al_2O_3 and MgO contents of primitive mantle (PM) were calculated based on the primitive mantle composition of McDonough & Sun (1995).

3.4.3 Processes that could modify the geochemistry of FI

3.4.3.1 Atmospheric contamination

While the atmospheric concentration of He is relatively low, the heavy noble gases have accumulated during the evolution of the Earth and so are more prone to contamination. This process can partially or completely mask the original signature recorded by the minerals. The systematics of Ne and Ar isotopes (and complementarily the ^{4}He/^{20}Ne ratio) in WG xenoliths highlight the air contamination in FI, resulting in a mixing between mantle- and atmosphere-derived noble gases (Table 3). The plot of the three Ne isotopes in Fig. 13 shows that our data fall along the theoretical mixing line between air and a MORB-like mantle, defined by Sarda et al. (1988) and Moreira et al. (1998) at ^{21}Ne/^{22}Ne = 0.06 and ^{20}Ne/^{22}Ne = 12.5. Similarly, ^{40}Ar/^{36}Ar values are well below the theoretical ratio in the mantle (^{40}Ar/^{36}Ar up to 44,000; e.g., Burnard et al., 1997; Moreira et al., 1998) or typical mantle-derived samples (e.g., Kaneoka, 1983; Ozima and Podosek, 1983; Allègre et al., 1987), confirming the presence of a certain amount of contamination by atmosphere-derived fluids. Such evidence has also been found in other European as well as worldwide SCLM xenoliths (Valbracht et al., 1996; Matsumoto et al., 1998, 2000, 2001, 2002; Yamamoto et al., 2004; Gautheron et al., 2005; Martelli et al., 2011; Correale et al., 2012, 2016).

Several hypotheses were invoked to explain the presence of air in FI as indicated by the Ne- and Ar-isotope data from mantle xenoliths: (1) contamination of the xenoliths as they are brought from the mantle to the surface, caused by the percolation of melts or volatiles in the xenoliths (i.e., Buikin et al., 2005; Gautheron et al., 2005), (2) air entrapment in microcracks of the minerals during or after the eruptive activity (i.e., Martelli et al., 2011; Correale et al., 2012), and (3) mantle contamination at depth from the dehydration of atmospheric gases from subducting oceanic crust (i.e., Matsumoto et al., 1998, 2000, 2001; Yamamoto et al., 2004; Gurenko et al., 2006). Our observations make the first two hypotheses unlikely because we found no difference between Ol and Px, with the latter having entrapped FI related to the metasomatic agent. In addition, detailed observations of Ol and Px did not produce any evidence of microcracks, since their presence would have produced systematic differences between the analysed minerals. We therefore consider the third hypothesis to be the most reasonable, although there is no evidence of a recent subduction in this part of Europe, with the last subduction event dated to the Ordovician-Devonian period (Kryza et al., 2011). More likely, the recent model proposed by Faccenna et al. (2010 and references therein) proposes that slab fragmentation within the upper mantle may influence outside-arc alkaline magmatism generated both ahead of the slab in the back-arc region and around the lateral edges of the slab. In fact, other geochemical tracers in erupted rocks (Sr, Nd, and Pb isotopes; Lustrino and Wilson, 2007) provide evidence for the recycling of subduction-related volatiles in the European mantle.

The most widely accepted model for explaining the noble-gas geochemistry of SCLM assumes a type of steady state resulting from the mixing between fluids infiltrating from the asthenosphere and those already present in the lithosphere and originating from the recycling of crustal- and atmosphere-derived noble gases introduced from past subduction events into the European mantle (Gautheron and Moreira, 2002; Gautheron et al., 2005). In the case of WG mantle xenoliths, the presence of amphiboles could indicate the presence of hydrous fluids originating from a previous (fossil) subduction event, in accordance with the model proposed by Faccenna et al. (2010).

As is the case in subduction-related settings (i.e., arc volcanoes), Ne- and Ar-isotope ratios are systematically lower and close to theoretical values in the atmosphere (Hilton et al., 2002; Martelli et al., 2014; Di Piazza et al., 2015; Rizzo et al., 2015; Robidoux et al., 2017; Battaglia et al., 2018), irrespective of whether Ol phenocrysts or mantle xenocrysts are analyzed.

3.4.3.2 Diffusive fractionation of He

The clearest evidence from the chemistry of FI is that the He/CO_2, $He/^{40}Ar^*$, He/N_2^*, and $He/^{21}Ne^*$ (not shown) ratios are systematically lower in Cpx and Opx than in Ol (Fig. 18a and 18b). This pattern is not observed for ratios that do not include He [i.e., $CO_2/^{40}Ar^*$, $^{40}Ar^*/N_2^*$, and $^{21}Ne^*/N_2^*$ (not shown); Fig. 18c], which show at least a partial overlapping of data between Ol and Px. This difference might originate from the diffusive loss of He from mantle minerals (e.g., Burnard et al., 1998, 2004 and references therein), which increases from Ol to Cpx. This hypothesis is supported by the diffusion coefficient (D) being significantly higher for He than for the other noble gases (e.g., $D_{4He}/D_{40Ar} = 3.16$ in solid mantle; Burnard, 2004; Yamamoto et al., 2009), N_2^*, and CO_2.

Figure 19 plots $He/^{40}Ar^*$ and He/CO_2 versus the He concentration to determine if the decreases in these ratios are associated with a clear decrease in the He concentration, as expected if partial loss occurs. Such a tendency is clearer for Ol than for Px, while it is less evident or absent for He/CO_2 versus He (Fig. 19). In the case of the diffusive loss of He, we should also expect an isotope fractionation of $^3He/^4He$ due to the appreciable difference in D_{3He} and D_{4He} among mantle minerals that is proportional to the atomic mass ($D_{3He}/D_{4He} = 1.15$; Trull and Kurz, 1993; Burnard, 2004; Yamamoto et al., 2009 and references therein.). However, plotting the He concentration versus Rc/Ra (Fig. 14a) for Ol reveals no obvious variations of the $^3He/^4He$ ratio for decreasing He, with the isotope ratio varying over a very narrow range (5.9–6.2 Ra). Moreover, Opx and Cpx display higher $^3He/^4He$ ratios (6.3–6.9 Ra) than Ol for comparable He contents. This behavior is the opposite of what would be expected in the presence of He diffusive loss (e.g., Burnard, 2004; Harrison et al., 2004; Nuccio et al., 2008), as also suggested by plots of $He/^{40}Ar^*$, $He/^{21}Ne^*$ (not shown), He/N_2^* (not shown), and He/CO_2 versus Rc/Ra (Fig. 20a and 20b).

Together these observations indicate that the observed data variability cannot be explained by a partial loss of He. A process of diffusive fractionation of noble gases within the mantle can also be excluded because this would lead to decreases in both $He/^{40}Ar*$ and $^3He/^4He$ (Yamamoto et al., 2009). Finally, diffusive fractionation cannot explain our data irrespective of the assumed starting conditions. If this process had occurred in Ol and Px, it would be successively erased by the new injection of trapped fluids, especially within Px.
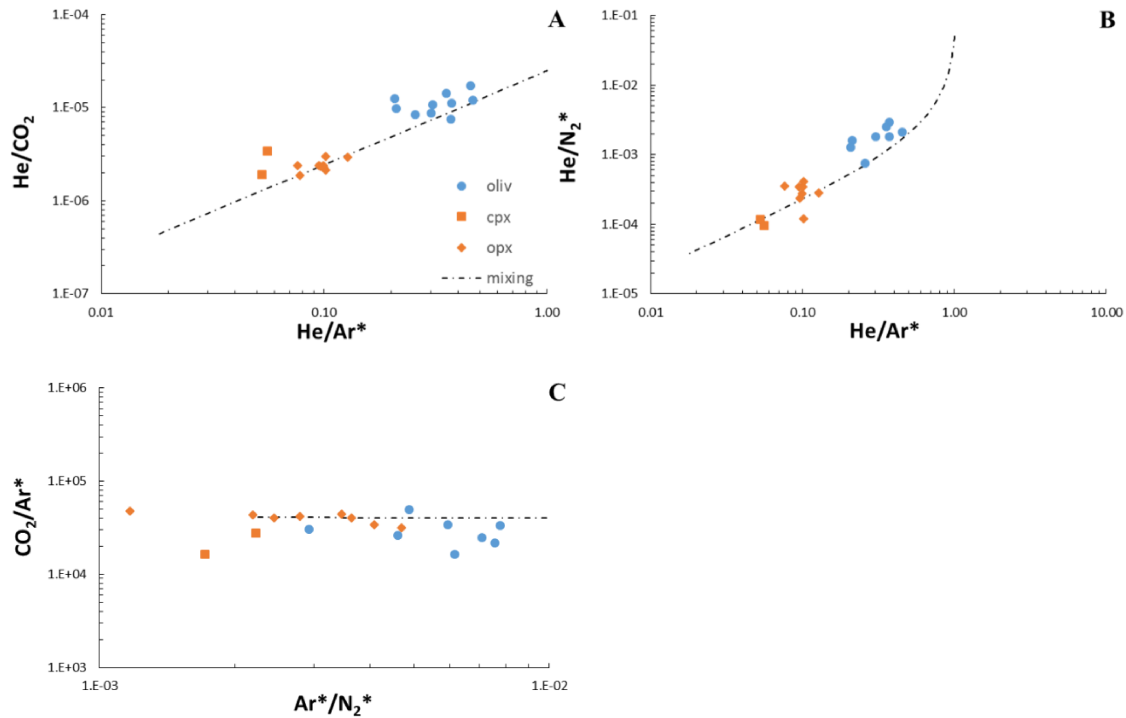
Figure 18. He/Ar* versus A) He/CO_2 and B) He/N_2*, and C) $Ar*/N_2*$ versus $CO_2/Ar*$ in FI. The black dotted line represents binary mixing between two endmembers: (1) the residual mantle having He/Ar* = 1, $He/CO_2 = 2.5 \times 10^{-5}$, $He/N_2* = 5 \times 10^{-2}$, $Ar*/N_2* = 5 \times 10^{-2}$, and $CO_2/Ar* = 4 \times 10^4$, and (2) the metasomatic agent having $He/Ar* = 1.7 \times 10^{-2}$, $He/CO_2 = 3.7 \times 10^{-7}$, $He/N_2* = 3.7 \times 10^{-5}$, $Ar*/N_2* = 2.1 \times 10^{-3}$, and $CO_2/Ar* = 4.7 \times 10^4$. These two endmembers were assumed based on the minimum and maximum concentrations of single species in the three mineral phases and in order to fit the entire data set.
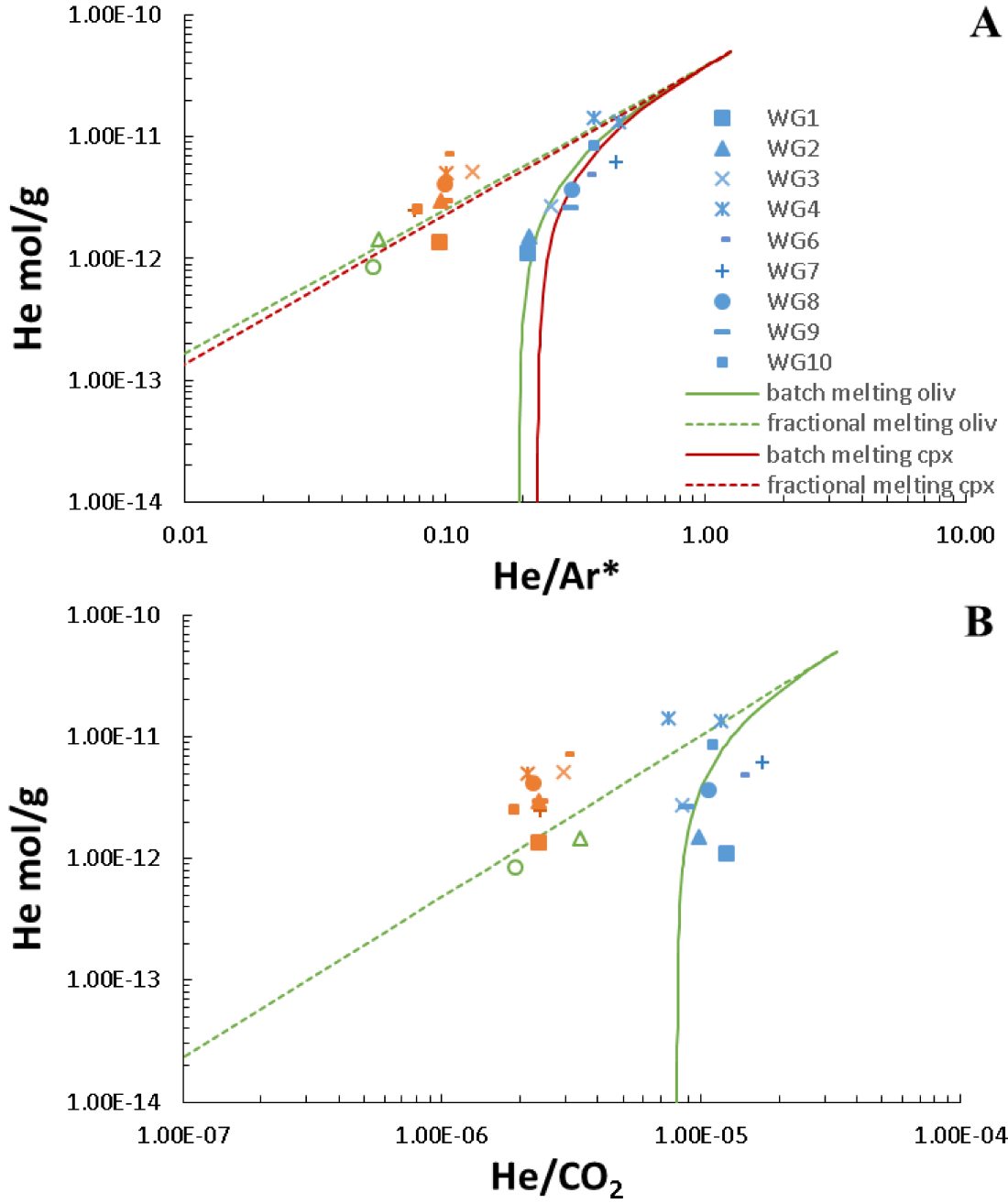
Figure 19. He/Ar* and He/CO₂ versus the He concentration. Modal batch and fractional equilibrium melting were modeled using the following equations:

$$C_i^m = \frac{C_i^s}{\left[F + D_i^{\frac{cryst}{melt}} \cdot (1-F)\right]} \; batch\; melting \qquad C_i^m = \left[C_i^s \cdot \left(\frac{1}{D_i^{\frac{cryst}{melt}}}\right) \cdot (1-F)^{\left(\frac{1}{D_i^{\frac{cryst}{melt}}}-1\right)}\right] fractional\; melting$$

where C_i^m and C_i^s are the concentrations of the ith species in the melt and solid source, respectively; F is the melting fraction, which varies from 0 to 1; and $D_i^{\frac{cryst}{melt}}$ is the crystal–melt partitioning coefficient of the ith species. The coefficients for the crystal–melt partitioning of He, Ar, and CO₂ for Ol and Cpx are as follows: $^{Ol/melt}D_{He} = 1.7 \times 10^{-4}$, $^{Ol/melt}D_{Ar} = 1.1 \times 10^{-3}$, $^{Ol/melt}D_{CO2} = 7 \times 10^{-4}$ (assumed in order to fit data), $^{Cpx/melt}D_{He} = 2 \times 10^{-4}$, and $^{Cpx/melt}D_{Ar} = 1.1 \times 10^{-3}$. The starting conditions for modeling are He = 5×10^{-11} mol/g, He/Ar* = 1.3, and He/CO₂ = 3.3×10^{-5}.
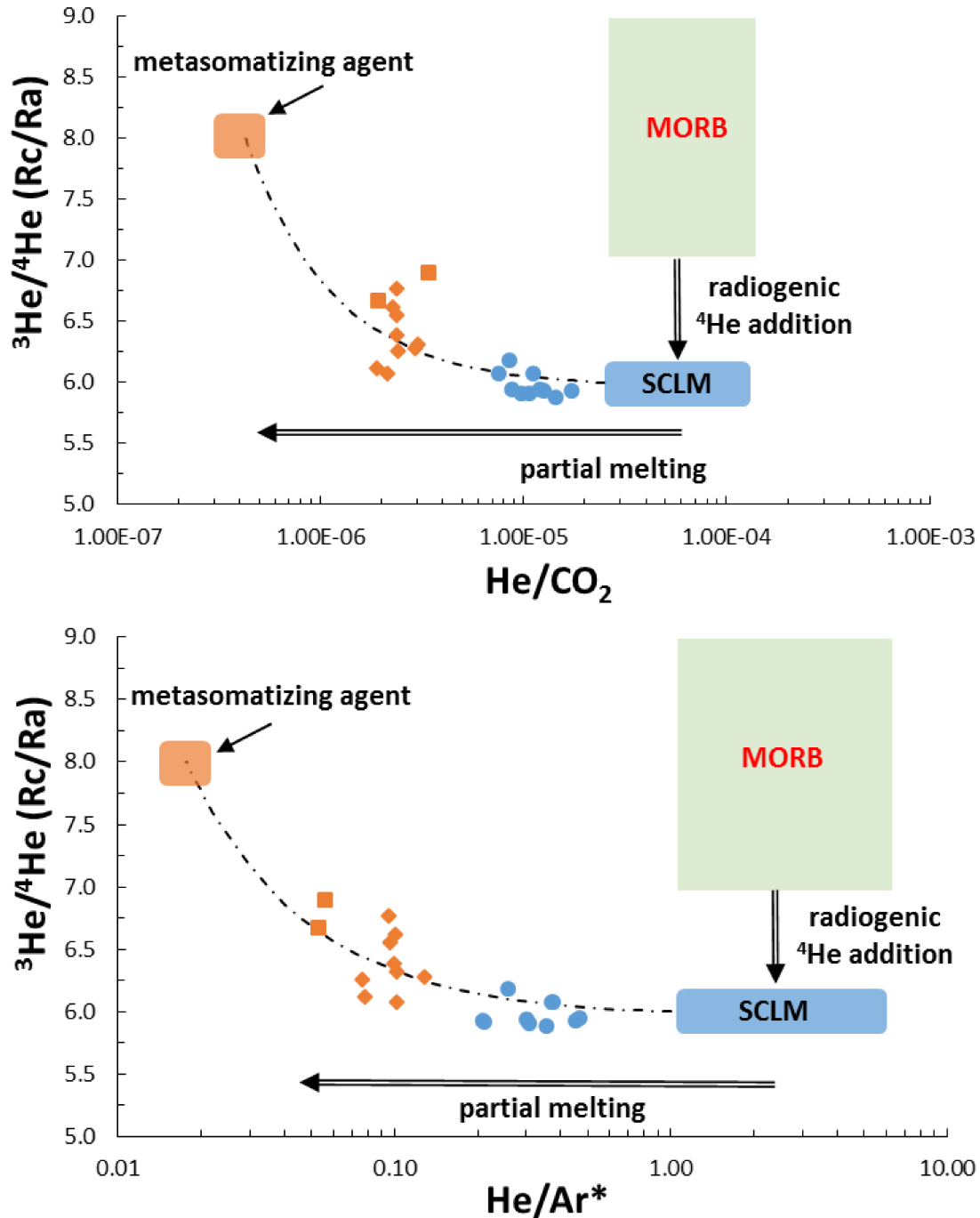
Figure 20. He/CO$_2$ and He/Ar* versus ^{3}He/^{4}He corrected for air contamination (Rc/Ra values). The green, blue, and orange rectangles are the same as in Fig. 18. The black dotted line represents binary mixing between two endmembers: (1) the residual mantle (blue rectangle) having He/CO$_2$ = 2.5×10^{-5}, He/Ar* = 1, and ^{3}He/^{4}He = 6 Ra, and (2) the metasomatic agent (orange rectangle) having He/CO$_2$ = 3.7×10^{-7}, He/Ar* = 1.7×10^{-2}, and ^{3}He/^{4}He = 8 Ra.

3.4.3.3 Partial melting of the mantle

Plotting He/^{40}Ar* versus the ^{40}Ar* concentration (Fig. 21a) and He/CO$_2$ versus the CO$_2$ concentration (Fig. 21b) reveals that the decreases in these ratios within Ol are accompanied by decreases in the absolute concentrations (although this is less clear for CO$_2$), as observed when plotting versus the He

concentration (Fig. 19a and 19b). This suggests that the process responsible for the variability within Ol modified the entire chemistry of FI. On the other hand, the decrease in these ratios from Ol to Cpx is associated with either no change or only a slight increase in the mean concentration of each species (Figs. 19 and 21). We argue that the decreases in these ratios among Ol and Px are not caused by the same process underlying the variability in Ol, and also that the timing of the processes is probably different. We therefore focus on the effect that partial melting has on the chemistry of FI within Ol resembling the residual mantle. This is supported by the evidence from petrography and mineral chemistry indicating that Ol with Fo>89 can be considered as a residuum from the partial melting of lithospheric mantle (Matusiak-Małek et al., 2017; Table 2). Ol from samples WG4$_{II}$, WG7$_{II}$, and WG10$_{II}$ show Fo<89 and could have been partially influenced by metasomatic process leading to partial recrystallization and thus entrapment of new FI. In this view the ^{3}He/^{4}He ratio does not show any relation with the forsterite content (Fig. 22), while He/^{40}Ar* decreases slightly at Fo>89 and reflects increasing extents of partial melting.
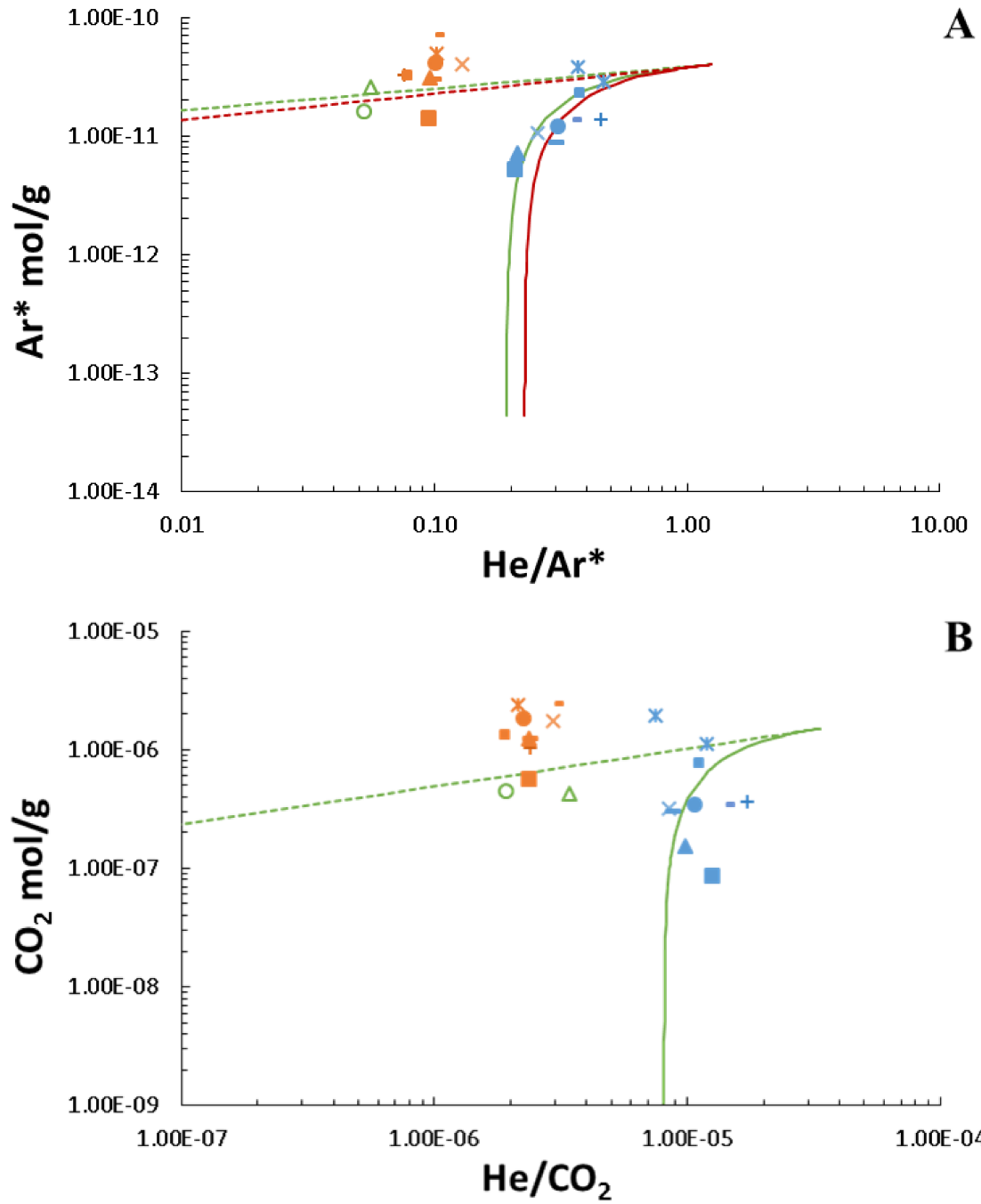
Figure 21. a) He/Ar* versus Ar* concentration and b) He/CO₂ versus CO₂ concentration. The modeling of the modal batch and fractional equilibrium melting and starting conditions are the same as in Fig. 19.
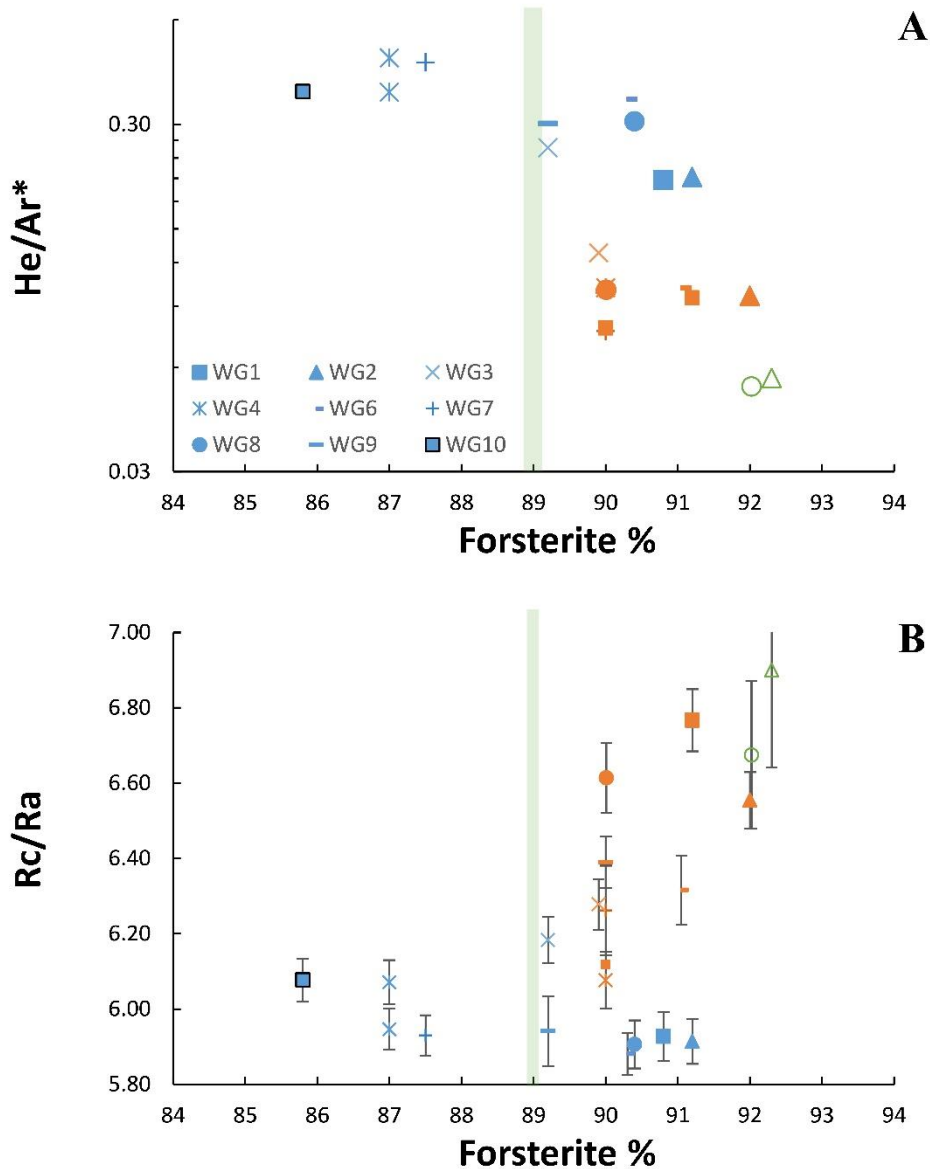
Figure 22. Forsterite content in Ol versus He/Ar* and ^{3}He/^{4}He corrected for air contamination (Rc/Ra). The blue rectangle separates Ol of group A (Fo>89) from those of group B (Fo<89).

Assuming the presence of crystal–melt partitioning of noble gases for Ol and Cpx (Heber et al., 2007), we modeled the trend of partial melting for batch and fractional melting of mantle in the spinel stability field. For the starting composition in the crystal, we assumed He = 5×10^{-11} mol/g, Ar = 4×10^{-11} mol/g, and CO$_2$ = 1.5×10^{-6} mol/g. Briefly, we chose to use the highest Ar* and CO$_2$ concentrations measured in Ol, while the He content was chosen so that the He/^{40}Ar* ratio was within the reported range for mantle production (He/^{40}Ar* = 1–5; Marty, 2012). We considered the He and ^{40}Ar* concentrations versus He/^{40}Ar* (Figs. 19 and 21), for which partitioning coefficients are known and more data are available in the literature for similar applications elsewhere (e.g., Burnard, 2004; Yamamoto et al., 2009). A particularly interesting observation was that the batch equilibrium melting

trend fits most of the Ol data, especially those with Fo>89, whereas Px cannot be explained by this process. The chemical variation of FI within Ol traces the partial melting trend, and this is in accordance with the main lithophile-elements-based melting models (Matusiak-Małek et al., 2017; present study). However, estimations of the degree of melting based on noble-gas modeling yield much lower percentages (<1%) than the common petrological estimations (20–30% melt; Fig. 17). This large discrepancy could be due to us measuring noble gases in the FI, while partitioning coefficients are given for a crystal–melt. In other words, we did not measure noble gases in the crystal lattice where we should expect that our estimations match those of lithophile-elements-based melting models. We argue that there is a general equilibrium between FI and the crystal lattice, and this explains why noble gases (and their relative ratios) follow the partial melting trend. In any case we use our tracers only as a proxy for the occurrence of partial melting, and not to speculate about the extent of this process.

3.4.3.4 Mantle metasomatism

While the geochemistry of FI in Ol reflects variable extents of partial melting, that of Cpx and (at least partially) Opx cannot be explained by this process, and suggests a contribution from at least one additional process postdating the partial melting. Matusiak-Małek et al. (2017) argued that xenoliths from WG reflect a polyphase lithospheric mantle evolution, which started with up to 30% of melting from the protolith that left a harzburgitic residuum, with this residuum subsequently metasomatized by carbonated hydrous silicate melt related to Cenozoic volcanism. This metasomatic event is responsible for the recrystallization of Cpx, Opx (at least partially), and amphiboles, resulting in the entrapment of secondary FI (e.g., Fig. 16D) whose chemical and isotope composition resemble that of fluids dissolved in the metasomatizing agent. Matusiak-Małek et al. (2017) highlighted that the enrichment of LREE in Cpx relative to primitive mantle is a proxy of a metasomatic process, and that both Cpx itself as well as Opx (at least partially) have to be considered secondarily. Such a metasomatic history is typical for the lithospheric mantle located beneath the northern margin of the Bohemian Massif (e.g., Brandl et al., 2015), although WG is the only locality where hydrous minerals have been found.

Considering that we measured progressively lower $He/^{40}Ar^*$, $He/^{21}Ne^*$ (not shown), He/N_2^*, and He/CO_2 ratios in Opx and Cpx than in Ol (Table 3 and Figs. 18, 19, 21, and 17), it is reasonable to suppose that the fluids entrapped during metasomatism were somehow depleted in He and rich in CO_2. Cpx shows the highest $^3He/^4He$ ratios close to the lower limit of MORB (Fig. 14), indicating that fluids associated with the metasomatic agent originally had a MORB-like signature. This can also be observed in the C-isotope composition of CO_2, although it is less evident, which manifests in

Opx as a mean $\delta^{13}C$ of –4.1‰ (Fig. 15), which is very close to the upper limit of the MORB range ($-8‰ < \delta^{13}C < -4‰$; Marty and Jambon, 1987; Javoy and Pineau, 1991; Macpherson and Mattey, 1994; Sano and Marty, 1995; Deines, 2002). Unfortunately, it was not possible to make any measurement(s) in Cpx, which we would have expected to show values well within the MORB range. On the other hand, Ol has a mean $\delta^{13}C$ of –3.8‰ (Fig. 15), which could indicate a slight contamination of the residual mantle—possibly due to limestone originating from an old subduction component—as also shown by the lowest $^3He/^4He$ ratio of our data set (~6 Ra).

Considering that most of the studied Ol samples (WG1$_{II}$, WG2$_{II}$, WG3$_{II}$, WG6$_{II}$, WG8$_{II}$, and WG9$_{II}$) represent the residual mantle, while Cpx and some of the Opx (and Ol) samples (WG4$_{II}$, WG7$_{II}$, and WG10$_{II}$) are partially or completely modified by the metasomatic process, we argue that FI from Ol and Px represent a mixing of two endmembers: (1) a residuum after partial melting, characterized by narrow variability of $^3He/^4He$ (~6 Ra) and $\delta^{13}C$ (~ –3.8‰), and (2) a metasomatic agent, characterized by more-primitive and He-depleted fluids originating from an asthenosphere melt, originally with a MORB-like $^3He/^4He$ ratio (~8 Ra) and $\delta^{13}C$ ~ −4.2‰ (Figs. 15b and 20). This mixing hypothesis seems reasonable because our extraction procedure (single-step crushing) would result in the analysis of the total amount of FI released from crushing ~0.02 to ~1 g of crystals. We cannot exclude that these crystals contemporarily hosted primary and/or secondary FI (Fig. 16A-16D) belonging to the residual mantle and/or to the metasomatic agent. The boundary conditions of the mixing model were chosen as follows: for the residual mantle we assumed a mean $^3He/^4He$ ratio of 6 Ra, which is within the range of European SCLM (6.32±0.39 Ra; Gautheron et al., 2005), while for the metasomatic agent we assumed the mean $^3He/^4He$ ratio of the MORB range (i.e., 8 Ra). Consequently, the He/CO$_2$ and He/^{40}Ar* ratios were chosen to fit our data. It should be noted that assuming lower $^3He/^4He$, He/CO$_2$, and He/^{40}Ar* ratios would not change the final interpretation, considering that the maximum $^3He/^4He$ ratio measured in Cpx is close to the lower limit of the MORB range (Fig. 20).

3.5 Inferences about the mantle features beneath the north-easternmost part of the Eger (Ohře) Rift

3.5.1 Origin of the $^3He/^4He$ signature

The chemistry of FI coupled to the petrology of mantle xenoliths from WG provides evidence that a complex history of processes contributed to the local mantle composition at the time of the xenolith incorporation into the melts ascending in the volcanic system. The range of $^3He/^4He$ ratios measured in Ol and Px (5.9–6.9 Ra; Fig. 14) suggests that the mantle beneath the north-easternmost part of the Eger (Ohře) Rift is slightly radiogenic relative to the typical MORB range (8±1 Ra; e.g., Graham, 2002). This feature appears to be common to other central and western European magmatic provinces

(i.e., Eifel, French Massif Central, Pannonian Basin, Calatrava, and Tallante; ^{3}He/^{4}He is 6.32±0.39 Ra), whose noble gases in mantle xenoliths were analyzed using the same extraction method used in the present study (i.e., single-step crushing) (Gautheron et al., 2005; Martelli et al., 2011). Gautheron et al. (2005) discussed three interpretative models for justifying this signature in the SCLM: (1) the addition of ^{4}He-rich fluids/melts due to dehydration of the subducting plate (e.g., Yamamoto et al., 2004), (2) the recent and localized infiltration of a MORB-like He composition from the asthenosphere mixing with a more-radiogenic isotope signature residing in the lithosphere (e.g., Dunai and Porcelli, 2002), and (3) continuous (and extensive) He enrichment of SCLM in the steady state (Gautheron and Moreira, 2002). All of these three models are valid, and they can explain the features of the mantle beneath the north-easternmost part of the Eger (Ohře) Rift and its closest surroundings.

We have already inferred a direct mantle contamination of atmospheric gases from dehydration of subducting oceanic crust. This process could also account for contamination of a MORB-like source by radiogenic ^{4}He, finally resulting in residual mantle with a ^{3}He/^{4}He ratio of ~6 Ra. In this respect, the model proposed by Faccenna et al. (2010) would perfectly fit this scenario. The second model is essentially the same as what we argue in Section 3.4.1 occurring in the mantle beneath the study area. In this respect the residual mantle represented by Ol with Fo>89 could result from model 1 or be due to the steady-state conditions of SCLM established by the continuous metasomatic flux of MORB-like He from the asthenosphere and the production of radiogenic ^{4}He from the decay of U and Th in crustal rocks recycled into the mantle by previous subduction events (model 3). Instead, metasomatic fluids ascending from the asthenosphere are preferentially trapped in Cpx and have a MORB-like signature, as reflected in hypotheses 2 and 3.

3.5.2 Implications for the source of magmatism

The origin of CEVP magmatism is vigorously debated and far from being fully understood. Seismic tomography studies have inferred the presence of mantle plumes beneath certain regions, such as the French Massif Central and Eifel, whereas geochemical and petrological studies of erupted products seem to exclude this hypothesis (Lustrino and Carminati, 2007; Lustrino and Wilson, 2007). In alternative to classical plumes, a more recent and intriguing model proposed by Faccenna et al. (2010) invokes a subduction-triggered decompression melting. This debate might be resolvable by considering He and Ne isotopes, which represent powerful tracers for assessing the origin of fluids, although the latter are sensitive to air contamination. The proportion of primordial nuclides (^{3}He, and also ^{20}Ne and ^{22}Ne) is higher in the lower mantle than in the degassed MORB, which exhibits relatively uniform ratios (Ozima and Podosek, 1983; Moreira, 2013 and references therein). The

plume-related magmatism is expected to have a ^{3}He/^{4}He ratio above the MORB range (>9 Ra) and a lower ^{21}Ne/^{22}Ne ratio for a given ^{20}Ne/^{22}Ne (i.e., a lower ratio of nucleogenic Ne to primordial Ne) than MORB melts (e.g., Moreira, 2013 and references therein). This has already been observed in classical hotspot settings such as the Galapagos Islands (Fig. 13; Kurz et al., 2009) and Iceland, Reunion, and Hawaii (e.g., Rison and Craig, 1983; Kurz et al., 2009; Füri et al., 2010, 2011).

The ^{3}He/^{4}He ratios observed beneath the north-easternmost part of the Eger (Ohře) Rift (5.9–6.9 Ra) are significantly lower not only than typical plume-related ratios but also MORB-like ratios (Fig. 14). This range is comparable to those for other European regions where no plume is present (Gautheron et al., 2005; Moreira et al., 2018). However, while the above reasoning suggests that there is no compelling evidence of plume signatures beneath the study area, other studies have inferred a plume contribution in European mantle based on Ne and Xe isotopes, although the ^{3}He/^{4}He ratios are lower than expected for a mantle influenced by a plume (Buikin et al., 2005; Caracausi et al., 2016). We did not analyze Xe isotopes in the present study, instead we only evaluated Ne isotopes that showed that the FI included in the WG xenoliths are consistent with mixing between air and a MORB-like mantle (Fig. 13). Our data also overlap the range of values found by Gautheron et al. (2005) when applying the same method (single-step crushing) to mantle xenoliths from the French Massif Central, Pannonian Basin, and Eifel, and those authors interpreted their results in the same way. Since Buikin et al. (2005) extracted FI from minerals using a less-conservative method (in terms of releasing noble gases from the crystal lattice), it is difficult to compare their results with ours. We therefore argue that the magmatism in the north-easternmost part of the Eger (Ohře) Rift probably does not originate from the presence of a mantle plume, and instead suggest alternative explanations such as lithosphere extension (Plomerova et al., 2007; Ulrych et al., 2011) or decompression melting (Faccenna et al., 2010).

3.5.3 Origin of CO_2

As indicated in previous sections, FI of mantle xenoliths from WG are dominated by CO_2, as observed in many other mantle xenoliths worldwide (Deines, 2002 and references therein; Gautheron et al., 2005; Sapienza et al., 2005; Correale et al., 2015; Créon et al., 2017). This finding was confirmed by Ladenberger et al. (2009) using Raman spectroscopy in a different suite of xenoliths from the same locality. Those authors reported that these mantle xenoliths contain large amounts of FI, and infer that their minimum entrapment depth is 31–38 km, which is consistent with both seismic evidence (Babuska and Plomerova, 2001; Majdanski et al., 2006) and petrological evidence (Matusiak-Małek et al., 2017 and references therein) from various xenoliths in the region. The presence of CO_2-rich inclusions represents evidence of fluid circulation within the local mantle. Matusiak-Małek et al.

(2017) argued that metasomatism involves the percolation of an alkaline silicate melt containing a CO_2-rich vapor phase rather than a true carbonatite, which is supported by the large amount of CO_2 released from FI and by $\delta^{13}C$ varying between −4.7‰ and −3.1‰ and not being related to the CO_2 concentration (Fig. 15a). Such a lack of a correlation between $\delta^{13}C$ and the CO_2 concentration excludes any influence of magmatic degassing. In support of this, we modeled the trends in the variation of $\delta^{13}C$, the CO_2 concentration, and the He/CO_2 ratio due to this process in the melt in both open- and closed-system equilibrium conditions (Fig. 15a and 15b). The boundary conditions used are reported in the caption of Figure 15.

The range of isotope ratios reported above is mostly close to the upper limit of the MORB range (−8‰ < $\delta^{13}C$ < −4‰; Marty and Jambon, 1987; Javoy and Pineau, 1991; Macpherson and Mattey, 1994; Sano and Marty, 1995; Deines, 2002). However, allowing for the stated uncertainty (±0.3‰), the measured $\delta^{13}C$ values overlap those of primary igneous carbonatites (−8‰ < $\delta^{13}C$ < −5‰; Jones et al., 2013 and references therein). In addition, the most-^{13}C-enriched values found in Ol ($\delta^{13}C$ up to −3.1‰) could indicate slight contamination of the residual mantle—possibly by recycled limestone— beneath the study area, as inferred by the $^3He/^4He$ ratio being the lowest for our data set (~6 Ra). This supports the recycling of sediments with a small proportion (<0.1%) of carbonate in the SCLM.

We also considered the relationship between $\delta^{13}C$ and the $CO_2/^3He$ ratio. Figure 23 plots the FI data together with the ranges suggested for a MORB-like mantle (−8‰ < $\delta^{13}C$ < −4‰ and $CO_2/^3He$ ~ 1– 2×10^9; Sano and Marty, 1995) and limestone (−1‰ < $\delta^{13}C$ < +1‰ and $CO_2/^3He$ ~ 1×10^{13}; Sano and Marty, 1995), as well as their relative mixing trends. As argued for the differences in the He/CO_2 ratio between Ol and Px, we infer that the differences in the $CO_2/^3He$ ratio among mineral phases probably reflects mixing between a residual mantle characterized by $\delta^{13}C$ = −3.8‰ and $CO_2/^3He$ ~ 3.6×10^9 and a metasomatic agent having $\delta^{13}C$ = −4.2‰ (at the upper limit of MORB range) and $CO_2/^3He$ ~ 1.3×10^{11}. In detail, the geochemistry of FI in Px would result from the modification of residual mantle due to partial melting and metasomatism. The residual mantle (i.e., SCLM) would represent a MORB-like mantle modified by the addition of <0.1% limestone presumably inherited by a previous (fossil) subduction event (Fig. 23). It is worth noting that Correale et al. (2015) used a similar analytical approach to invoke a similar process for explaining the $\delta^{13}C$ signature of the mantle source beneath the Hyblean Plateau in southeast Sicily, Italy. Importantly, the average $\delta^{13}C$ values and $CO_2/^3He$ ratios of FI from Hyblean mantle xenoliths ($\delta^{13}C$ ~ −3.1‰ and $CO_2/^3He$ ~ 5.1×10^9) fall within the ideal ranges assumed for the pure (unmetasomatized) residual mantle beneath the north-easternmost part of the Eger (Ohře) Rift (Fig. 23). These data are actually consistent with the trend for binary mixing between a MORB mantle and limestone. Greater recycling into the mantle of carbonates, as occurs in certain active subduction settings (Aiuppa et al., 2017), would increase the

proportion of limestone involved in this mixing. This has already been observed by Gennaro et al. (2017) in FI from cumulates from Stromboli arc volcano (Italy); those authors inferred that the local mantle wedge is contaminated by CO_2 coming from the decarbonation of the sediments carried by the subducting Ionian slab (Fig. 23).
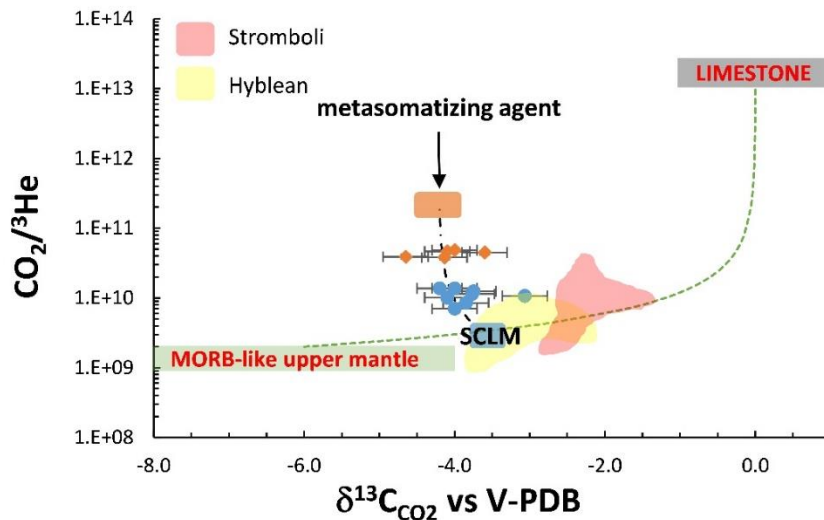
Figure 23. C-isotope composition ($\delta^{13}C$) versus $CO_2/^3He$. The green, blue, orange, and gray rectangles are the same as in Figs. 18 and 20. Data from the Hyblean Plateau and Stromboli are from Correale et al. (2015) and Gennaro et al. (2017), respectively. The green dotted curve represents the binary mixing between a MORB-like upper mantle having $\delta^{13}C = -6‰$ and $CO_2/^3He = 2 \times 10^9$, and limestone having $\delta^{13}C = 0‰$ and $CO_2/^3He = 1 \times 10^{13}$ (Marty and Jambon, 1987; Javoy and Pineau, 1991; Sano and Marty, 1995). The black dotted line represents binary mixing between two endmembers: (1) the residual mantle (blue rectangle) having $CO_2/^3He = 4.8 \times 10^9$ and $\delta^{13}C = -3.5‰$, and (2) the metasomatic agent (orange rectangle) having $CO_2/^3He = 2.4 \times 10^{11}$ and $\delta^{13}C = -4‰$.

3.6 Comparison with gases emitted along the Eger (Ohře) Rift

The Eger (Ohře) Rift is part of the ECRS and has been characterized by the occurrence of intense intraplate magmatism (e.g., Prodehl et al., 1995; Ulrych et al., 2011, 2016; Andreani et al., 2014). Although there is currently no ongoing volcanic activity at the ECRS, the presence of strong CO_2 degassing and persistent seismicity indicates that magmatism is still active at depth (Weinlich et al., 1999; Špaček et al., 2006; Hrubcová et al., 2017 and references therein). Most of the CO_2 degassing along the Eger (Ohře) Rift occurs in the central axis and shows a clear magmatic signature (–4‰ < $\delta^{13}C$ < –2‰ and $^3He/^4He$ up to 6.3 Ra), while the magmatic component decreases with distance from the degassing locations, as indicated by decreasing $^3He/^4He$ ratios (Weinlich et al., 1999; Bräuer et al., 2004, 2008, 2011; Hrubcová et al., 2017 and references therein). As far as we are aware, the most-studied gas emissions are located in the western Eger (Ohře) Rift, at the boundary between Germany and the Czech Republic (i.e., Cheb Basin). The long-term monitoring of these emissions has revealed increasing $^3He/^4He$ ratios due to the link between ascending magmatic fluids and intracrustal seismicity (Bräuer et al., 2011). In contrast, the eastern Eger (Ohře) Rift has been subject to far less scrutiny, and to the best of our knowledge no He- and C-isotope data are available for surface gases. However, episodes of CO_2 emissions have been reported in the proximity of the main volcanic regions (e.g., Nízký Jeseník Mountains), and these might be related to the local magmatism (Špaček et al., 2006); however, this needs to be confirmed in a detailed study of the geochemistry of these fluids.

The lack of noble-gas measurements and CO_2-isotope data for gas emissions from the eastern Eger (Ohře) Rift makes it impossible to directly compare with our measurements in FI from WG mantle xenoliths. Nevertheless, considering that most of the magmatic gases emitted at or beneath the western Eger (Ohře) Rift (Bublák mofette, Cheb Basin) are interpreted as derived directly from the mantle beneath the region (Bräuer et al., 2004, 2008), we can make some comparative speculations. While the highest $^3He/^4He$ ratios measured for the Bublák mofette (up to 6.3 Ra; Bräuer et al., 2011) fall within the range of ratios measured in FI from WG (5.9–6.9 Ra), suggesting an homogeneous mantle source along the rift, $\delta^{13}C$ is significantly higher for the CO_2 emissions ($\delta^{13}C \sim -2‰$, Bräuer et al., 2008, 2011) than in FI ($-4.7‰ < \delta^{13}C < -3.1‰$). This discrepancy can be interpreted in two ways: (1) the mantle beneath the western Eger (Ohře) Rift has a slightly different isotope signature of CO_2, which is possibly related to interactions between carbonate-derived fluids and the residual mantle, or (2) $\delta^{13}C$ of mantle CO_2 is homogeneous along the Eger (Ohře) Rift, and the Bublák mofette emits gases that are slightly contaminated by intracrustal carbonate. The second hypothesis seems to be the most plausible given the homogeneous $^3He/^4He$ ratios along the Eger (Ohře) Rift and the presence of isolated carbonate deposits in the Cheb Basin (Buzek et al., 1996).

3.7 Summary and conclusions

We have presented the first measurements of the concentration and isotope composition of noble gases and CO_2 in FI trapped in Ol and Px separated from ultramafic xenoliths hosted in WG basanite rocks that erupted a few tens of kilometers outside the north-easternmost part of the Eger (Ohře) Rift in Lower Silesia, southwest Poland. Data from FI were integrated with the evidence from petrography and geochemistry for minerals in order to define the mantle features beneath this sector of the European SCLM. This study highlights that Ol and Px (especially Cpx) may trap FI, recording different processes and timings that have occurred within the lithospheric mantle. The main results can be summarized as follows:

- Ultramafic xenoliths are mostly spinel-bearing harzburgites that sometimes contain amphiboles. Ol are classified into two groups based on forsterite contents: (1) $Fo_{88.9-91.5}$, which accounts for a fertile-to-residual mantle, and (2) $Fo_{85.5-88.1}$, which indicates large interactions with circulating (basic) melts. This dichotomy is also related to Opx and Cpx, which show two ranges of Mg# values (87–90 and 91–93, respectively) and clear evidence of recrystallization.

- The chemistry of FI is dominated by CO_2, with N_2 being the second-most-abundant species, and indicates that some Ol samples primarily represent a residual mantle depleted after various episodes of melt extractions, while the chemistry of Opx and Cpx suggests the overprinting of at least one metasomatic event postdating the partial melting. This event involved carbonated hydrous silicate melt related to Cenozoic volcanism that resulted in the entrapment of CO_2-rich inclusions. $\delta^{13}C$ relative to V-PDB is -3.8 ± 0.4‰ in Ol and -4.1 ± 0.4‰ in Opx, mostly falling at the upper limit of the MORB range (-8‰ $< \delta^{13}C < -4$‰), although a small percentage of carbonate recycling from a previous (fossil) subduction event cannot be excluded.

- The $^3He/^4He$ ratio corrected for air contamination (Rc/Ra values) is 6.7–6.9 Ra in Cpx, 6.3–6.8 Ra in Opx, and 5.9–6.2 Ra in Ol. The decrease in $^3He/^4He$ from Cpx to Ol is decoupled from the He concentration, thereby excluding any influence of diffusive fractionation from FI.

The systematics of Ne and Ar isotopes indicate that most of the data are consistent with mixing between air and a MORB mantle. This evidence, together with that from the measured $^3He/^4He$ ratios, excludes the presence of a classical plume of the lower mantle beneath the study area. The geochemistry of FI results from a mixing of two endmembers: (1) the residual mantle, resulting from partial melting of European SCLM, and (2) the metasomatic agent, which is strongly He-depleted, CO_2-rich, and originally characterized by MORB-like $^3He/^4He$ ratios.

Chapter – 4 –

Geochemistry of noble gases and CO₂ in fluid inclusions from lithospheric mantle beneath Eastern Transylvanian Basin

4. Geochemistry of noble gases and CO₂ in fluid inclusions from lithospheric mantle beneath Eastern Transylvanian Basin

4.1 Introduction

Xenoliths representing mantle wedge fragments as defined by Arai and Ishimaru (2008) are rarely found in post-collisional, subduction-related geodynamic settings. They have been collected especially in arc volcanics of the western Pacific like Kamchatka, Japan, Philippines, Papua New Guinea, Vanuatu both in rear-arc position or in the frontal volcanoes and allowed to reconstruct dynamics and metasomatic processes occurring in the mantle wedge of large, mature subduction zones (Yoshikawa et al., 2016 and references therein; Bénard et al., 2018 and references therein). Mantle wedge xenoliths are rarer in eastern Pacific and Atlantic subduction systems (e.g. Brandon and Draper, 1996; Parkinson et al., 2003; Faccini et al., 2013). In Europe, the tectonic complexity and peculiar characteristics of the recent subduction zones (Edward and Grasemann, 2009) as well as the unique presence of ultramafic enclaves in alkaline volcanic products makes it more difficult to establish if they come from a subduction context and can thus be representative of the mantle wedge. In some cases, however, a subduction-related metasomatism has been recognized both from mineral (Coltorti et al., 2007a; Bianchini et al., 2011 and 53 references therein) and fluid inclusion compositions (Martelli et al., 2011 and references therein; Créon et al., 2017 and references therein). The Pannonian Basin is one of the most promising areas for the investigation of subduction influence on the magma sources. Its evolution, indeed, has been literally defined as "an interplay of subduction and diapiric uprise in the mantle" (Konečný et al., 2002) where landlocked oceanic lithosphere sections foundered (i.e. expire via sinking into the asthenosphere under their own unstable mass, Edward and Grasemann 2009) causing subduction zone arching and retreat via slab roll-back and consequent asthenospheric doming and corner flow. It comprises several districts (Styria Basin and Burgenland, Little and Great Hungarian Planes and Transylvanian Basin), whose complex evolution from Neogene to Quaternary saw the systematic eruption of alkaline and ultrapotassic magmas after the main calc-alkaline volcanic activity (Seghedi and Downes, 2011) within variable time spans (1-10 Ma, Pécskay et al., 1995a, b). This would imply major changes in the magma source that should be reflected in the textural-chemical-petrological characteristics of the upper mantle. Among all xenolith occurrences in the Pannonian Basin, those entrained in the Na-alkaline lavas of Perşani Mts in the Eastern Transylvanian Basin, erupted very close to the youngest calc-alkaline volcanic fields linked to the final stages of subduction along the Carpathian Bend area (Seghedi et al., 2011 and references therein), are the most promising candidates for representing the mantle wedge of a Mediterranean-type subduction zone. In this paper, we present the results of the petrological and noble gases study of a new suite of mantle xenoliths from Perşani Mts, unveiling the presence of

different kinds of metasomatism: one related to the injection of alkaline melts similar to the host magma and another definable as a pervasive refertilization of the mantle domain by calc-alkaline subduction-related melts. Both types of metasomatism are intimately linked to the major geodynamic changes occurred in the area.

4.2 Petrographic outline

4.2.1 Sample classification

Lherzolite is the most common rock type, with a total of 30 out of 34 samples. The main characteristic is the almost ubiquitous presence of disseminated pargasitic amphibole, texturally equilibrated with the other constituent minerals and whose modal abundance varies between traces and 11.5 %. Two harzburgites (one with amphibole and one anhydrous), an amphibole-bearing olivine-clinopyroxenite and an anhydrous dunite complete the collection. Lherzolite LAG52 displays an amphibole vein. Detailed observations of microstructures and olivine Crystal Preferred Orientation carried out on several hundred of PMVF mantle xenoliths by Falus et al. (2011) revealed that PMVF xenoliths recorded deformation by dislocation creep under different ranges of temperature, stress and strain rate conditions. This resulted in a continuous textural gradation from coarse-grained to fine-grained, mylonitic types, these last making up to about 15% of the ultramafic rocks. Such a textural transition is evident in our suites although only one sample is patently mylonitic. Coarse- to medium-grained samples are predominant and can satisfactorily be described on the basis of the petrographic classification of Mercier and Nicolas (1975). Following these considerations, PMVF lherzolites were divided into two main textural groups (Table 1). A detailed petrographic description is provided in ESM1.

4.2.2 Protogranular group

This group includes all samples matching the protogranular type as described by Mercier and Nicolas (1975). It can be further divided into two sub-groups, on the basis of some peculiar textural features: *Protogranular s.s. (Pr s.s.)* and *Protogranular with small, rounded grains (Pr srg)* (Table 1; ESM1). Both *Pr s.s.* and *Pr srg* find a correspondence to the coarse-grained peridotites described by Falus et al. (2011) who, however, defined them as being porphyroclastic showing such a continuous variation in grain size that the distinction between porphyroclasts and recrystallized grains has been hindered. These kinds of texture would form at high-temperature (as also noted by Chalot-Prat and Boullier, 1997), low-stress conditions like those prevailing at deep levels within the lithosphere and at lithosphere/asthenosphere boundary. We chose to classify them as Protogranular on the basis of their close resemblance to the Mercier and Nicolas (1975) type description, being aware of the fact that no

"pristine" un-deformed lithospheric mantle portions are probably preserved anywhere on Earth and all textural types actually are the result of a series of deformation and recrystallization events.

4.2.3 Porphyroclastic group

This group includes all samples patently porphyroclastic. It is divided into two sub-groups according to some peculiar textural features: *Porphyroclastic with large, rounded grains (Po lrg)* and *Porphyroclastic s.s. (Po s.s.).* (Table 1; ESM1). *Po lrg* and *Po s.s.* find a strict correspondence with intermediate to fine-grained porphyroclastic peridotites described by Falus et al. (2011). This texture would indicate lower temperatures (Chalot-Prat and Boullier, 1997) and higher stress conditions with respect to those endured by the Protogranular group, suggesting that these samples may come from shallower depth, probably the upper levels of the lithospheric mantle.

4.2.4 Description of the fluid inclusions

Irrespective of textural type, FI are remarkably scarce in PMVF mantle xenoliths and very small in dimensions (only few μm across). As observed in other occurrences of Central Europe (Rizzo et al., 2018 and references therein) and according to the classification of Roedder (1984), FI occur i) as primary inclusions, generally isolated or arranged in short, tiny trails and/or ii) as secondary inclusions, often forming cluster stripes or trails along plans. In PMVF xenoliths, primary FI could not be clearly identified within single, coarse-grained olivine or pyroxenes; in some samples they were totally absent. The few observed FI are secondary inclusions as trails aligned in planes within the same crystal and/or developed along grain boundaries. Trails of secondary inclusions crossing or straddling between two different crystals were not found.

Table 1: Petrographic description, main average petrological data, temperature-pressure-fO_2 estimates and modes for the analyzed PMVF mantle xenoliths. See text for further explanations and model references.

SAMPLE	TEXT. GROUP	Sub-group	OCK TYP	fo	cr#	T (°C)* BK	T (°C)* Taylor	T (°C)* O'N&W	P (GPa)§	fO_2	MODAL ABUNDANCES (WT%)				
											ol	opx	cpx	sp	amph
BARQ 4	Protogran	Pr s.s.	Lh	89.9 ±0.12	8.93 ±0.09	1056 ±5.9	1009 ±5.4	1027 ±2.0		- 0.60 ±0.47	56.2	23.6	17	3.2	0
LAG 2	Protogran	Pr s.s.	Lh(a)	90.5 ±0.03	13 ±0.57	1048 ±0.7	1003 ±12	1003 ±3.4	2.7 ±0.05	0.05 ±0.08	62.2	21.8	11	4	1
LAG 21	Protogran	Pr s.s.	Lh(a)	89.7 ±0.17	12 ±2.12	1018 ±12	989 ±12	1017	2.6 ±0.05	-0.02	58.8	21	14.2	5.3	0.7
LAG 24	Protogran	Pr s.s.	Lh(a)	89.8 ±0.11	9.48 ±0.22	1036 ±6.6	984 ±0.6	989 ±8.1	2.7 ±0.05	- 0.78 ±0.11	61.8	22.7	12.7	1.8	1
LAG 51	Protogran	Pr s.s.	Lh(a)	90.3 ±0.31	9.91 ±0.42	1023 ±14	997 ±11	1022 ±45	2.5 ±0.05	0.34 ±0.48	60.8	21.6	12.1	3.1	2.4
LAG 52	Protogran	Pr s.s.	Lh(a)	89.3 ±0.20	15.8 ±1.50	992 ±6.7	978 ±12	958 ±16	2.7 ±0.07	0.13 ±0.24	59.6	26.3	8.1	2	4
TRE 2	Protogran	Pr s.s.	Lh(a)	90.7 ±0.07	15.5 ±0.49	1008 ±2.3	980 ±2.6	970 ±9.8	2.6 ±0.06	- 0.75 ±0.04	64.6	21	12.5	0.8	1.1
LAG 1	Protogran	Pr srg	Lh(a)	89.5 ±0.05	9.73 ±0.22	1010 ±3.5	983 ±0.5	994 ±27	2.7 ±0.08	- 0.35 ±0.12	56.5	17.3	21.9	3.5	0.8
TRE 3	Porphyroc	Po lrg	Lh(a)	90.0 ±0.04	10.9 ±0.06	970 ±0.7	950 ±3.2	979 ±27	2.8 ±0.03	- 0.23 ±0.12	38.5	37	19.5	3	2
TRE 1	Porphyroc	Po s.s.	Lh	91.5 ±0.27	31.2 ±2.49	897 ±6.2	890 ±1.7	939 ±12		- 1.22 ±0.30	70.9	25	2.8	1.3	0
TRE 4	Porphyroc	Po s.s.	Lh(a)	90.0 ±0.13	9.23 ±2.37	843 ±12	858 ±18	961 ±3.9	2.7 ±0.1	0.24 ±0.35	60.5	27	9.3	1.9	3.8

(a) contains amphibole

* temperatures calculated at 2.0 GPa

§ pressure estimated using BK temperat

BK, Taylor and O'N&W stands for Brey and Köhler (1990), Taylor (1998) and O'Neil and Wall (1987) modified by Ballhaus et al. (1991) thermom

± indicates standard deviations on about 4 mineral pairs for the geothermometers and single minerals for the geobarometer

4.3 Whole rock and mineral chemistry

4.3.1 Whole rock major and trace elements

Whole rock compositions were determined for the 15 samples, representative of all the recognized textural tpes. Xenoliths belonging to the Protogranular group (*Pr s.s.* and *Pr srg*) have lower MgO (38.4 – 45.8 wt%) and higher SiO_2 (43.9 – 45.3 wt%), TiO_2 (0.11 – 0.17 wt%), Al_2O_3 (3.26 – 4.31 wt%) and CaO (2.44 – 4.88 wt%) than those belonging to the Porphyroclastic group (*Po s.s.* and *Po lrg*; MgO, 41.8 – 45.8 wt%; SiO_2, 43.5 – 44.7 wt%; TiO_2, 0.06 - 0.14 wt%; Al_2O_3, 2.05 – 3.26 wt%; CaO, 1.03 – 2.44 wt%). Na_2O (< 0.42 wt%) and FeOtot (6.77 – 8.17 wt%,) are similar in both Groups, with only one sample with FeOtot content as high as 9.33 wt%.

Ni, Cr and Co contents are very similar for all textural types (1829 - 2244 ppm, 1882 - 3444 ppm and 105 – 115 ppm, respectively) while Zr and V tend to be lower in Porphyroclastic (2.7 – 7.7 and 40.6 – 63.5 ppm, respectively) than in Protogranular group (4.4 – 9.7 and 61.2 – 78.5 ppm, respectively). No difference was observed between amphibole-bearing and anhydrous samples, although the latter are too scarce to be statistically representative.

4.3.2 Mineral major elements

4.3.2.1 Olivine

Irrespective of the textural group, primary olivine has forsteritic component (Fo) ranging from 88.9 to 91.8 (Table 1; ESM2-1), the lowest values belonging to grains close to the amphibole vein of lherzolite LAG52, while the highest being recorded in the large porphyroclasts of anhydrous harzburgite TRE1. The NiO varies from 0.34 to 0.43 wt% and have no correlation with Fo nor with textural group. According to Herzberg et al. (2016), such high NiO is typical of depleted lithologies, although Straub et al. (2011) found akin contents for olivine in equilibrium with basaltic melts. Idiomorphic secondary olivine in veins and glassy patches are characterized by higher Fo (90.7 – 94.1) and lower NiO contents (down to 0.15 wt%) than those of primary olivine.

4.3.2.2 Clinopyroxene

Primary clinopyroxene (cpx) exhibit a large range of mg# (89.0 - 92.9) and Al_2O_3 (3.27 -8.16 wt%) (Fig. 24A; ESM2-1). Cpx of *Pr s.s., Pr srg* and *Po lrg* sub-groups are more fertile than those in *Po s.s* sub-group. This is in agreement with Szabó et al. (1995a), who also noticed higher basaltic components in the less deformed xenoliths. In composite sample TRE4, cpx in the clinopyroxenitic portion have lower mg# and higher Al_2O_3 than cpx in the peridotitic matrix (Fig. 24A). TiO_2 is always lower than 0.71 wt%, with the lowest values found in cpx of anhydrous harzburgite TRE1 (Fig. 24B).

As already noticed by Falus et al. (2008), a positive correlation between Al_2O_3 and Na_2O is observed, with *Po s.s.* and *Pr s.s.* falling respectively at the lowest and highest trend ends (Fig. 24C).

Secondary cpx can be divided into three types based on mg# and Al_2O_3 contents (Fig. 24D). Type 1 are found around amphibole close to glassy patches whereas type 2 includes small idiomorphic cpx in glassy patches and rims of spongy primary pyroxenes. Type 1 have equal to lower mg# at increasing Al_2O_3 values with respect to their associated primary cpx, while type 2 have higher mg# at similar or lower Al_2O_3 contents. Type 3 can be observed only as crystallites in host basalt veinlets and are characterized by a sharp decrease in mg# and an increase in Al_2O_3 with respect to primary cpx. All three types of secondary cpx generally have higher TiO_2 and Cr_2O_3 and equal or lower CaO and Na_2O contents with respect to their primary counterpart.
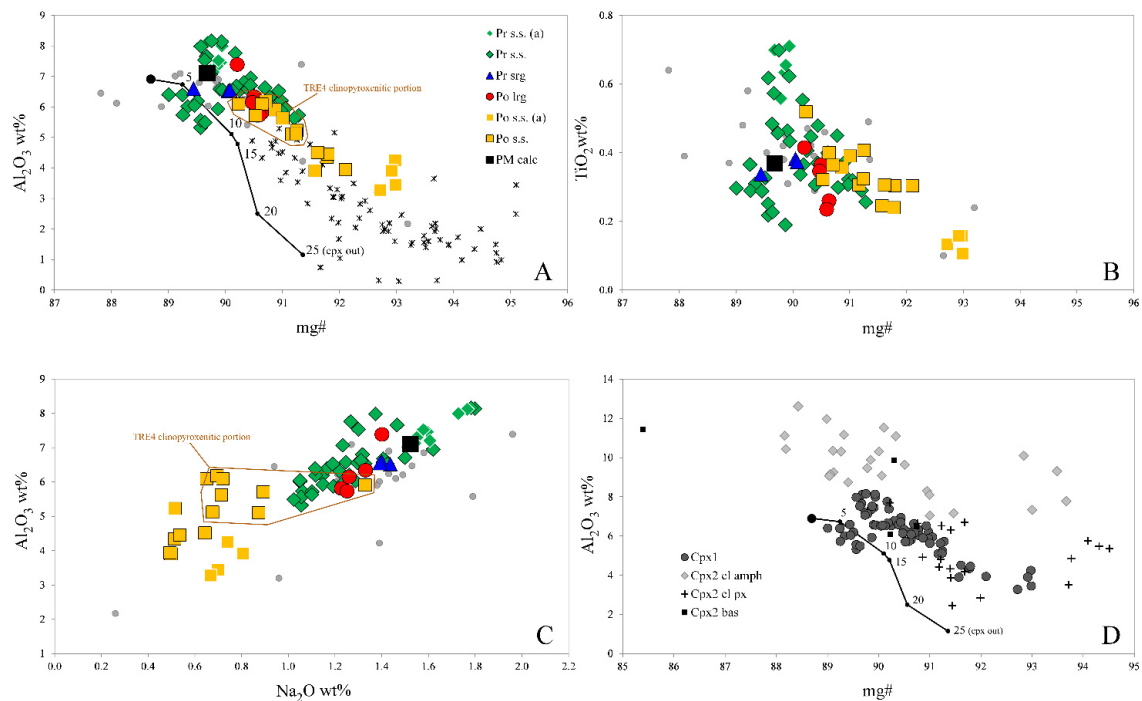
Fig. 24: Mg# vs Al_2O_3 (A) and TiO_2 (B) and Al_2O_3 vs Na_2O (C) of primary cpx and mg# vs Al_2O_3 (D) of all cpx (both primary and secondary) in PMVF mantle xenoliths. (a), anhydrous samples. Black square ("PM calc"), PM cpx composition calculated through mass balance from Bulk Silicate Earth of McDonough and Sun (1995) and Johnson et al. (1990) modes. Thick line in (A) and (D), cpx melting model according to Bonadiman and Coltorti (2019). Small grey dots, PMVF cpx data from Vaselli et al. (1995). Primary cpx (black asterisks) from Pacific arc mantle wedge xenoliths (Abe et al., 1998; Mc Innes et al., 2001; Brandon and Draper, 1996; Kepezhinskas et al., 1996; Arai et al., 2004; Bryant and Yogodzinsky, 2007; Ishimaru et al., 2007) are also reported for comparison in (A).

4.3.2.3 Orthopyroxene

Orthopyroxene (opx) have mg# varying from 89.1 to 92.1(Fig. 25A, ESM2-1). Analogously to olivine, the lower values characterize opx close to the amphibole vein in LAG52 while the highest

values are recorded by anhydrous harzburgite TRE1. TRE1 opx also have the lowest Al_2O_3 contents (2.84 – 3.62 wt%) of the entire PMVF xenolith suite (2.84 – 5.90 wt%). No remarkable major element compositional difference could be observed between porphyroclasts and neoblasts. However, in contrast with what stated by Szabó et al. (1995a), Vaselli et al. (1995) and Falus et al. (2008), a slight difference in geochemical composition coupled with textural variations can be detected. Ca indeed allows a good discrimination between the textural groups, with protogranular types having higher CaO contents than porphyroclastic types (Fig. 25B).
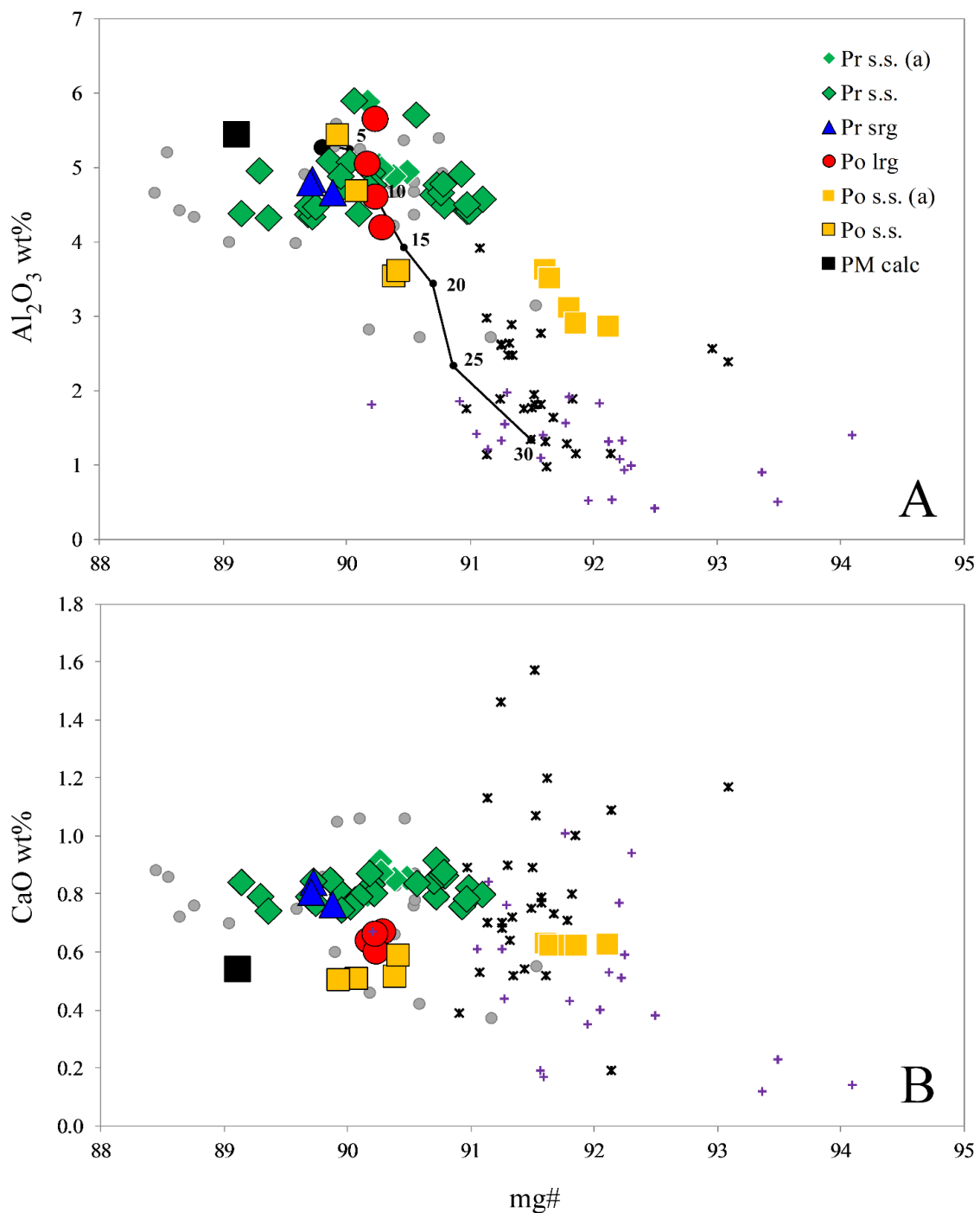
Fig. 25. Mg# vs Al_2O_3 (A) and CaO (B) of opx in PMVF mantle xenoliths, divided by textural sub-groups. (a), anhydrous samples. Black square ("PM calc"), PM opx composition calculated through mass balance from Bulk Silicate Earth of McDonough and Sun (1995) and Johnson et al. (1990) modes. Thick line, opx melting model according to Bonadiman and Coltorti (2019). Small grey dots, PMVF opx data from Vaselli et al. (1995). Primary (black asterisks) and secondary (violet crosses) opx from Pacific arc mantle wedge xenoliths (Brandon and Draper, 1996; Kepezhinskas et al., 1996; Arai et al., 2003, 2004; Bryant and Yogodzinsky, 2007; Ishimaru et al., 2007) are also reported for comparison.

4.3.2.4 Amphibole

Disseminated amphiboles are the overall dominant textural type in the PMVF mantle xenoliths. While several vein amphiboles have been previously found and described within PMVF ultramafic xenoliths (Vaselli et al., 1995; Zanetti et al., 1995), only the vein of sample LAG 52 can be compared to those described in the literature.

Disseminated amphibole mg# spans from 86.8 (LAG52) to 89.5 (TRE2) (Fig. 26A; ESM2-1); amphibole from *Pr s.s.*, *Pr srg* and *Po lrg* are rather constant in composition within the same sample, with Al_2O_3 contents in the narrow range of 15.3 - 16.3 wt%, while those of the composite sample TRE4 (*Po s.s.*) goes from 14.6 to 16.2 wt%, the higher variability being recorded in the clinopyroxenitic portion. On the whole, Al_2O_3 contents are among the highest for calcic amphibole in European mantle xenoliths (Styrian Basin, Coltorti et al., 2007a; Massif Central, Touron et al., 2008; Eifel, Witt-Eickshen et al., 1998; Balaton, Szabó et al., 1995; Zanetti et al., 1995, Bali et al., 2002; Ntaflos et al., 2017 and Tallante, Coltorti et al., 2007b) and, more broadly, in mantle xenoliths occurring in both intraplate (for example Ionov and Hofmann 1995; Lee et al., 2000; Moine et al., 2001; Ionov et al., 2002) and suprasubduction (for example Kepezhinskas et al., 1996; Abe et al., 1998; Grégoire et al., 2001; Franz et al., 2002; Ishimaru and Arai 2008; Yoshikawa et al., 2016) geodynamic settings, at comparable mg# (ESM3-1). CaO in amphiboles of *Pr s.s.*, *Pr srg* and *Po lrg* textural sub-groups is lower with respect to those of the *Po s.s.* sub-group. The abundance of transition elements such as Cr_2O_3 and TiO_2 has no link to textural type while Na_2O and K_2O respectively show mild positive and negative correlations with mg#.

Amphibole vein of LAG52 is characterized by the lowest mg# and the highest K_2O. Its Na_2O, Al_2O_3 and Cr_2O_3 are lower and TiO_2 is higher (Fig. 26B) with respect to disseminated amphibole in the same sample. A continuous variation between LAG52 vein amphibole, the veins analyzed by Vaselli et al. (1995) and PMVF pargasitic to kaersutitic amphibole MXC (Downes et al., 1995; Zanetti et al., 1995; Demény et al., 2005) can be observed (Fig. 26B). This behavior confirms the findings of Vaselli et al. (1995) (in their Fig. 26) but it has to be underlined that a gap in the trends between disseminated amphiboles and vein amphiboles and selvages is always present for mg#, alkalis and Cr_2O_3.
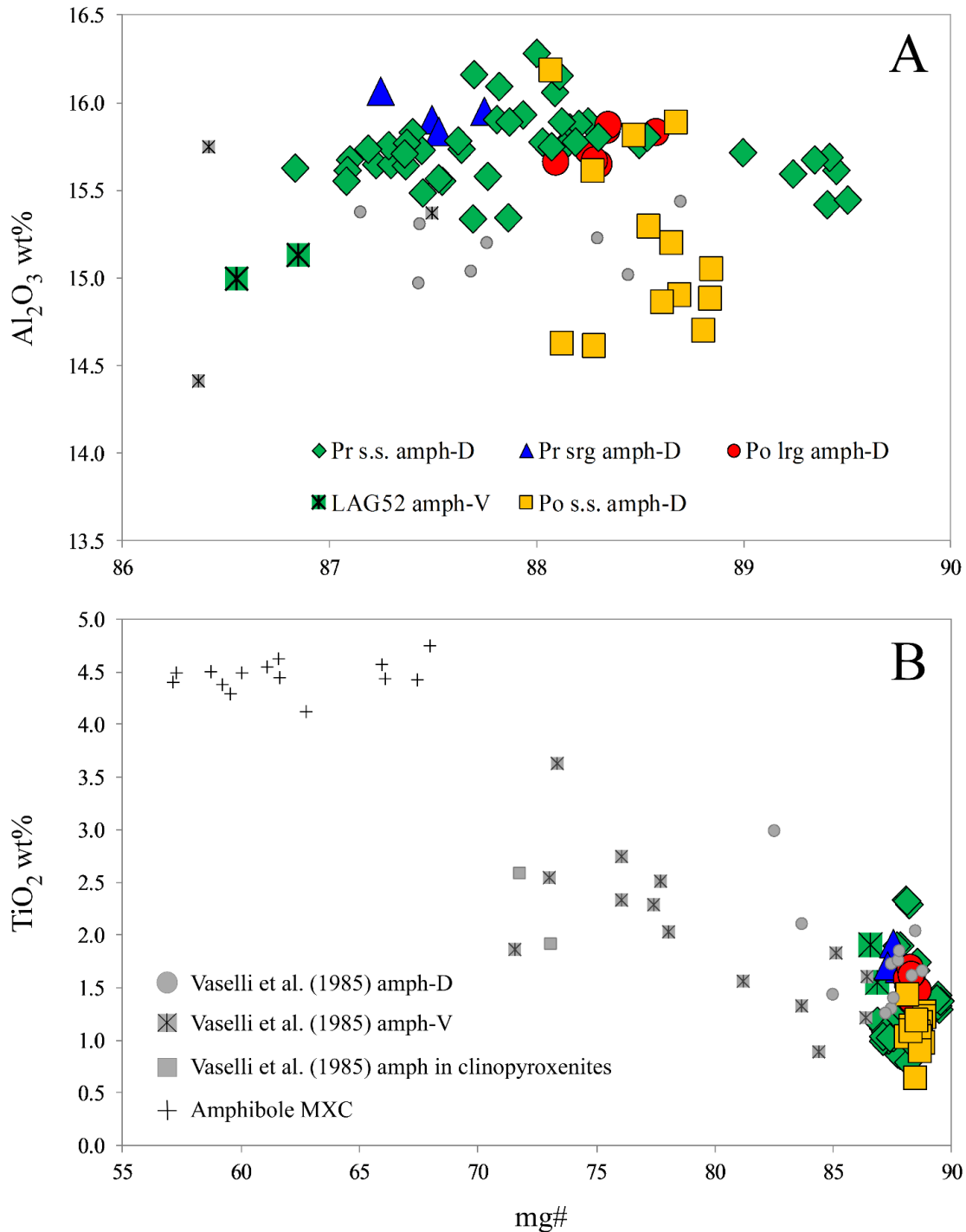
Fig. 26. Mg# vs Al_2O_3 (A) and TiO_2 (B) of disseminated (amph-D) and vein (amph-V) amphiboles in PMVF mantle xenoliths, divided by textural sub-groups. Small grey dots, asterisks and squares are disseminated amphiboles, vein amphiboles and amphiboles in clinopyroxenites in PMVF ultramafic xenoliths reported by Vaselli et al. (1995). Small black crosses, amphibole megacrystals (MXC) found in Persani Mts pyroclastic deposits by Downes et al. (1995) and Zanetti et al. (1995).

4.3.2.5 Spinel

All samples host primary spinel and the few secondary spinel do not show remarkable chemical differences. For sake of clarity, we describe the primary spinel only.

They are Al-rich (Table1; ESM2-1), with very low cr# (6.64 - 16.0) but high mg# (74.8 – 79.19), comparable to that of abyssal peridotite spinel (Shibata and Thompson, 1986; Dick, 1989; Bonatti et al., 1992, 1993; Dick and Natland, 1996; Seyler et al., 2003; Schmädicke et al., 2011). Al-rich spinel associated to LAG52 vein amphiboles are also relatively iron rich (mg# 70.6 – 71.4), whereas primary spinel of the anhydrous harzburgite TRE1 are clearly distinct, having comparable mg# (71.8-74.6) but the highest cr# (28.6-34.6) values of the entire xenolith population. (Fig. 27) In the Olivine-Spinel Mantle Array (OSMA, ESM3-2) all spinel fall in the lower end of the continental peridotites field, with the only exception of TRE1.
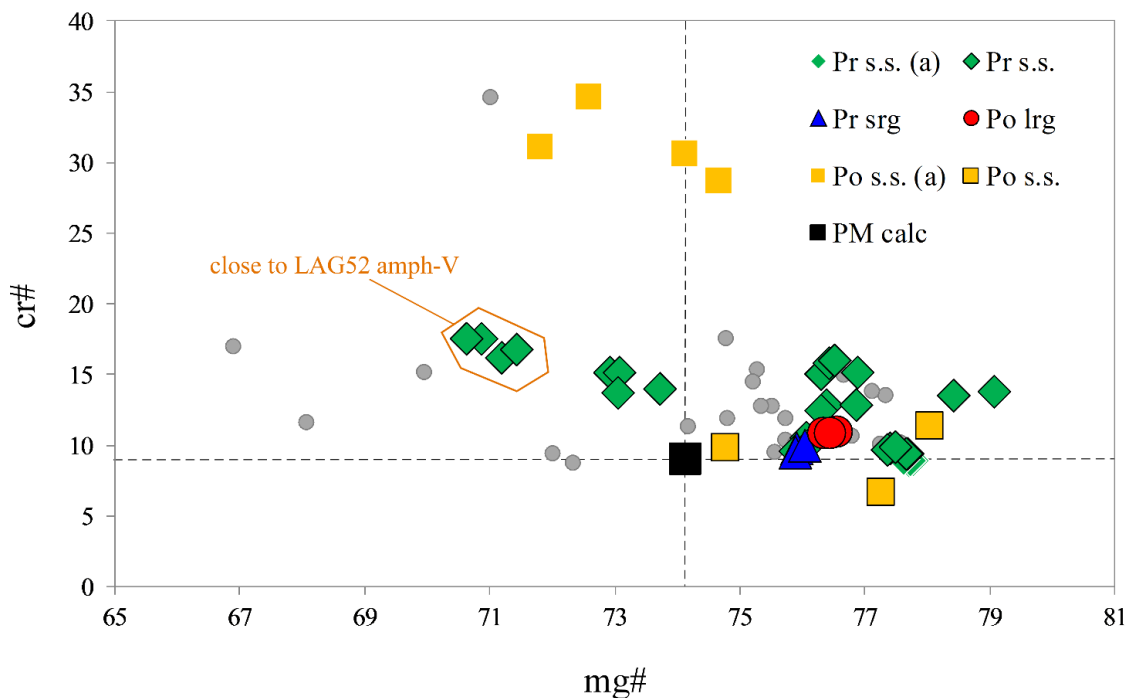
Fig. 27. Mg# vs cr# of primary spinel in PMVF mantle xenoliths, divided by textural sub-groups. (a), anhydrous samples. Black square ("PM calc"), PM spinel composition calculated through mass balance from Bulk Silicate Earth of McDonough and Sun (1995) and Johnson et al. (1990) modes. Small grey dots, PMVF spinel data from Vaselli et al. (1995).

4.3.3 Mineral trace elements

Pyroxenes and amphiboles were measured by LAM-ICP-MS with an average of 5 spots *per* sample. Within the single nodule, trace element content of each phase resulted very homogeneous, with almost no variations between cores and rims. For this reason, the mean concentration of each element was calculated, for most of the minerals, in all samples (ESM2-2). This reduced dataset was used for modeling. On the basis of chondrite-normalized REE patterns, pyroxenes have been divided into three groups.

4.3.3.1 Clinopyroxenes

Cpx in each sample generally fall within a single group but samples BARQ4 and TRE4 have cpx belonging to two groups.

Group 1 (including BARQ4, LAG21, LAG24 and TRE4) is represented by cpx characterized by slightly Light (LREE) to Middle (MREE) rare earth element convex-upward depleted patterns (Fig. 28A), with $(La/Yb)_N$ spanning from 0.34 to 0.48. The smooth convexity of the pattern can be measured by $(Eu/Yb)_N$, varying between 0.92 to 1.54 (average 1.24). In this Group, Heavy rare earth element (HREE) contents are slightly variable, with $(Yb)_N$ ranging from 9.35 to 13.3. In Chondrite-normalized trace element diagrams (Fig. 28B), they show variable degrees of enrichments in Th and U (up to 8.34 and 37.4, respectively) and a ubiquitous Ti negative anomaly; Zr and Hf can be decoupled.

Group 2 (including BARQ4, LAG1, TRE2 and TRE4), at the first glance, has mostly the same REE profile of Group 1 but it actually has flatter M to HREE $[(Eu/Yb)_N = 0.71 - 1.11$; average 0.94)], highly variable HREE contents $[(Yb)_N, 8.83 - 19.0)]$ and slight enrichments in La and Ce $[(La/Yb)_N = 0.16 - 0.74)]$ (Fig. 28C). In chondrite normalized trace element patterns Group 2 cpx are similar to those of Group 1 but for a slight Sr positive anomaly (Fig. 28D).

Group 3 (including LAG51, LAG52 and TRE1) is the most LREE enriched (Fig. 28E), with the highest $(La/Yb)_N$ ratios of the whole suite (1.42 – 2.57) and spoon-shaped REE patterns. These cpx also have the highest Th and U contents, up to 48 and 102 x Chondrite, respectively (Fig. 28F). HREE are comparable to those of the other Groups $[(Yb)_N, 8.94 – 12.6]$. This Group includes cpx of anhydrous harzburgite TRE1, showing the same REE profile with the lowest M-HREE contents.

There is no neat correspondence between the types recognized from texture and major elements and cpx Groups according to their trace element inventory. It can be noted that cpx modal content increases in the sequence Group 3 - Group 1 – Group 2 (Table 1).
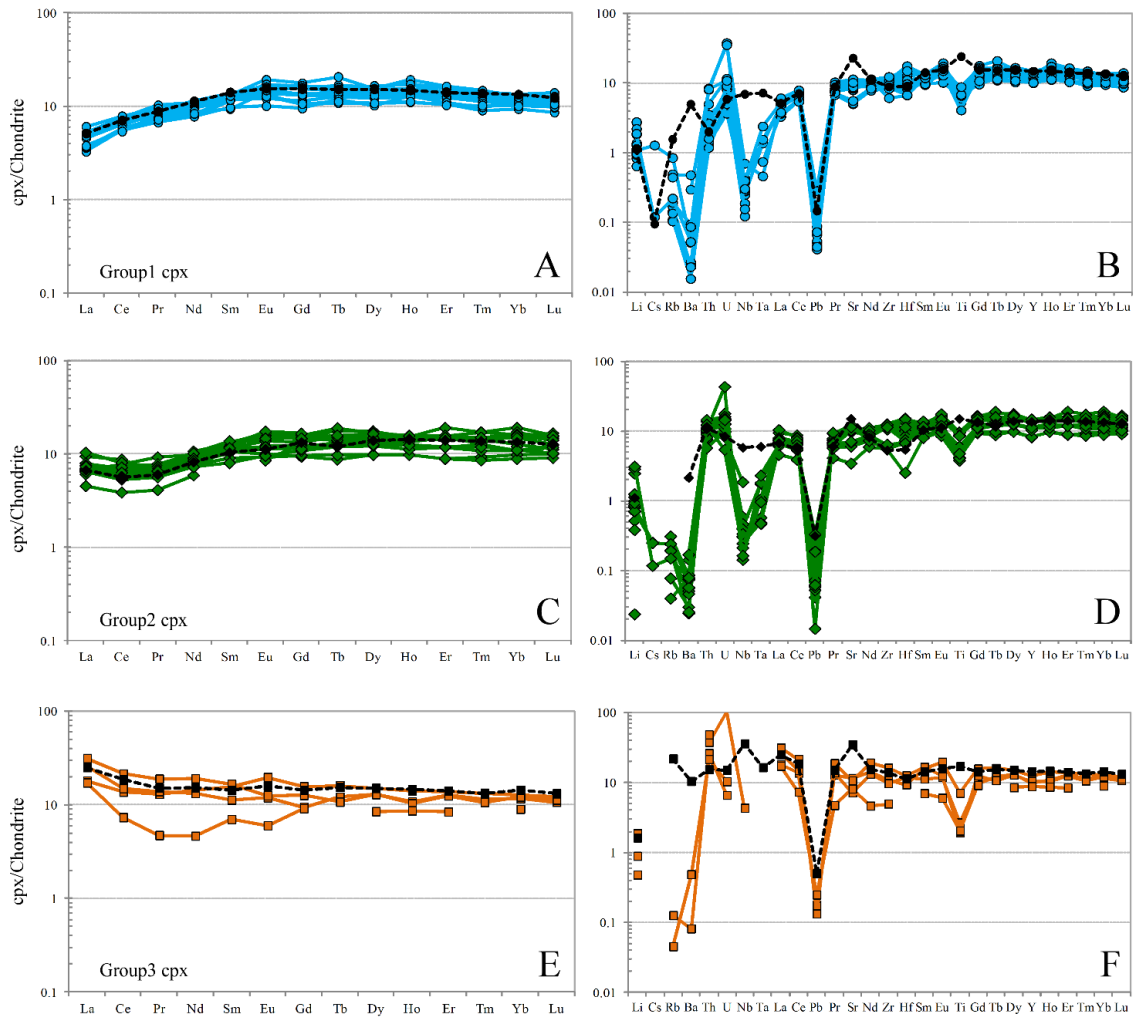
Fig. 28. Chondrite normalized REE (A, C, E) and trace element (B, D, F) patterns of cpx in PMVF mantle xenoliths, divided in three Groups according to their geochemical features (see text for further explanations). Average patterns of disseminated amphibole associated to the different cpx Groups (black dotted lines) are also reported for comparison.

4.3.3.2 Orthopyroxenes

For all PMVF lherzolites, opx Chondrite-normalized trace element patterns are characterized by steep REE patterns and positive Zr-Hf and Ti anomalies (Fig. 29). Opx associated to Group 1 cpx are the most depleted (beside a slight La enrichment) (Fig. 29A), with ubiquitous Sr negative anomaly {Sr*= Sr/[(Sm+Nd)/2], 0.15 – 0.42} and low Th contents (up to 0.34 x Chondrite) (Fig. 29B). Group 2 opx show LREE enrichments concordant with those of the associated cpx (Fig. 29C); they largely overlap opx of Group 1 with higher Th (up to 3.12 x Chondrite) and less pronounced Sr negative anomalies (Sr*, 0.28 – 1.02) (Fig. 29D). Opx associated with Group 3 cpx show an overall La to Tb enrichment (Fig. 28E) and the highest Th contents (up to 3.72 x Chondrite) but have similar Sr* to that of Group 2 opx (0.45 – 0.47) (Fig. 29F).
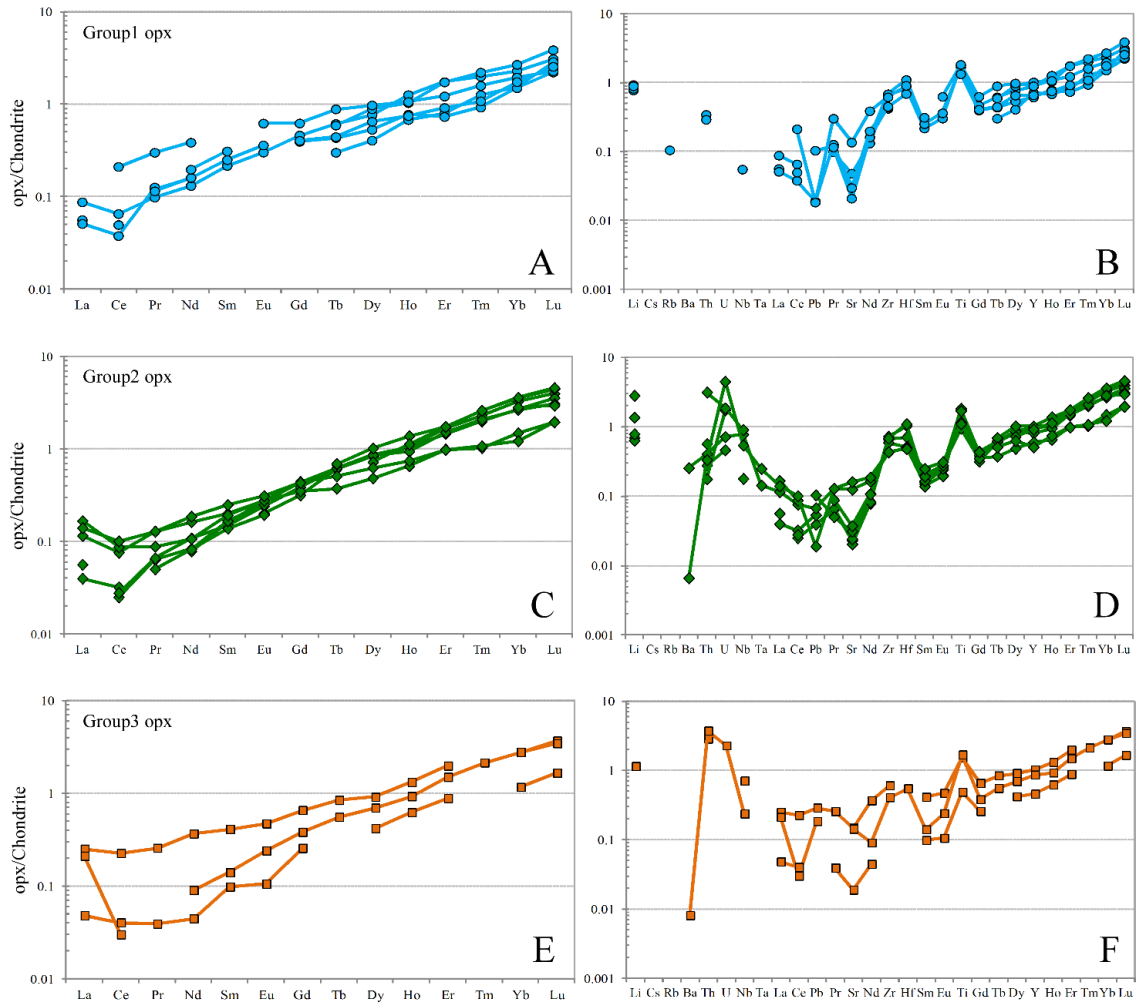
Fig. 29. Chondrite normalized REE (A, C, E) and trace element (B, D, F) patterns of opx in PMVF mantle xenoliths, divided in three Groups according to their geochemical features (see text for further explanations).

4.3.3.3 Amphiboles

Chondrite-normalized trace element and REE patterns of disseminated amphibole mimic very well those of the coexisting cpx (Fig. 30) in each sample and, on average, for each Group.

Group 1 amphiboles have the most depleted [$(La/Yb)_N$, 0.26 – 0.48], well-defined convex upward REE patterns [$(Eu/Yb)_N$, 0.94 – 1.36] (Fig. 30A); they show either Nb-Ta positive or negative anomalies (Fig. 30B) even though their contents are low (Nb, up to 3.04 ppm; Ta, up to 0.21 ppm). Positive Nb-Ta anomalies are always associated with negative Th-U anomalies and *vice versa*, thus the higher Th and U values (up to 6.34 and 17 x Chondrite, respectively) are reached in amphiboles with the lowest Nb contents. Group 1 is also characterized by the most pronounced Ti positive anomalies (Ti* = Ti/[(Eu+Gd)/2], 0.9 – 2.3; average 1.6).

Group 2 includes amphiboles showing slight La and Ce enrichments [$(La/Yb)_N$, 0.33 – 0.83] and less convex REE pattern [$(Eu/Yb)_N$, 0.5 – 1.21] with respect to Group 1 amphiboles (Fig. 30C). The opposite behavior between Nb-Ta and Th-U anomalies persists (Fig. 30D), with similar Nb and Ta

contents (Nb, up to 3.61 ppm; Ta, 0.28 ppm, respectively) and a slight increase of Th spike (13.6 x Chondrite). Ti negative anomaly tend to reduce in this Group (Ti*, 0.9 – 2.1, average 1.4).

Amphiboles falling within Group 3 are remarkably enriched in LREE [(La/Yb)$_N$, 1.37 – 2.17] with respect to the previous groups, forming smooth spoon-shaped patterns (Fig. 30E). They have Th and U values similar to those of the other groups (up to 16.9 and 15, respectively) but reach the highest Nb contents (63 x Chondrite) among disseminated amphiboles (Fig. 30F).

Amphibole vein in sample LAG52 is included in Group 3 and is shown as a single average (Fig. 30E,F) due to the similarity between the various analyzed spots. It is characterized by a pronounced REE fractionated pattern with L-MREE enrichments [(La/Yb)$_N$, 4], the highest HFSE contents [(Nb)$_N$, 150 x Chondrite; (Zr)$_N$, 92 x Chondrite; (Hf)$_N$, 2.7 x Chondrite] and a feeble negative Ti anomaly (Ti*, 0.7). Its pattern fit well those of amphibole veins found in both PMVF peridotites and clinopyroxenites by Zanetti et al. (1995), Vaselli et al. (1995) and Chalot-Prat and Bouillier (1997) (ESM3-3). Like for major elements, trace element budget of these veins also show many similarities with amphibole MXC (ESM3-3, Zanetti et al., 1995; Downes et al., 1995) which, however, are on average characterized by slightly lower LREE and a remarkable Ti positive anomaly (Ti*, 1.71 – 4.08).
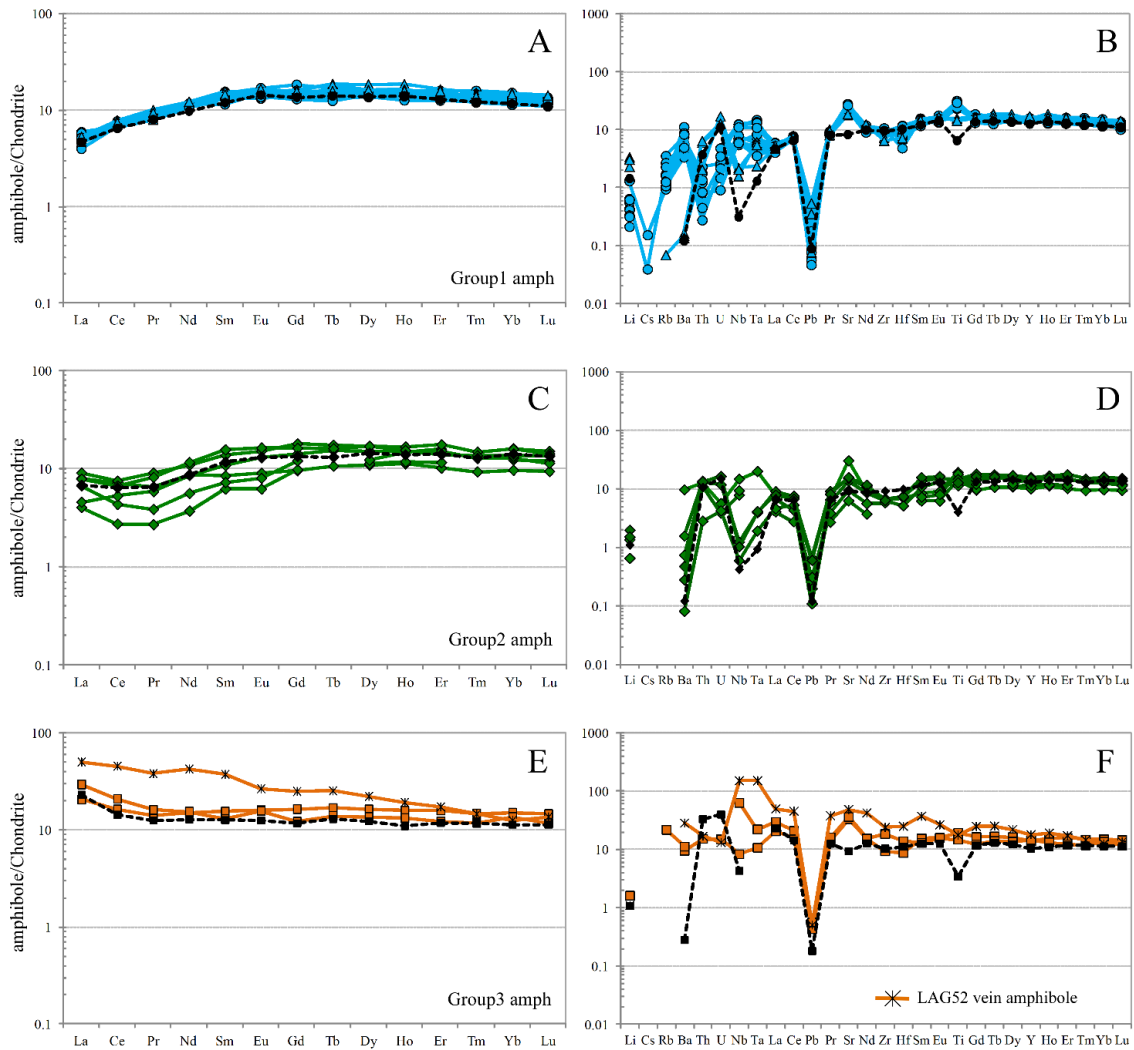
Fig. 30. Chondrite normalized REE (A, C, E) and trace element (B, D, F) patterns of amphibole in PMVF mantle xenoliths, divided in three Groups according to their geochemical features (see text for further explanations). Average patterns of the associated different cpx Groups (black dotted lines) are also reported for comparison. The pattern with asterisk symbol represents LAG52 vein amphibole.

4.3.4 Noble gas elemental and isotopic compositions

Olivine systematically show the lowest concentration of ^{4}He and ^{40}Ar*, while cpx and opx have a comparable range of values (ESM3-4). The highest concentration for the three minerals is found in LAG52 that also shows the lowest mg#. ^{4}He is positively correlated with ^{40}Ar*, indicating that ^{4}He-rich FI are also ^{40}Ar*-rich and, reasonably, rich in the other gas species.

The ^{4}He/^{20}Ne ratio is 0.7-41.7 in ol, 11–1960 in opx, and 8.3–1394 in cpx (ESM2-3). The ^{40}Ar/^{36}Ar ratio is 286–326 in ol, 350–879 in opx, and 319–1867 in cpx (ESM2-3). The ^{20}Ne/^{22}Ne and ^{21}Ne/^{22}Ne ratios are 9.8–10.0 and 0.0283–0.0327, respectively, in olivine, 9.8–10.1 and 0.0291–0.0342 in opx, and 9.9–10.1 and 0.0290–0.346 in cpx (ESM2-3 and Fig. 31).

The ^{3}He/^{4}He ratio corrected for air contamination (Rc/Ra value) is 1.5–5.9 Ra in olivine, 5.4–6.8 Ra in opx, and 2.2–6.8 Ra in cpx (ESM2-3 and Fig. 32). The highest ^{3}He/^{4}He values within olivine were measured in LAG52 and TRE2 (5.4 and 5.9 Ra, respectively), and only in the case of LAG52 it corresponds to the highest concentration of ^{4}He (94 ×10^{-14} mol/g) and ^{40}Ar* (42×10^{-14} mol/g) (Fig. 32). At progressively lower concentration of ^{4}He and ^{40}Ar*, ^{3}He/^{4}He values decrease. The highest ^{3}He/^{4}He ratios in opx and cpx are measured in TRE1 and TRE2 (Fig. 32; ESM2-3).
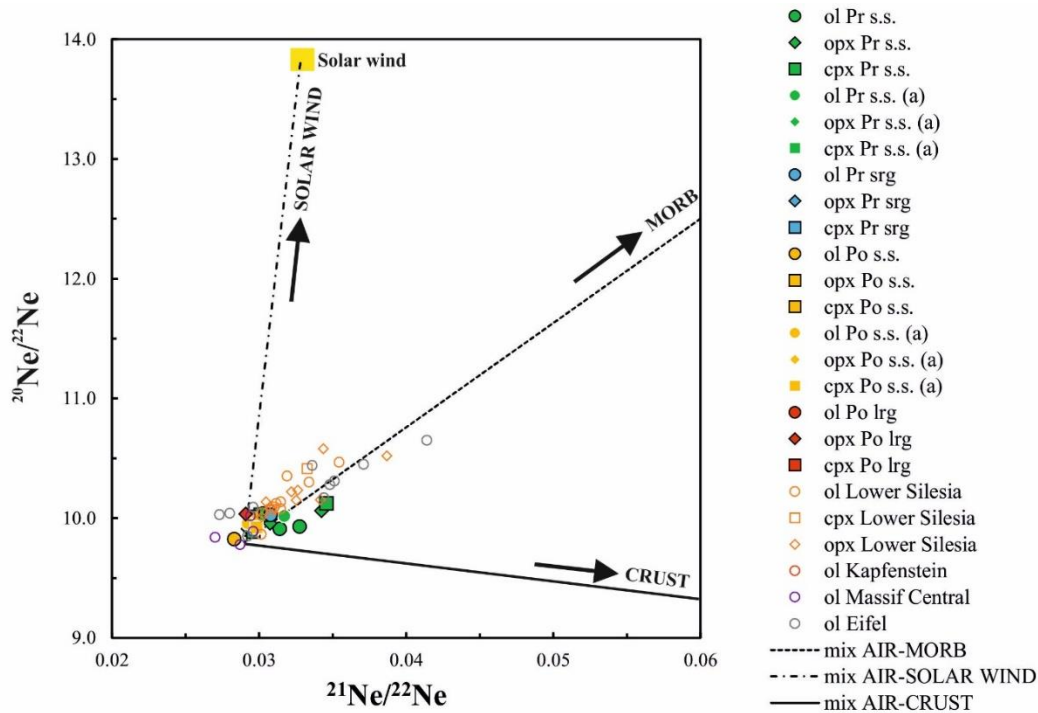
Fig. 31. Diagram of ^{21}Ne/^{22}Ne versus ^{20}Ne/^{22}Ne measured in fluid inclusions of PMVF xenoliths. Olivine abbreviated as "ol". The black dashed and dotted lines represent binary mixing between air (^{21}Ne/^{22}Ne = 0.0290 and ^{20}Ne/^{22}Ne = 9.8) and i) MORB mantle as defined by Sarda et al. (1988) and Moreira et al. (1998) at ^{21}Ne/^{22}Ne = 0.06 and ^{20}Ne/^{22}Ne = 12.5; ii) CRUST as defined by Ballentine (1997) and references therein at ^{21}Ne/^{22}Ne = 0.6145 (mean of 0.469-0.76) and ^{20}Ne/^{22}Ne = 0.3; iii) SOLAR WIND as defined by Heber et al. (2009) at ^{21}Ne/^{22}Ne = 0.0328 and ^{20}Ne/^{22}Ne = 13.8. Data from other European localities are also reported (French Massif Central, Eifel, and Kapfenstein in Pannonian Basin, Gautheron et al., 2005; Calatrava and Tallante, Martelli et al., 2011; Lower Silesia, Rizzo et al., 2018).
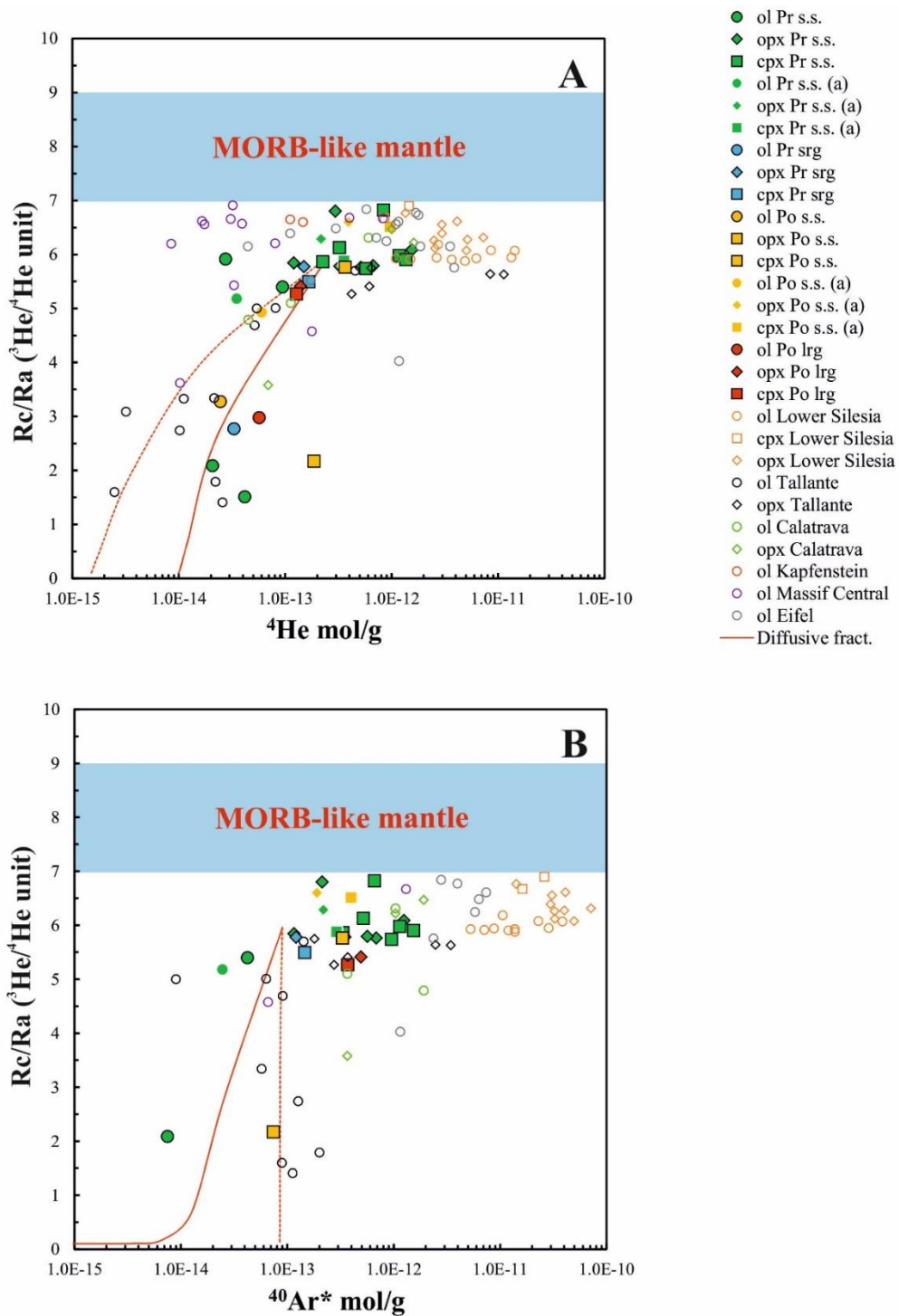
Fig. 32. Concentrations of a) ^4He and b) $^{40}Ar^*$ versus $^3He/^4He$ corrected for air contamination (Rc/Ra values). Olivine abbreviated as "ol". The blue bar indicates the range of $^3He/^4He$ ratios for a MORB-like mantle (8±1 Ra; Graham, 2002). The two diffusive fractionation paths are modeled based on the approach of Burnard et al. (1998), Burnard (2004) and Yamamoto et al. (2009), taking into account the diffusion coefficient (D) of ^3He, ^4He, and $^{40}Ar^*$ (D_{3He}/D_{4He} = 1.15 and D_{4He}/D_{40Ar} = 3.16 in solid mantle; Trull and Kurz, 1993; Burnard, 2004; Yamamoto et al., 2009). Starting and final conditions as well as further details on modeling are reported in the text. Data from other European localities as in Fig. 31 caption.

4.4 Discussion

4.4.1 Mineral equilibrium and temperature estimation

The Mg and Fe equilibrium exchange (Brey and Köhler, 1990) among peridotite minerals allows evaluating how much mineral pairs match equilibrium, coherently with their Fe/Mg distribution. Irrespective of textural type and amphibole modal percentage, the Fe/Mg exchange between olivine and opx of PMVF samples reproduces, within the experimental error, the slope of olivine-opx lines calculated for temperatures varying between 927 and 727 °C (1300 - 1100 °K) in the pressure range of 1.5 - 2.0 GPa, (Brey and Köhler, 1990). Olivine-cpx and opx-cpx pairs, distinguished by textural types, also reflect ideal Fe/Mg equilibrium (Brey and Köhler, 1990) in the same temperature and pressure ranges. Minerals in close proximity to host basalts veinlets, showing destabilization due to local thermal effects, were discarded.

Equilibrium between olivine and spinel was also evaluated, by comparing the Fe/Mg distribution among the coexisting minerals with the ideal equilibrium distribution of Fe^{2+} and Mg between olivine and the aluminum component in (Mg-Fe)–bearing spinel end members (i.e. spinel s.s. and hercynite, Jamieson and Roeder, 1984). Spinel end-members were calculated assuming that all Ti and Fe^{3+} (as determined by stoichiometry) form ulvöspinel and magnetite components, respectively. Taking into account the diffusion corrections (Lehmann, 1983), Fe-Mg distribution coefficient between olivine and Al-spinel is estimated in the range of 0.90 - 1.23 (Jamieson and Roeder, 1984) at T= 1000-1200 °C.

The relevant presence of disseminated amphibole (generally less than 4% but up to 11.5 wt% in one case, Table 1; ESM1) in PMVF peridotites cannot be ignored when discussing the potential intra-mineral equilibrium conditions. Experimentally determined Fe-Mg distribution coefficient ($Kd_{Fe-Mg}^{cpx-amph}$) between cpx and amphibole in basanite melts is (on average) 0.76 ± 0.21 (Hawthorne and Oberti 2007; Pilet et al., 2010). This value is also constrained by Ca contents and the subsolidus equilibrium between the two minerals is resolved with [Ca/(Ca+Mg+Fetot)] ~ 1.6 (Forshaw et al. 2019), a condition fully satisfied by amphibole/cpx pairs in PMVF peridotitic xenoliths.

In the light of these findings, temperature estimations have been carried out using the two pyroxene equations of Brey and Köhler (1990) and Taylor (1988) (Table 1). Brey and Köhler (1990) geothermometer yielded temperatures spanning from 843 to 1056 °C at 2.0 GPa, with standard deviations for each sample (from ±0.7 to ±14) lower than the methodological error (±24°C). Taylor (1998) formula gave comparable results (858-1009 °C at 2.0 GPa), with differences between the two methods always lower than 60°C. Regardless the geothermometers used, *Po s.s.* always recorded temperatures between 111 and 148 °C lower, on average, than the other three textural sub-groups. It has to be noted that *Po lrg* are intermediate between the Protogranular group and *Po s.s*, suggesting

a decrease in temperature at increasing "porphyroclastic degree" in PMVF samples, in agreement with the results of Falus et al. (2008) and what has been observed for other mantle xenolith suites from the Pannonian Basin (Embey-Isztin et al., 2001; Ntaflos et al., 2017).

4.4.2 Oxygen fugacity and pressure conditions

Assuming that thermodynamic parameters are known and activity/composition relations can be assessed, oxygen fugacity (fO$_2$) in mantle peridotites may be calculated from the heterogeneous redox equilibria:

Fayalite (olivine) + O$_2$ (fluid) = Ferrosilite (opx) + Magnetite (spinel).

The calculation is hampered by uncertainties in the activity/composition relations of magnetite component in spinel (Mattioli and Wood, 1988; Wood and Virgo, 1989). Since magnetite solid solution is low in mantle spinel ($\leq$ 2.5% in this xenolith population), typical analytical errors translate into considerable fO$_2$ uncertainties. We applied the semi-empirical equation of Ballhaus et al. (1991), using the magnetite composition/activity model of Wood and Virgo (1989). The fO$_2$ calculated in terms of divergence from the fayalite-magnetite-quartz (FMQ) buffer are in the restricted range of -1.22 - +0.34, with the lowest values belonging to the *Po s.s.* anhydrous harzburgite TRE1 (Table 1; ESM3-5). These values are comparable to those typical for both off-craton Sub-Continental Lithospheric Mantle (SCLM) and supra-subduction zones (Foley, 2011; Bénard et al., 2018) and to those calculated for Pannonian Basin mantle xenoliths by Szabó et al. (1995b). A vague positive correlation between fO$_2$ and the modal percentage of the redox sensitive phase amphibole have been observed; such a correlation seems to be in agreement with the result of Sorbadere et al. (2018) who observed an increase in oxygen fugacity with the increase of H$_2$O content in a peridotitic system, but was not observed in other cases of amphibole-bearing mantle xenolith populations (Bonadiman et al., 2014).

The pressure of amphibole formation could be tentatively estimated. Recently, Mandler and Grove (2016) made a series of experiments to quantify the effects of pressure, temperature, bulk composition and H$_2$O content on the stability of amphibole in the Earth's mantle. They established that alkali content of amphibole is a linear function of pressure and temperature and less dependent on bulk compositional variations and water contents, allowing to formulate an empirical thermobarometer for pargasite-bearing garnet (and spinel) peridotites. To avoid circular reference, we introduced in the eq. 1 of Mandler and Grove (2016) the temperatures calculated from Brey and Köhler (1990) geothermometer. According to the Mandler and Grove (2016) equation, PMVF amphibole-bearing lherzolites equilibrated between 2.5 and 2.7 GPa (Table 1), which seem rather high pressures as no garnet is present in their mineral assemblage. These rocks have bulk Cr$_2$O$_3$/Al$_2$O$_3$ ratios (0.09-0.14)

comparable to the experimental fertile hydrous (H_2O= 0.65wt%) lherzolite (0.10), in which the spinel–garnet transition occurs below 2.5 GPa. Taking into account the experimental error and the different water content between natural and experimental lherzolites, the pressure prediction for PMVF amphibole equilibration are therefore consistent with these samples having last equilibrated in the upper pressure limit of the spinel stability field (O'Neill 1981; Klemme 2007; Ziberna et al. 2013). Consequently, a rather deep origin of PMVF mantle xenoliths cannot be discarded. The opx-cpx-spinel clusters found within some samples could be symptomatic of a former garnet as suggested by Falus et al. (2000), which hypothesized a mantle domain moving from a garnet bearing region at pressures higher than 3.0 GPa to a shallower level (1.9 - 2.1 GPa), inferring an upwelling of the PMVF mantle section of 40-60 km. This occurred in the frame of a highly arcuate subduction zone, where rapid tectonic changes were strictly correlated to accelerated slab steepening (Edward and Grasemann, 2009), asthenospheric uprise (Mason et al., 1998; Harangi, 2001; Seghedi et al., 2004; Kovács et al., 2018) in a post-collisional stage and regional stress redistribution (Seghedi et al., 2011 and references therein).

4.4.3 Processes that modify the geochemistry of FI

4.4.3.1 Atmospheric contamination

FI isotope composition of Ne and Ar and, complementarily, the $^4He/^{20}Ne$ ratio in PMVF xenoliths highlights a variable air contamination (Fig. 34, ESM2-3), which progressively decreases from olivine to cpx, probably due to the increasing concentration of He-Ne-Ar trapped in FI of the pyroxenes. This is clearly shown by the three Ne isotopes plot (Fig. 31), in which our data fall along or slightly below the theoretical mixing line between air and a MORB-like mantle, defined by Sarda et al. (1988) and Moreira et al. (1998) at $^{21}Ne/^{22}Ne = 0.06$ and $^{20}Ne/^{22}Ne = 12.5$. A similar indication comes from the $^{40}Ar/^{36}Ar$ and $^3He/^{36}Ar$ values (Fig. 33), which are well below the theoretical ratio in the mantle ($^{40}Ar/^{36}Ar$ up to 44,000 and $^3He/^{36}Ar$~0.45; e.g., Burnard et al., 1997; Moreira et al., 1998; Ballentine et al., 2005), and fall along the binary mixing between air and a MORB-like mantle.

The presence of atmospheric contamination is also evident in FI-related noble gas data of other European SCLM xenoliths [Eifel (Germany) and Massif Central (France), Gautheron et al., 2005; Calatrava and Tallante (Spain), Martelli et al., 2011 (not shown in Fig. 33); Lower Silesia (NE Eger Rift, SW Poland), Rizzo et al., 2018]. For sake of homogeneity, we compare our data with those from other mantle xenoliths locations that were analyzed by single-step crushing and for which $^{40}Ar/^{36}Ar$ data are available. Data from Eifel and Lower Silesia are slightly out from this binary mixing due to different $^4He/^{40}Ar*$ and $^3He/^4He$ ratios (Fig. 34), probably related to distinct mantle features and processes occurred therein. Beside this, mantle xenoliths from PMVF (this study), Calatrava and

Tallante show the highest air contamination at comparable ^{4}He concentrations that are likely proportional to the total FI gas content.

As summarized by Rizzo et al. (2018), air in FI from mantle xenoliths could be linked to i) a direct contamination in the SCLM, ii) a contamination acquired by xenoliths during magma ascent, or iii) a post-eruptive entrapment in mineral micro-cracks. Because Perşani volcanism is partly coeval with the post-collisional calc-alkaline magmatism of the South Harghita Mountains, outcropping only 40 Km eastward (Szakács et al., 1993; Seghedi et al., 2004, 2011, 2016; Lustrino and Wilson, 2007), the first hypothesis is, in our opinion, the most reasonable. This hypothesis could also explain the high air contamination found by Martelli et al (2011) in mantle xenoliths from Tallante, which underwent a metasomatism by subduction-related fluids possibly linked to the Cenozoic Betic subduction, although the authors favour the third hypothesis.
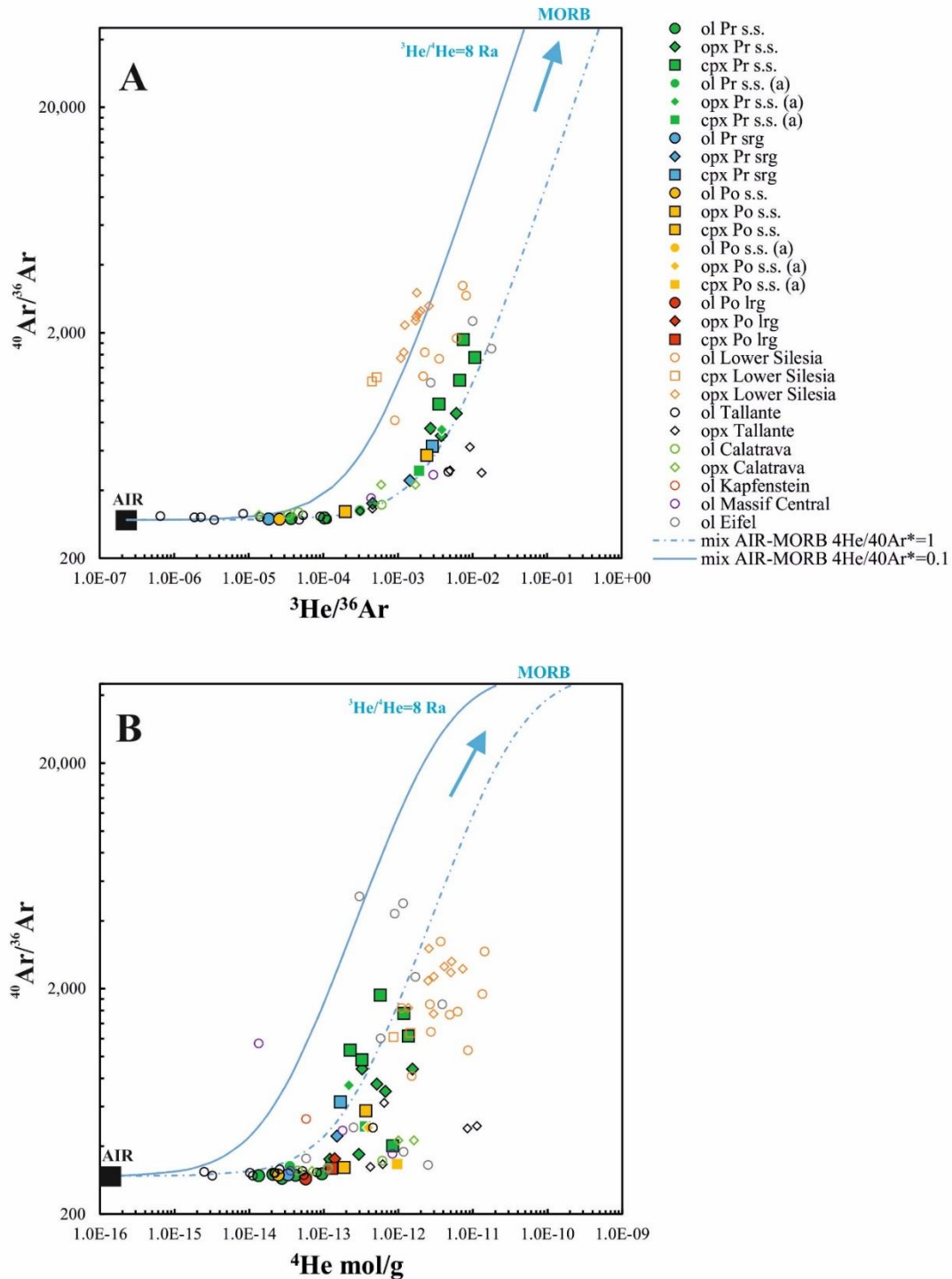
Fig. 33. a) ^{3}He/^{36}Ar and b) ^{4}He (mol/g) versus ^{40}Ar/^{36}Ar. Olivine abbreviated as "ol". The continuous and dashed turquoise lines represent binary mixing between air [^{40}Ar/^{36}Ar = 295.5, ^{3}He/^{36}Ar = 2.3×10^{-7} and ^{4}He = 1.1×10^{-16} (arbitrarily fixed to fit data)] and MORB mantle as defined by Burnard et al. (1997), Moreira et al. (1998), and Ballentine et al. (2005) at ^{40}Ar/^{36}Ar = 44,000, ^{3}He/^{36}Ar = 0.49 and ^{4}He = 1.0×10^{-10} (arbitrarily fixed to fit data), considering ^{3}He/^{4}He = 8, ^{4}He/^{40}Ar* = 1 and ^{4}He/^{40}Ar* = 0.1. Data from other European localities as in Fig. 31 caption.
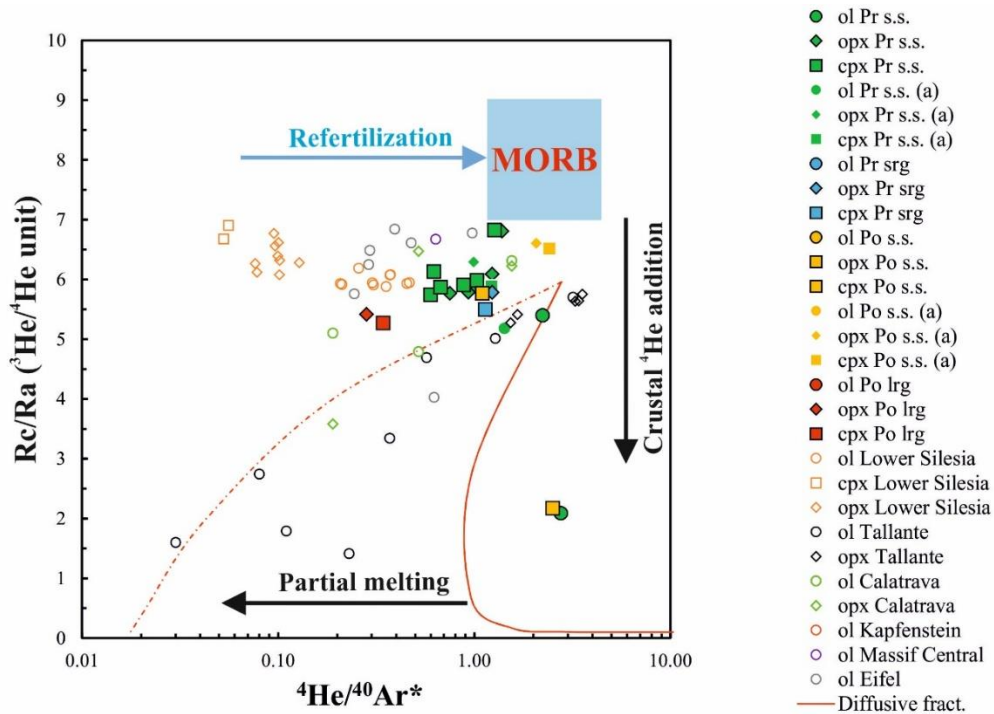
Fig. 34. ^{4}He/^{40}Ar* versus ^{3}He/^{4}He corrected for air contamination (Rc/Ra values). Olivine abbreviated as "ol". The blue rectangle indicates MORB (^{3}He/^{4}He = 8±1 Ra; Graham, 2002; ^{4}He/^{40}Ar* = 1–5; Marty, 2012). The two diffusive fractionation paths are modeled as reported in Fig. 32. Data from other European localities as in Fig. 31 caption.

4.4.3.2 Diffusive fractionation

^{4}He and ^{40}Ar* in PMVF xenoliths are systematically lower in olivine than in cpx and opx (ESM3-4), with the former having the narrowest range of ^{4}He/^{40}Ar* (1.4-2.7), within the reported range for mantle production (^{4}He/^{40}Ar* = 1–5; Marty, 2012). Opx and cpx vary from 0.3 to 2.1 and 0.3 to 2.5, respectively, including values below the mantle production range (Fig. 34). These observations suggest that mantle processes such as partial melting and/or refertilization/metasomatism fundamentally modulate the chemical variability of FI. However, comparing ^{4}He and ^{40}Ar* with ^{3}He/^{4}He (Fig. 32) we notice that, at concentrations of ^{4}He and ^{40}Ar* below ~1.0-2.0×10^{-13} mol/g, ^{3}He/^{4}He values decrease. On the contrary, opx and cpx do not show any significant difference in the ^{3}He/^{4}He values that could be related to ^{4}He and ^{40}Ar* concentrations, except cpx from sample TRE4 that has ^{4}He and ^{40}Ar* below ~1.0-2.0×10^{-13} mol/g and a ^{4}He/^{40}Ar* value of 2.5 (Figs. 32 and 34). In addition, opx and cpx from sample TRE3 show the lowest ^{3}He/^{4}He and ^{4}He/^{40}Ar* values.

These differences may originate by preferential diffusive loss of ^{4}He and ^{40}Ar* (e.g., Burnard et al., 1998; Burnard, 2004; Yamamoto et al., 2009 and references therein), which depends on the diffusion coefficient (D), significantly higher for ^{4}He than for ^{40}Ar* (D_{4He}/D_{40Ar} = 3.16 in solid mantle; Burnard, 2004; Yamamoto et al., 2009). In the case of diffusive loss of helium, we should also expect that ^{3}He/^{4}He fractionates due to the appreciable difference in D_{3He} and D_{4He} among mantle minerals

(D_{3He}/D_{4He} = 1.15; Trull and Kurz, 1993; Burnard, 2004; Yamamoto et al., 2009 and references therein).

In Figs. 32 and 34 we model two possible path of diffusive fractionation of He, ^{40}Ar*, ^{3}He/^{4}He, and ^{4}He/^{40}Ar* during mantle melting, based on the approach of Burnard et al. (1998), Burnard (2004) and Yamamoto et al. (2009). As starting mantle composition, we assumed ^{4}He = 2.5×10^{-13} mol/g, ^{40}Ar* = 9.0×10^{-14} mol/g, and ^{3}He/^{4}He = 5.9 Ra. These values were chosen because, immediately below these values, a decrease of ^{3}He/^{4}He is noticed and the ^{4}He/^{40}Ar* ratio was within the reported range for mantle production (^{4}He/^{40}Ar* = 1–5; Marty, 2012). The ^{3}He/^{4}He was chosen considering the mean ratio in olivine, opx and cpx among data apparently not modified from this process. For the constant concentration of the element in the magma (called Cf in Yamamoto et al., 2009), we assumed two different concentrations of ^{4}He and ^{40}Ar* in order to fit our data and those from the literature (see ESM3-4 and Fig. 34 caption for further explanations).

According to our modelling, olivine and cpx from TRE4 and opx and cpx from TRE3 fit the paths of diffusive fractionation. Thus, it is likely that this process modified the noble gases composition of the residual mantle during its melting, but it can be appreciated only in those portions where the concentration of noble gases was low (i.e., ^{4}He and ^{40}Ar* below ~1.0-2.0×10^{-13} mol/g). A process of diffusive fractionation can also explain the data from Calatrava and Tallante mantle xenoliths with concentrations of ^{4}He and ^{40}Ar* below of 1.0-2.0×10^{-13} mol/g (Fig. 32 and 34), as also argued by Martelli et al. (2011). This concentration thus represents a cut off line below which the data cannot be used for considerations on the residual mantle characteristics. It is worth noting, however, that mantle xenoliths from Eifel, French Massif Central, and Styria Basin with ^{4}He concentration below 1.0-2.0×10^{-13} mol/g do not show any similar variation, suggesting that diffusive fractionation did not occur in these localities or occurred in different conditions, such as to avoid remarkable modification of the FI composition. We argue that this process probably regards only specific portions of European (and worldwide?) SCLM but we have no further arguments to constraints an aspect that is beyond the scope of this study. As far as PMVF FI compositions are concerned, in the following discussions we focus on data not affected by diffusive fractionation.

4.4.4 Melting and refertilization events

Modal and whole rock compositions of PMVF mantle xenoliths have been compared to existing melting models for off-craton peridotites, in order to puzzle out the melting history of the sampled lithospheric section. Comparing MgO contents with modal percentage of olivine, opx and cpx (ESM3-6), the trends depicted are concordant with the depletion model trends of Niu et al. (1997), although a tendency towards lower modal olivine and higher cpx can be observed. The

Porphyroclastic group have higher MgO contents with respect to Protogranular group. TiO_2 and Al_2O_3 positive correlation would depend upon melt extraction (Takazawa et al., 2000; Ionov, 2007 and references therein). However, considering our data together with those of Vaselli et al. (1995) (ESM3-7), about two thirds of the samples fit equilibrium melting paths between 2 and 3 GPa, while the remaining (including the majority of our samples) do not follow any residual evolution line, even considering polybaric decompression melting (Ionov and Hoffmann, 2007 and references therein). With only few exceptions, these samples have less iron with respect to the expected Al_2O_3 content, this latter being even higher with respect to the corresponding MgO predicted by models for any kind of melting evolution (ESM3-7), both at constant and decreasing P (Niu, 2004; Ishimaru et al., 2007). Thus, the extremely Al_2O_3-rich compositions of some PMVF mantle xenoliths do not find an explanation if only partial melting is taken into account.

Similar information is given by mineral phase composition. Johnson et al. (1990) proposed the most used, mineral focused model to predict the melting degree for batch and fractional melting, based on cpx REE patterns, while more recently Scott et al. (2016) proposed a similar approach for opx. Bonadiman and Coltorti (2011, 2018) and Upton et al. (2011) attempted to infer the partial melting degree of a mantle lithotype based on major element composition of opx, cpx and spinel. As it is well known, cpx is the most important incompatible trace element repository within an anhydrous peridotite, constraining the overall REE budget. Obviously this is not true when a volatile-bearing phase is present, taking into account that amphibole partitioning coefficients are higher than those of cpx for most incompatible elements (see for example Ionov et al., 1997; Witt-Eickschen and Harte 1994). Disseminated amphibole is almost ubiquitous within the PMVF xenoliths, with trace element patterns perfectly mimicking those of cpx apart for elements which are preferentially incorporated in the amphibole crystal lattice (Figs. 28, 29, 30). The ubiquitous similarity between the trace element patterns of the two minerals - regardless of textural positions or presence of amphibole vein - is a strong indication of disseminated amphibole genesis via cpx hydration, followed by subsolidus re-equilibration. Since amphibole grew over cpx, some differences should be expected between cpx patterns in anhydrous and hydrous parageneses. However, the patterns of cpx from anhydrous lherzolite BARQ4 are perfectly comparable with those of cpx from lherzolites LAG21 and LAG24, having 0.7 and 1% of modal disseminated amphibole, respectively. For this reason, no re-distribution modeling backward from amphibole to cpx has been developed and we assumed that the trace element contents of cpx correspond to the original composition, i.e. should represent a suitable indicator of the partial melting degree. Batch, fractional and incremental (with 1% increment for each step) melting modeling were thus developed following the Johnson et al. (1990) equations, using as starting composition the primordial, fertile cpx proposed by Bonadiman et al. (2005) for spinel peridotites.

The best fit between model and real cpx was obtained for fractional melting (ESM3-8), although many of the samples (BARQ4, LAG21, LAG24, LAG51, TRE4) have HREE and MREE values higher than those of the primordial cpx, while LREE can be variably enriched or depleted. Cpx from lherzolite LAG52 perfectly overlaps the pattern of primordial cpx, while lherzolites LAG1, TRE1 and TRE2 indicate very low degrees of partial melting, between 1 and 5 %. Thus, according to cpx REE composition, PMVF xenolith represent a very fertile mantle that, however, cannot be explained just invoking low-degree melting processes. This conclusion is further enhanced by checking out the opx. According to the model of Scott et al., (2016), indeed, opx REE patterns indicate substantially higher degrees of melting (ESM3-9). The comparison has been developed based on HREE (since LREE are highly variable and more prone to be modified by post-melting processes) and taking into account that the model starts from the DMM source by Workman and Hart (2005), already slightly depleted by 2-4 % melt extraction. Protogranular group opx would have been affected by a melting event between 12 and 20%, whereas Porphyroclastic group opx would record a melt fraction (F) from 20 to 25%, with TRE1 being the most depleted. Using the approach developed by Bonadiman and Coltorti (2018) in the CMAS-Fe system for pressures varying between 1 to 3 GPa and temperatures between 900 and 1300 °C, (which takes also into account the subsolidus re-equilibration), the opx major element composition indicates rather low degrees of partial melting (mainly < 15%), although the fit with the theoretical curve is rather limited (Fig. 25A). The indication of low degree of melting comes from the high Al_2O_3 contents that in some samples (BARQ4, LAG24 and LAG2) is higher than that of a primordial opx. As far as mg# is concerned, some samples shift toward higher values and only one (LAG52, the sole with an amphibole vein) towards lower values with respect to the theoretical curve at constant Al_2O_3 value. Taking into account the existing Fe and Mg equilibrium between opx and olivine, as well as the Fo and NiO content of the latter - unlikely for low degree of melting - it can be hypothesized that Al_2O_3 has been added to the system after the partial melting. If this is the case and the opx composition is reported on the curve following the mg#, the obtained degrees of F appear well comparable with those estimated by the HREE in opx. Support for this line of reasoning comes from the composition of primary (and secondary) opx in xenoliths representative of the mantle wedges, entrained in calc-alkaline lavas from Kamchatka (Kepezhinskas et al., 1996; Bryant et al., 2007; Ishimaru et al., 2007; Ionov, 2010; Ionov et al., 2013) and Philippines (Arai et al., 2004; Yoshikawa et al., 2016) (Fig. 25A). These opx match quite well the theoretical line and have high mg# - similar to those of TRE1 – coupled with very low Al_2O_3 contents. It is then reasonable to put forward that PMVF xenoliths were residua of partial melting degrees comparable to those of typical sub-arc mantle that were successively affected by an Al_2O_3 enrichment. The event would have also increased the modal percentage of opx, considering that some PMVF xenoliths have

a paragenesis moving toward ol-websterites, with opx modal contents up to 36.2%, much higher than that of a primordial, fertile mantle (25%, Johnson et al., 1990). A SiO_2-saturated, Al_2O_3-rich metasomatizing melt could increase the opx modal content with mg# buffered by the matrix, concomitantly with, or followed by, a textural re-equilibration and re-crystallization. This reorganization could have occurred under the stress regime consequent to slab steepening/sinking and to asthenosphere uprise, that pushed upward the overlying lithospheric mantle column (Falus et al., 2000, 2008, 2011). Enhanced recrystallization of newly formed ("secondary") opx in a mantle wedge can completely delete its initial replacement texture so that it looks like a primary phase (Arai and Ishimaru, 2008).

A similar interpretation can be put forward for cpx major elements, having mg# values compatible with melting degrees $\geq$ 25%, but showing Al_2O_3 contents higher than those expected by theoretical calculations. Thus their Mg and Fe contents, being buffered by the matrix, can be considered as good indicators of the partial melting degree, while Al_2O_3 and REE can be related to the enrichment process. As for opx, in Fig. 24A the composition of cpx from various subarc settings, such as Kamchatka (Kepezhinskas et al., 1996; Bryant et al., 2007; Ishimaru et al., 2007; Ionov, 2010), Philippines (Arai et al., 2003, 2004; Yoshikawa et al., 2016), Japan (Abe et al., 1998), Cascade Range (Brandon and Draper, 1996) and Lihir (McInnes et al., 2001) is reported. In all cases, cpx with mg# equal or exceeding the degree of partial melting after which cpx is exhausted (F= 22-25%, Hellebrand et al., 2001; Bernstein et al., 2007; Sobardere et al., 2018) are found, but they show a remarkable Al_2O_3 enrichment with respect to the theoretical curve. It is likely that these cpx were newly formed, growing over a strongly depleted opx in an originally harzburgitic matrix (which buffered the mg#) from an Al_2O_3-rich melt. Alternatively, cpx could have been generated by exsolution from opx and successively texturally re-organized and enriched by an Al_2O_3-rich metasomatizing melt. In the Protogranular group it is evident that cpx are newly formed, with Al_2O_3 and modal content exceeding the PM values. A similar observation is valid for the Porphyroclastic group that, however, do not show an analogous level of enrichment. Cpx from anhydrous harzburgite TRE1 have the highest mg# and the lowest Al_2O_3 content, probably because this sample was less affected by the enrichment process and/or started from the most residual composition.

In this framework, the metasomatic process that affected the mantle domain beneath Persani Mts. can be more properly considered as a refertilization that not only modified the composition of the various phases, but also consistently increased the pyroxene modal abundance. Pyroxenes increased at expenses of olivine, as observed by Falus et al. (2008), who described some textures where opx replaces olivine. Spinel was also most probably enriched and/or added to the peridotitic matrix during

the refertilization, as testified by its modal abundance, up to 5.3 % in some samples (Table 1 ESM), and very high Al_2O_3 content (ESM3-2).

4.4.5 Refertilization geodynamic context and subsequent alkaline metasomatism

The geochemical affinity of the refertilizing melt can be evaluated thanks to the presence of disseminated amphibole. According to Coltorti et al. (2007b), the geochemical imprint of a metasomatizing agent can be traced back by using key elements (particularly Nb and in general the HFSE, which are highly immobile during chromatoghraphic fractionation processes, Ionov et al., 2002) and their ratios. In Zr/Nb vs Ti/Nb (Fig. 35A) and Zr/Nb vs Ti/Zr (Fig. 35B) diagrams, disseminated amphiboles fall entirely within the "subduction-related" field, a remarkable indication that they were generated by a subduction-related melt, probably a basalt originating from a lithosphere modified by fluids released by the sinking slab. The subducted oceanic plate is still visible today as evidenced by geophysical surveys under the seismically active Vrancea Zone in the southeastern edge of the Carpathian arc (Martin et al., 2006; Edwards & Grasemann 2009; Ismail-Zadeh et al., 2012). Post-collisional magmatism along the East Carpathian range migrated and rejuvenated from NW, where the oldest occurrences are found (10.2 Ma), to SE in the South Harghita volcanic field where the activity is younger than 1 Ma (Mason et al., 1996; Seghedi et al., 2011, 2016 and references therein). The South Harghita calc-alkaline volcanic activity was the last expression of a post-collisional, convergent margin dynamic (Seghedi et al., 2011 and references therein). Asthenospheric upwelling, linked to slab roll-back, was associated with extensional Na and K-alkaline volcanism (Koněcný et al., 2002; Seghedi et al., 2011). The calc-alkaline volcanism of the South Harghita developed between 5.3 and 0.3 Ma, with two gaps respectively between 3.9-2.8 and 1.0 Ma (Seghedi et al., 2011; Molnar et al., 2018). During the last gap, the building of Na-alkaline volcanic edifices of Perşani Mts took place (1.2-0.6 Ma), about 40 km to the west (Fig. 4). The last eruptive phase of Perşani Mts occurred contemporaneously with the final stages of South Harghita volcanic activity around 0.6 Ma (Szakács and Seghedi 1995; Pécskay et al., 1995b; Seghedi et al., 2011; Molnar et al., 2018). Although calc-alkaline products do not outcrop in the Perşani Mts, a cognate basaltic block found within the pyroclastic deposits show a clear arc signature (Downes et al., 1995; Mason et al., 1996) and is perfectly comparable to some Călimani-Ghurghiu-Harghita (CGH) basaltic andesites (ESM3-10), supporting the idea that, also in this area, a calc-alkaline magmatic phase (now buried) preceded the alkaline stage.

It is thus likely that the mantle under Perşani Mts. Underwent large-scale interaction with calc-alkaline magmas and maybe the majority of melt volumes were trapped and consumed at depth during the refertilization process. The great majority of calc-alkaline magmas of Călimani-Gurghiu-Harghita

volcanic chains are differentiated to various degrees and cover different magmatic affinities from low-K andesites to shoshonites (Harangi 2001; Seghedi et al., 2004). The most primitives have Al_2O_3 contents ranging between 16 and 21 wt% and Y as high as 28 ppm (Mason et al., 1996); one of them has Al_2O_3 and MgO around 19.5 and 5 wt%, respectively. This magma is considered as the parental melt of the Călimani series, with $^{87}Sr/^{86}Sr$ and $^{143}Nd/^{144}Nd$ ratios of 0.70525 and 0.51275, respectively, explained by the authors as the result of slight AFC processes that occurred within the crust or, alternatively, of sediment subduction and consequent source contamination. Such a composition fit reasonably well the requirements of the melt responsible for the mantle refertilization recorded in PMVF mantle xenoliths.

Disseminated amphiboles clearly have a subduction-related origin while the amphibole vein of lherzolite LAG52 fall in the intraplate field (Fig. 35A, B), showing a striking resemblance with amphibole MXC collected in the pyroclastic deposits of the Perşani Mts (Fig. 35). Continuous variation trends from vein amphiboles to MXC can be observed, with a constant decrease in mg#, Al_2O_3, Na_2O and Cr_2O_3 and an increase in TiO_2 (Fig. 26B) and K_2O. Oxygen and δD isotopic composition of MXC from Perşani and from the Carpathian-Pannonian region support their mantle origin. They are interpreted as fractionation product of basaltic melts (similar to the host alkali basalts, Zanetti et al., 1995) derived by various degrees of partial melting of an asthenospheric source contaminated by fluids released from subducted serpentinites or blueschist like those occurring in the Meliata-Vardar series (Demény et al., 2012 and references therein).

Interaction of PMVF mantle with alkaline melts have been already documented and there is good agreement that amphibole vein generation is the main result of this process. Olivine-clinopyroxenites also found as xenoliths in the Perşani Mts volcanics probably represent fractionation products of these alkaline melts formed at depth, within the mantle (Zanetti et al., 1995; Vaselli et al., 1995; Downes et al., 1995; Chalot-Prat & Boullier 1997; Downes, 2001). Because disseminated amphiboles result from reaction/hydration of cpx, it can be deduced that the two kinds of amphiboles represent different metasomatic episodes that occurred at different times. Having the interaction with calc-alkaline magmas occurring first, we argue that vein amphibole generation was subsequent to the onset of disseminated amphiboles and may represent the last metasomatic event recorded by PMVF mantle xenoliths. According to Zanetti et al. (1995), some vein amphiboles may represent the "frozen" composition of the alkaline magma travelling through the mantle (Fig. 36). Beside the variable enrichments in LREE, chondrite-normalized REE patterns of LAG52 vein amphiboles are very similar to those found in literature, including amphiboles of clinopyroxenites and MXC. Although the explanation by Zanetti et al. (1995) may be realistic, adcumulates are unlikely to perfectly match a liquid composition (Holness et al., 2017) and vein amphibole are indeed lower in L- and MREE

with respect to Perşani Mts lavas. We have thus calculated the melt in equilibrium with LAG52 vein amphibole using $Kd^{amph/alkaline\ melt}$ from GERM database and it resulted almost indistinguishable from the real Perşani alkaline magmas. Calculated cpx in equilibrium with the obtained melt (Fig. 37) is identical to the real cpx from PMVF clinopyroxenites (Vaselli et al., 1995; Chalot-Prat & Boullier, 1997). It has to be underlined that both natural and calculated cpx have completely different compositions, in term of major and trace elements, with respect to those occurring in the refertilized mantle xenoliths. The "magmatic" cpx derived from the alkaline melt/s have different REE patterns (in particular higher LREE and lower HREE, Fig. 37) with respect to the peridotitic ones and could have never been generated by the same liquid. Even using a chromatographic model (Ionov et al., 2002), we could not obtain such HREE enriched diopsides (Yb, 14.4 x Chondrite) starting from the alkaline cpx (Yb, 7.4 x Chondrite) supposing that the alkaline melt was the sole metasomatic agent that acted within PMVF mantle. These considerations further support the hypothesis that cpx and disseminated amphiboles are strictly related and are the result of a previous, calc-alkaline, extremely pervasive refertilization event, distinct from the subsequent alkaline metasomatic episode. The latter, on the other hand, resulted in the generation of amphibole veins within the peridotite and in the crystallization of amphibole-bearing clinopyroxenites and MXC. These magmas, very similar to those erupted by the Persani volcanoes and generated by a new source, crossed the studied lithospheric mantle section in more recent times (most probably after the onset of post-collisional tectonics, Seghedi et al., 2011), at the relatively shallow depth reached in consequence of asthenospheric doming, under a fragile regime. This allowed vein formation with very limited diffusive effects, only detectable as slight LREE and Nb enrichments in some of the pre-existing pyroxenes and their associated amphiboles (Group 2 and 3, Figs. 28 and 30), especially in close proximity of the amphibole vein.
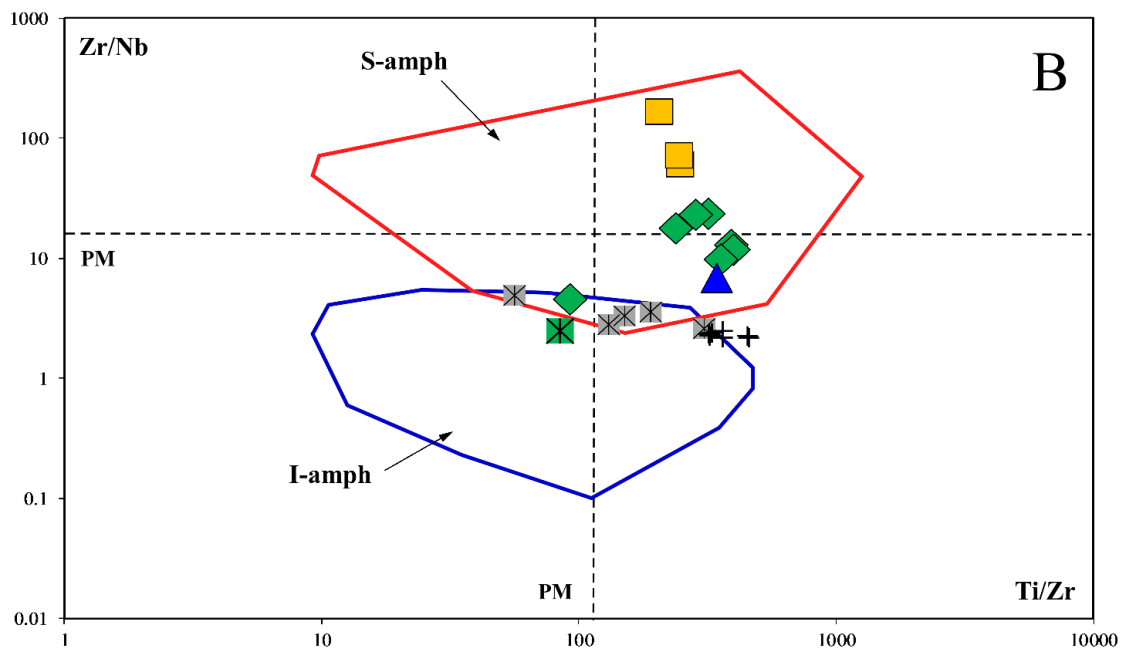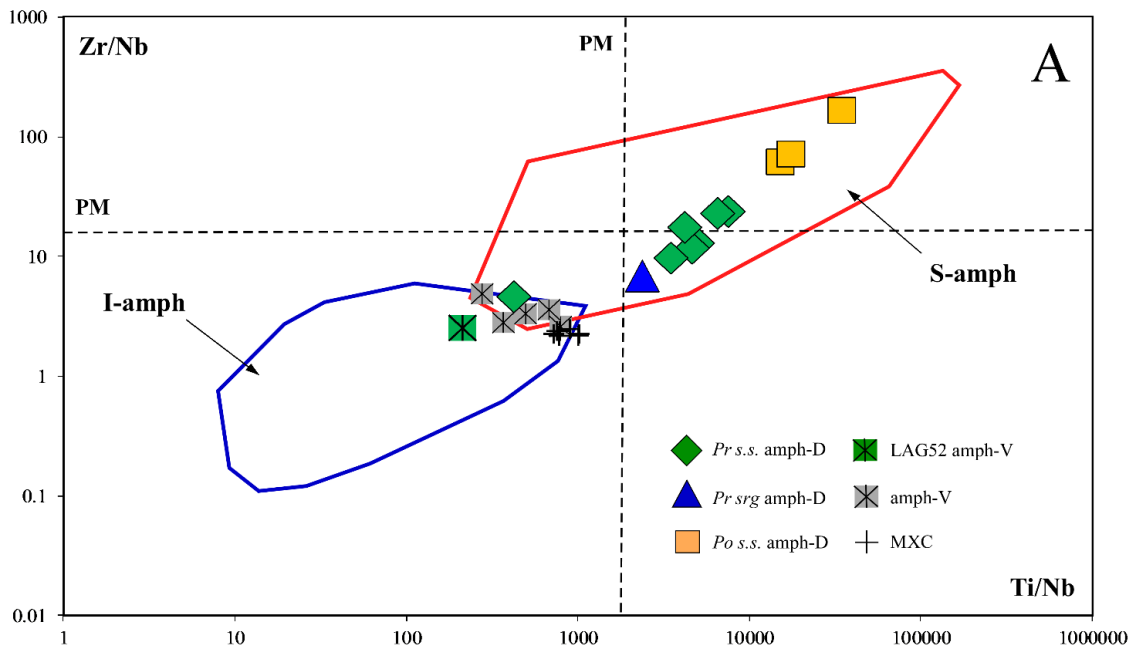
Fig. 35. Discrimination diagrams for amphibole geodynamic affinity by Coltorti et al. (2007). I-amph and S-amph indicate Intraplate amphibole and Subductive amphibole, respectively. Amph-V and MXC are the composition of PMVF vein amphibole and Perşani Mts. megacrystals, respectively, as reported by Zanetti et al. (1995).
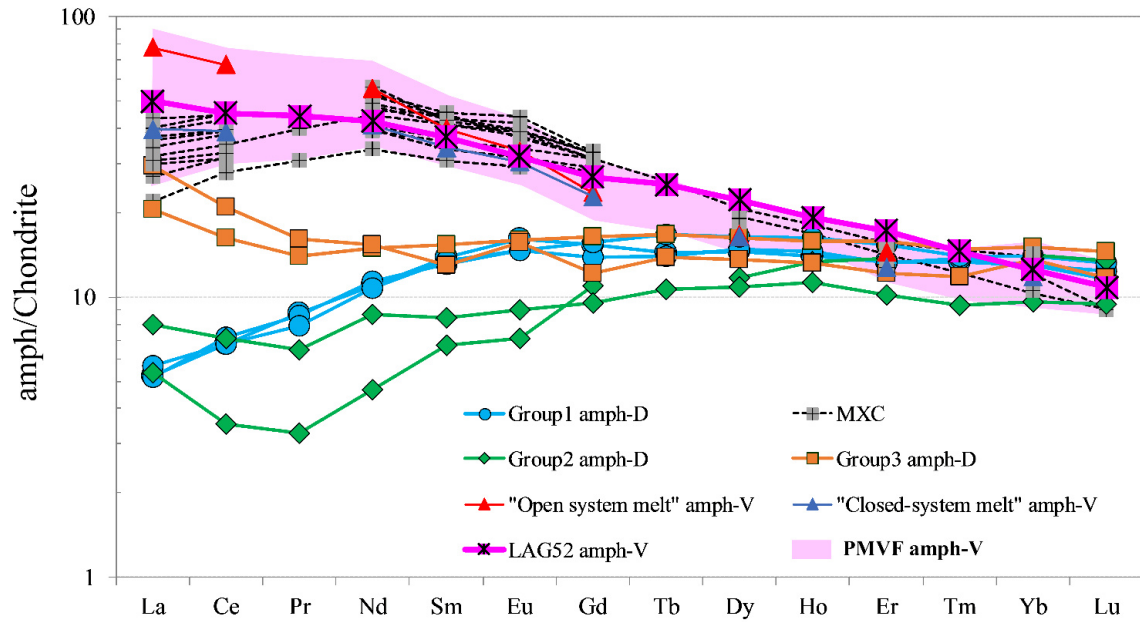
Fig. 36. Chondrite-normalized, average REE patterns of PMVF disseminated amphibole (symbols as in Fig. 30, abbreviations as in Fig. 26) and LAG52 vein amphibole (PMVF amph-V) compared to literature data of PMVF vein amphibole (pink shaded field, Zanetti et al., 1995; Vaselli et al., 1995; Chalot-Prat and Boullier, 1997) and Perşani Mts. megacrystals (MXC, grey asterisks, Downes et al., 1995; Zanetti et al., 1995). Red and cyan triangles are megacrystal compositions representing frozen alkaline melts at open and closed system conditions, according to Zanetti et al. (1995).
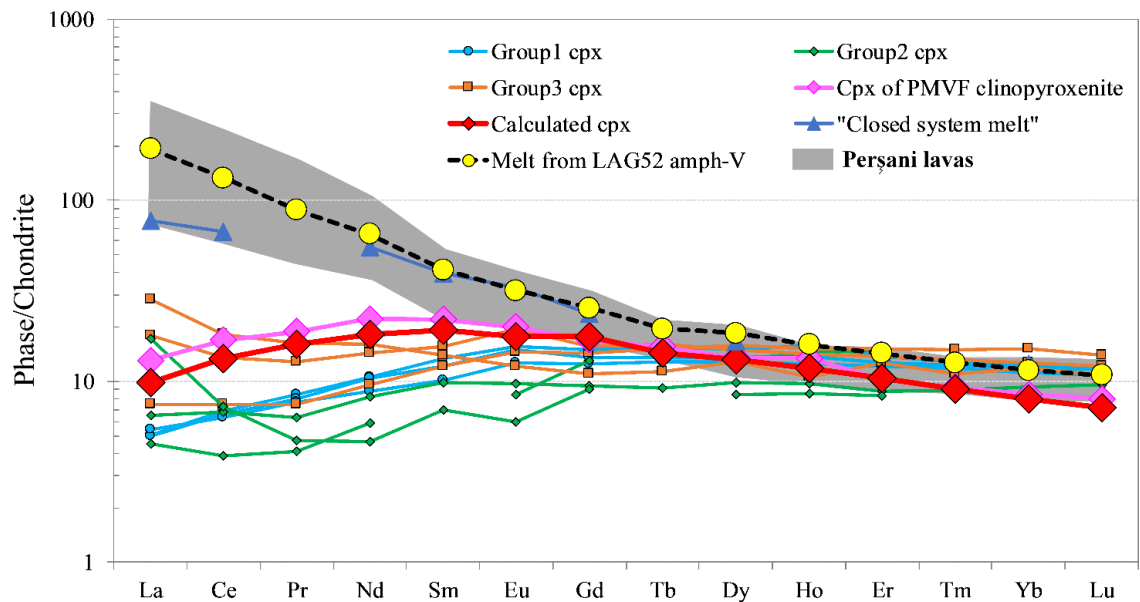
Fig. 37. Chondrite-normalized REE patterns of the calculated melt in equilibrium with LAG52 amphibole vein (yellow dots) and the calculated cpx (red diamonds) in equilibrium with this melt. Frozen alkaline metasomatic melt according to Zanetti et al. (1995) (cyan triangles), composition of cpx in a PMVF clinopyroxenite (pink diamonds, Chalot-Prat and Boullier, 1997), average PMVF disseminated cpx (symbols as in Fig. 28) and Perşani Mts. lavas (Downes et al., 1995; Harangi et al., 2013) are reported for comparison.

4.4.6 Melting and refertilization processes as deduced from noble gas compositions

The petrography and mineral chemistry of PMVF ultramafic xenoliths revealed that the extent of melt extraction from local mantle was certainly higher than what can be estimated by the paragenesis only, mainly composed by pyroxene-rich lherzolites as the result of an extensive re-fertilization of previous depleted mantle precursors.

In order to further help in deciphering this history, we compared ^{4}He and ^{40}Ar* concentrations and ^{4}He/^{40}Ar* in FI with the mg#. In a recent study from Lower Silesia, Rizzo et al. (2018) showed that the chemistry of FI and minerals coupled to ^{4}He/^{40}Ar* ratio may provide insights of the extent of partial melting, as well as on the occurrence of metasomatic processes that masked the pristine SCLM characteristics. This is related to the different crystal–melt partitioning of ^{4}He and ^{40}Ar* for olivine and cpx (Heber et al., 2007).

Olivine of PMVF xenoliths represent the most likely candidate for identifying the residual mantle, bearing in mind that increasing mg# should indicate higher extent of partial melting, leading to a depleted lithology (Herzberg et al., 2016; Rizzo et al., 2018). In the few samples not affected by diffusive fractionation (LAG52, BARQ4, TRE2), a progressive decrease of ^{4}He and ^{40}Ar* concentrations at increasing mg# (from 89.2 to 90.7) can be noticed (Fig. ESM3-11 A-B), which is compatible with a partial melting effect. This is supported by the ^{4}He/^{40}Ar* ratio that decreases from 2.2 to 1.4 at increasing mg#, being ^{4}He/^{40}Ar* within the reported range for mantle production. This indicates that the extent of partial melting was low. Indeed, as for comparison, olivine from Lower Silesia mantle having a ^{4}He/^{40}Ar* ~0.3 record a residual mantle that was strongly depleted (25–30% of partial melting, Rizzo et al., 2018). Alternatively, we may suppose that olivine recrystallized during or after a metasomatic/refertilization process by trapping FI with ^{4}He/^{40}Ar* typical of mantle production. If so, we would not have any more trace of primary FI resembling the residual mantle features. However, the very small number of reliable olivine data (i.e., not affected by diffusive fractionation) does not give robustness to these inferences.

Looking at opx and cpx, most of the samples do not show any relation between ^{4}He, ^{40}Ar* concentrations, ^{4}He/^{40}Ar* ratios and Mg# (ESM3-11). The only exception is for LAG52 that has the highest ^{4}He and ^{40}Ar* concentrations at the lowest mg#, compatible with low extent of partial melting relatively to the other samples; however, in terms of ^{4}He/^{40}Ar* this sample has not the highest values (ESM3-11), as expected in case of partial melting as the main process. This means that LAG52 did not maintain any memory of the partial melting history. In terms of ^{4}He/^{40}Ar*, opx and cpx present a He/^{40}Ar* in the range 0.2-1.2, without any particular trend. Apart sample TRE3, opx and cpx have ^{4}He/^{40}Ar*>0.6. These values are not compatible with the degrees of melting estimated by using mineral chemistry. This behaviour suggests that most of opx and cpx recrystallized, as consequence

of the refertilization process, by trapping a new population of FI with a distinct composition that masked the partial melting history. Interestingly, opx and cpx of samples TRE1, TRE2, and TRE4 plot above the range of values, showing mg# > 90.9 and ^{4}He/^{40}Ar* between 1.3 and 2.5. In detail, these samples show a gradual increase of mg# and ^{4}He/^{40}Ar* that cannot be explained with either partial melting or with refertilization process, due to their strong depletion. The most reasonable explanation for the FI chemistry of these samples involves the entrapment of secondary FI from the latest alkaline metasomatism or from the host magma that resemble more "magmatic-like" ^{4}He/^{40}Ar* values. This interpretation is further supported by the ^{3}He/^{4}He values (6.5-6.8 Ra), which are the highest of the entire dataset and clearly higher than the other opx (5.4-6.4 Ra) and cpx (5.3-6.1) as well as of olivine (5.2-5.9 Ra) (ESM3-11). It is worth noting that two of these samples belong to the low-temperature, high-stress *Po. s.s.* textural sub-group (Table 1), probably more prone to fluid percolation. We argue that the ^{3}He/^{4}He signature of fluids trapped in opx and cpx of samples TRE1, TRE2, and TRE4 can be related to MORB-like asthenospheric fluids that penetrated the local mantle and partially mixed with residual fluids contaminated by the recycling of crustal (subduction-related) material.

Resuming, the comparison of FI and mineral chemistry mostly points toward a local mantle originally depleted by rather high extents of partial melting and then re-fertilized by subduction-related fluids. A small portion of the mantle also bears memory of the latest alkaline metasomatism or the infiltrated host magma.

4.4.7 Subduction of crustal material and the origin of alkaline magmatism

In order to make inferences on the noble gas signature of SCLM beneath PMVF, we now focus on the He and Ne isotope compositions and compare them with other European localities.

The range of ^{3}He/^{4}He measured in olivine (only three reliable measures from LAG52, BARQ4, and TRE2), opx, and cpx (excluding sample TRE1, TRE2, and TRE4) is 5.8±0.2 Ra (Figs. 32, 34 and ESM3-11). This range is comparable to the few ^{3}He/^{4}He measurements existing for xenoliths from PMVF and analysed with a crushing technique, which yielded 5.6 and 6.0 Ra (Althaus et al., 1998; Kis et al., 2019). However, the authors do not provide details on what mineral phase they analysed nor does Althaus et al. (1998) state what type of crushing (single- or multi-step) was used to extract noble gases. This suggests that the mantle beneath PMVF is more radiogenic than the typical MORB range (8±1 Ra; Graham, 2002). Previous studies carried out in other mantle xenoliths from western and central European volcanic provinces (i.e., Eifel, French Massif Central, Pannonian Basin, Calatrava, Tallante, and Lower Silesia) yielded a ^{3}He/^{4}He range of 6.3±0.4 Ra (Gautheron et al., 2005; Martelli et al., 2011; Rizzo et al., 2018). Therefore, we could conclude that the mantle beneath

PMVF is within the European SCLM range. However, if we compare the range of values measured in each of the European locations, some differences can be underlined (Figs. 32 and 34). Mantle xenoliths from Eifel, French Massif Central, Pannonian Basin, Calatrava, and Lower Silesia in fact show ^{3}He/^{4}He of 6.5±0.3 Ra, 6.4±0.2 Ra, 6.5±0.1 Ra, 6.3±0.1 Ra, and 6.2±0.3 Ra, respectively, while those from Tallante and PMVF have 5.6±0.1 Ra and 5.8±0.2 Ra, respectively. For sake of clarity, we point out that data from Eifel, French Massif Central, and Pannonian Basin are from only olivine (Gautheron et al., 2005), while those from Calatrava involve olivine and opx (Martelli et al., 2011), and those from Lower Silesia were obtained from olivine, opx, and cpx (Rizzo et al., 2018) like in this study. PMVF and Tallante show the lowest range of ^{3}He/^{4}He, while the other European locations are comparable and have slightly but significantly higher ratios.

Gautheron et al. (2005) justified the average ^{3}He/^{4}He signature of the European SCLM, proposing two interpretative scenarios: i) a recent and local metasomatism by a MORB-like He composition rising from the asthenosphere and mixing with a more-radiogenic isotope signature produced in the lithosphere or ii) a global SCLM steady state in which a flux of ^{3}He-rich fluids originated from the asthenosphere mixes with ^{4}He-rich fluids/melts recycled in the lithosphere from U-Th decay of crustal material. This material could derive from dehydration of active or fossil subducting slabs (e.g., Yamamoto et al., 2004; Faccenna et al., 2010).

Therefore, the ^{3}He/^{4}He signature of mantle beneath PMVF can be interpreted with the models proposed by Gautheron et al. (2005), assuming an enhanced recycling of crustal material in the local lithosphere with respect to other European portions. This crustal material addition can be justified considering the recent subduction that occurred in eastern Carpathians (Seghedi et al., 2011 and references therein), similarly to what has been inferred for Tallante (Martelli et al., 2011 and references therein).

The low noble gases (and CO_2) concentration, as well as the ^{3}He/^{4}He in PMVF mantle xenoliths with respect to other parts of the European SCLM (Gautheron et al., 2005; Rizzo et al., 2018), support a subduction-related imprint of fluids circulating in the local mantle at the time of re-fertilization.

The apparent paradox between a fluid-rich environment, such as the subduction setting, and the low concentration of noble gases, could be reconciled by inferring that these fluids were reasonably richer in H_2O than in CO_2. Because CO_2 is the main carrier of noble gases at whatever depth of circulation (i.e., mantle or crust; Anderson, 1998), this could explain the low ^{4}He and ^{40}Ar* concentrations in FI from PMVF. The diffusive fractionation of noble gas observed in these mantle portions could also evidence protracted mantle recrystallization due to the stresses related to asthenospheric upwelling.

Ne isotope ratios give indications similar to the ^{3}He/^{4}He ratio. Indeed, Fig. 31 shows that PMVF ^{21}Ne/^{22}Ne and ^{20}Ne/^{22}Ne plot along or slightly below the theoretical mixing line between air and a

MORB-like mantle. Data slightly below this mixing line can be interpreted as a three component mixing that includes crustal material (see caption for further details on crustal end-member) (Kennedy et al., 1990; Ballentine, 1997; Ballentine et al., 2005). This supports the idea based on $^3He/^4He$ ratio that mantle beneath PMVF was metasomatized/refertilized by subduction-related fluids that was responsible for recycling of crustal material in the local SCLM. Mason et al. (1996) indeed invoked a fluid modified depleted mantle as the source of South Harghita calc-alkaline magmas. According to the authors, such a source may have been contaminated by the subduction of a small amount of Oligocene flysch material from the Carpathians accretionary wedge; however, the main crustal component was not identified.

Finally, the evidences from He and Ne isotope compositions exclude the presence of a plume below PMVF. In fact, the plume-related signature should have $^3He/^4He$ values above the MORB range (>9 Ra) and a lower $^{21}Ne/^{22}Ne$ ratio for a given $^{20}Ne/^{22}Ne$ than MORB melts (Kurz et al., 2009; Moreira, 2013 and references therein) (Figs. 31 and 32). As stated above, the ranges of He and Ne isotope ratios are comparable to those for other European regions where no plume is present (Gautheron et al., 2005; Moreira et al., 2018).

4.4.8 Comparison with gases emitted in the Eastern Carpathians

In the south-eastern Carpathian-Pannonian Region either anorogenic or orogenic magmas erupted since 11 Ma (Szakács et al., 1993; Seghedi et al., 2004, 2011). Although volcanic activity in the PMVF seems now extinct, the presence of strong CO_2 degassing in the neighbouring Ciomadul volcanic area (about 40 km to the east) may indicate that magmatism is still active at depth (Oncescu et al., 1984; Althaus et al., 2000; Vaselli et al., 2002; Popa et al., 2012; Kis et al., 2017, 2019 and references therein). Indeed, many gas emissions are present (Althaus et al., 2000; Vaselli et al., 2002 Kis et al., 2017, 2019 and references therein), emitting to the atmosphere a huge amount of CO_2 (8.7×10^3 t/y) comparable to other >10 kyr dormant volcanoes worldwide (Kis et al., 2017). This CO_2 emission pose a hazard for local inhabitants and visitors (Kis et al., 2017, 2019).

These gas manifestations are the closest to the mantle xenoliths outcropping area when comparing the noble gas composition. The $^3He/^4He$ values from Stinky Cave (Puturosul), Doboşeni, and Balvanyos are up to 3.2, 4.4, and 4.5 Ra, respectively, indicating the presence of a magmatic source at depth not yet completely cooled down (Althaus et al., 2000; Vaselli et al., 2002). In the Ciomadul area, Kis et al. (2019) measured $^3He/^4He$ up to 3.1 Ra, arguing that these values are indicative of a mantle lithosphere strongly contaminated by subduction-related fluids and post-metasomatic ingrowth of radiogenic ^4He. This hypothesis differs from that proposed by Althaus et al. (2000) and Vaselli et al. (2002) and presumes a small scale (~40 km) spatial heterogeneity in the local mantle of

~3 Ra, considering that the range of ^{3}He/^{4}He measured in mantle xenoliths from PMVF is up to 6.8 Ra (Kis et al., 2019 and this study).

The hypothesis by Kis et al. (2019) is in some circumstances in contradiction with their same considerations, as well as with previous studies. Kis et al. (2019) indicate that 3% of crustal assimilation could be sufficient to lower the ^{3}He/^{4}He of a hypothetical local mantle (5.95 Ra, as they measured in cpx from a PMVF xenolith) to their measured values (3.1 Ra), in accordance with the petrological evidences in calc-alkaline rocks provided by Mason et al. (1996). Kis et al. (2019) however, favor the hypothesis that 3.1 Ra is representative of the local mantle signature. In their magma ageing calculation, starting from the U and Th content in a selected dacite, Kis et al. (2019) suggest that after 30 Kyr (last eruption at Ciomadul) the ^{3}He/^{4}He ratio of 5.95 Ra could be lowered at 4.65 Ra. Because this value is higher than 3.1 Ra measured in their study, Kis et al. (2019) consider this process unlikely. We point out that Vaselli et al. (2002) measured up to 4.4 and 4.5 Ra in Doboşeni and Balvanyos gases, respectively, and note that these values are comparable to their calculation outcome. However, Kis et al. (2019) ignore Vaselli et al. (2002) values that instead support the reliability of magma ageing process in explaining the isotopic signature of gas emissions. In the conclusions, Kis et al. (2019) conclude that the mantle below Ciomadul has a low ^{3}He/^{4}He signature but also argue that variable degrees of interaction with crustal gases may occur, although some of them can survive this interaction maintaining their primary signature.

For the above reasons, we consider it more likely that magmatic gases from Ciomadul volcano are not representative of local mantle but are released from a cooling and aging of magma that resides within the crust or are contaminated by crustal fluids during transport to the surface, as already proposed by Althaus et al. (2000) and Vaselli et al. (2002).

4.5 Conclusions

The lithospheric mantle beneath the Eastern Transylvanian Basin was investigated through a suite of ultramafic xenoliths mainly composed of lherzolites with minor harzburgites and olivine-clinopyroxenites. The formers are extremely fertile (cpx content up to 22%) and characterized by the almost ubiquitous presence of disseminated amphibole and a continuous textural variation from recrystallized protogranular to porphyroclastic types.

Petrographic features, whole rock and mineral chemistry and noble gases (He, Ne, Ar) systematics in FI reveal a complex evolution of this mantle section. Porphyroclastic samples still bear clues of variable degrees of partial melting, as testified by high mineral mg# and depleted opx M-HREE patterns. On the other hand, the high cpx modal contents and the Al_2O_3 contents and REE patterns of the pyroxenes in the protogranular samples are not compatible with simple melting processes, but can

be explained by a pervasive refertilization event that erased, in most of the cases, the evidence of the pristine depleted parageneses. The high Al_2O_3 contents of pyroxenes and spinel and the HFSE ratios of disseminated amphiboles point toward a calc-alkaline nature for the refertilizing magma that was similar to the most primitive basalts of the Călimani series. A further support to this hypothesis derive from the finding, within PMVF pyroclastic sequences, of a lithic cognate of calc-alkaline affinity 1Ma older that the alkali basalts comparable to some basaltic andesites of the CGH chain (Downes et al., 1995). The studied mantle section also shows evidences of interaction with melts of different kind, visible from slight LREE enrichments in pyroxenes and amphibole vein formation. This metasomatic event is linked to the passage of alkaline melts similar to the host lavas, as testified by the close resemblance between the amphibole vein and the megacrystals also found in the Perşani Mts pyroclastic deposits.

In PMVF xenoliths, FI are mostly secondary. The isotope compositions of Ne and Ar and $^4He/^{20}Ne$ ratio highlights a variable air contamination, progressively decreasing from olivine to cpx. This contamination seems a local mantle feature inherited from the recycling of subduction-related fluids, occurring during the last orogenic event in Eastern Carpathians. Diffusive fractionation likely modified the noble gases composition of the residual mantle during its melting, but this process can be appreciated only in olivine with ^4He and $^{40}Ar^*$ concentrations below ~ 1.0-2.0×10^{-13} mol/g. The comparison of ^4He and $^{40}Ar^*$ concentrations as well as $^4He/^{40}Ar^*$ with the mg# of olivine, opx, and cpx does not show clear variations due to partial melting, thus, we infer that most of the pyroxenes recrystallized, as consequence of the refertilization process by subduction-related melts. A small portion of the mantle also bears memory of the latest alkaline metasomatism or the host magma, as testified by $^4He/^{40}Ar^*$ and $^3He/^4He$ values in those samples more texturally prone to fluid infiltration. Excluding these latter, the range of $^3He/^4He$ measured in olivine, opx, and cpx is 5.8±0.2 Ra, which is more radiogenic than the typical MORB mantle (8±1 Ra) and among the lowest values proposed for western and central European volcanic provinces (6.3±0.4 Ra). We argue that the $^3He/^4He$ signature of mantle beneath PMVF reflects an enhanced recycling of crustal material in the local lithosphere with respect to other European portions. Ne isotope ratios give indications similar to the $^3He/^4He$ ratio, with $^{21}Ne/^{22}Ne$ and $^{20}Ne/^{22}Ne$ data plotting along, or slightly below, the theoretical mixing line between air and a MORB-like mantle. Data slightly below this mixing line can be interpreted as a three component mixing that includes crustal material. This supports the idea based on $^3He/^4He$ ratio that mantle beneath PMVF was metasomatized/refertilized by subduction-related fluids responsible for the recycling of crustal material in the local SCLM.

The evidences from He and Ne isotope compositions exclude the presence of a plume below PMVF.

Comparing the xenolith $^3\text{He}/^4\text{He}$ signature with that of CO_2-dominated gas emissions located around Ciomadul volcanic complex (up to 4.5 Ra), located only about 40 km to the east of our study area, we conclude that surface gases are not representative of the local mantle. Rather, they are released from a cooling and aging magma residing within the crust or, alternatively, they are contaminated by crustal fluids during their rise toward the surface.

ESM1 – Petrographic description of PMVF xenoliths

Protogranular group

This group includes all samples matching the protogranular type as described by Mercier and Nicolas (1975). It can be further divided into two sub-groups, on the basis of some peculiar textural features.

Protogranular s.s. (Pr s.s.). Seventeen samples (LAG2, LAG3, LAG5, LAG9, LAG13, LAG14, LAG20, LAG21, LAG23, LAG24, LAG26, LAG50, LAG51, LAG52, BARQ3, BARQ4 and TRE2) fall within this sub-group. Olivine and orthopyroxene are coarse-grained (up to 9 mm across) and inequigranular, with the largest crystals showing a slight kink-banding. Frequent triple junctions between the smaller grains can be observed. The large pyroxenes are generally characterized by exolution lamellae, while smaller ones are optically homogeneous. Spinel is ubiquitously present as the unique aluminous phase, with a lobated and/or holly-leaf shape and, more rarely, as tiny subhedral crystals at the junctions between olivine. In some samples spinel are elongated and aligned. Amphibole is present in the great majority of *Pr.s.s.* samples and occur as disseminated crystals texturally associated with pyroxenes and/or spinel; it can also appear as lamellae in pyroxene crystals. Lherzolite LAG52 is cut by an amphibole vein. Some xenoliths are characterized by the sporadic presence of spinel-orthopyroxene-clinopyroxene clusters similar to those described by Falus et al. (2000), interpreted by the authors as sub-solidus reactions between garnet and olivine when transitioning into the spinel stability field. Few samples show signs of host basalt infiltration, visible as black or yellow-glassy veinlets and patches crosscutting the thin section. In the proximity of these veins clinopyroxene, spinel and amphibole are texturally disturbed (cloudy and sieved) and develop rims composed by small idiomorphic secondary phases (olivine, clinopyroxene, spinel). Tiny plagioclase crystals may also be found within these veins.

Protogranular with small, rounded grains (Pr srg). Five (LAG1, LAG25, LAG55, BARQ2 and BARQ5) out of 34 samples fall in this textural sub-group, differing from *Pr s.s.* essentially for the remarkable roundness of all grains, which have smooth and lobated edges. The peculiar characteristic of this sub-group is the almost total absence of exolution lamellae in pyroxenes. Spinel is the unique aluminous phase, with textural appearance similar to that in *Pr s.s.* sub-group. Amphibole is always present, associated with orthopyroxene, clinopyroxene and/or spinel. Host basalt infiltration is absent.

Porphyroclastic group

This group includes all samples patently porphyroclastic. It is divided into two sub-groups according to some peculiar textural features.

Porphyroclastic with large, rounded grains (Po lrg). This sub-group includes only four samples (LAG8, LAG22, LAG10A and TRE3) out of 34. Its main feature is the presence of large (up to 8 mm

across) orthopyroxene and clinopyroxene porphyroclasts with smooth, rounded/lobated edges. Exolution lamellae generally occur in the center of the porphyroclasts but disappear at the rims. Kink-banding is a common feature only in the rare large olivine crystals but is totally absent in the smaller grains. Spinel ubiquitously occur as lobated or holly-leaf crystals, in clusters with pyroxenes and between olivine. Amphibole is always present, associated with pyroxenes and spinel. No host basalt infiltration could be observed.

Porphyroclastic s.s. (Po s.s.). Six samples (LAG6, LAG10B, BARQ1, TRE1, TRE4 and TRE5) are characterized by a texture that fits the porphyroclastic texture (Mercier and Nicolas, 1975). Olivine porphyroclasts are characterized by significant kink-banding which is lacking in the neoblasts. The great majority of orthopyroxene occurs as large crystals (up to 1.5 cm across) with undulate extinction, irregular or straight edges and exolution lamellae in the center of the grain. This latter characteristic is also observed in clinopyroxene, which is always smaller than orthopyroxene. Small (3-4 mm across), optically homogeneous pyroxenes are also present. Spinel has a lobate shape and is sometimes associated with pyroxenes; holly-leaf shaped grains are rare. The majority of *Po s.s.* samples contain amphibole, mainly as tiny crystals usually associated with pyroxenes and/or spinel. Sample TRE4 is classified as a lherzolite but, from the textural point of view, it is a composite xenolith characterized by a portion composed of clinopyroxene, amphibole and spinel. This portion intermingles with a porphyroclastic region of the sample where clinopyroxene is scarce. Host basalt infiltration veinlets and isolated glassy patches may be found in this sub-group, similar to what has been observed in *Pr s.s.* samples.

Table 1 ESM: Summary of petrographic data for PMVF mantle xenoliths

SAMPLE	TEXTURAL GROUP	Sub-group	ROCK TYPE*	MODAL ABUNDANCES (WT%)				
LA GRUIU				ol	opx	cpx	sp	amph
LAG 1	Protogranular	*Pr srg*	Lh(a)	56.5	17.3	21.9	3.5	0.8
LAG 2	Protogranular	*Pr s.s.*	Lh(a)	62.2	21.8	11.0	4.0	1.0
LAG 3	Protogranular	*Pr s.s.*	Lh(a)	44.2	27.0	15.5	1.8	11.5
LAG 5	Protogranular	*Pr s.s.*	Hz(a)	77.3	20.0	2.0	0.5	0.2
LAG 6	Porphyroclastic	*Po s.s.*	Lh(a)	69.2	21.0	8.0	1.6	0.2
LAG 8	Porphyroclastic	*Po lrg*	Lh(a)	58.4	18.0	19.0	3.2	1.4
LAG 9	Protogranular	*Pr s.s.*	Lh(a)	54.2	25.0	15.0	4.0	1.8
LAG 10A	Porphyroclastic	*Po lrg*	Lh(a)	49.8	29.0	17.0	1.8	2.4
LAG 10B	Porphyroclastic	*Po s.s.*	Lh(a)	65.3	23.0	10.5	1.0	0.2
LAG 11	Pecilitic	-	Ol-Cpxite(a)	12.1	0.0	82.8	0.1	5.0
LAG 13	Protogranular	*Pr s.s.*	Lh(a)	52.7	23.0	17.0	4.3	3.0
LAG 14	Protogranular	*Pr s.s.*	Lh(a)	46.7	30.0	16.0	4.4	2.9
LAG 20	Protogranular	*Pr s.s.*	Lh(a)	58.6	20.0	17.0	3.8	0.6
LAG 21	Protogranular	*Pr s.s.*	Lh(a)	58.8	21.0	14.2	5.3	0.7
LAG 22	Porphyroclastic	*Po lrg*	Lh(a)	39.2	35.0	21.0	3.1	1.7
LAG 23	Protogranular	*Pr s.s.*	Lh(a)	61.7	20.0	15.0	2.0	1.3
LAG 24	Protogranular	*Pr s.s.*	Lh(a)	61.8	22.7	12.7	1.8	1.0
LAG 25	Protogranular	*Pr srg*	Lh(a)	59.7	22.0	8.0	5.0	5.3
LAG 26	Protogranular	*Pr s.s.*	Lh(a)	67.4	18.5	8.2	3.9	2.0
LAG 50	Protogranular	*Pr s.s.*	Lh(a)	63.7	20.2	10.5	3.0	2.6
LAG 51	Protogranular	*Pr s.s.*	Lh(a)	60.8	21.6	12.1	3.1	2.4
LAG 52	Protogranular	*Pr s.s.*	Lh(a)	59.6	26.3	8.1	2.0	4.0
LAG 55	Protogranular	*Pr srg*	Lh(a)	53.3	18.0	7.5	1.2	20**
BARC								
BARQ 1	Porphyroclastic	*Po s.s.*	Lh(a)	63.9	22.0	9.3	4.3	0.5
BARQ 2	Protogranular	*Pr srg*	Lh(a)	71.8	22.0	5.0	1.1	0.1
BARQ 3	Protogranular	*Pr s.s.*	Lh	64.6	22.8	9.3	3.3	0.0
BARQ 4	Protogranular	*Pr s.s.*	Lh	56.2	23.6	17.0	3.2	0.0
BARQ 5	Protogranular	*Pr srg*	Lh(a)	71.1	16.0	10.0	2.8	0.1
TRE 1	Porphyroclastic	*Po s.s.*	Hz	70.9	25.0	2.8	1.3	0.0
TRE 2	Protogranular	*Pr s.s.*	Lh(a)	64.6	21.0	12.5	0.8	1.1
TRE 3	Porphyroclastic	*Po lrg*	Lh(a)	38.5	37.0	19.5	3.0	2.0
TRE 4	Porphyroclastic	*Po s.s.*	Lh(a)	60.5	27.0	9.3	1.9	3.8
TRE 5	Porphyroclastic	*Po s.s.*	Lh(a)	50.1	22.0	23.3	4.2	0.4
TRE 6	Mylonitic	-	Dn	93.2	0.0	6.0	0.8	0.0

* (a) contains amphibole
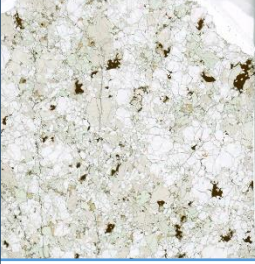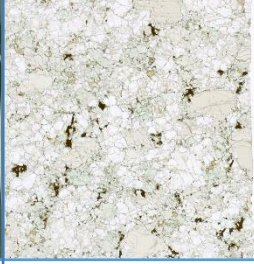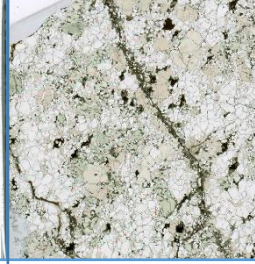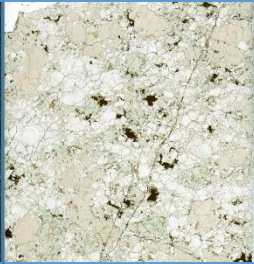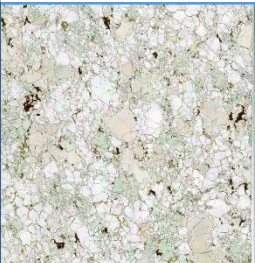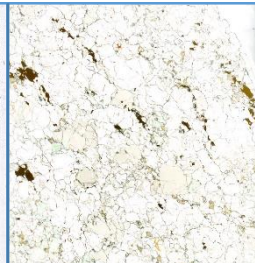
** amphibole mainly present as coating around the xenolith

Anhydrous melting trend at 1 GPa (Niu et al.,1997)

Anhydrous melting trend at 2 GPa (Niu et al.,1997)

Hydrous melting trends at 1 GPa (Bénard et al., 2017). Red, 0.1% H_2O; light blue, 0.5% H_2O; green, 1% H_2O

■ PM

● PMVF (Vaselli et al., 1995)

◆ Pr s.s.

▲ Pr srg

● Po lrg

■ Po s.s.

✖ Dunite, Clinopyroxenite

Ol

Opx

Cpx
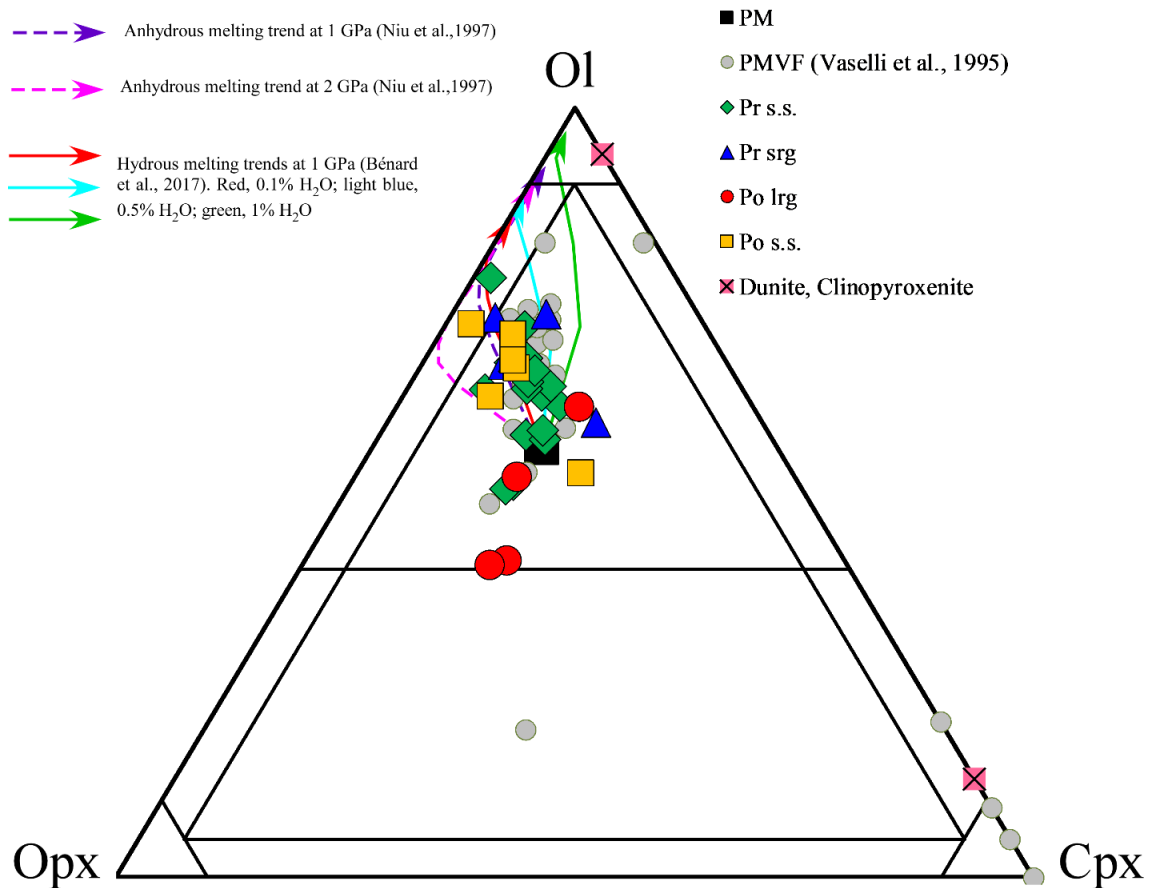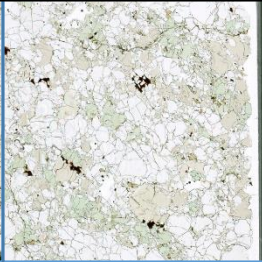
Classification diagram for PMVF ultramafic xenoliths, divided by textural sub-groups: green diamonds, *Pr s.s.*; blue triangles, *Pr srg*; red circles, *Po lrg*; yellow squares, *Po s.s.*; light red crossed squares, cumulates (a mylonitic dunite and a clinopyroxenite). Grey circles are PMVF ultramafic xenoliths data from Vaselli et al. (1995). Black square, PM modal composition from Johnson et al. (1990). Dotted pink and purple lines are melting paths at 2 and 1 GPa, respectively (Niu et al., 1997) while red, light blue and green lines are hydrous melting paths at 1 GPa and 0.1 (red), 0.5 (light blue) and 1 (green) % of H_2O (Bènard et al., 2018).

SNAPSHOTS OF THE THIN SECTIONS

LAG1	LAG2	LAG3
LAG5	LAG6	LAG8
LAG9	LAG10A/B	LAG11

LAG13	LAG14	LAG20
LAG21	LAG22	LAG23
LAG24	LAG25	LAG26

LAG50	LAG51	LAG52
LAG55	BARQ1	BARQ2
BARQ3	BARQ4	BARQ5

TRE1	TRE2	TRE3
TRE4	TRE5	TRE6

ESM2 – Additional Tables
Table ESM2-1 Olivine

Sample	BARQ4	BARQ4	LAG21	LAG24	LAG24	LAG51	LAG51	LAG51	LAG52	LAG52	LAG52	TRE2	TRE2	LAG2	LAG2	LAG1	LAG1	TRE3	TRE3	TRE1	TRE1	TRE4	TRE4
Rock type	Lh	Lh	Lh(a)	Lh(a)	Lh(a)	Lh(a)	Lh(a)	Lh(a)	Lh(a)	Lh(a)	Lh(a)	Lh(a)	Lh(a)	Lh(a)	Lh(a)	Lh(a)	Lh(a)	Lh(a)	Lh(a)	Hz	Hz	Lh(a)	Lh(a)
Sub-group	Pr s.s.	Pr s.s.	Pr s.s.	Pr s.s.	Pr s.s.	Pr s.s.	Pr s.s.	Pr s.s.	Pr s.s.	Pr s.s.	Pr s.s.	Pr s.s.	Pr s.s.	Pr s.s.	Pr s.s.	Pr srg	Pr srg	Po lrg	Po lrg	Po s.s.	Po s.s.	Po s.s.	Po s.s.
phase	oll core	oll core	oll core	oll core	oll core	oll core	oll rim	oll core	oll rim	oll core	oll core	oll core	oll rim	oll core	oll core	oll core	oll core	oll core	oll core	oll core	oll core	oll rim	oll core
SiO2	39.85	40.13	39.75	40.41	40.27	41.06	41.16	40.87	40.23	40.19	40.05	40.81	40.54	40.28	40.18	40.07	40.29	40.54	40.25	40.38	40.55	40.04	39.99
TiO2	0.02	0.02	0.03	0.00	0.01	0.00	0.00	0.00	0.00	0.00	0.01	0.00	0.01	0.00	0.01	0.03	0.00	0.01	0.00	0.01	0.03	0.00	0.02
Al2O3	0.03	0.03	0.01	0.02	0.02	0.01	0.03	0.03	0.01	0.02	0.01	0.00	0.03	0.02	0.03	0.01	0.03	0.00	0.00	0.01	0.01	0.02	0.00
FeO	10.05	9.81	10.15	9.97	10.12	9.40	9.47	9.35	10.51	10.39	10.63	9.18	9.14	9.41	9.45	10.39	10.32	9.92	9.84	8.40	8.66	9.89	10.00
MnO	0.17	0.16	0.14	0.16	0.16	0.16	0.14	0.10	0.17	0.16	0.15	0.14	0.14	0.11	0.10	0.17	0.14	0.16	0.14	0.15	0.12	0.14	0.13
MgO	49.33	49.49	49.73	49.79	49.31	49.57	49.52	49.67	49.29	49.38	49.23	50.02	50.39	50.28	50.32	49.29	49.43	50.13	49.93	50.94	50.75	49.93	49.89
CaO	0.08	0.09	0.06	0.09	0.05	0.05	0.07	0.06	0.06	0.07	0.07	0.07	0.08	0.06	0.08	0.07	0.07	0.04	0.06	0.05	0.05	0.02	0.03
Na2O	0.01	0.00	0.02	0.00	0.00	0.00	0.01	0.01	0.03	0.02	0.02	0.00	0.00	0.02	0.02	0.00	0.00	0.00	0.00	0.00	0.00	0.01	0.00
K2O	0.02	0.02	0.01	0.01	0.00	0.00	0.00	0.00	0.04	0.01	0.01	0.01	0.00	0.02	0.00	0.01	0.00	0.00	0.01	0.00	0.00	0.00	0.01
Cr2O3	0.02	0.00	0.00	0.00	0.01	0.00	0.00	0.09	0.02	0.01	0.05	0.03	0.01	0.00	0.00	0.02	0.00	0.00	0.00	0.00	0.00	0.00	0.00
NiO	0.36	0.37	0.38	0.43	0.40	0.35	0.36	0.40	0.39	0.41	0.39	0.41	0.40	0.40	0.38	0.35	0.37	0.40	0.39	0.40	0.40	0.40	0.39
Tot	99.94	100.13	100.29	100.87	100.36	100.61	100.77	100.59	100.74	100.65	100.62	100.66	100.73	100.60	100.58	100.42	100.65	101.21	100.61	100.34	100.55	100.45	100.46
Si	0.982	0.986	0.978	0.986	0.988	0.999	1.000	0.995	0.985	0.985	0.983	0.993	0.986	0.983	0.981	0.984	0.986	0.985	0.984	0.984	0.986	0.981	0.980
Ti	0.000	0.000	0.001	0.000	0.000	0.000	0.000	0.000	0.000	0.000	0.000	0.000	0.000	0.000	0.000	0.001	0.000	0.000	0.000	0.000	0.001	0.000	0.000
Al	0.001	0.001	0.000	0.001	0.001	0.000	0.001	0.001	0.000	0.001	0.000	0.000	0.001	0.001	0.001	0.000	0.001	0.000	0.000	0.000	0.000	0.001	0.000
Fe II	0.207	0.202	0.209	0.203	0.208	0.191	0.192	0.193	0.215	0.213	0.218	0.187	0.186	0.192	0.193	0.213	0.211	0.202	0.201	0.171	0.176	0.203	0.205
Mn	0.004	0.003	0.003	0.003	0.003	0.003	0.003	0.002	0.004	0.003	0.003	0.003	0.003	0.002	0.002	0.004	0.003	0.003	0.003	0.003	0.002	0.003	0.003
Mg	1.812	1.812	1.823	1.810	1.803	1.798	1.794	1.802	1.799	1.803	1.801	1.814	1.827	1.829	1.831	1.804	1.803	1.816	1.819	1.849	1.839	1.823	1.823
Ca	0.002	0.002	0.002	0.002	0.001	0.001	0.002	0.002	0.002	0.002	0.002	0.002	0.002	0.002	0.002	0.002	0.002	0.001	0.002	0.001	0.001	0.001	0.001
Na	0.000	0.000	0.001	0.000	0.000	0.000	0.000	0.000	0.001	0.001	0.001	0.000	0.000	0.001	0.001	0.000	0.000	0.000	0.000	0.000	0.000	0.000	0.000
K	0.001	0.001	0.000	0.000	0.000	0.000	0.000	0.000	0.001	0.000	0.000	0.000	0.000	0.001	0.000	0.000	0.000	0.000	0.000	0.000	0.000	0.000	0.000
Ni	0.007	0.007	0.008	0.008	0.008	0.007	0.007	0.008	0.008	0.008	0.008	0.008	0.008	0.008	0.007	0.007	0.007	0.008	0.008	0.008	0.008	0.008	0.008
Cr	0.000	0.000	0.000	0.000	0.000	0.000	0.000	0.002	0.000	0.000	0.001	0.001	0.000	0.000	0.000	0.000	0.000	0.000	0.000	0.000	0.000	0.000	0.000
SumCat	3.018	3.014	3.023	3.014	3.012	3.001	3.000	3.005	3.016	3.016	3.017	3.007	3.013	3.018	3.019	3.016	3.014	3.015	3.017	3.017	3.014	3.019	3.020
mg#	89.74	89.99	89.73	89.90	89.67	90.38	90.31	90.45	89.31	89.44	89.19	90.66	90.76	90.49	90.47	89.42	89.51	90.00	90.04	91.53	91.26	90.00	89.89

Table ESM2-1 Cpx

Sample	BARQ4	BARQ4	BARQ4	LAG21	LAG21	LAG24	LAG24	LAG51	LAG51	LAG51	LAG52	LAG52	LAG52	TRE2	TRE2	LAG2	LAG2	LAG1	LAG1	TRE3	TRE3	TRE1	TRE1	TRE4	TRE4	TRE4
Rock type	Lh	Lh	Lh	Lh(a)	Lh(a)	Lh(a)	Lh(a)	Lh(a)	Lh(a)	Lh(a)	Lh(a)	Lh(a)	Lh(a)	Lh(a)	Lh(a)	Lh(a)	Lh(a)	Lh(a)	Lh(a)	Lh(a)	Lh(a)	Hz	Hz	Lh(a)	Lh(a)	Lh(a)
Sub-group	Pr s.s.	Pr s.s.	Pr s.s.	Pr s.s.	Pr s.s.	Pr s.s.	Pr s.s.	Pr s.s.	Pr s.s.	Pr s.s.	Pr s.s.	Pr s.s.	Pr s.s.	Pr s.s.	Pr s.s.	Pr s.s.	Pr s.s.	Pr srg	Pr srg	Po lrg	Po lrg	Po s.s.	Po s.s.	Po s.s.	Po s.s.	Po s.s.
phase	cpx1 core	cpx1 core	cpx1 core	cpx1 core	cpx1 rim	cpx1 core	cpx1 rim	cpx1 core	cpx1 core	cpx1 core	cpx1 core	cpx1 core	cpx1 core	cpx1 core	cpx1 core	cpx1 core	cpx1 core	cpx1 core	cpx1 core	cpx1 core	cpx1 core	cpx1 core	cpx1 core	cpx1 core	cpx1 core	cpx1 core
SiO2	50.31	49.93	49.92	50.78	50.71	50.45	51.04	51.98	50.74	51.30	50.72	50.74	50.68	51.02	51.21	51.11	50.91	50.94	50.75	50.95	50.51	52.13	51.46	51.15	50.12	52.14
TiO2	0.65	0.70	0.71	0.41	0.43	0.62	0.48	0.45	0.55	0.48	0.31	0.33	0.29	0.32	0.30	0.31	0.37	0.38	0.37	0.36	0.41	0.11	0.16	0.24	0.40	0.32
Al2O3	7.52	8.12	7.99	6.53	6.55	8.14	6.94	6.32	7.76	7.53	6.01	6.19	6.04	6.20	6.02	6.58	6.71	6.52	6.55	6.34	7.38	3.45	4.24	4.34	6.08	5.71
FeO	3.09	3.08	3.03	3.10	3.22	3.00	2.97	2.93	2.96	3.16	2.83	3.34	3.35	2.83	2.92	3.06	3.00	3.13	3.12	2.96	2.94	2.31	2.22	2.67	2.92	3.00
MnO	0.11	0.11	0.09	0.10	0.12	0.09	0.11	0.09	0.07	0.09	0.11	0.10	0.10	0.08	0.08	0.09	0.08	0.10	0.07	0.10	0.09	0.06	0.07	0.11	0.08	0.09
MgO	15.40	15.03	15.22	16.09	16.14	15.02	15.78	16.16	15.25	15.34	16.00	15.98	15.95	16.02	16.14	16.16	15.94	15.87	15.89	15.83	15.21	17.21	16.48	16.75	15.87	16.11
CaO	19.84	19.52	19.81	20.79	20.63	19.82	20.14	21.16	20.96	20.99	21.11	21.25	21.21	20.93	20.62	20.41	20.58	20.48	20.54	21.05	20.72	22.63	22.38	23.19	22.57	22.28
Na2O	1.58	1.77	1.73	1.33	1.30	1.80	1.62	1.22	1.27	1.30	1.05	1.12	1.05	1.26	1.29	1.41	1.50	1.44	1.39	1.33	1.40	0.70	0.74	0.51	0.72	0.89
K2O	0.00	0.01	0.03	0.02	0.01	0.01	0.02	0.03	0.02	0.00	0.05	0.01	0.03	0.01	0.02	0.01	0.01	0.00	0.01	0.01	0.01	0.01	0.00	0.02	0.01	0.01
Cr2O3	0.70	0.78	0.84	0.69	0.68	0.82	0.76	0.54	0.71	0.99	0.91	0.85	0.92	1.14	0.91	0.89	0.91	0.63	0.70	0.74	0.95	0.81	1.37	0.63	0.58	0.47
NiO	0.00	0.01	0.05	0.04	0.04	0.04	0.05	0.05	0.05	0.02	0.07	0.03	0.04	0.06	0.07	0.03	0.08	0.06	0.04	0.03	0.01	0.03	0.01	0.07	0.02	0.02
Tot	99.20	99.07	99.42	99.86	99.85	99.80	99.91	100.92	100.34	101.20	99.73	99.93	99.66	99.86	99.58	100.05	100.08	99.55	99.45	99.73	99.72	99.45	99.14	99.68	99.37	101.05
Si	1.827	1.814	1.808	1.832	1.831	1.820	1.839	1.858	1.827	1.834	1.840	1.835	1.840	1.844	1.855	1.840	1.833	1.844	1.839	1.843	1.830	1.893	1.879	1.858	1.826	1.867
Ti	0.018	0.019	0.019	0.011	0.012	0.017	0.013	0.012	0.015	0.013	0.008	0.009	0.008	0.009	0.008	0.008	0.010	0.010	0.010	0.010	0.011	0.003	0.004	0.007	0.011	0.009
Al	0.322	0.348	0.341	0.278	0.279	0.346	0.295	0.266	0.329	0.317	0.257	0.264	0.258	0.264	0.257	0.279	0.285	0.278	0.280	0.270	0.315	0.148	0.182	0.186	0.261	0.241
Fe III	0.020	0.022	0.026	0.028	0.027	0.021	0.023	0.016	0.014	0.013	0.024	0.026	0.024	0.022	0.021	0.025	0.027	0.024	0.025	0.024	0.018	0.022	0.016	0.026	0.025	0.014
Fe II	0.074	0.072	0.066	0.066	0.070	0.070	0.066	0.072	0.075	0.082	0.079	0.075	0.078	0.064	0.068	0.067	0.063	0.071	0.070	0.065	0.071	0.048	0.052	0.055	0.064	0.076
Mn	0.003	0.003	0.003	0.003	0.004	0.003	0.003	0.003	0.002	0.003	0.003	0.003	0.003	0.002	0.002	0.003	0.002	0.003	0.002	0.003	0.003	0.002	0.002	0.003	0.002	0.003
Mg	0.833	0.814	0.821	0.865	0.869	0.808	0.847	0.861	0.818	0.817	0.865	0.861	0.863	0.863	0.871	0.867	0.855	0.856	0.858	0.853	0.821	0.931	0.897	0.907	0.862	0.860
Ca	0.772	0.760	0.769	0.804	0.798	0.766	0.777	0.811	0.809	0.804	0.821	0.823	0.825	0.811	0.800	0.787	0.794	0.794	0.798	0.816	0.804	0.880	0.876	0.903	0.881	0.855
Na	0.111	0.125	0.121	0.093	0.091	0.126	0.113	0.085	0.089	0.090	0.074	0.079	0.074	0.088	0.091	0.098	0.105	0.101	0.098	0.093	0.098	0.049	0.052	0.036	0.051	0.062
K	0.000	0.000	0.001	0.001	0.000	0.000	0.001	0.001	0.001	0.000	0.002	0.000	0.001	0.000	0.001	0.000	0.000	0.000	0.000	0.000	0.000	0.000	0.000	0.001	0.000	0.000
Cr	0.020	0.022	0.024	0.020	0.019	0.023	0.022	0.015	0.020	0.028	0.026	0.024	0.026	0.033	0.026	0.025	0.026	0.018	0.020	0.021	0.027	0.023	0.040	0.018	0.017	0.013
SumCat	4.000	3.999	3.999	4.001	4.000	4.000	3.999	4.000	3.999	4.001	3.999	3.999	4.000	4.000	4.000	3.999	4.000	3.999	4.000	3.998	3.998	3.999	4.000	4.000	4.000	4.000
mg#	89.87	89.68	89.94	90.25	89.94	89.93	90.44	90.78	90.17	89.64	89.34	89.51	89.45	90.98	90.80	90.39	90.44	90.05	90.08	90.50	90.21	92.99	92.98	91.78	90.64	90.53

Table ESM2-1 Opx

Sample	BARQ4	BARQ4	LAG21	LAG21	LAG24	LAG24	LAG51	LAG51	LAG51	LAG52	LAG52	LAG52	TRE2	TRE2	LAG2	LAG2	LAG1	LAG1	TRE3	TRE3	TRE1	TRE1	TRE4	TRE4	TRE4
Rock type	Lh	Lh	Lh(a)	Lh(a)	Lh(a)	Lh(a)	Lh(a)	Lh(a)	Lh(a)	Lh(a)	Lh(a)	Lh(a)	Lh(a)	Lh(a)	Lh(a)	Lh(a)	Lh(a)	Lh(a)	Lh(a)	Lh(a)	Hz	Hz	Lh(a)	Lh(a)	Lh(a)
Sub-group	Pr s.s.	Pr s.s.	Pr s.s.	Pr s.s.	Pr s.s.	Pr s.s.	Pr s.s.	Pr s.s.	Pr s.s.	Pr s.s.	Pr s.s.	Pr s.s.	Pr s.s.	Pr s.s.	Pr s.s.	Pr s.s.	Pr srg	Pr srg	Po lrg	Po lrg	Po s.s.	Po s.s.	Po s.s.	Po s.s.	Po s.s.
phase	opx core	opx core	opx rim	opx core	opx core	opx core	opx core	opx core	opx core	opx core	opx core	opx core	opx core	opx rim	opx core	opx core	opx core	opx core	opx core	opx core	opx core	opx core	opx core	opx core	opx core
SiO2	54.18	53.10	53.62	53.98	53.27	54.02	55.30	55.11	55.34	53.61	54.36	54.39	54.65	54.64	54.15	53.51	54.13	54.27	53.95	53.42	54.59	54.90	53.94	54.94	53.71
TiO2	0.11	0.14	0.07	0.10	0.19	0.11	0.11	0.16	0.04	0.10	0.09	0.05	0.08	0.07	0.06	0.14	0.09	0.07	0.07	0.10	0.04	0.04	0.06	0.08	0.10
Al2O3	4.87	5.88	4.92	4.74	5.90	4.76	4.59	5.07	4.33	4.96	4.37	4.33	4.41	4.50	4.66	5.71	4.84	4.65	5.04	5.64	3.62	4.68	3.52	4.68	5.42
FeO	6.31	6.30	6.43	6.63	6.44	6.43	6.08	6.60	6.66	6.98	6.85	6.79	5.94	5.98	6.12	6.15	6.76	6.64	6.48	6.41	5.59	5.61	6.62	6.49	6.65
MnO	0.13	0.13	0.14	0.19	0.15	0.14	0.13	0.12	0.14	0.17	0.16	0.14	0.12	0.15	0.15	0.16	0.14	0.16	0.14	0.16	0.14	0.13	0.16	0.17	0.15
MgO	33.26	32.44	33.20	33.33	32.76	33.30	33.35	33.42	33.44	32.68	33.44	33.27	33.64	33.80	33.76	33.14	33.14	33.08	33.37	33.24	34.28	34.59	33.73	34.26	33.34
CaO	0.85	0.80	0.83	0.68	0.78	0.80	0.79	0.76	0.74	0.79	0.79	0.84	0.82	0.78	0.87	0.84	0.84	0.77	0.64	0.60	0.63	0.62	0.50	0.51	0.50
Na2O	0.09	0.12	0.10	0.09	0.10	0.10	0.08	0.08	0.08	0.09	0.09	0.11	0.08	0.07	0.13	0.09	0.08	0.08	0.05	0.07	0.04	0.04	0.02	0.02	0.03
K2O	0.00	0.01	0.00	0.00	0.01	0.00	0.02	0.00	0.00	0.02	0.01	0.03	0.01	0.00	0.03	0.01	0.00	0.00	0.00	0.00	0.02	0.02	0.02	0.00	0.00
Cr2O3	0.29	0.45	0.32	0.33	0.49	0.33	0.27	0.29	0.38	0.44	0.28	0.35	0.47	0.46	0.38	0.59	0.30	0.30	0.45	0.53	0.73	0.71	0.38	0.27	0.51
NiO	0.08	0.11	0.13	0.09	0.12	0.11	0.11	0.10	0.12	0.13	0.07	0.08	0.11	0.11	0.13	0.11	0.11	0.09	0.12	0.11	0.10	0.08	0.15	0.07	0.08
Tot	100.18	99.49	99.76	100.28	100.22	100.10	100.83	101.70	101.82	99.97	100.53	100.38	100.33	100.50	100.44	100.38	100.46	100.13	100.29	100.24	99.80	100.20	100.18	100.40	100.51
Si	1.864	1.842	1.852	1.856	1.835	1.860	1.892	1.871	1.878	1.855	1.866	1.870	1.876	1.871	1.855	1.836	1.861	1.871	1.855	1.836	1.881	1.882	1.855	1.885	1.843
Ti	0.003	0.004	0.002	0.003	0.005	0.003	0.003	0.004	0.001	0.003	0.002	0.001	0.002	0.002	0.002	0.004	0.002	0.002	0.002	0.003	0.001	0.001	0.002	0.002	0.003
Al	0.197	0.240	0.200	0.192	0.240	0.193	0.185	0.203	0.195	0.202	0.177	0.176	0.178	0.182	0.188	0.231	0.196	0.189	0.204	0.229	0.147	0.141	0.190	0.142	0.219
Fe III	0.017	0.016	0.022	0.022	0.019	0.019	0.006	0.011	0.011	0.019	0.021	0.020	0.015	0.016	0.025	0.020	0.016	0.019	0.018	0.021	0.018	0.019	0.022	0.020	0.019
Fe II	0.165	0.167	0.164	0.169	0.167	0.166	0.168	0.176	0.178	0.183	0.175	0.175	0.156	0.155	0.151	0.157	0.175	0.176	0.168	0.163	0.143	0.141	0.168	0.166	0.172
Mn	0.004	0.004	0.004	0.006	0.004	0.004	0.004	0.003	0.004	0.005	0.005	0.004	0.004	0.003	0.004	0.004	0.004	0.005	0.004	0.005	0.004	0.004	0.005	0.005	0.004
Mg	1.705	1.677	1.709	1.708	1.682	1.709	1.700	1.691	1.691	1.685	1.711	1.705	1.721	1.725	1.723	1.695	1.698	1.700	1.710	1.703	1.760	1.767	1.728	1.751	1.705
Ca	0.031	0.030	0.031	0.029	0.030	0.029	0.029	0.028	0.027	0.029	0.029	0.031	0.030	0.029	0.032	0.031	0.031	0.028	0.024	0.022	0.023	0.023	0.018	0.019	0.018
Na	0.006	0.008	0.007	0.006	0.007	0.007	0.005	0.005	0.005	0.006	0.006	0.007	0.005	0.005	0.009	0.006	0.006	0.005	0.003	0.005	0.003	0.003	0.001	0.001	0.002
K	0.000	0.000	0.000	0.000	0.001	0.000	0.001	0.000	0.000	0.001	0.000	0.001	0.001	0.000	0.001	0.001	0.000	0.000	0.000	0.000	0.001	0.001	0.001	0.000	0.000
Cr	0.008	0.012	0.009	0.009	0.013	0.009	0.007	0.008	0.010	0.012	0.008	0.010	0.013	0.012	0.010	0.016	0.008	0.008	0.012	0.014	0.020	0.019	0.010	0.007	0.014
SumCat	4.000	4.000	4.000	4.000	4.001	4.000	4.000	4.000	4.000	4.000	4.000	4.000	4.000	4.000	4.000	4.000	4.000	4.000	4.000	4.001	4.001	4.000	4.000	3.999	3.999
mg#	90.38	90.17	90.20	89.96	90.06	90.22	90.72	90.02	89.95	89.29	89.69	89.73	90.99	90.97	90.77	90.56	89.72	89.88	90.17	90.23	91.62	91.65	90.08	90.39	89.93

Table ESM2-1 Amphibole

Sample	LAG21		LAG24		LAG51			LAG52			TRE2		LAG2		LAG1		TRE3		TRE4			
Rock type	Lh(a)	Lh(a)	Lh(a)	Lh(a)	Lh(a)	Lh(a)	Lh(a)	Lh(a)	Lh(a)	Lh(a)	Lh(a)	Lh(a)	Lh(a)	Lh(a)	Lh(a)	Lh(a)	Lh(a)	Lh(a)	Lh(a)	Lh(a)	Lh(a)	Lh(a)
Sub-group	Pr s.s.	Pr s.s.	Pr s.s.	Pr s.s.	Pr s.s.	Pr s.s.	Pr s.s.	Pr s.s.	Pr s.s.	Pr s.s.	Pr s.s.	Pr s.s.	Pr s.s.	Pr s.s.	Pr srg	Pr srg	Po lrg	Po lrg	Po s.s.	Po s.s.	Po s.s.	Po s.s.
phase	amph-D core	amph-D core	amph-D rim	amph-D core	amph-D core	amph-D core	amph-D core	amph-D core	amph-D core	amph-V in vein	amph-D core	amph-D core	amph-D core	amph-D core	amph-D core	amph-D core	amph-D core	amph-D core	amph-D core	amph-D core	amph-D core Clinopxte portion	
SiO_2	41.99	41.98	42.24	42.31	43.30	43.39	43.16	42.57	42.06	43.11	42.56	42.51	41.90	42.40	42.16	42.07	42.53	42.26	42.71	42.40	43.99	43.47
TiO_2	1.90	1.91	2.34	2.33	0.94	0.98	0.88	1.14	1.22	1.92	1.33	1.40	1.46	1.52	1.93	1.71	1.49	1.59	1.22	1.17	1.08	1.19
Al_2O_3	15.90	15.73	15.77	15.75	16.06	15.89	16.28	15.34	15.78	15.00	15.69	15.67	15.89	15.75	15.83	16.06	15.84	15.66	14.88	14.89	14.61	15.29
Al2O3	4.40	4.46	4.29	4.26	4.38	4.44	4.42	4.48	4.54	4.93	3.85	3.87	4.24	4.32	4.50	4.60	4.24	4.32	4.12	4.13	4.36	4.21
MnO	0.07	0.06	0.04	0.07	0.03	0.08	0.03	0.06	0.06	0.06	0.07	0.06	0.07	0.05	0.05	0.09	0.08	0.06	0.04	0.08	0.07	0.05
MgO	17.79	17.76	17.69	17.66	18.18	18.07	18.18	18.19	18.05	17.81	18.23	18.19	17.87	17.99	17.72	17.66	18.02	17.95	18.43	18.18	18.43	18.27
CaO	10.98	10.79	10.52	10.37	11.19	11.11	11.22	10.94	11.07	11.24	10.80	11.04	10.75	10.67	10.72	10.67	11.00	11.17	12.06	11.82	11.66	11.73
Na_2O	3.61	3.65	3.71	3.81	3.09	3.15	3.27	3.22	3.25	2.91	3.52	3.68	3.71	3.66	3.60	3.68	3.74	3.64	3.17	3.24	3.47	3.25
K_2O	0.08	0.11	0.17	0.17	0.84	0.84	0.78	0.63	0.50	1.34	0.04	0.04	0.23	0.22	0.24	0.25	0.08	0.10	0.00	0.01	0.00	0.02
Cr_2O_3	1.01	1.04	1.10	1.01	0.84	0.88	1.01	1.09	1.18	0.37	1.39	1.38	1.28	1.17	1.02	1.03	1.04	1.14	1.19	1.23	1.15	0.84
NiO	0.14	0.15	0.09	0.09	0.13	0.11	0.11	0.12	0.12	0.09	0.12	0.14	0.11	0.13	0.12	0.10	0.13	0.11	0.07	0.11	0.10	0.09
Tot	97.88	97.65	97.97	97.83	98.98	98.93	99.34	97.77	97.82	98.78	97.60	97.97	97.51	97.87	97.90	97.91	98.19	98.00	97.89	97.26	98.93	98.39
Si	5.849	5.859	5.872	5.887	5.957	5.978	5.924	5.927	5.857	6.006	5.905	5.902	5.853	5.889	5.869	5.854	5.900	5.887	5.963	5.958	6.072	6.017
Ti	0.199	0.200	0.245	0.244	0.097	0.102	0.091	0.119	0.128	0.201	0.139	0.146	0.153	0.159	0.202	0.179	0.155	0.167	0.128	0.124	0.112	0.124
Al	2.611	2.588	2.584	2.583	2.605	2.581	2.634	2.518	2.590	2.463	2.566	2.565	2.616	2.578	2.598	2.634	2.590	2.572	2.449	2.467	2.377	2.495
Fe III	0.305	0.315	0.299	0.299	0.308	0.298	0.307	0.342	0.347	0.234	0.343	0.302	0.322	0.333	0.312	0.322	0.299	0.287	0.257	0.263	0.250	0.259
Fe II	0.208	0.206	0.199	0.197	0.196	0.214	0.201	0.180	0.182	0.340	0.104	0.148	0.173	0.169	0.212	0.213	0.193	0.217	0.224	0.222	0.253	0.229
Mn	0.008	0.007	0.005	0.008	0.003	0.009	0.003	0.007	0.007	0.007	0.008	0.007	0.008	0.006	0.006	0.011	0.009	0.007	0.005	0.010	0.008	0.006
Mg	3.693	3.694	3.665	3.662	3.728	3.710	3.719	3.774	3.746	3.698	3.769	3.764	3.720	3.723	3.676	3.662	3.725	3.727	3.835	3.807	3.791	3.769
Ca	1.639	1.613	1.567	1.546	1.650	1.640	1.650	1.632	1.652	1.678	1.605	1.642	1.609	1.588	1.599	1.591	1.635	1.667	1.804	1.780	1.724	1.740
Na	0.975	0.988	1.000	1.028	0.824	0.842	0.870	0.869	0.878	0.786	0.947	0.991	1.005	0.986	0.972	0.993	1.006	0.983	0.858	0.883	0.929	0.872
K	0.014	0.020	0.030	0.030	0.147	0.148	0.137	0.112	0.089	0.238	0.007	0.007	0.041	0.039	0.043	0.044	0.014	0.018	0.000	0.002	0.000	0.004
Ni	0.016	0.017	0.010	0.010	0.014	0.012	0.012	0.013	0.013	0.010	0.013	0.016	0.012	0.015	0.013	0.011	0.014	0.012	0.008	0.012	0.011	0.010
Cr	0.111	0.115	0.121	0.111	0.091	0.096	0.110	0.120	0.130	0.041	0.152	0.151	0.141	0.128	0.112	0.113	0.114	0.126	0.131	0.137	0.125	0.092
SumCat	15.63	15.62	15.60	15.61	15.62	15.63	15.66	15.61	15.62	15.70	15.56	15.64	15.65	15.61	15.61	15.63	15.65	15.67	15.66	15.67	15.65	15.62
mg#	87.81	87.64	88.03	88.08	88.09	87.87	88.00	87.86	87.62	86.55	89.42	89.34	88.25	88.13	87.53	87.25	88.34	88.09	88.84	88.70	88.28	88.55

Table ESM2-1 Spinel

Sample	BARQ4		LAG21		LAG24		LAG51		LAG52			TRE2		LAG2		LAG1		TRE3		TRE1		TRE4	
Rock type	Lh	Lh	Lh(a)	Lh(a)	Lh(a)	Lh(a)	Lh(a)	Lh(a)	Lh(a)	Lh(a)	Lh(a)	Lh(a)	Lh(a)	Lh(a)	Lh(a)	Lh(a)	Lh(a)	Lh(a)	Lh(a)	Hz	Hz	Lh(a)	Lh(a)
Sub-group	Pr s.s.	Pr s.s.	Pr s.s.	Pr s.s.	Pr s.s.	Pr s.s.	Pr s.s.	Pr s.s.	Pr s.s.	Pr s.s.	Pr s.s.	Pr s.s.	Pr s.s.	Pr s.s.	Pr s.s.	Pr srg	Pr srg	Po lrg	Po lrg	Po s.s.	Po s.s.	Po s.s.	Po s.s.
phase	spl core	spl core	spl core	spl rim	spl rim	spl core	spl core	spl core	spl core	spl rim	spl core	spl rim	spl core	spl core	spl rim	spl rim	spl core	spl core	spl core	spl core	spl rim	spl core	spl rim
SiO_2	0.04	0.05	0.03	0.91	0.05	0.03	0.03	0.05	0.05	0.04	0.03	0.04	0.02	0.04	0.01	0.06	0.03	0.01	0.03	0.00	0.06	0.01	0.08
TiO_2	0.11	0.11	0.11	0.48	0.09	0.10	0.07	0.06	0.04	0.07	0.07	0.09	0.07	0.10	0.07	0.12	0.10	0.07	0.08	0.10	0.08	0.06	0.27
Al_2O_3	59.82	59.80	58.40	53.95	59.86	59.43	58.56	58.20	52.76	52.20	55.23	54.84	54.12	56.38	56.09	59.53	59.00	58.33	57.84	42.66	41.92	58.62	56.40
FeO	10.84	10.94	11.73	10.39	10.83	10.88	10.92	11.78	13.86	13.70	13.02	11.10	11.19	11.48	11.30	11.90	11.70	11.44	11.40	11.40	12.56	12.42	11.01
MnO	0.10	0.08	0.11	0.09	0.09	0.11	0.09	0.10	0.14	0.08	0.10	0.10	0.10	0.10	0.08	0.13	0.11	0.11	0.08	0.11	0.17	0.11	0.05
MgO	21.29	21.28	20.91	21.18	21.15	20.90	21.10	21.18	19.22	19.23	19.80	20.72	20.36	20.84	21.08	21.01	20.83	20.71	20.77	18.33	17.96	20.66	21.98
CaO	0.01	0.00	0.00	0.22	0.01	0.01	0.01	0.02	0.00	0.07	0.02	0.01	0.00	0.00	0.06	0.02	0.00	0.00	0.00	0.00	0.00	0.00	0.04
Na_2O	0.00	0.02	0.00	0.04	0.01	0.00	0.00	0.00	0.00	0.02	0.00	0.00	0.00	0.01	0.00	0.00	0.00	0.00	0.00	0.00	0.00	0.01	0.02
K_2O	0.01	0.00	0.01	0.00	0.00	0.00	0.01	0.01	0.00	0.00	0.00	0.01	0.01	0.01	0.00	0.00	0.00	0.01	0.01	0.01	0.01	0.00	0.01
Cr_2O_3	8.77	8.88	10.23	12.56	9.21	9.56	9.53	10.20	15.24	15.73	13.11	14.63	15.19	12.43	12.29	9.31	9.71	10.58	10.51	28.02	28.10	9.43	10.71
NiO	0.37	0.38	0.45	0.38	0.43	0.37	0.40	0.41	0.31	0.36	0.37	0.37	0.35	0.38	0.39	0.38	0.41	0.44	0.37	0.25	0.25	0.44	0.42
Tot	101.37	101.53	101.97	100.21	101.72	101.39	100.72	102.01	101.63	101.50	101.75	101.93	101.43	101.75	101.41	102.46	101.89	101.70	101.08	100.87	101.11	101.76	100.98
Si	0.001	0.001	0.001	0.024	0.001	0.001	0.001	0.001	0.001	0.001	0.001	0.001	0.001	0.001	0.000	0.002	0.001	0.000	0.001	0.000	0.002	0.000	0.002
Ti	0.002	0.002	0.002	0.009	0.002	0.002	0.001	0.001	0.001	0.001	0.001	0.002	0.002	0.002	0.002	0.002	0.002	0.001	0.002	0.002	0.002	0.001	0.005
Al	1.781	1.778	1.743	1.648	1.779	1.776	1.760	1.735	1.624	1.610	1.678	1.659	1.650	1.697	1.692	1.763	1.760	1.747	1.742	1.376	1.355	1.753	1.695
Fe III	0.040	0.040	0.050	0.030	0.030	0.030	0.040	0.060	0.060	0.060	0.050	0.040	0.030	0.050	0.050	0.040	0.040	0.040	0.040	0.010	0.030	0.060	0.080
Fe II	0.190	0.190	0.200	0.190	0.200	0.200	0.190	0.190	0.240	0.240	0.230	0.200	0.210	0.200	0.190	0.210	0.210	0.210	0.200	0.250	0.260	0.210	0.160
Mn	0.002	0.002	0.002	0.002	0.002	0.002	0.002	0.002	0.003	0.002	0.002	0.002	0.002	0.002	0.002	0.003	0.002	0.002	0.002	0.003	0.004	0.002	0.001
Mg	0.801	0.800	0.789	0.818	0.795	0.789	0.802	0.798	0.748	0.750	0.761	0.792	0.785	0.793	0.804	0.787	0.785	0.784	0.791	0.747	0.734	0.781	0.835
Ca	0.000	0.000	0.000	0.006	0.000	0.000	0.000	0.001	0.000	0.002	0.001	0.000	0.000	0.000	0.002	0.001	0.000	0.000	0.000	0.000	0.000	0.000	0.001
Na	0.000	0.001	0.000	0.002	0.000	0.000	0.000	0.000	0.000	0.001	0.000	0.000	0.000	0.000	0.000	0.000	0.000	0.000	0.001	0.000	0.000	0.000	0.001
K	0.000	0.000	0.000	0.000	0.000	0.000	0.000	0.000	0.000	0.000	0.000	0.000	0.000	0.000	0.000	0.000	0.000	0.000	0.000	0.000	0.000	0.000	0.000
Cr	0.175	0.177	0.205	0.257	0.184	0.192	0.192	0.204	0.314	0.325	0.267	0.297	0.311	0.251	0.249	0.185	0.194	0.213	0.212	0.606	0.609	0.189	0.216
Ni	0.008	0.008	0.009	0.008	0.009	0.008	0.008	0.008	0.008	0.008	0.008	0.008	0.007	0.008	0.008	0.008	0.008	0.008	0.008	0.005	0.006	0.005	0.005
SumCat	3.000	2.999	3.001	2.994	3.002	3.000	2.996	3.000	2.997	3.000	2.999	3.001	2.998	3.004	2.999	3.001	3.002	3.006	2.998	2.999	3.003	3.005	3.005
mg#	77.768	77.614	76.053	78.410	77.669	77.398	77.492	76.209	71.188	71.432	73.047	76.883	76.429	76.388	76.869	75.880	76.032	76.332	76.449	74.129	71.808	74.785	78.062
cr#	8.956	9.055	10.516	13.507	9.352	9.738	9.840	10.522	16.232	16.817	13.735	15.176	15.840	12.881	12.814	9.497	9.939	10.848	10.868	30.584	31.018	9.745	11.298

Table ESM2-2 Cpx

Sample	BARQ4			LAG21		LAG24		LAG51	LAG52		TRE2	LAG1	TRE1	TRE4		
Rock type	Lh	Lh	Lh	Lh(a)	Lh(a)	Lh(a)	Lh(a)	Lh(a)	Lh(a)	Lh(a)	Lh(a)	Lh(a)	Hz	Lh(a)	Lh(a)	Lh(a)
Sub-group	Pr s.s.	Pr s.s.	Pr s.s.	Pr s.s.	Pr s.s.	Pr s.s.	Pr s.s.	Pr s.s.	Pr s.s.	Pr s.s.	Pr s.s.	Pr srg	Po s.s.	Po s.s.	Po s.s.	Po s.s.
phase	cpx	cpx	cpx	cpx	cpx	cpx	cpx	cpx	cpx	cpx	cpx	cpx	cpx	cpx	cpx	cpx
n*	3	4	2	3	2	3	2	3	3	2	3	3	3	1	1	4
Li	1.368	0.903	1.300	1.831	1.150	1.503	1.755	0.753	1.386	2.922		1.708		3.860	4.260	3.390
Cs		0.152	0.047	0.239										<0.0127	<0.0174	0.022
Rb	0.044	0.833	0.067	0.224	0.171	0.050	0.038		0.044	0.016		0.067		<0.033	0.059	0.057
Ba	0.132	0.193	0.123	0.416	1.145	0.064	0.037		0.196	1.161		0.137		<0.076	0.056	0.135
Th	0.298	0.284	0.260	0.183		0.041	0.037	1.085	0.758	0.618		0.323	1.393	0.420	0.144	0.065
U	0.111	0.089	0.082	0.206	0.046	0.029	0.043	0.819	0.052	0.082		0.194		0.128	0.092	0.056
Nb	0.086	0.228	0.078	0.093	0.049	0.089	0.069	1.060				0.043		<0.036	0.097	0.038
Ta	0.015	0.007	0.007	0.013		0.022						0.020		<0.00	0.033	0.010
La	1.815	1.921	1.534	1.164	1.224	1.128	1.230	4.237	6.122	7.378	1.076	1.541	4.049	1.785	1.233	0.846
Ce	4.815	4.638	4.220	4.065	4.315	4.080	4.025	8.349	9.060	13.048	2.372	4.118	4.467	3.480	4.610	3.435
Pb	0.148	0.150	0.149	0.234	0.114	0.132		0.442	0.417	0.329		0.153	0.612	0.470	0.696	0.129
Pr	0.783	0.640	0.715	0.795	0.816	0.747	0.780	1.224	1.306	1.782	0.390	0.596	0.446	0.541	0.974	0.668
Sr	78.95	74.47	71.94	58.89	58.53	69.31	70.00	82.85	51.71	76.56	24.77	85.14	58.55	43.64	82.02	44.05
Nd	4.770	4.248	4.458	4.757	5.125	4.693	4.970	6.662	6.157	8.862	2.756	3.835	2.160	3.380	5.100	3.821
Zr	44.69	43.54	44.34	42.07	40.78	39.37	35.90	41.90	37.42	62.03	21.20	22.72	19.14	21.50	23.44	32.49
Hf	1.526	1.193	0.915	1.673	1.060	1.086	0.806	0.994	1.239	1.330		0.757		0.268	0.707	0.918
Sm	1.938	1.761	1.895	2.026	2.072	1.839	1.880	2.394	1.712	2.530		1.509	1.066	1.220	1.790	1.615
Eu	0.896	0.753	0.878	1.005	0.814	0.829	0.906	1.136	0.688	0.724	0.493	0.559	0.347	0.555	0.925	0.729
Ti**	3837	3777	4197	3161	2820	3509	3197	3128	1183	853	1676	1866	906	1807	2338	2593
Gd	3.168	2.657	3.022	3.362	2.810	2.803	2.764	3.208	1.935	2.577	2.667	1.948	1.868	2.220	3.170	2.258
Tb	0.606	0.515	0.572	0.656	0.504	0.521	0.492	0.598	0.450	0.399		0.345		0.450	0.549	0.448
Dy	4.126	3.874	3.987	4.077	3.535	3.470	3.390	3.801	3.281	3.251	3.363	2.492	2.146	3.120	3.810	2.835
Y	21.57	21.85	22.47	21.40	20.94	19.44	19.40	19.69	15.50	16.25	22.95	12.86	13.72	17.38	21.28	16.58
Ho	0.832	0.857	0.873	1.012	0.771	0.794	0.753	0.795	0.607	0.581	0.807	0.553	0.486	0.630	0.806	0.692
Er	2.560	2.437	2.568	2.519	2.050	2.160	2.039	2.269	2.101	2.055	2.462	1.466	1.383	1.950	2.230	1.843
Tm	0.365	0.372	0.399	0.356	0.298	0.315	0.315	0.336	0.293	0.269		0.227		0.320	0.318	0.269
Yb	2.633	2.630	2.450	2.152	2.052	2.071	1.931	2.142	1.970	2.055	2.035	1.582	1.520	1.850	2.070	1.739
Lu	0.345	0.381	0.341	0.311	0.297	0.297	0.296	0.308	0.270	0.285		0.242		0.313	0.269	0.243

* number of averaged analyses

** Ti from EMP

Table ESM2-2 Opx

Sample	BARQ4		LAG21	LAG24			LAG51	LAG52	TRE2	LAG1	TRE1	TRE4
Rock type	Lh	Lh	Lh(a)	Lh(a)	Lh(a)	Lh(a)	Lh(a)	Lh(a)	Lh(a)	Lh(a)	Hz	Lh(a)
Sub-group	*Pr s.s.*	*Pr s.s.*	*Pr s.s.*	*Pr s.s.*	*Pr s.s.*	*Pr s.s.*	*Pr s.s.*	*Pr s.s.*	*Pr s.s.*	*Pr srg*	*Po s.s.*	*Po s.s.*
phase	opx	opx	opx	opx	opx	opx	opx	opx	opx	opx	opx	opx
n*	11	3	8	1	1	3	3	3	3	5	5	2
Li	1.227	1.039		1.210	1.450	1.335	1.801			2.129		4.399
Cs				<0.0129	<0.0095							
Rb				<0.0203	<0.028	0.037						
Ba				<0.0140	<0.0146					0.612	0.019	0.016
Th	0.005	0.012		<0.0147	0.008	0.010	0.083		0.091	0.012	0.108	0.010
U	0.014	0.004		<0.0146	<0.0136				0.015	0.006	0.018	0.036
Nb		0.044		0.014	<0.0157		0.174		0.221	0.191	0.058	0.133
Ta				<0.0091	<0.0123					0.002		0.003
La		0.012	0.017	0.012	<0.0124		0.059	0.050	0.039	0.027	0.011	0.033
Ce	0.017	0.017	0.040	0.023	0.129	0.030	0.138	0.018	0.053	0.046	0.025	0.061
Pb		0.184	0.255	0.047	0.045		0.711	0.456		0.165		0.047
Pr	0.006	0.005	0.010	0.012	0.029	0.011	0.024		0.008	0.012	0.004	0.012
Sr	0.175	0.191	0.287	0.217	0.982	0.183	1.071	1.037	0.270	0.903	0.137	1.159
Nd	0.050	0.038	0.068	<0.047	0.180	0.084	0.170	0.042	0.050	0.076	0.021	0.087
Zr	2.282	2.646	2.581	1.617	2.377	1.704	2.342	1.583		1.656		1.668
Hf	0.055	0.104	0.102	<0.062	0.096	0.073		0.058		0.053		0.051
Sm	0.023	0.024	0.036	<0.061	<0.064	0.047	0.063	0.021	0.029	0.031	0.015	0.038
Eu	0.014	0.013	0.019	<0.0145	0.036		0.027	0.014	0.016	0.016	0.006	0.018
Ti**	811	760	772	642	809	591	684	746	511	421	217	488
Gd	0.079	0.077	0.095	<0.057	0.128	0.082	0.134	0.078	0.090	0.072	0.053	0.088
Tb	0.023	0.024	0.023	0.011	0.033	0.016	0.031	0.021		0.014		0.019
Dy	0.216	0.236	0.211	0.103	0.247	0.150	0.231	0.177	0.182	0.123	0.106	0.159
Y	1.271	1.565	1.482	1.107	1.394	0.994	1.609	1.350	1.431	0.941	0.716	0.796
Ho	0.053	0.068	0.065	0.038	0.060	0.043	0.074	0.052	0.064	0.037	0.035	0.042
Er	0.250	0.273	0.288	0.132	0.202	0.136	0.326	0.247	0.288	0.163	0.146	0.162
Tm	0.053	0.060	0.054	0.032	0.040	0.026		0.054		0.026		0.027
Yb	0.450	0.554	0.423	0.259	0.332	0.276	0.472	0.470	0.477	0.252	0.197	0.206
Lu	0.078	0.105	0.088	0.073	0.058	0.060	0.093	0.087	0.075	0.050	0.042	0.049

* number of averaged analyses

** Ti from EMP

Table ESM2-2 Amphibole

Sample	LAG21	LAG21	LAG24	LAG24	LAG51	LAG52	LAG52	TRE2	TRE2	LAG1	TRE4	TRE4	TRE4
Rock type	Lh(a)	Lh(a)	Lh(a)	Lh(a)	Lh(a)	Lh(a)	Lh(a)	Lh(a)	Lh(a)	Lh(a)	Lh(a)	Lh(a)	Lh(a)
Sub-group	*Pr s.s.*	*Pr s.s.*	*Pr s.s.*	*Pr s.s.*	*Pr s.s.*	*Pr s.s.*	*Pr s.s.*	*Pr s.s.*	*Pr s.s.*	*Pr srg*	*Po s.s.*	*Po s.s.*	*Po s.s.*
phase	amph-D	amph-D	amph-D	amph-D	amph-D	amph-D	amph-V	amph-D	amph-D	amph-D	amph-D	amph-D	amph-D
n*	2	6	1	3	3	3	2	2	3	4	2	2	3
Li	0.600	1.445	0.960	0.550	2.537		1.732			1.021	2.118	4.397	3.407
Cs		0.018	<0.0245										
Rb	1.077	0.511	0.557	0.419		7.607						0.024	
Ba	15.35	14.51	20.82	13.15	22.91	27.06	68.20	1.78	3.77	23.32	0.20	0.37	0.71
Th	0.051	0.025	0.035	0.039	0.441		0.490	0.319	0.394	0.371	0.082	0.116	0.315
U		0.015	<0.035	0.033	0.120		0.106	0.031		0.045	0.034	0.113	0.109
Nb	1.475	1.612	2.730	2.903	2.043	15.537	37.097	1.925	2.292	3.608	0.146	0.460	0.353
Ta	0.082	0.071	0.205	0.173	0.150	0.309	2.116			0.278	0.027	0.059	0.063
La	1.321	1.145	1.147	1.299	4.861	6.968	11.855	0.957	1.583	1.888	1.082	1.189	1.751
Ce	4.110	4.190	4.520	4.240	9.917	12.770	27.752	1.680	2.648	4.340	3.234	4.795	4.403
Pb	0.269	0.311	0.223	0.134	1.068	1.388	1.257		0.762	0.487	0.269	0.528	1.477
Pr	0.840	0.827	0.809	0.828	1.324	1.526	4.200	0.256	0.367	0.614	0.555	0.857	0.842
Sr	170	158	200	197	240	262	352	45	68	219	99	130	118
Nd	5.205	5.037	5.440	5.179	6.968	7.196	19.769	1.732	2.620	4.051	3.998	5.710	5.403
Zr	34.83	37.10	35.07	33.98	35.96	71.03	92.77		22.30	24.77	24.43	28.13	25.22
Hf	1.225	0.782	1.220	0.902	0.933	1.471	2.671			0.747	0.547	1.080	0.778
Sm	2.100	2.136	1.760	2.257	2.358	1.980	5.692	0.950	1.108	1.290	1.646	2.292	2.237
Eu	0.943	0.920	0.874	0.831	0.923	0.909	1.838	0.360	0.464	0.521	0.752	0.872	0.928
Ti**	11136	10515	13667	13537	8557	6545	7841	6262	7975	8531	5024	6942	6151
Gd	3.040	3.290	2.830	2.874	3.355	2.497	5.508	2.013	2.472	1.961	2.914	3.360	3.400
Tb	0.508	0.568	0.498	0.544	0.626	0.520	0.942			0.398	0.576	0.690	0.613
Dy	3.496	3.879	3.760	3.727	4.129	3.461	5.628	2.848	3.108	2.755	3.835	4.410	4.227
Y	23.19	23.65	21.48	20.79	21.79	22.88	28.13	18.02	24.02	15.67	21.47	23.49	25.06
Ho	0.753	0.828	0.849	0.795	0.892	0.751	1.085	0.665	0.840	0.636	0.856	0.991	0.905
Er	2.100	2.334	2.180	2.200	2.614	2.018	2.853	1.908	2.629	1.680	2.508	2.539	2.603
Tm	0.316	0.362	0.374	0.323	0.377	0.301	0.371			0.237	0.325	0.381	0.359
Yb	2.106	2.292	2.340	2.087	2.551	2.308	2.128	2.090	2.726	1.639	2.186	2.467	2.493
Lu	0.284	0.304	0.332	0.296	0.369	0.297	0.275	0.302	0.382	0.238	0.289	0.362	0.355

* number of averaged analyses

** Ti from EMP

amph-D, disseminated amphibole

amph-V, vein amphibole

Table ESM2-3 Noble gas in fluid inclusions

Table ESM2-3 - Geochemistry of fluid inclusions hosted in minerals forming mantle xenoliths from PMVF. Oliv stands for olivine, cpx for clinopyroxene, and opx for orthopyroxene; n.a. indicates not available, n.m. stands for not measured. ^{40}Ar* was not calculated in those samples where ^{40}Ar/^{36}Ar was available but lower than 300.

Sample	Mineral	weight (g)	^{4}He mol/g	^{20}Ne mol/g	^{21}Ne mol/g	^{22}Ne mol/g	^{40}Ar mol/g	^{36}Ar mol/g	^{40}Ar* mol/g	^{4}He/^{20}Ne	^{4}He/^{40}Ar*	R/Ra	Rc/Ra	Err Rc/Ra +/-	^{40}Ar/^{36}Ar	Err (%)	^{38}Ar/^{36}Ar	Err (%)	^{20}Ne/^{22}Ne	Err 20/22 +/-	^{21}Ne/^{22}Ne	Err 21/22 +/-	^{3}He	^{3}He/^{36}Ar
LAG51	Oliv	0.72951	1.58E-14	7.25E-15	2.01E-17	6.95E-15	n.m.	n.m.	n.a.	2.2	n.a.	n.m.	n.m.	n.m.	n.m.	n.m.	n.m.	n.m.	9.91	0.03	0.0314	0.00044	n.a.	n.a.
LAG52	Oliv	0.72483	9.43E-14	5.04E-15	1.36E-17	4.84E-15	2.06E-12	6.83E-15	4.23E-14	18.7	2.23	5.32	5.40	0.209	301.7	0.05	0.18733	0.19	9.93	0.04	0.0327	0.00065	7.08E-19	1.04E-04
LAG2	Oliv	0.70675	2.07E-14	5.81E-16	4.12E-19	5.57E-16	4.88E-13	1.63E-15	7.51E-15	35.7	2.76	2.07	2.09	0.258	300.1	0.18	0.18869	0.19	n.m.	n.m.	n.m.	n.m.	6.02E-20	3.70E-05
LAG21	Oliv	0.7169	1.34E-14	2.03E-14	5.82E-17	1.95E-14	1.80E-12	6.09E-15	n.a.	0.7	n.a.	n.m.	n.m.	n.m.	295.6	0.06	0.18742	0.19	10.04	0.02	0.0303	0.00025	n.a.	n.a.
BARQ4	Oliv	0.7025	3.50E-14	4.90E-15	1.89E-17	6.63E-15	2.65E-13	8.12E-16	2.46E-14	5.1	1.42	4.80	5.18	0.323	325.8	0.32	0.19334	0.19	10.02	0.03	0.0317	0.00046	2.52E-19	3.11E-04
LAG1	Oliv	0.71426	3.31E-14	1.47E-14	4.22E-17	1.41E-14	2.07E-12	6.92E-15	n.a.	2.3	n.a.	2.48	2.77	0.284	298.5	0.05	0.18843	0.19	10.03	0.02	0.0308	0.00033	1.28E-19	1.84E-05
TRE-4	Oliv	0.82059	2.46E-14	1.21E-15	3.47E-18	1.16E-15	1.29E-12	4.33E-15	n.a.	20.4	n.a.	3.24	3.28	0.266	298.0	0.06	0.18741	0.19	9.82	0.09	0.0110	0.00110	2.91E-18	2.59E-05
TRE-1	Oliv	1.19089	6.02E-14	5.18E-14	1.52E-16	4.88E-14	2.42E-11	8.20E-14	n.a.	1.2	n.a.	3.78	4.93	0.091	295.1	0.00	0.18551	0.19	9.96	0.01	0.0292	0.00018	4.12E-19	n.a.
TRE-2	Oliv	1.27606	2.76E-14	4.54E-15	1.35E-17	4.28E-15	1.81E-12	6.29E-15	n.a.	6.1	n.a.	5.64	5.92	0.144	287.8	0.00	0.18258	0.18	n.m.	n.m.	n.m.	n.m.	2.27E-19	n.a.
TRE-3	Oliv	1.10012	5.71E-14	5.76E-14	1.68E-16	5.43E-14	9.09E-12	3.18E-14	n.a.	1.0	n.a.	2.26	2.98	0.083	286.1	0.00	0.18235	0.18	n.m.	n.m.	n.m.	n.m.	2.37E-19	n.a.
LAG24	Oliv	1.16645	4.18E-14	1.00E-15	2.93E-18	9.45E-16	8.62E-13	2.90E-15	n.a.	41.7	n.a.	1.51	1.51	0.114	297.4	0.06	0.18667	0.19	9.93	0.05	0.0291	0.00089	8.78E-20	n.a.
LAG1	Opx	0.45897	1.49E-13	6.95E-16	1.47E-18	6.66E-16	3.66E-13	8.27E-16	1.21E-13	215.2	1.23	5.77	5.78	0.182	442.4	0.56	0.18739	0.19	9.83	0.23	n.m.	n.m.	1.20E-18	1.45E-03
LAG52	Opx	0.62378	1.54E-12	7.75E-15	2.33E-17	7.44E-15	1.89E-12	2.15E-15	1.25E-12	199.1	1.23	6.08	6.09	0.090	877.6	0.13	0.18718	0.19	9.98	0.03	0.0300	0.00049	1.31E-17	6.07E-03
BARQ4	Opx	0.68572	2.17E-13	1.92E-15	5.79E-18	1.84E-15	3.63E-13	4.87E-16	2.19E-13	112.8	0.99	6.27	6.29	0.122	744.0	0.54	0.21295	0.21	9.91	0.08	0.0299	0.00129	1.90E-18	3.89E-03
LAG51	Opx	0.70574	5.15E-13	3.00E-15	6.96E-18	2.88E-15	1.13E-12	1.50E-15	6.86E-13	171.5	0.75	5.75	5.76	0.088	752.8	0.20	0.18779	0.19	10.06	0.03	0.0342	0.00109	4.12E-18	2.75E-03
LAG21	Opx	0.91336	1.20E-13	1.08E-14	3.07E-17	1.04E-14	7.44E-13	2.13E-15	1.16E-13	11.1	1.04	5.70	5.84	0.136	350.1	0.14	0.18744	0.19	9.96	0.02	0.0307	0.00040	9.76E-19	4.59E-04
LAG2	Opx	0.70223	6.70E-13	7.18E-15	2.12E-17	6.89E-15	9.84E-13	1.41E-15	5.68E-13	93.3	1.18	5.78	5.79	0.074	699.2	0.22	0.19806	0.20	9.91	0.03	0.0292	0.00049	5.40E-18	3.83E-03
TRE-4	Opx	0.14468	3.64E-13	6.60E-15	1.95E-17	6.33E-15	6.85E-13	1.20E-15	3.32E-13	55.1	1.18	5.73	5.76	0.064	573.0	0.68	0.23387	0.23	10.01	0.06	0.0296	0.00130	2.91E-18	2.44E-03
TRE-1	Opx	1.0626	3.94E-13	2.79E-16	1.03E-18	2.63E-16	4.90E-13	1.01E-15	1.90E-13	1408.5	2.07	6.60	6.60	0.081	483.1	0.00	0.18096	0.18	10.03	0.02	0.0291	0.00039	3.61E-18	n.a.
TRE-2	Opx	1.02899	2.95E-13	5.80E-16	1.82E-18	5.46E-16	1.09E-12	2.96E-15	2.13E-13	508.8	1.38	6.80	6.80	0.083	367.5	0.00	0.18534	0.18	n.m.	n.m.	n.m.	n.m.	2.37E-18	n.a.
TRE-3	Opx	1.11913	1.39E-13	5.94E-15	1.72E-17	5.60E-15	3.12E-12	8.89E-15	4.95E-13	23.5	0.28	5.35	5.41	0.081	351.1	0.06	0.18315	0.18	10.03	0.02	0.0291	0.00039	1.05E-18	n.a.
LAG24	Opx	0.99661	3.25E-13	1.66E-16	5.05E-19	1.56E-16	5.25E-13	5.97E-16	3.49E-13	1959.8	0.93	5.78	5.78	0.084	879.5	0.30	0.20017	0.20	n.m.	n.m.	n.m.	n.m.	2.61E-18	n.a.
LAG51	Cpx	0.46538	5.73E-13	5.51E-15	1.65E-17	5.27E-15	1.14E-12	6.08E-16	9.56E-13	104.0	0.60	5.73	5.74	0.091	1867.3	0.47	0.20754	0.21	10.03	0.04	0.0301	0.00054	4.58E-18	7.52E-03
LAG21	Cpx	0.29793	3.23E-13	4.51E-15	1.29E-17	4.30E-15	7.48E-13	7.75E-16	5.19E-13	71.6	0.62	6.10	6.13	0.130	965.6	0.66	0.21744	0.22	9.90	0.02	0.0290	0.00094	2.75E-18	3.55E-03
TRE-4	Cpx	0.0718	1.86E-13	4.35E-15	4.61E-17	4.13E-15	9.16E-13	2.85E-15	7.43E-14	42.8	2.51	2.16	2.17	0.077	321.6	1.14	0.16051	0.16	n.m.	n.m.	n.m.	n.m.	4.12E-18	1.98E-04
LAG2	Cpx	0.53856	1.18E-12	2.48E-15	8.43E-18	2.35E-15	1.42E-12	9.13E-16	1.15E-12	477.4	1.03	5.98	5.98	0.076	1551.2	0.45	0.17961	0.18	10.12	0.07	0.0346	0.00081	9.82E-18	1.08E-02
LAG52	Cpx	0.32425	1.36E-12	9.93E-16	4.62E-18	9.43E-16	2.03E-12	1.65E-15	1.54E-12	1368.2	0.88	5.90	5.90	0.066	1230.9	0.46	0.17870	0.18	n.m.	n.m.	n.m.	n.m.	1.12E-17	6.77E-03
BARQ4	Cpx	0.2825	3.57E-13	4.20E-16	6.68E-18	3.98E-16	7.39E-13	1.51E-15	2.92E-13	849.9	1.22	5.88	5.88	0.132	488.9	0.64	0.19450	0.19	n.m.	n.m.	n.m.	n.m.	2.92E-18	1.93E-03
LAG1	Cpx	0.50514	1.67E-13	2.09E-15	1.18E-17	1.98E-15	2.77E-13	4.42E-16	1.47E-13	79.8	1.14	5.48	5.50	0.144	627.6	1.20	0.19236	0.19	9.96	0.07	0.0298	0.00050	1.27E-18	2.88E-03
TRE-1	Cpx	0.53353	9.63E-13	5.69E-15	1.71E-17	5.37E-15	3.55E-12	1.07E-14	3.99E-13	169.1	2.41	6.50	6.51	0.072	332.9	0.06	0.18460	0.18	9.92	0.03	0.0298	0.00052	8.72E-18	n.a.
TRE-2	Cpx	0.52521	8.36E-13	2.87E-15	8.56E-18	2.70E-15	2.52E-12	6.29E-15	6.61E-13	291.8	1.27	6.82	6.82	0.074	400.6	0.07	0.18527	0.18	9.89	0.06	0.0296	0.00082	7.93E-18	n.a.
TRE-3	Cpx	0.4656	1.27E-13	1.53E-14	4.37E-17	1.44E-14	5.05E-12	1.58E-14	3.71E-13	8.3	0.34	5.10	5.27	0.123	319.0	0.05	0.18293	0.18	n.m.	n.m.	n.m.	n.m.	9.33E-19	n.a.
LAG24	Cpx	0.50807	2.25E-13	1.61E-16	3.32E-19	1.52E-16	4.62E-13	4.33E-16	3.34E-13	1393.6	0.67	5.86	5.86	0.110	1067.4	0.57	0.20185	0.20	n.m.	n.m.	n.m.	n.m.	1.83E-18	n.a.

ESM3 – Additional Figures
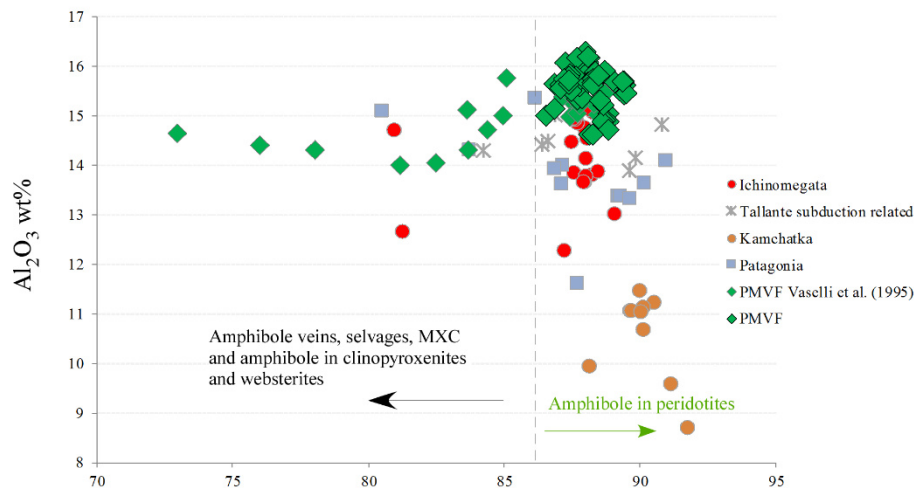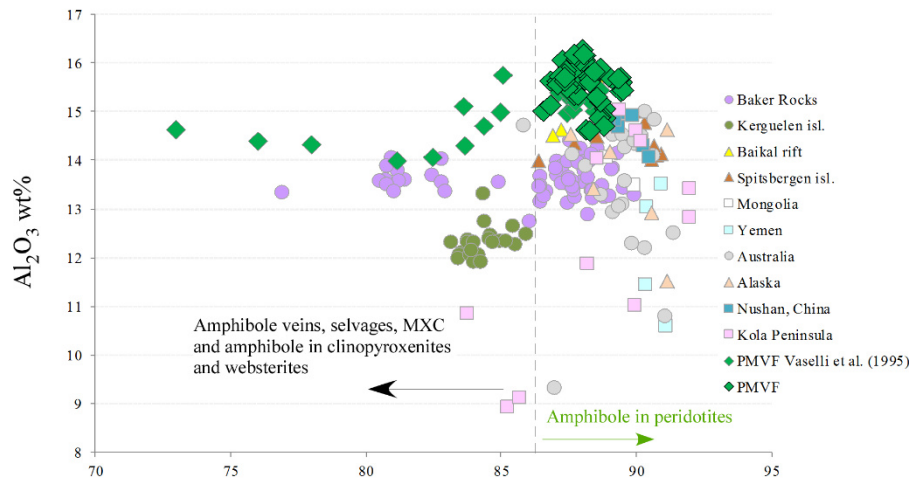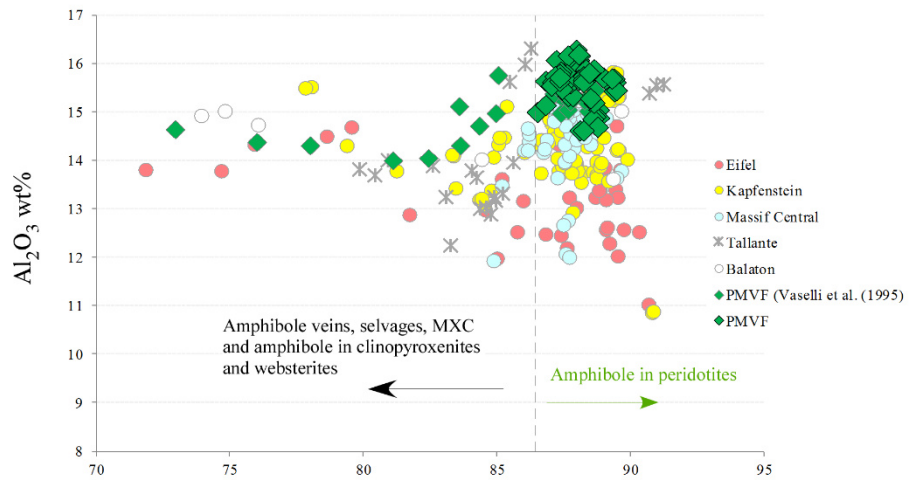
ESM3-1: Mg# vs Al₂O₃ of PMVF amphiboles (this work and Vaselli et al., 1995) in comparison with other European mantle xenolith (Styrian Basin, Coltorti et al., 2007a; Massif Central, Touron et al., 2008; Eifel, Witt-Eickshen et al., 1998; Balaton, Szabó et al., 1995a; Zanetti et al., 1995, Bali et al., 2002; Ntaflos et al., 2017 and Tallante, Coltorti et al., 2007b) and with mantle xenoliths from both intraplate (Francis, 1976; Ionov and Hofmann 1995; Chazot et al., 1996; Lee et al., 2000; Moine et al., 2001; Ionov et al., 2002; Coltorti et al., 2004; Powell et al., 2004; Xu and Bodinier, 2004; Beard

et al., 2007) and suprasubduction (Kepezhinskas et al., 1996; Abe et al., 1998; Grégoire et al., 2001; Franz et al., 2002; Ishimaru and Arai 2008; Yoshikawa et al., 2016) geodynamic settings. Dashed light grey line at mg# = 86 discriminates, on average, the field of amphiboles within peridotites from amphibole veins, megacrystals (MXC) and selvages and amphiboles in other ultramafic lithologies, like clinopyroxenites and websterites, also present in the various suites.
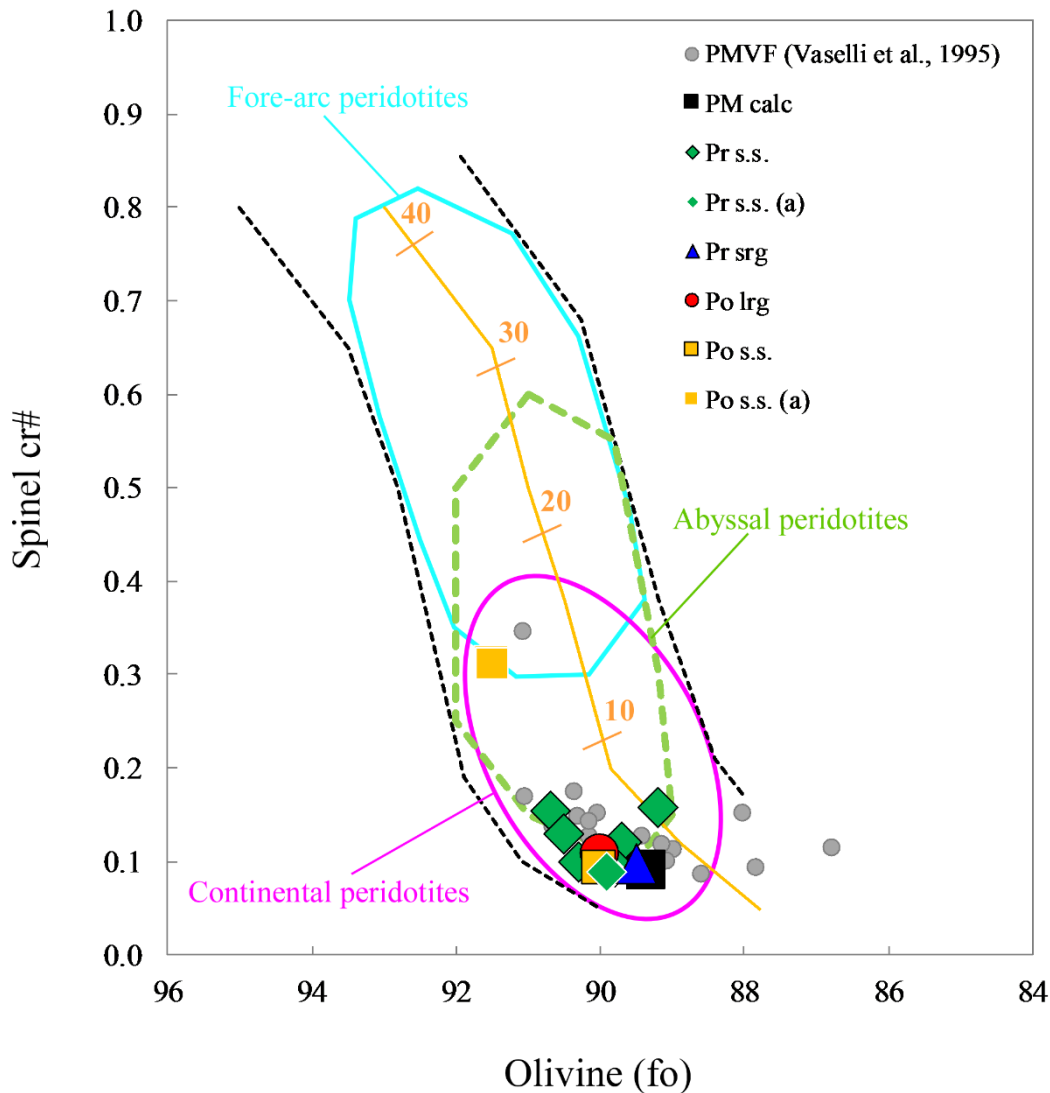
ESM3-2: Olivine-Spinel Mantle Array (OSMA) diagram for PMVF mantle xenoliths, divided by textural sub-groups (see main text for further explanations). Data from Vaselli et al. (1995) are reported for comparison. PM calc, olivine and spinel compositions calculated through mass balance from Bulk Silicate Earth of McDonough and Sun (1995) and Johnson et al. (1990) modes. All fields (abyssal, continental and fore arc peridotites) and partial melting line from Amhed et al. (2016).
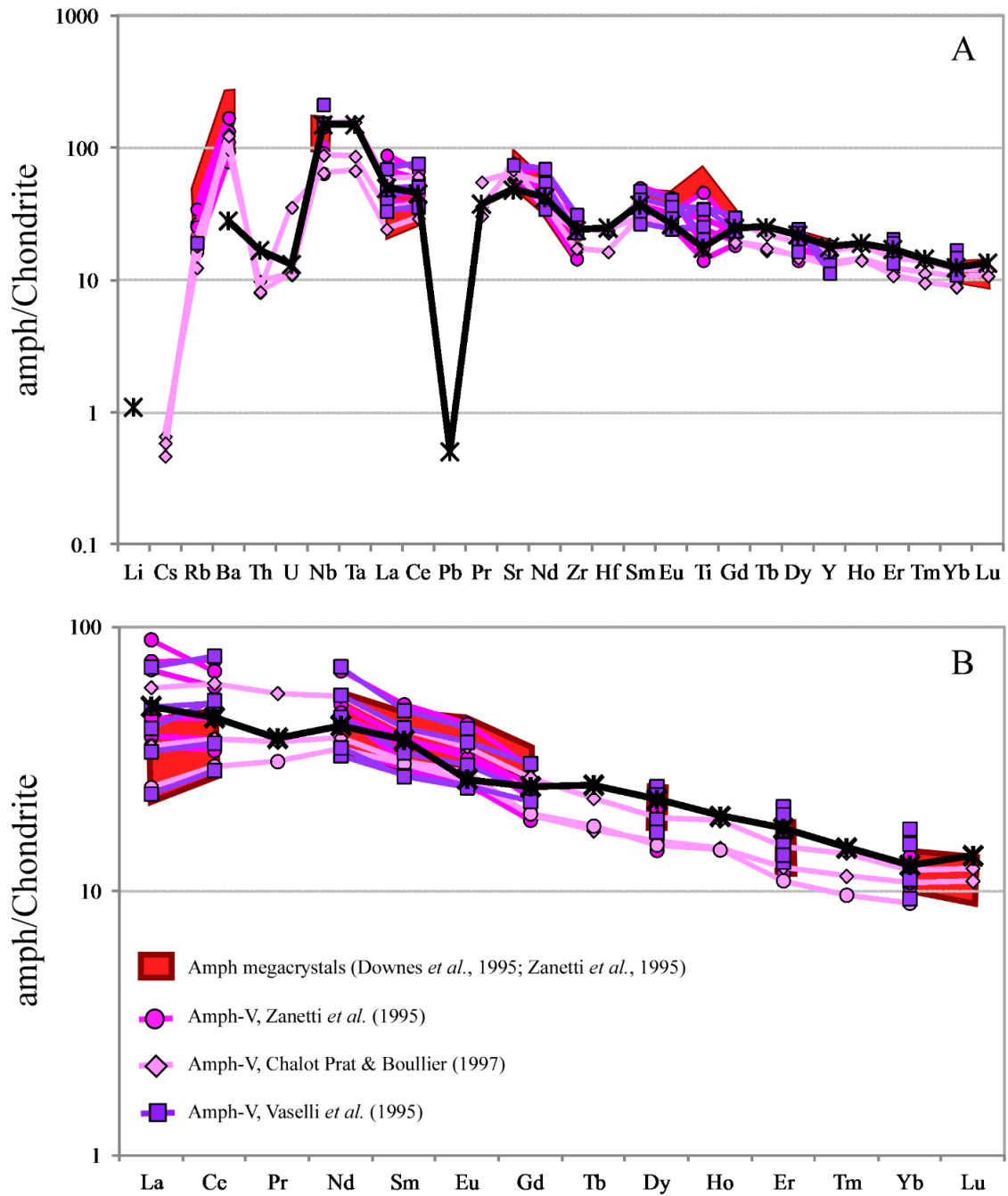
ESM3-3. Chondrite-normalized trace element (A) and REE (B) patterns of LAG52 amphibole vein (black asterisks) in comparison to literature data for PMVF amphibole veins (amph-V, Vaselli et al., 1995; Zanetti et al., 1995; Chalot-Prat and Boullier, 1997) and Perşani Mts. amphibole megacrystals (Downes et al., 1995; Zanetti et al., 1995).
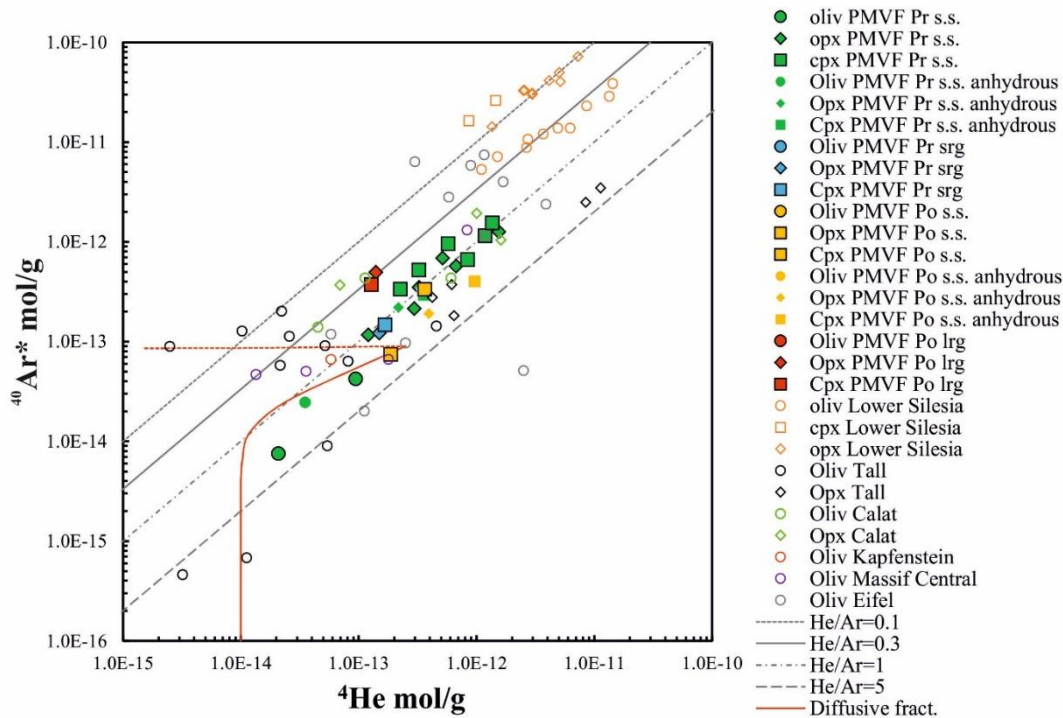
ESM3-4. Elemental concentration of ^{4}He and ^{40}Ar* measured in fluid inclusions of olivine (oliv), opx and cpx of PMVF xenoliths. The two diffusive fractionation paths are modeled as reported in Fig. 32 and in the text. Data from other European localities are as in Fig. 31 caption.
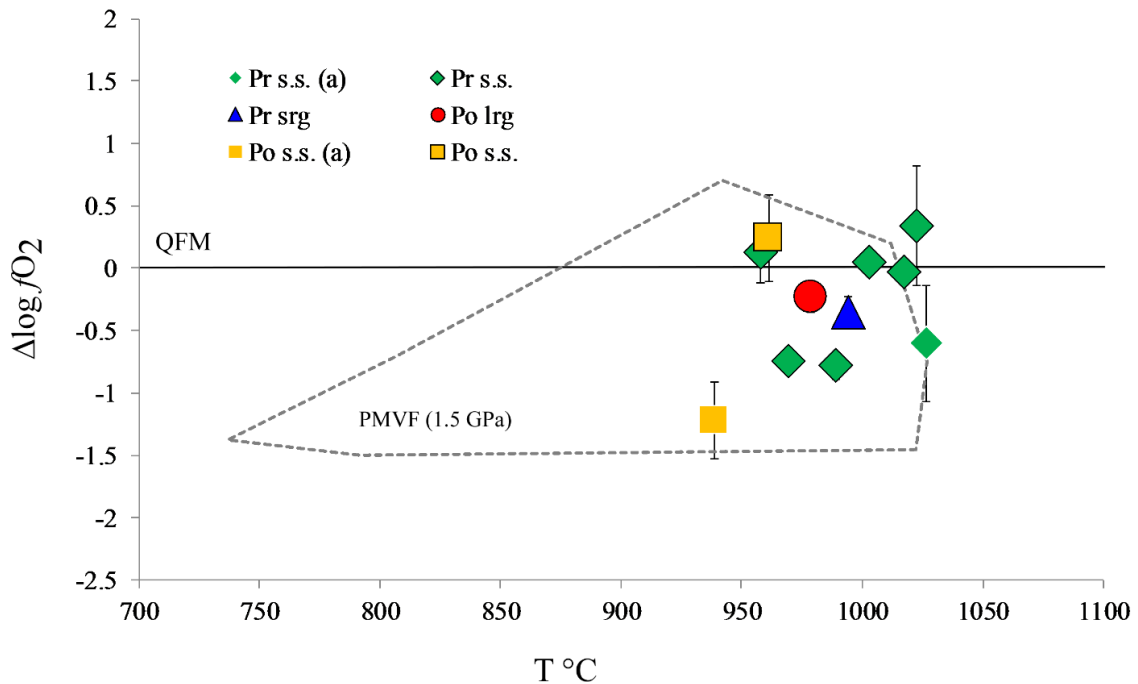
ESM3-5. ΔlogfO$_2$ vs temperature for PMVF mantle xenoliths, divided by textural sub-groups. Redox conditions were estimated at 2.0 GPa using the Ballhaus et al. (1991) oxygen geobarometer equation, on the basis of olivine–spinel temperatures obtained from the O'Neill and Wall (1987) thermometer modified by Ballhaus et al. (1991). Oxygen fugacities calculated at 1.5 GPa by Szabó et al. (1995b) for PMVF ultramafic xenoliths are reported for comparison (dashed line field).
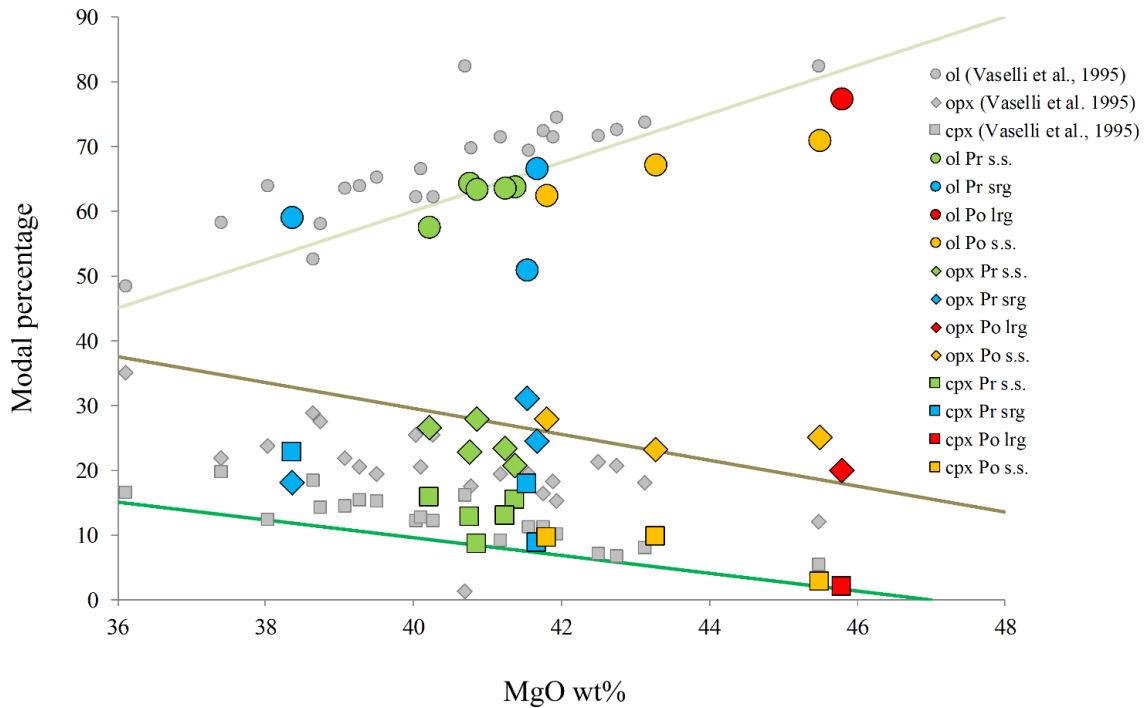
ESM3-6. Whole rock MgO wt% vs modal percentages of olivine (ol), opx and cpx of PMVF mantle xenoliths, divided by textural sub-groups. Grey symbols, PMVF ultramafic xenolith whole rock data from Vaselli et al. (1995). Depletion trends by Niu et al. (1997).
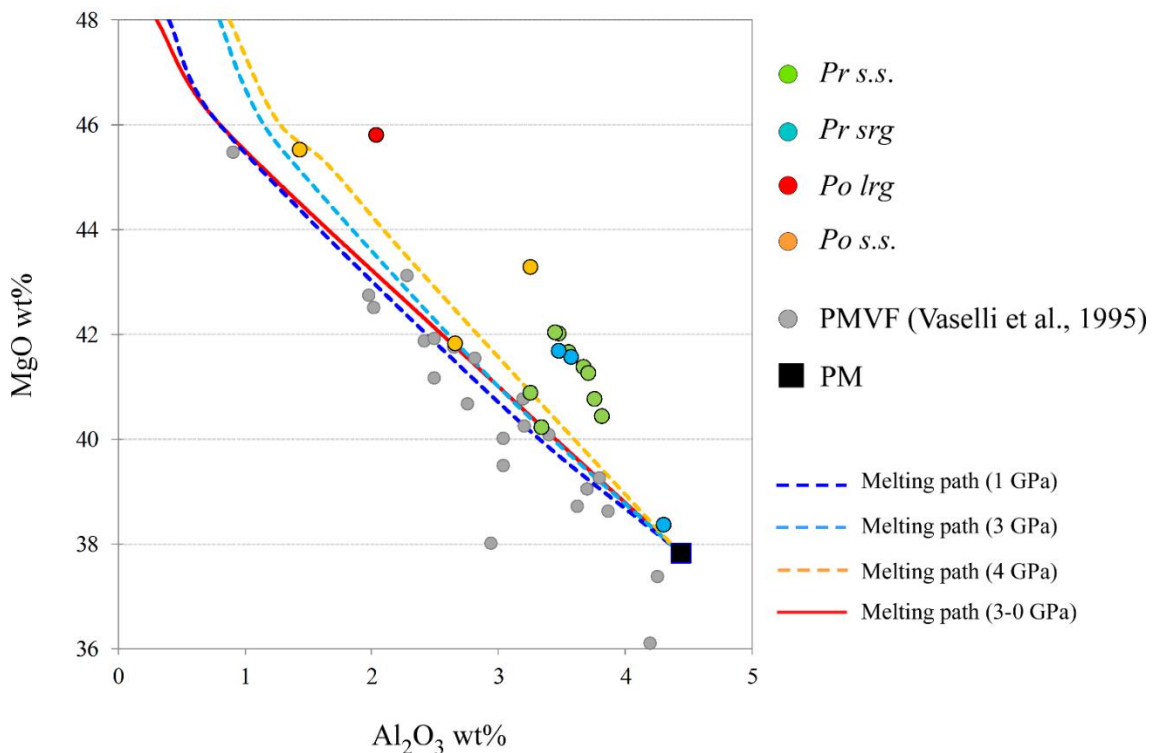
ESM3-7. Whole rock Al_2O_3 vs MgO for PMVF mantle xenoliths, divided by textural sub-groups. Grey circles, PMVF ultramafic xenoliths whole rock data from Vaselli et al. (1995). PM composition from McDonough and Sun (1995). Melting path lines at constant P (blue dotted line, 1 GPa; light blue dotted line, 3 GPa; yellow dotted line, 4 GPa) and polybaric melting path (red line, 3-0 GPa) (Ionov and Hoffmann, 2007 and references therein) are also reported.
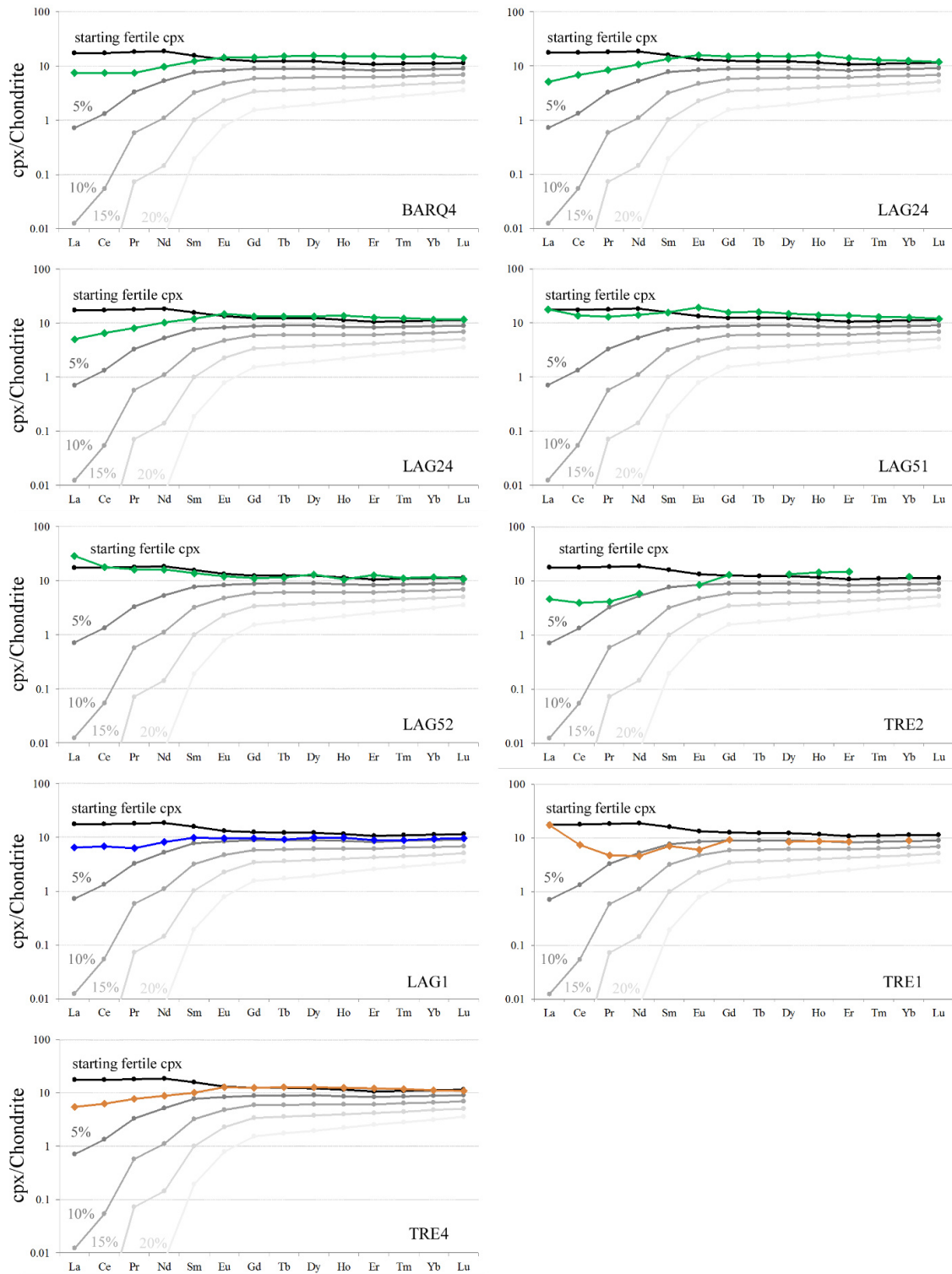
ESM3-8. Average Chodrite-normalized REE patterns of cpx in PMVF mantle xenoliths, divided by textural sub-groups: green, *Pr s.s.*; blue, *Pr srg*; yellow, *Po s.s.*. Patterns in shades of grey are cpx composition for variable degrees of F (5, 10, 15, 20%) according to the fractional melting model of Johnson et al. (1990), starting from the fertile cpx composition (black pattern) of Bonadiman et al. (2005).
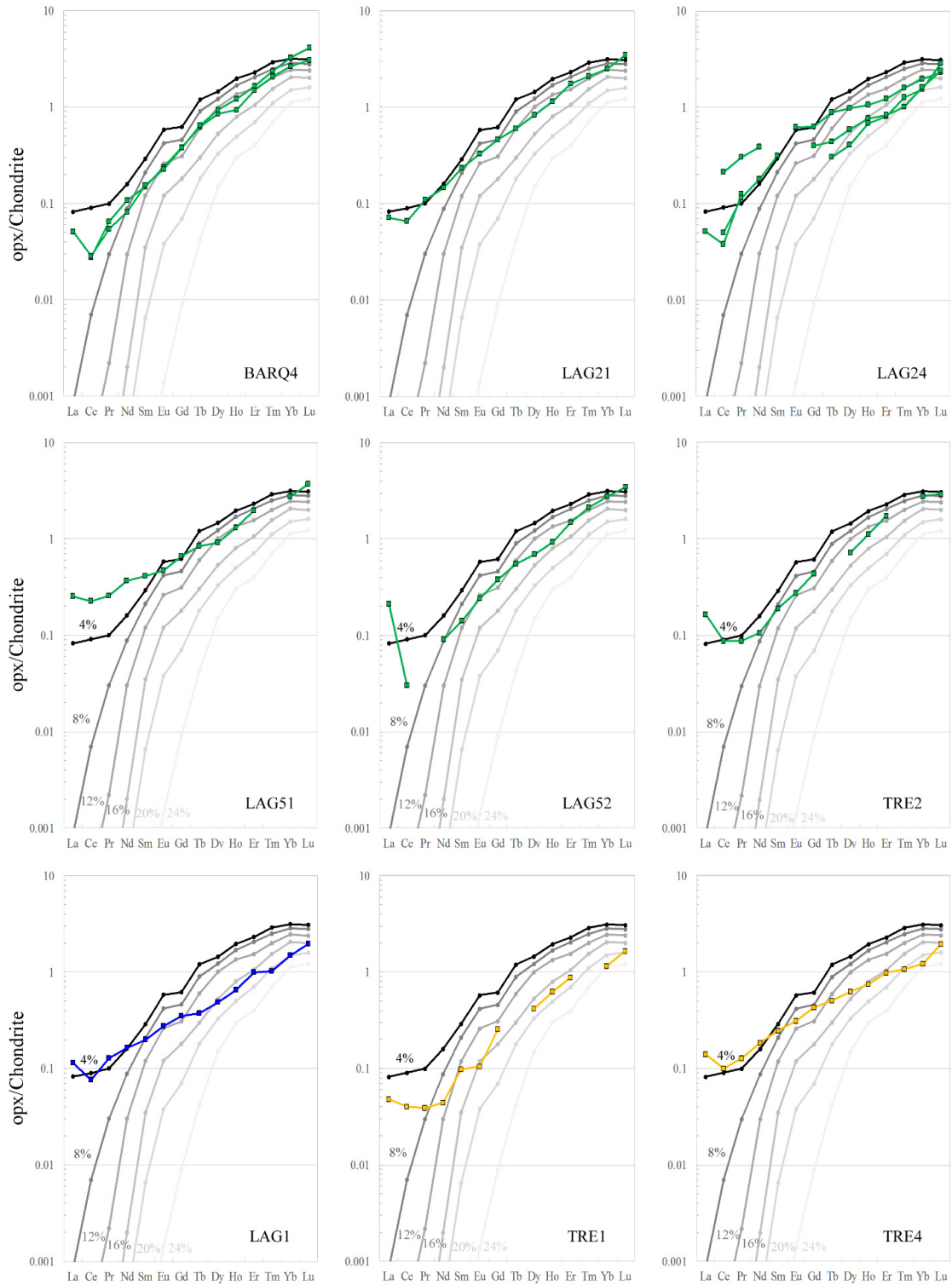
ESM3-9. Chodrite-normalized REE patterns of opx in PMVF mantle xenoliths, divided by textural sub-groups: green, *Pr s.s.*; blue, *Pr srg*; yellow, *Po s.s.*. Patterns in shades of grey are opx composition for variable degrees of F (8, 12, 16, 20, 24 %) according to the fractional melting model of Scott et al. (2016), starting from the DMM opx composition of Workman and Hart (2005).
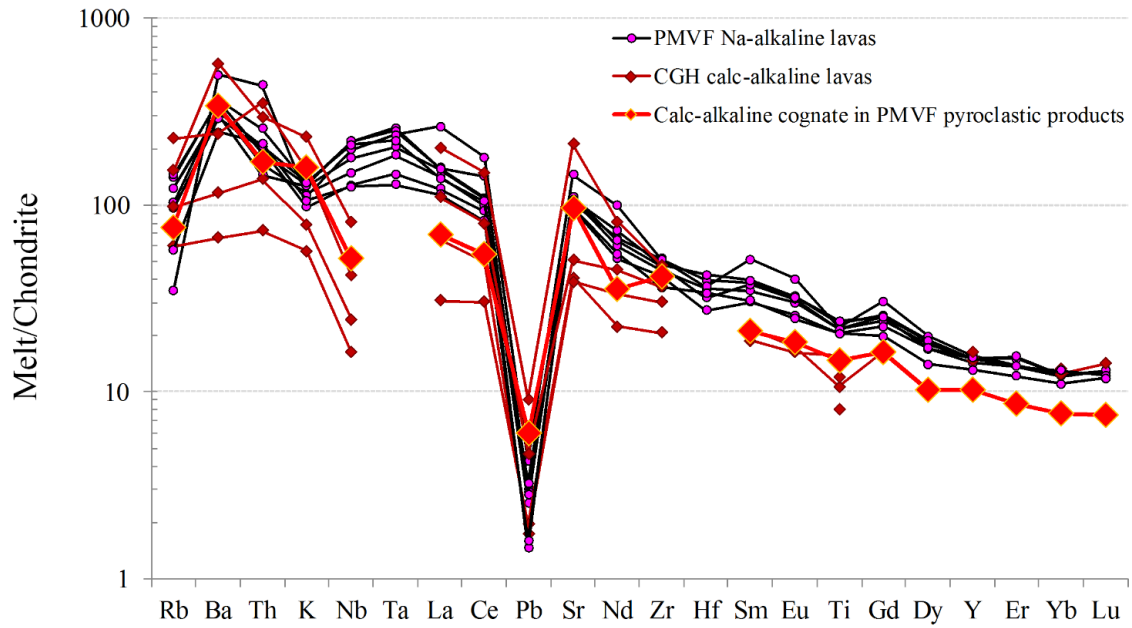
ESM3-10. Chondrite-normalized trace element patterns of some Eastern Transylvanian Basin basic magmas (all mg# ≥ 58). Pink circles, PMVF Na-alkaline basalts (Downes et al., 1995; Harangi et al., 2013); dark red diamonds, Călimani-Ghurghiu-Harghita (CGH) calc-alkaline basaltic andesites (Mason et al., 1996; Harangi and Lenkey, 2007); red diamond, composition of a calc-alkaline basaltic cognate found in PMVF pyroclastic deposits (Downes et al., 1995).
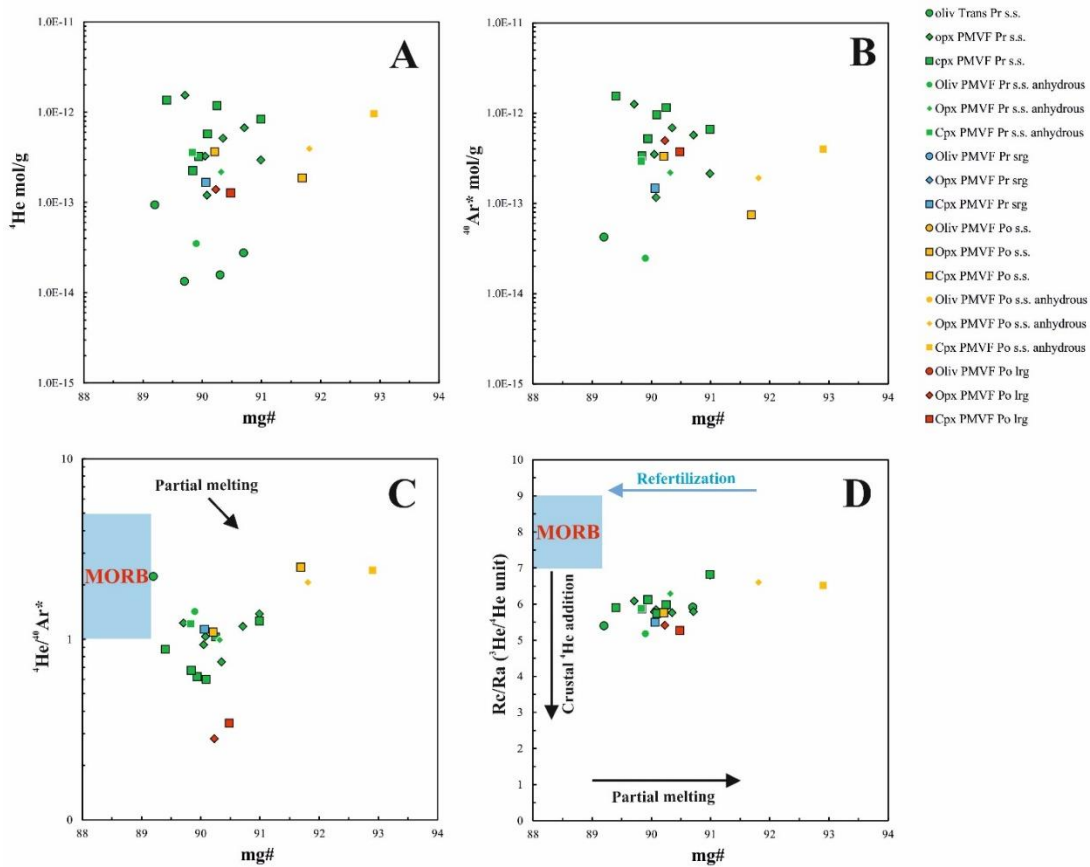
ESM3-11. Mg# vs A) ^{4}He, B) ^{40}Ar*, C) ^{4}He/^{40}Ar*, and D) ^{3}He/^{4}He corrected for air contamination (Rc/Ra values). Abbreviations as in ESM3-4. MORB range is reported for ^{4}He/^{40}Ar* and ^{3}He/^{4}He corrected for air contamination (Rc/Ra values). Further details are in the text.

Chapter – 5 –

Geochemistry of noble gases and CO_2 in fluid inclusions from lithospheric mantle beneath Eifel and Siebengebirge (Germany)

Enclosed:

Rizzo, A.L., Coltorti, M., Faccini, B., Casetta, F., Ntaflos, T. (2020). Petrology and volatile content of lithospheric mantle beneath Eifel and Siebengebirge volcanic fields (Germany). In prep.

5. Geochemistry of noble gases and CO_2 in fluid inclusions from lithospheric mantle beneath Eifel and Siebengebirge (Germany)

5.1 Introduction

The integrated study of fluid inclusions (FI) composition (He, Ne, Ar, CO_2), petrography and mineral chemistry in mantle xenoliths representative of Sub Continental Lithospheric Mantle (SCLM) is a unique opportunity for constraining its geochemical features and evaluating the processes and the evolution that modified the original composition. An additional benefit of this type of studies is the possibility of better constraining the composition of fluids rising through the crust and used for volcanic or seismic monitoring.

In this respect, the volcanic areas of Eifel and Siebengebirge in Germany represent a great opportunity to test this scientific approach for three main reasons. First, these volcanic centers developed in the core of the CEVP where there is a debate on whether the continental rift was triggered by the presence of a plume (Ritter et al., 2001; Keyser et al., 2002; Ritter, 2007 and references therein). Second, Eifel and Siebengebirge formed in Quaternary (0.5-0.01 Ma) and Tertiary (30-6 Ma) thus spanning a wide range of age that gives the opportunity to verify any temporal evolution of mantle features and processes that occurred therein. Third, Eifel area is characterized by the presence of CO_2-dominated gas emissions and weak earthquakes that testify that magmatic activity in Eifel is nowadays dormant, but not ended (e.g., Giggenbach et al., 1991; Griesshaber et al., 1992; Aeschbach-Hertig et al., 1996; Bräuer et al., 2005, 2013; Schmincke, 2007). It is thus important to better constraining the noble gas signature expected in surface gases in case of magmatic unrest.

This work focuses on the study of mantle xenoliths sampled in the West Eifel and Siebengebirge volcanic areas (Germany) and aims to update the knowledge on the local SCLM. Gautheron et al. (2005) carried out a first characterization of noble gases in FI of crystals analyzed by crushing technique (as in our study) but this was limited to olivines and to West Eifel eruptive centers. Here, we integrate that study by analyzing olivines, orthopyroxenes and clinopyroxenes from a new suite of samples and by including two eruptive centers from Siebengebirge volcanic field (Siebengebirge quarry and Eulenberg maar).

5.2 Results

5.2.1 Petrography

5.2.1.1 West Eifel volcanic field

Meerfelder Maar mantle xenoliths include five anhydrous (MM4, MM6, MM7, MM9, MM10), two amphibole-bearing (MM2, MM3) and one phlogopite-amphibole bearing lherzolites (MM8), one

amphibole-bearing harzburgite (MM5) and one phlogopite-bearing wehrlite (MM1) (Table 5.1; Fig. 38).

Half of the samples have coarse- to medium-grained textures that vary between pure (MM2, MM3, MM9) to slightly foliated (MM4, MM7) protogranular types (Mercier & Nicolas, 1975). On the other hand, the remaining have a peculiar texture, transitional between protogranular and tabular (MM5, MM10) or mosaic equigranular (MM6, MM8) (Mercier & Nicolas, 1975). Wehrlite MM1 has mosaic equigranular texture.

Olivine is often fractured and characterized by kink-banding; it is the phase that reaches the largest dimensions in all samples. Pyroxenes are smaller and generally show exolution lamellae. Spinel has vermicular to holly-leaf shape in MM4, MM7 and MM9 whereas it is small, subhedral and rounded in all other samples. In this latter case, spinel can be either included in olivine or found between cpx and opx or at the triple junctions in the equigranular areas. Spinel of wehrlite MM1 has a shape with intermediate characteristics between holly-leaf and rounded-subhedral.

Amphibole is present as small, well-equilibrated crystals associated to cpx and/or spinel in lherzolite MM2. In MM3 it can be only found within an infiltrating melt vein and in the lherzolitic matrix in the proximity of this vein; in the latter case, it grows around the primary cpx. In harzburgite MM5 and lherzolite MM8 amphibole seems to occupy the textural position of a previous phase (probably cpx) and it often shows reaction rims, where glass and tiny subhedral to euhedral secondary phases (mainly cpx and spinel) are present. A similar texture can be observed in lherzolite MM10 but, in this case, no amphibole is present and the reaction involves primary cpx and spinel.

In wehrlite MM1, strongly pleochroic phlogopite can be found either in association with infiltrating veinlets from the host basalt or texturally equilibrated, close to spinels. In lherzolite MM8, phlogopite has textural position and relationships with other minerals similar to the amphiboles.

Xenoliths from Dreis-Bruck (Dreiser Weiher) and Gees show a large variability in terms of rock types and textures (Table 5.2; Fig. 38).

Dreis-Bruck collection includes five anhydrous lherzolites (DBR3, DBR5, DBR6, DBR8, DBR9), one anhydrous harzburgite (DBR7), one anhydrous wehrlite (DBR2), one amphibole-phlogopite-bearing wehrlite (DBR4), one ol-clinopyroxenite (DBR11) and two anhydrous composite xenoliths: a lherzolite/ol-clinopyroxenite (DBR1) and a lherzolite crosscut by a dunite channel (DBR10). These last two samples will be described as separate parts and respectively named DBR1 Pd and DBR1 Px and DBR10 Pd and DBR10 Dn.

Lherzolites DBR1 Pd, DBR3, DBR5, DBR6, DBR8 and DBR9 share a medium-grained protogranular texture, with spinel present as blobs and/or vermicular crystals. Olivine and opx have the biggest dimensions while cpx is always smaller. Kink-banding and fracturing are a common

feature in olivine as exolution lamellae in both pyroxenes. In DBR5, DBR6, DBR8 and DBR9, spinels are anisotropic, aligned and elongated in one direction while the other minerals are broadly isotropic. Harzburgite DBR7 has tabular equigranular texture with rounded, subhedral spinel generally associated with cpx. Olivine is kinked; opx have exolution lamellae while cpx has not. All crystals tend to be anisotropic and aligned. Similarly to MM10, a peculiar reaction texture can be observed, with destabilized cpx whose only the shapes remain, filled with glass and tiny, subhedral to euhedral secondary crystals of cpx and spinel. Voids are also visible in these glassy patches.

DBR2 has a coarse-grained, recrystallized cumulitic texture where cpx reaches the biggest dimensions. Engulfment contacts can be observed between the cpx aggregates and the nearby olivine, suggesting a crystallization order ol → cpx. Olivine has a remarkable kink-banding and frequent triple junctions while no exolution lamellae are present in the cpx. Spinel is very rare, small and rounded and located between olivine crystals.

Wehrlite DBR4 has tabular equigranular texture altered by a massive melt infiltration. In areas where the melt/rock ratio is higher, olivine can be found as elongated tabular crystals mixed with smaller cpx in a dark, glassy matrix. On the other hand, where the melt did not totally impregnate the rock, olivine and cpx have sharp contacts. Amphibole and phlogopite can be found texturally equilibrated with cpx and olivine in the preserved areas, while they show resorbed rims when surrounded by the black glass. Tiny secondary cpx and olivine crystals can be noticed within the glass.

DBR1 Px and DBR11 are medium to very coarse-grained ol-clinopyroxenites with ad-cumulitic and ortho-cumulitic texture, respectively. Crystallization order is ol → cpx. In DBR1 Px, cpx has cloudy, spongy rims. Its contact with the lherzolite is gradual and can be identified by a wehrlitic band whose cpx are similar to those of the ol-clinopyroxenite. Trails of fluid inclusions are present within cpx.

Composite sample DBR10 consists of a medium-fine-grained protogranular lherzolite cut by a spinel-rich dunitic channel. The contact between the two lithologies is indented, with some pyroxenes from the lherzolite that have been incorporated among the olivines of the channel.

Gees nodule collection includes three anhydrous harzburgites (GE3, GE4, GE10), one anhydrous lherzolite (GE6), one anhydrous ol-websterite (GE1), one anhydrous ol-clinopyroxenite (GE7), one amphibole-bearing wehrlite (GE9) and three phlogopite-bearing wehrlites (GE2, GE5, GE8) (Table 5.3; Fig. 38).

The harzburgites and the lherzolite are characterized by porphyroclastic texture with opx as the largest porphyroclasts; all opx are deformed and have well-developed exolution lamellae and cleavage. Spinel is the only aluminous phase and has vermicular to holly-leaf shape. It is very often characterized by a thick reaction rim composed of tiny secondary phases, mainly cpx. In all these rocks, the few primary cpx are completely spongy.

The wehrlites and the ol-clinopyroxenite have ortho-cumulitic texture with a backbone made by subhedral, inequigranular olivine crystals, often fractured and kink-banded. Anhedral green cpx and rounded spinel (frequently clustered) occupy the intercumulus spaces together with phlogopite. In some samples (GE2, GE7, GE9), basalt infiltration occurred, visible as small glassy veins surrounding the minerals and causing local destabilization of cpx and spinel. GE7 is characterized by a banded structure, with layers richer in cpx and layers richer in olivine while, in GE8, a sub-millimetre phlogopite vein cut the sample.

Ol-websterite GE1 has ad-cumulitic texture composed by coarse-grained opx and cpx that slowly decrease in size towards a corner, where the texture turns ortho-cumulitic with olivine crystals as backbone and pyroxenes as intercumulus phases. Tiny rounded spinel are also associated to the pyroxenes. Cpx destabilization is widespread, visible as spongy surfaces, composed by secondary phases surrounded by a glass film. Fluid inclusions are frequent, especially in cpx.

5.1.1.2 Siebengebirge volcanic field

Siebengebirge mantle xenoliths were sampled from two locations: the Siebengebirge quarry and the Eulenberg maar. Those from Siebengebirge quarry are mainly harzburgites (SB2, SB3, SB4, SB5) with minor dunites (SB1, SB7, SB9) and only one lherzolite (SB6) (Table 5.4; Fig. 38). Sample SB8 is heavily altered and the majority of its constituent minerals cannot be recognized but for few opx and cpx, thus it will not be further treated. All xenoliths are anhydrous and spinel is the only aluminous phase.

The harzburgites and lherzolite have coarse-grained porphyroclastic texture. Opx reaches the largest dimensions and is present only as porphyroclasts with well-developed exolution lamellae; it can develop thin spongy reaction rims. Olivine is inequigranular, with single individuals that may almost reach the dimensions of opx and numerous smaller neoblast crystals. Kink-banding is ubiquitous. Primary cpx can be identified especially in the lherzolite but they are all spongy or cribrose. Serpentinization is present in all samples and alteration is diffuse (especially in spongy cpx) so that it is difficult to distinguish the tiny secondary phases in the pyroxene reaction zones. Spinel has holly-leaf shape and in some samples (SB2, SB3) it is elongated and aligned.

Dunites have texture varying from mildly porphyroclastic to mosaic equigranular tending towards II generation protogranular (Mercier & Nicolas, 1975). Olivine is fractured and characterized by kink-banding, while spinel is rounded and generally arranged in aligned clusters. Secondary green cpx is present around the spinel clusters and is largely altered.

Eulenberg mantle xenoliths (EUL1, EUL2, EUL3, EUL4, EUL5, EUL6, EUL7) are all porphyroclastic harzburgites and are very similar to Siebengebirge harzburgites (Table 5.5; Fig. 38),

but some primary cpx seem to be preserved. These cpx are small and have well-developed exsolution lamellae.
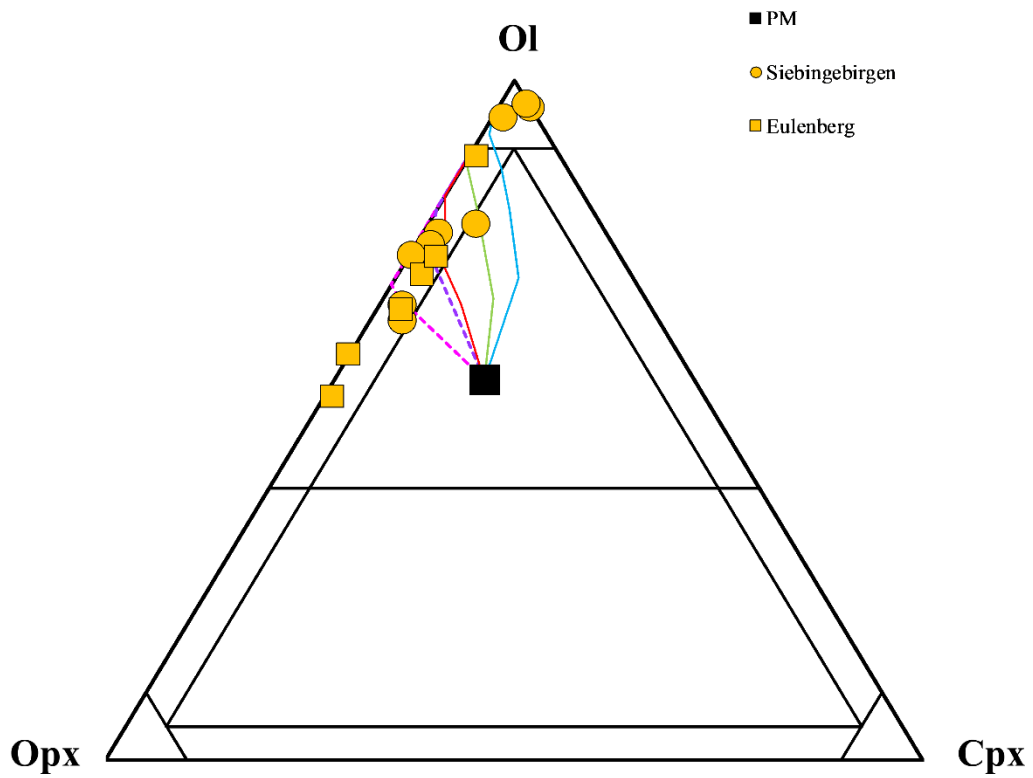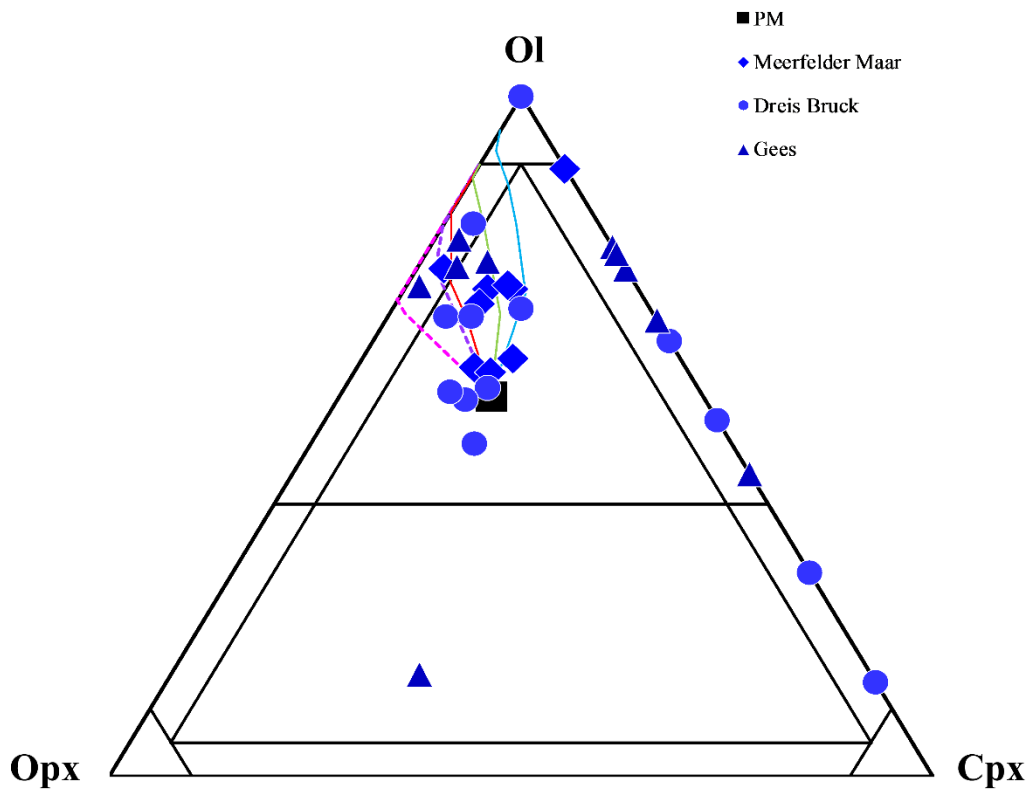
Figure 38. Ultramafic classification diagram for West Eifel (blue symbols) and Siebingebirge (yellow symbols) xenoliths. Black square, PM modal composition from Johnson et al. (1990). Dotted pink and purple lines are melting paths at 2 and 1 GPa, respectively (Niu et al., 1997) while red, light blue and green lines are hydrous melting paths at 1 GPa and 0.1 (red), 0.5 (light blue) and 1 (green) % of H2O (Bènard et al., 2018).

5.2.2 Mineral chemistry

5.2.2.1 Olivine

Olivine in West Eifel ultramafic xenoliths are characterized by a large compositional variation, especially between the typical mantle lithologies (harzburgites and lherzolites) and those of different origin (reaction products and/or cumulates). Fo varies from 83.4 to 91.6 while NiO spans between 0.16 to 0.42 wt%, with a direct correlation between the two (Fig. 39). Harzburgites and lherzolites have Fo and NiO respectively higher than 88.6 and 0.31 wt%.

On the other hand, olivine in Siebengebirge xenoliths have very restitic compositions, with Fo varying from 90.5 to 91.8 and NiO going from 0.31 to 0.43, typical of depleted mantle lithologies (Herzberg et al., 2016).
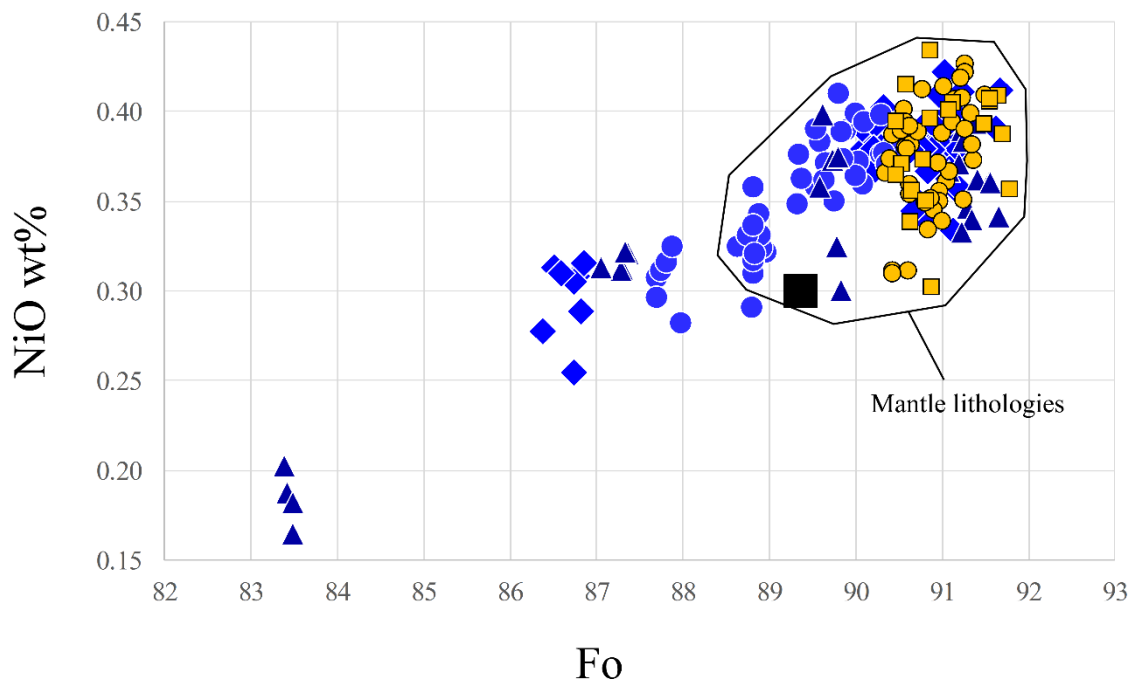
Figure 39. Fo vs NiO content of olivine in West Eifel and Siebingebirge xenoliths. Symbols as in Fig. 38. Black square, Primordial Mantle (PM) olivine composition calculated through mass balance from Bulk Silicate Earth of McDonough and Sun (1995) and Johnson et al. (1990) modes.

5.2.2.2 Clinopyroxene

Cpx in West Eifel ultramafic xenoliths have a very large compositional spectrum, with mg# and Al_2O_3 varying from 84.4 to 92.6 and from 2.22 to 8.65 wt%, respectively (Fig. 40A). Compared to the melting model of Bonadiman and Coltorti (2018), no fit for the great majority of them can be discerned (Fig. 40A). Cpx can indeed reach very high Al_2O_3 contents, even higher than those estimated for a primordial phase in an undepleted, primitive mantle. Cpx in both lherzolites and harzburgites (mg# $\geq$ 88.7) and in other ultramafic parageneses (mg# < 88.7) may have low and high Al_2O_3 contents. In mg# vs TiO_2 diagram (Fig. 40B), cpx in xenoliths from West Eifel align on a trend of increasing TiO_2 content at decreasing mg#, with the exception of ol-websterite GE1 whose cpx have remarkably low TiO_2.

Siebengebirge cpx are almost all secondary in mantle xenoliths from Siebengebirge quarry while those in the Eulander collection are remnants of the primary phase. In the first case, they have mg# spanning from 88.6 to 94.1 and Al_2O_3 from 0.66 to 5.10 wt% (Fig. 40A); they do not fit with the melting curve. Eulander primary cpx are more homogeneous (mg#, 91.6 – 94.1; Al_2O_3, 1.43 – 3.98 wt%) but their mg# are too high with respect to the model. Remarkably, TiO_2 content in Siebengebirge quarry cpx increases up to 1.21 wt% but in Eulander cpx it is very low (0.006 – 0.22 wt%) (Fig. 40B), as expected for a restitic phase.
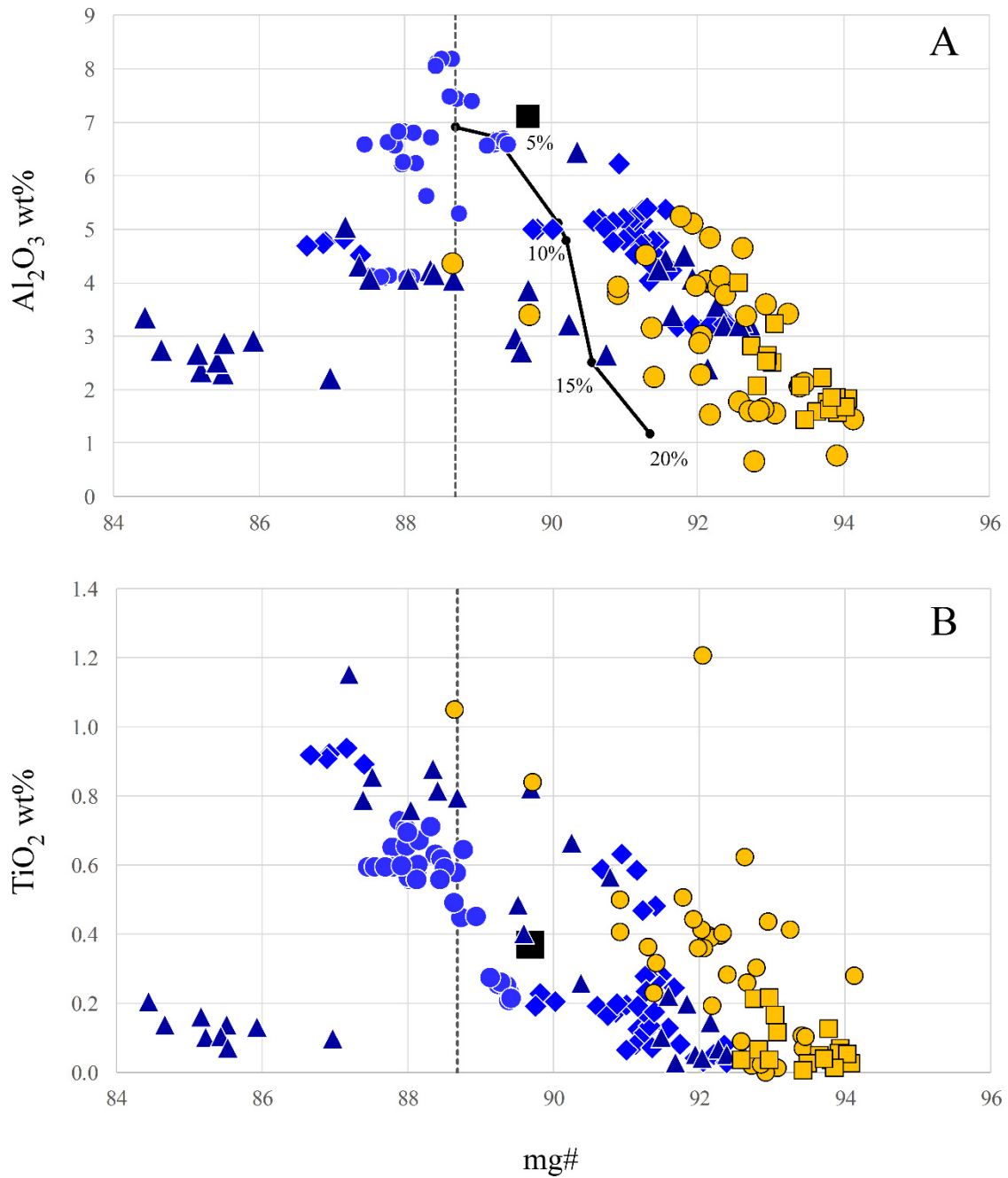
Figure 40. Mg# vs Al$_2$O$_3$ (A) and TiO$_2$ (B) for cpx in West Eifel and Siebingebirge xenoliths. Symbols as in Fig. 38. Black square in (A), PM cpx composition calculated through mass balance from Bulk Silicate Earth of McDonough and Sun (1995) and Johnson et al. (1990) modes. Thick line in (A), cpx melting model by Bonadiman and Coltorti (2018). Dotted line represents mg# threshold for mantle cpx.

5.2.2.3 Orthopyroxene

Opx composition in West Eifel xenoliths is rather constant within each sample. On the whole, mg# vary between 84.3 and 92.2 (Fig. 41A). A large variation in Al$_2$O$_3$ content can be observed (1.47 – 6.47 wt%, Fig. 41A); similarly to cpx, many opx are more fertile than a primordial phase in an

undepleted, primitive mantle. There is a partial fit with the melting model by Bonadiman and Coltorti (2018), with ol-websterite GE1 still being the farthest from the curve. TiO_2 is very low for the majority of opx (Fig. 41B) but it tends to increase in the most fertile mantle phases.

Siebengebirge quarry and Eulander opx are more depleted than those in West Eifel xenoliths, with a partial overlap of both mg# (90.6 – 92) and Al_2O_3 (bdl – 3.36 wt%), but with values even more depleted than what predicted by the model for 25% degree of partial melting (F%) (Fig. 41A). TiO_2 contents are also generally low (bdl - 0.23 wt%, Fig. 41B).
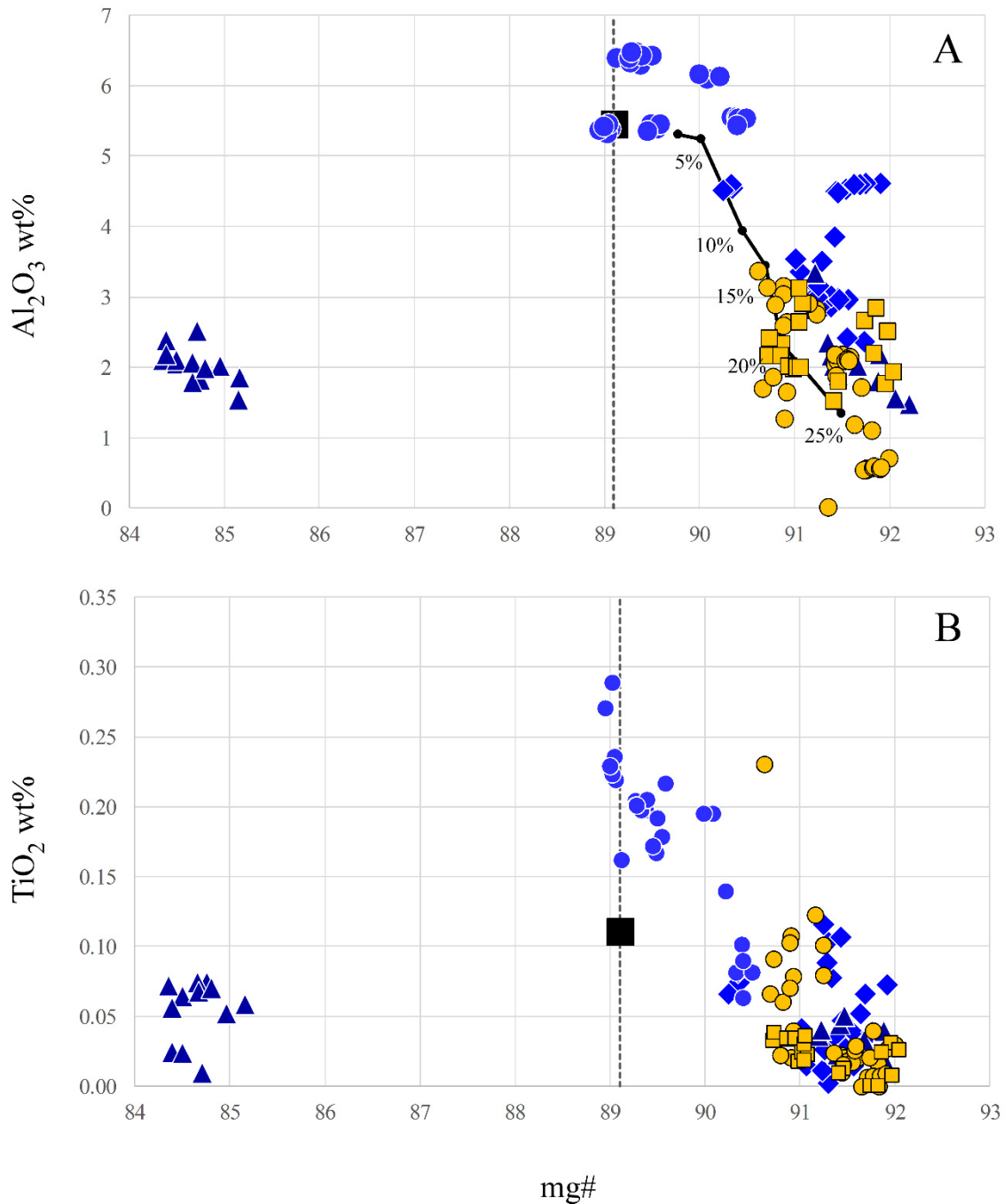
Figure 41. Mg# vs Al$_2$O$_3$ (A) and TiO$_2$ (B) for opx in West Eifel and Siebingebirge xenoliths. Symbols as in Fig. 38. Black square in (A), PM opx composition calculated through mass balance from Bulk Silicate Earth of McDonough and Sun (1995) and Johnson et al. (1990) modes. Thick line in (A), cpx melting model by Bonadiman and Coltorti (2018). Dotted line represents mg# threshold for mantle opx.

5.2.2.4 Spinel

Spinel in West Eifel ultramafic xenoliths have mg# and cr# varying from 40.8 to 77.5 and from 9.54 to 57.2, respectively. The lower mg# values belong to spinel in ol-websterite GE1. Spinel in Siebengebirge xenoliths have mg# between 49.6 to 77.3 and cr# from 15.8 to 81.7 thus, even if the mg# interval is similar, they are much more Cr-rich than those of West Eifel. Siebengebirge quarry spinel are bimodal, with a Cr-rich group and an Al-rich group. This can be noticed also in the Olivine-Spinel Mantle Array (OSMA) diagram (Fig. 42), where the Cr-rich group is partly located in the upper segment of the depletion trend and partly outside, in the crystal fractionation area.
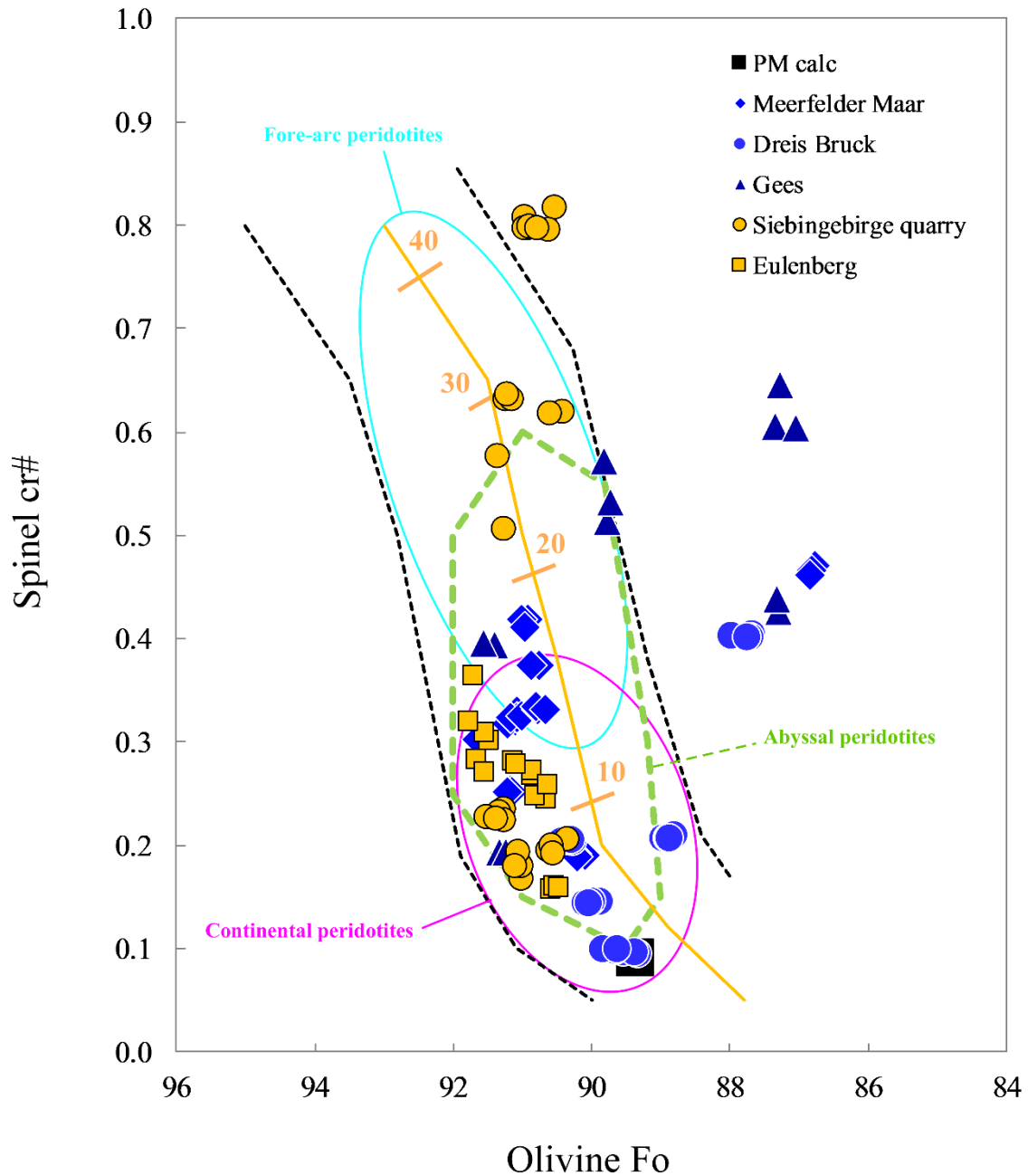
Figure 42. Olivine-Spinel Mantle Array (OSMA) diagram for West Eifel and Siebengebirge ultramafic xenoliths. Symbols as in Fig. 38. PM calc, olivine and spinel compositions calculated through mass balance from Bulk Silicate Earth of McDonough and Sun (1995) and Johnson et al. (1990) modes. All fields (abyssal, continental and fore arc peridotites) and partial melting line from Amhed et al. (2016).

5.2.3 Chemistry of FI

The chemistry of FI hosted in West Eifel and Siebengebirge xenoliths is reported in Table 5.6 and shown in Figure 43. $^{40}Ar*$ is within the range of 0.3–65.7×10^{-12} mol/g, while ^{4}He ranges from 0.1×10^{-12} to 40.8×10^{-12} mol/g (Fig. 43A) and ^{3}He from 0.7×10^{-18} to 330×10^{-18} mol/g (Table 5.6). The gas

mixture is dominated by CO_2, which spans in a wide range from 2.5×10^{-11} to 1.3×10^{-6} mol/g (Fig. 43B). N_2 corrected for atmospheric contamination (N_2*) represents the second major species, whose content varies from 0.09×10^{-9} to 11.1×10^{-9} mol/g (Fig. 43C). The atmospheric component in FI, which here is considered to be N_2+O_2+Ar, varies from 1.5×10^{-11} to 87.1×10^{-11} mol/g. The ^{20}Ne concentration ranges from 0.4×10^{-15} to 68.5×10^{-15} mol/g (Table 5.6). Finally, ^{21}Ne* varies from 0.6×10^{-19} to 81×10^{-19} mol/g (Fig. 43D).

The average numbers of mol/g of CO_2, N_2*, ^{40}Ar*, ^{21}Ne*, and ^4He are higher in Cpx and Opx than in Ol. In addition, samples from West Eifel are gas richer than those from Siebengebirge (Fig. 43), generally reflecting the same proportions among mineral phases above reported. Due to the extremely depleted lithology, it was not possible to make measurements in Cpx from Siebengebirge. CO_2 is positively correlated with N_2*, ^{40}Ar*, ^{21}Ne*, and ^4He, indicating that the CO_2-rich FI are also rich in the other gas species.
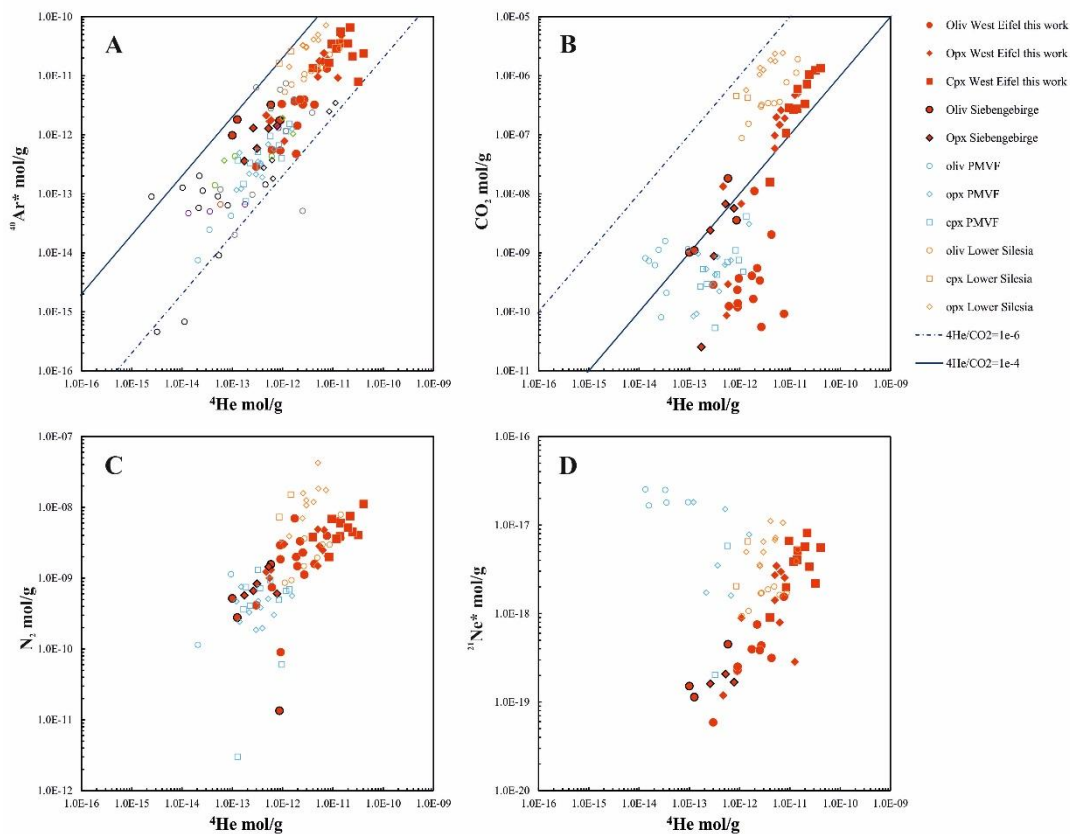
Figure 43. Elemental concentrations in mol/g measured in FI after single-step crushing of ^4He versus a) ^{40}Ar*, b) CO_2, c) N_2*; and d) ^{21}Ne*. Olivine abbreviated as "Oliv", Orthopyroxene as "Opx", and Clinopyroxene as "Cpx".

5.2.4 Isotope compositions of He, Ne, and Ar in FI

The ^{3}He/^{4}He ratio not corrected for air contamination (R/Ra) is 5.5–6.8 Ra in Ol, 3.1–6.8 Ra in Opx, and 5.6–6.8 Ra in Cpx (Table 5.6). The ^{4}He/^{20}Ne ratio is 182–1761 in Ol, 20–2754 in Opx, and 596–4929 in Cpx (Table 5.6). The ^{40}Ar/^{36}Ar ratio is 345–2344 in Ol, 328–7192 in Opx, and 1170–9797 in Cpx (Table 5.6). The ^{20}Ne/^{22}Ne and ^{21}Ne/^{22}Ne ratios are 9.8–11.0 and 0.0288–0.04372, respectively, in Ol, 9.8–10.9 and 0.0290–0.0386 in Opx, and 9.8–11.0 and 0.0298–0.0417 in Cpx (Table 5.6).

The ^{3}He/^{4}He ratio corrected for air contamination (Rc/Ra values) is 5.5–6.8 Ra in Ol, 3.1–6.8 Ra in Opx, and 5.6–6.8 Ra in Cpx (Table 5.6 and Fig. 44). There is no systematic difference in the Rc/Ra values among variable FI concentration, different mineral phases, and regional provenance of xenoliths (West Eifel and Siebengebirge) (Figs. 44 and 45). The only exception is for Opx from SB5 that show the lowest Rc/Ra values (in 2 measurements) and also the lowest ^{4}He, ^{40}Ar* and ^{3}He content (Fig. 45). It is worth noting that samples MM1, GE1, and DBR2 (Mg#<88) show ^{3}He/^{4}He ratio progressively decreasing from 6.4 to 5.5 Ra (Table 5.6).
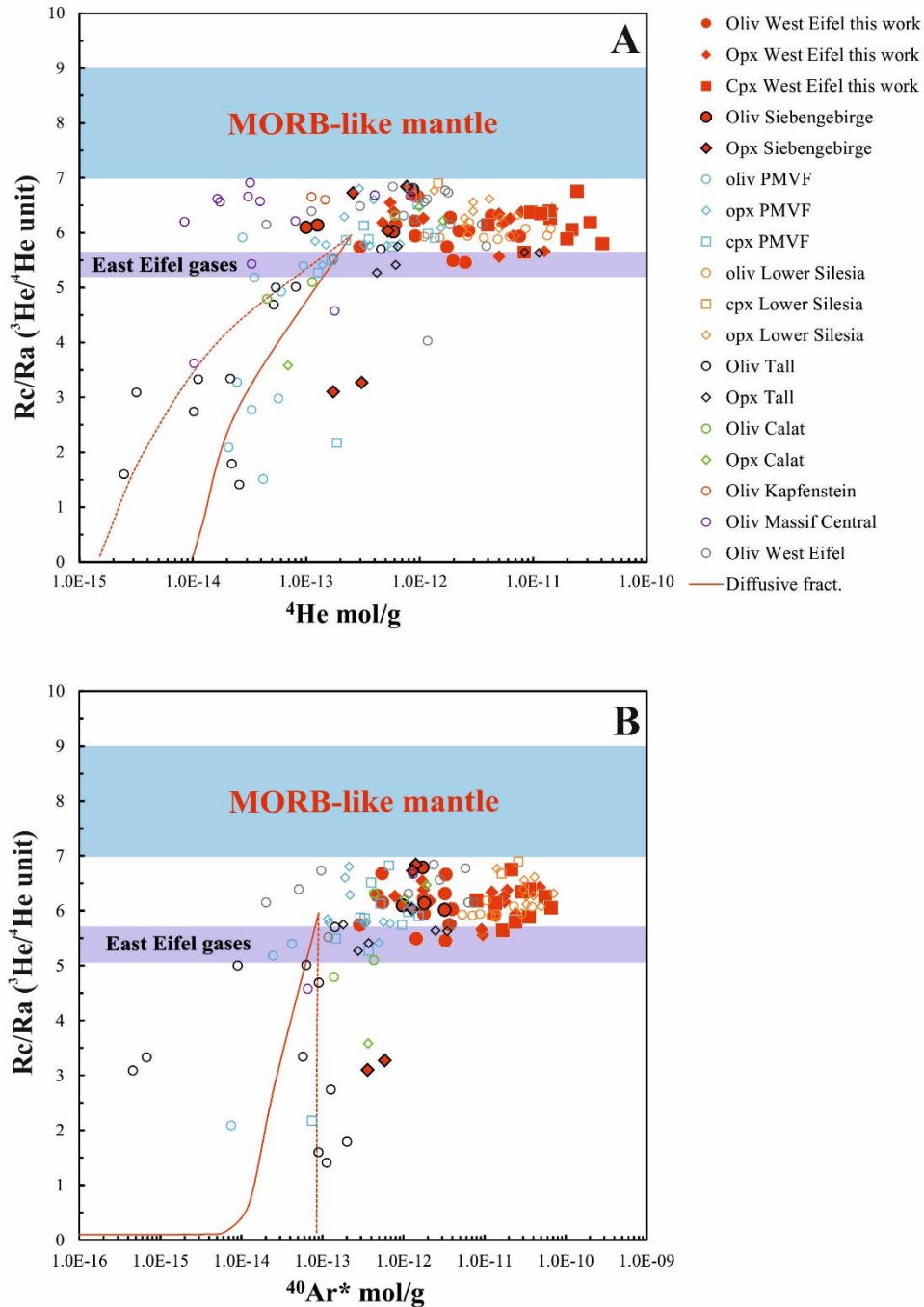
Figure 44. Concentrations of a) ^{4}He and b) ^{40}Ar* versus ^{3}He/^{4}He corrected for air contamination (Rc/Ra values). The blue bar indicates the range of ^{3}He/^{4}He ratios for a MORB-like mantle (8±1 Ra; Graham, 2002). The violet bar indicates the range of ^{3}He/^{4}He ratios measured in East Eifel surface gases (Giggenbach et al., 1991; Griesshaber et al., 1992; Aeschbach-Hertig et al., 1996; Bräuer et al., 2005, 2013). Available data from other European mantle xenoliths localities are also reported for comparison (French Massif Central, Eifel, and Kapfenstein from Gautheron et al., 2005; Calatrava and Tallante from Martelli et al., 2011; Lower Silesia from Rizzo et al., 2018; Persani Mts from Faccini et al., 2019). The two diffusive fractionation paths are modeled based on the approach of Burnard et al. (1998), Burnard (2004) and Yamamoto et al. (2009), taking into account the diffusion coefficient (D) of ^{3}He, ^{4}He, and ^{40}Ar* (D_{3He}/D_{4He} = 1.15 and

D_{4He}/D_{40Ar} = 3.16 in solid mantle; Trull and Kurz, 1993; Burnard, 2004; Yamamoto et al., 2009). Starting and final conditions as well as further details on modelling can be found in Faccini et al. (2019).
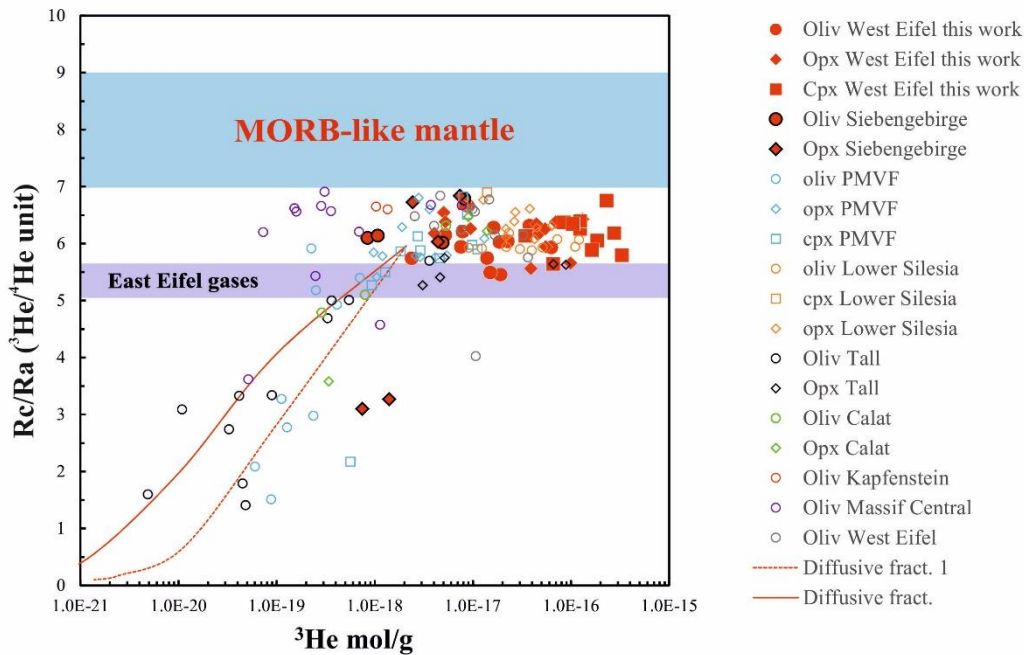
Figure 45. Concentrations of ^{3}He versus ^{3}He/^{4}He corrected for air contamination (Rc/Ra values). Available data from other European mantle xenoliths localities are also reported for comparison (French Massif Central, Eifel, and Kapfenstein from Gautheron et al., 2005; Calatrava and Tallante from Martelli et al., 2011; Lower Silesia from Rizzo et al., 2018; Persani Mts from Faccini et al., 2019). The blue and violet bars as well as the two diffusive fractionation paths are as in Fig. 44.

5.3 Discussion

5.3.1 Processes that could modify the geochemistry of FI

5.3.1.1 Atmospheric contamination

The isotopic compositions of Ne (^{20}Ne/^{22}Ne and ^{21}Ne/^{22}Ne), Ar (^{40}Ar/^{36}Ar), and ^{4}He/^{20}Ne in FI from Eifel and Siebengebirge xenoliths show variable extent of atmosphere-derived contamination, with Cpx and Opx poorly contaminated respect to Ol (Table 5.6). The extent of this contamination seems proportional to the concentration of gas species in FI, therefore it results that xenoliths from Siebengebirge are more contaminated respect to those from West Eifel. This is evident in the three Ne isotopes plot (Fig. 46), in which our data fall along the theoretical air-MORB mixing line defined by Sarda et al. (1988) and Moreira et al. (1998) at ^{21}Ne/^{22}Ne = 0.06 and ^{20}Ne/^{22}Ne = 12.5. Argon isotopes coupled to He isotopes give a similar indication, as it can be observed in Fig. 47 where xenoliths from West Eifel fall along the theoretical air-MORB mixing line defined by Moreira et al. (1998) and Ballentine et al. (2005) at ^{40}Ar/^{36}Ar up to 44,000 and ^{3}He/^{36}Ar~0.45. Similar indications were found by Gautheron et al. (2005) for Ne and Ar isotopes in Ol from West Eifel mantle xenoliths.

If we compare xenoliths from Eifel and Siebengebirge with those from other European localities that were analyzed by single-step crushing and for which $^{40}Ar/^{36}Ar$ data are available, we notice that some Cpx and Opx from West Eifel show the lowest atmosphere-derived contamination, irrespective of the concentration of gas species in FI. It is worth noting that $^{40}Ar/^{36}Ar$ values as high as 9,797 were never been measured in mantle xenoliths from Europe and, at the best of our knowledge, from worldwide continental areas. In fact, xenoliths from Lower Silesia are slightly more contaminated although they showed higher CO_2 and N_2* concentration, comparable ^{40}Ar* and ^{21}Ne* content but slightly lower He content than those from West Eifel (Fig. 47). Instead, xenoliths from Tallante and Calatrava (Spain, Martelli et al., 2011) as well as Persani Mts (Transylvania, Faccini et al., 2019 under revision) show the highest contamination among the studied European localities (Gautheron et al., 2005; Martelli et al., 2011; Correale et al., 2012; Rizzo et al., 2018), which tends toward $^{40}Ar/^{36}Ar$ more typical of subduction-related settings (e.g., Stromboli; Martelli et al., 2014). The contamination of FI by atmosphere-derived fluids is common in SCLM xenoliths from other worldwide localities (Valbracht et al., 1996; Matsumoto et al., 1998, 2000, 2001, 2002; Yamamoto et al., 2004; Gurenko et al., 2006; Correale et al., 2016, 2019). Although we cannot exclude that this contamination originates from post-eruptive entrapment in mineral micro-cracks (e.g., Nuccio et al., 2018) and/or during the ascent within the crust of magma bearing xenoliths (e.g., Gautheron et al., 2005), we argue that it represents a feature typical of SCLM mantle that was contaminated by the recycling of atmosphere-derived fluids due to active or fossil subductions (Matsumoto et al., 1998, 2000, 2001; Yamamoto et al., 2004; Sarda, 2004; Gurenko et al., 2006; Rizzo et al., 2018; Faccini et al., 2020). In addition to this recycling into the SCLM, we infer that the occurrence and superimposition to partial melting of metasomatic and refertilization processes play an additional role in defining the extent of atmosphere-derived contamination.
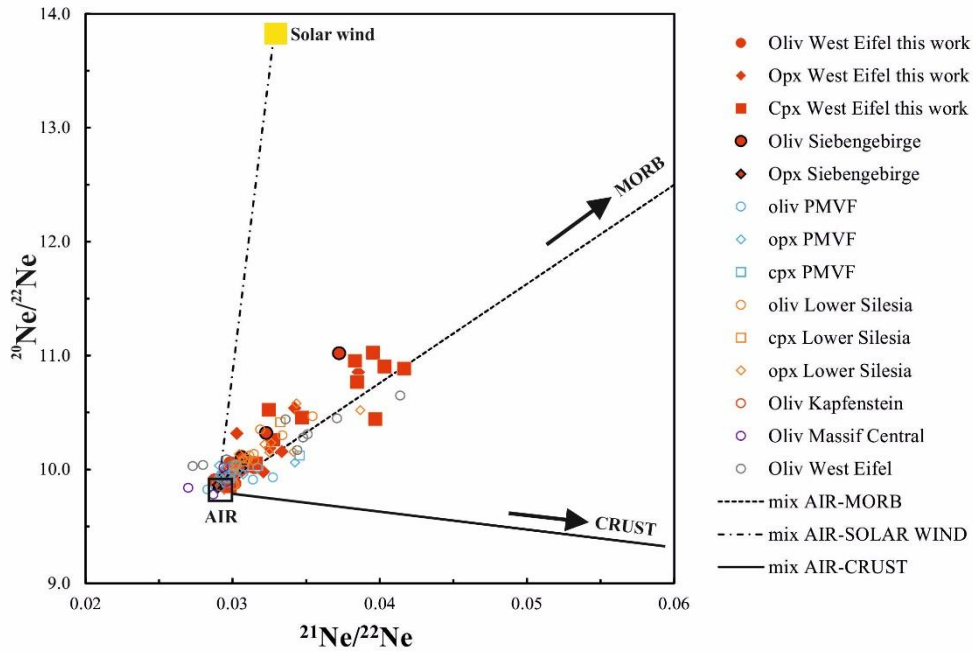
Figure 46. Diagram of $^{21}Ne/^{22}Ne$ versus $^{20}Ne/^{22}Ne$ measured in fluid inclusions of Eifel and Siebengebirge xenoliths. The black dashed and dotted lines represent binary mixing between air ($^{21}Ne/^{22}Ne = 0.0290$ and $^{20}Ne/^{22}Ne = 9.8$) and i) MORB mantle as defined by Sarda et al. (1988) and Moreira et al. (1998) at $^{21}Ne/^{22}Ne = 0.06$ and $^{20}Ne/^{22}Ne = 12.5$; ii) CRUST as defined by Ballentine (1997) and references therein at $^{21}Ne/^{22}Ne = 0.6145$ (mean of 0.469-0.76) and $^{20}Ne/^{22}Ne = 0.3$; iii) Solar Wind as defined by Heber et al. (2009) at $^{21}Ne/^{22}Ne = 0.0328$ and $^{20}Ne/^{22}Ne = 13.8$. Available data from other European mantle xenoliths localities are also reported for comparison (French Massif Central, Eifel, and Kapfenstein from Gautheron et al., 2005; Calatrava and Tallante from Martelli et al., 2011; Lower Silesia from Rizzo et al., 2018; Persani Mts from Faccini et al., 2019).
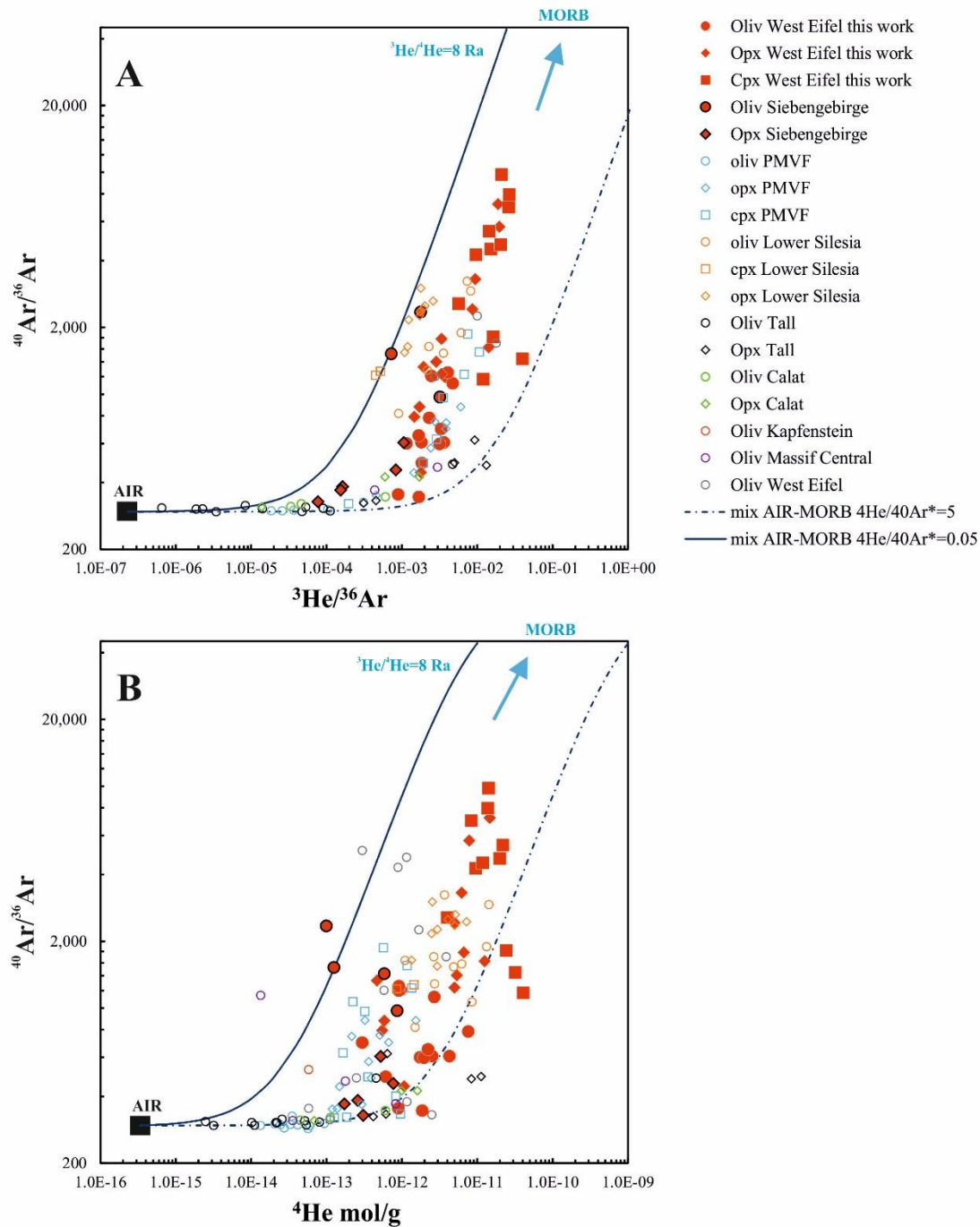
Figure 47. a) ^{3}He/^{36}Ar and b) ^{4}He (mol/g) versus ^{40}Ar/^{36}Ar. The continuous and dashed turquoise lines represent binary mixing between air [^{40}Ar/^{36}Ar = 295.5, ^{3}He/^{36}Ar = 2.3×10^{-7} and ^{4}He = 1.1×10^{-16} (arbitrarily fixed to fit data); Ozima and Podosek, 2002] and MORB mantle as defined by Moreira et al. (1998), and Ballentine et al. (2005) at ^{40}Ar/^{36}Ar = 44,000, ^{3}He/^{36}Ar = 2.45 and 0.0245 and ^{4}He = 1.0×10^{-9} (arbitrarily fixed to fit data), considering ^{3}He/^{4}He = 8, ^{4}He/^{40}Ar* = 5 and ^{4}He/^{40}Ar* = 0.05. Data from other European localities are also reported (French Massif Central, Eifel, and Kapfenstein from Gautheron et al., 2005; Calatrava and Tallante from Martelli et al., 2011; Lower Silesia from Rizzo et al., 2018; Persani Mts from Faccini et al., 2019).

5.3.1.2 Diffusive fractionation

When plotting $^3He/^4He$ versus the concentration of ^3He, ^4He, $^{40}Ar*$ (Figs. 44 and 45), we notice that Opx from xenolith SB5 show Rc/Ra values below the range of other xenoliths (3.1-3.3 Ra versus 5.5-6.8 Ra). This behaviour is similar to what observed in SCLM xenoliths from other European localities (Gautheron et al., 2005; Martelli et al., 2011; Faccini et al., 2019 under revision) and is typical of low ^3He, ^4He and $^{40}Ar*$ concentrations (Figs. 44 and 45), originating from preferential diffusive loss of ^3He, ^4He and $^{40}Ar*$ (e.g., Burnard et al., 1998; Burnard, 2004; Harrison et al., 2004; Yamamoto et al., 2009). This process depends on the diffusion coefficient (D), which is significantly higher for ^4He than for $^{40}Ar*$ (D_{4He}/D_{40Ar} = 3.16 in solid mantle; Burnard, 2004; Yamamoto et al., 2009). In case of diffusive loss of helium, we also expect to see $^3He/^4He$ fractionation due to the appreciable difference in D_{3He} and D_{4He} among mantle minerals (D_{3He}/D_{4He} = 1.15; Trull and Kurz, 1993; Burnard, 2004; Yamamoto et al., 2009 and references therein). Faccini et al. (2019) modeled data from Persani Mts (Transylvania) through two possible paths of diffusive fractionation of ^4He, $^{40}Ar*$, $^3He/^4He$, and $^4He/^{40}Ar*$ during mantle melting, based on the approach of Burnard et al. (1998), Burnard (2004) and Yamamoto et al. (2009). These paths are here reported to show that this process with assumed identical boundary conditions is valid also for the mantle beneath Siebengebirge (Figs. 44, 45 and 48). Further details on the modelling and adopted boundary conditions can be found in Faccini et al. (2019). Therefore, in the following discussion we exclude data of Opx from xenolith SB5 because modified by diffusive fractionation.
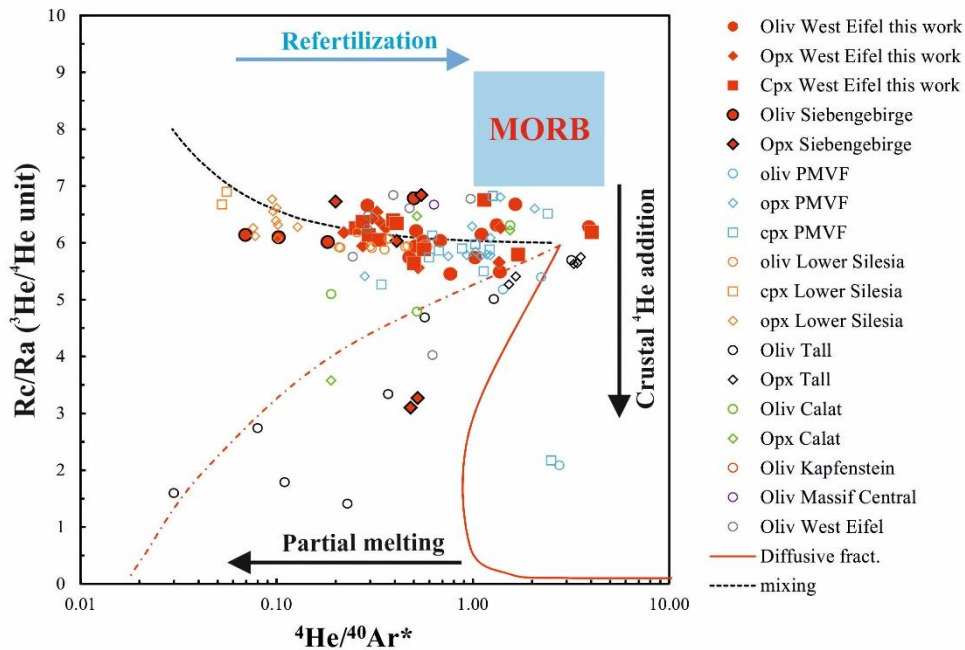
Figure 48. $^4He/^{40}Ar*$ versus $^3He/^4He$ corrected for air contamination (Rc/Ra values). The blue rectangle indicates the MORB-like ranges of $^3He/^4He$ (8±1 Ra; Graham, 2002) and $^4He/^{40}Ar*$ (1–5; Marty, 2012). Available data from other European mantle xenoliths localities are also reported for comparison (French Massif Central, Eifel, and Kapfenstein

from Gautheron et al., 2005; Calatrava and Tallante from Martelli et al., 2011; Lower Silesia from Rizzo et al., 2018; Persani Mts from Faccini et al., 2019). The black dotted line represents binary mixing between two endmembers: (1) the residual mantle (blue rectangle) having $^4He/^{40}Ar^* = 2.5$, and $^3He/^4He = 6$ Ra, and (2) a metasomatic agent having $^4He/^{40}Ar^* = 1.7 \times 10^{-2}$, and $^3He/^4He = 8$ Ra. The two diffusive fractionation paths are modeled as explained in Fig. 44 caption.

5.3.2 Partial melting of the mantle

5.3.1.1 Indications from mineral chemistry

The modal compositions and mineral chemistry of West Eifel and Siebengebirge mantle xenoliths is compared to the melting model proposed by Niu et al. (1997), Bènard et al. (2018), and Bonadiman and Coltorti (2018), in order to understand the melting history of the sampled lithospheric section. For this purpose, we exclude xenoliths showing cumulitic features.

Looking at the modal composition (Fig. 38), part of the samples align with the depletion model paths at 2 and 1 GPa by Niu et al. (1997), although a tendency towards lower modal olivine and higher opx can be seen especially in two xenoliths from Eulenberg. Instead, other xenoliths especially from West Eifel are better fitted by the hydrous melting paths at 1 GPa and 0.1 (red), 0.5 (light blue) and 1 (green) % of H_2O (Fig. 38).

The mineral chemistry gives further indications on the partial melting extent as well as on the occurrence of metasomatic processes. We consider the model proposed by Bonadiman and Coltorti (2018) to infer the partial melting degree of a mantle lithotype based on major element composition of opx, cpx and spinel, in which PM modal composition is assumed from Johnson et al. (1990). In the plot of Mg# vs Al_2O_3 in cpx, most of the xenoliths from West Eifel and in part of Siebengebirge do not fit the path of modeling by Bonadiman and Coltorti (2018) because they have less FeO with respect to the expected Al_2O_3 content, this latter being even higher with respect to the corresponding MgO predicted by the model. This implies that the extremely Al_2O_3-rich compositions of West Eifel cpx cannot be explained by partial melting alone and a metasomatism by Al_2O_3-rich melt should be considered. Instead, the same modeling applied to opx better matches most of xenoliths from the two areas, especially those from Siebengebirge volcanic field. In detail, xenoliths from West Eifel show partial melting extents moving from low degrees (<5-10%) in a few samples from Dreis-Bruck to ~20% in opx from Meerfelder Maar, except for a few xenoliths from Gees that reach ~25%, although they all show higher Al_2O_3 than expected from modeling (Fig. 41). Xenoliths from Siebengebirge volcanic field show partial melting extents from ~15% up to more than 25% in some samples from Siebengebirge quarry. It is worth noting that most of the xenoliths from Siebengebirge volcanic field fall along the modeling path.

Similar indications arise from OSMA diagram (Fig. 42) in which xenoliths from Siebengebirge quarry reach melting degrees up to 30%, according to the partial melting line from Amhed et al. (2016).

5.3.1.2 Indications from noble gas in fluid inclusions

The evidences from petrography and mineral chemistry show that West Eifel and Siebengebirge experienced complex and distinct partial melting histories, which seem partially masked by the more recent superimposition of metasomatic and/or refertilization processes as observed in West Eifel. In particular, xenoliths from Siebengebirge indicate that the mantle beneath this area experienced higher degree of melt extraction (~15-30%) respect to West Eifel (~0-25%) (Figs. 38, 41 and 42), with minor metasomatic process.

Concerning the chemistry of FI, in the case of partial melting as unique process marking their composition, during melts extraction we should expect a progressive depletion of noble gas content in FI of the residual mantle. This reasoning assumes equal number density of fluid inclusions in all the samples, so we think that every consideration must be limited at least within each mineral phase (e.g., olivine). This is due to the noble gas incompatibility with the mineral phase, as suggested by the crystal-melt partition coefficient indicated by Heber et al. (2007). As already evidenced by Rizzo et al. (2018), caution must be paid when modelling and estimating absolute degrees of partial melting by using data from FI, because the modelling is based on crystal-melt coefficients that presuppose the partition of noble gas in the crystal lattice rather than in FI. However, Rizzo et al. (2018) noticed that in case of equilibrium between FI and crystal lattice, the variation of noble gas concentrations and ratios (e.g., ^{4}He/^{40}Ar*) in FI follows the expected path based on crystal-melt partition coefficients while the estimated absolute percentage of partial melting remains unrealistic. This is more evident in Ol than in Opx and Cpx that often recrystallize in consequence of metasomatic and/or refertilization processes, as also highlighted by Rizzo et al. (2018) and Faccini et al. (2019).

If we consider that Ol with Mg#>88 are representative of the residual mantle, we must exclude from this discussion xenoliths MM1, GE1, DBR2 that show cumulates features (see Sections 5.2.1 and 5.2.2). Effectively, these samples have ^{4}He/^{40}Ar* in the range 0.5-4.0 that are more typical of magmatic values and fertile mantle (^{4}He/^{40}Ar*=1-5; Marty, 2012) (Figs. 48 and 49A). The concentrations of noble gas and CO_2 in FI of Ol from the other xenoliths do not show appreciable differences between West Eifel and Siebengebirge (Figs. 43 and 50), with the exception of He concentration that is slightly higher in West Eifel. Instead, FI in Opx and Cpx from West Eifel xenoliths are richer in volatiles than in those from Siebengebirge (only Opx are available), further suggesting the superimposition of other processes that reasonably masked the original composition

of the residual mantle beneath West Eifel and only involved this portion of Eifel (see Section 5.3.1.1) (Figs. 43 and 50). Focusing on $^4He/^{40}Ar^*$ of Ol, we highlight that xenoliths from Siebengebirge show $^4He/^{40}Ar^*$ in the range 0.50-0.07 that is much lower than in Ol from West Eifel (1.65-0.29) (Figs. 48 and 49A). This strongly points on a higher degree of melt extraction in the mantle beneath Siebengebirge (up to at least 30%), while West Eifel shows more fertile features. This interpretation is further supported by the comparison with $^4He/^{40}Ar^*$ measured in Ol from Lower Silesia mantle xenoliths that varied in the range 0.46-0.20 (Figs. 48 and 49A), whereas Matusiak-Malek et al. (2017) and Rizzo et al. (2018) based on mineral chemistry estimated up to 25-30% of melting from the protolith that left a harzburgitic residuum. This strenghtens our interpretation that the mantle beneath Siebengebirge is depleted after comparable or even higher extents of melting.

5.3.3 Mantle metasomatism and refertilization inferred from mineral chemistry and volatiles in fluid inclusions

As highlighted by Mg# vs Al_2O_3 contents in cpx, most of the xenoliths from West Eifel, especially those from Meerfelder Maar and Gees, fall out the modeling path by Bonadiman and Coltorti (2018) showing higher Al_2O_3 contents than expected (Fig. 40).

To explain this Al_2O_3-enrichment, it can be hypothesized that Al_2O_3 has been added to the system after partial melting. It is reasonable to suppose that West Eifel xenoliths are residua of partial melting degrees comparable to those of the mantle beneath Siebengebirge volcanic field (up to 25-30%) that was later affected by Al_2O_3 enrichment by metasomatizing silicate melt. The event would have also increased the modal percentage of opx, which explains why some West Eifel xenoliths have a paragenesis moving toward ol-websterites, with modal opx contents higher than that of fertile mantle (25%, Johnson et al., 1990). It is likely that cpx were newly formed, growing over strongly depleted opx in an originally harzburgitic matrix (which buffered the mg#) from an Al_2O_3-rich melt. Alternatively, cpx could have been generated by exsolution from opx and successively texturally re-organized and enriched by an Al_2O_3-rich metasomatizing melt.

In this framework, the metasomatic process that affected the mantle beneath the West Eifel can be more properly considered as a refertilization that not only modified the composition of the various phases, but also consistently increased the pyroxene modal abundance. This evidence is further supported by the enrichment trends shows in REE diagrams especially in pyroxene from Meerfelder Maar and Gees (Fig. 51) as well as by the geochemistry of noble gas in FI. Concurrently, a later interaction with an alkaline metasomatic agent similar to the host basalts could have caused the LREE enrichment in some pyroxenes and disseminated amphiboles and precipitation of vein amphiboles, as observed in Meerfelder Maar xenoliths.

The volatile content in FI supports the evidences from the petrography and mineral chemistry, that the composition of Cpx and (at least partially) of Opx of most of the studied xenoliths from West Eifel is no longer representative of the partial melting history and was modified by the superimposition of metasomatic and/or refertilization processes that caused the recrystallization of these mineral phases and reasonably the entrapment of a new population of FI. Therefore, these FI should resemble the chemical and isotopic composition of fluids dissolved in the involved melts. Effectively, most of the cpx and opx from West Eifel show a volatile content (CO_2, N_2*, noble gas) sensibly higher than in the xenoliths from Siebengebirge volcanic field, which are more compatible with partial melting effect. If compared to the Mg#, the volatile content Eifel does not show the path of variation expected in case of partial melting (decreasing values at increasing Mg#), while show small variations in terms of concentrations and absolute values comparable to xenoliths showing fertile mantle features (Fig. 50). The $^4He/^{40}Ar$* ratios show values up to 1.4, within the reported range for fertile mantle, that are not compatible with the corresponding Mg# values. This further supports the hypothesis of a mantle refertilization event that post-dated partial melting and Siebengebirge magmatism. When also considering the $^3He/^4He$ (Rc/Ra) vs Mg#, we argue that a late metasomatic event by asthenosphere-derived alkaline melts could have occurred in the mantle beneath West Eifel, due to $^3He/^4He$ as high as 6.8 Ra close to the lower limit of MORB range (Fig. 49B).
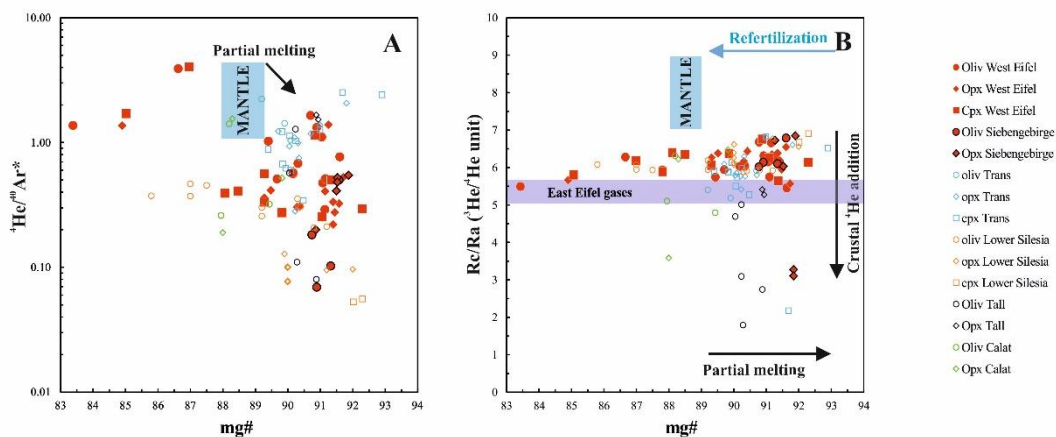
Figure 49. Mg# vs A) $^4He/^{40}Ar$*, and B) $^3He/^4He$ corrected for air contamination (Rc/Ra values). MORB range is reported for $^4He/^{40}Ar$* and $^3He/^4He$ as in Fig. 48 caption. The expected trend lines for partial melting or refertilization processes are reported. The vertical dotted line indicates the Mg# of fertile mantle. Below this values, xenoliths show cumulate features. Above this value, mantle xenoliths are progressively depleted due to partial melting. The violet bar in plot B) indicates the range of $^3He/^4He$ ratios measured in East Eifel surface gases (Giggenbach et al., 1991; Griesshaber et al., 1992; Aeschbach-Hertig et al., 1996; Bräuer et al., 2005, 2013).
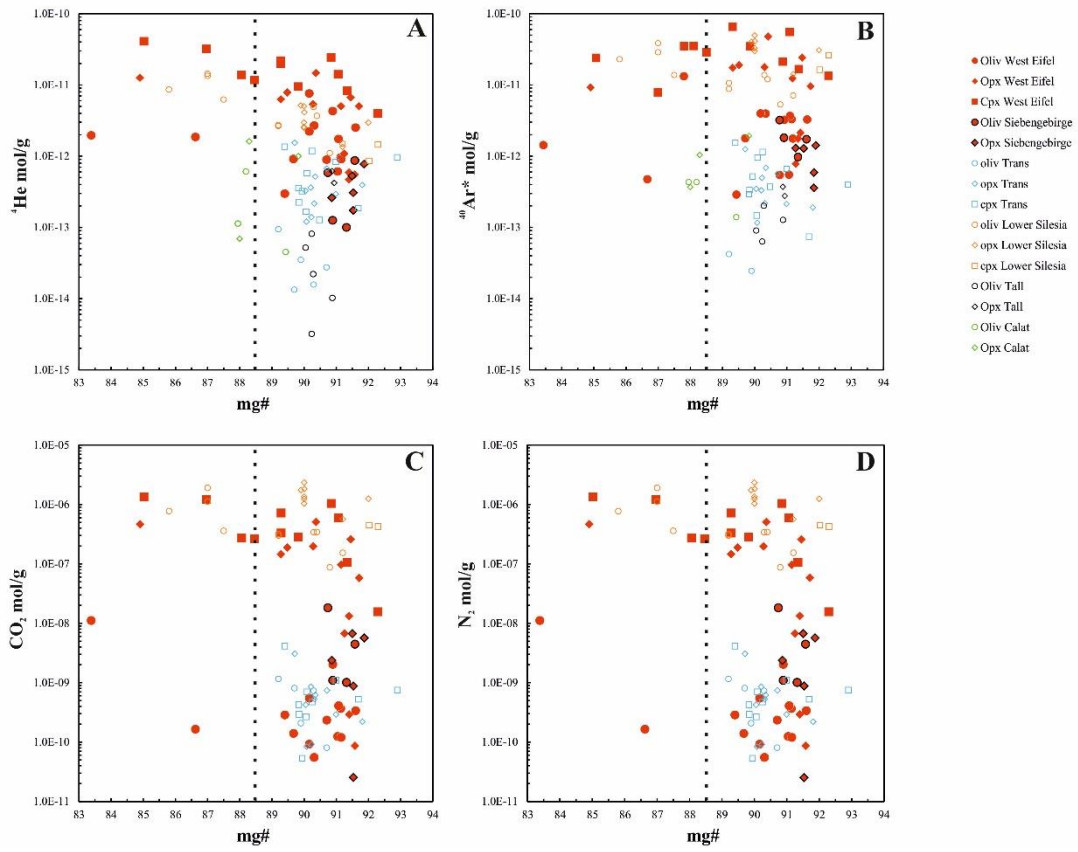
Figure 50. Mg# vs concentration in mol/g of A) ^{4}He, B) ^{40}Ar*, C) CO_2, and D) N_2*. The vertical dotted line indicates the Mg# of fertile mantle. Below this values, xenoliths show cumulate features. Above this value, mantle xenoliths are progressively depleted due to partial melting.

WEST EIFEL　　　SIEBENGEBIRGE
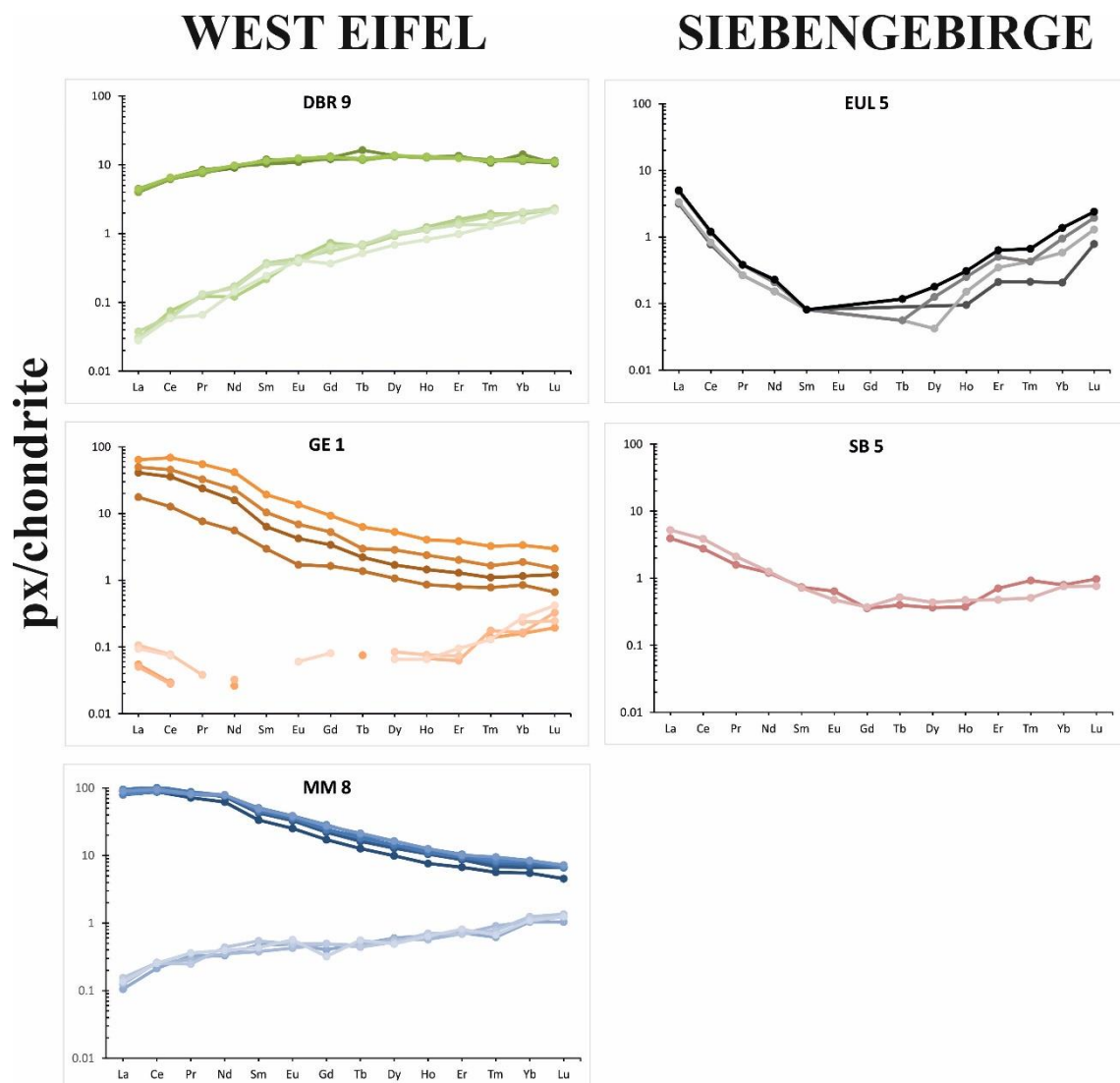
Figure 51. Chondrite normalized REE patterns of cpx (top lines in each plot) and opx (bottom lines in each plot) in West Eifel and Siebengebirge mantle xenoliths, representative of each of the studied locations.

5.3.4 Inferences about the mantle features beneath the West Eifel and Siebengebirge

5.3.4.1 Origin of the noble gas isotopic signature

With the aim of make inferences on the noble gas isotopic signature of the mantle beneath Eifel, we compare the results of the present work with those from previous studies on mantle xenoliths from the same area and from other European areas, in which FI where extracted with the same technique (in-vacuo crushing).

In terms of helium isotopes, we recall that Ol, Opx, and Cpx from West Eifel show ^{3}He/^{4}He of 5.5-6.7 Ra while those from Siebengebirge show 6.0-6.8 Ra. This range of values is comparable to that found by Gautheron et al. (2005) in Ol only from West Eifel (5.5-6.7 Ra) (Figs. 44 and 45). More in general, the ^{3}He/^{4}He signature of the mantle beneath Eifel and Siebengebirge is comparable with that

of other European localities (French Massif Central, Kapfenstein, Tallante and Calatrava, Lower Silesia, and Persani Mts.) that varies in the range 5.5-6.9 Ra (Gautheron et al., 2005; Martelli et al., 2011; Rizzo et al., 2018; Faccini et al., 2019). Considering that the magmatism of Siebengebirge is dated at ~30-6 Ma, we argue that the $^{3}He/^{4}He$ signature measured in Quaternary Eifel xenoliths can be extended backward in time without any significant variation. As proposed by Gautheron et al. (2005), the European $^{3}He/^{4}He$ signature could mostly result from 1) addition into the lithosphere of ^{4}He-rich fluids/melts derived from U-Th decay of crustal material from dehydration of subducting slabs, 2) a mixing between MORB-like astenospheric fluids and more radiogenic fluids circulating in the lithosphere in a steady state condition that could be balanced by either local or global metasomatism. Arguments in support of the second hypothesis relate to the homogeneous $^{3}He/^{4}He$ signature found by Gautheron and Moreira (2002) in other worldwide portions of SCLM that include Antarctic. However, more recent studies on mantle xenoliths from other European localities (Rizzo et al., 2018; Faccini et al., 2019) and West Antarctic Rift System (Correale et al., 2019 and references therein) that integrate the study of noble gas in FI with the petrography and mineral chemistry of the rocks highlight that the $^{3}He/^{4}He$ signature of SCLM of non-cratonic areas is wider than thought and local heterogeneities must be considered in response to the geodynamics. We think it is more reasonable to hypothesize that the steady state model proposed by Gautheron et al. (2005) involves the circulation of ^{4}He-rich fluids/melts derived from U-Th decay of crustal material from dehydration of subducting slabs rather than a simple U-Th radioactivity in the lithosphere. In fact, it appears not unrelated that the lowest $^{3}He/^{4}He$ values in Europe are found in Persani Mts. (Transylvania; 5.8±0.2 Ra) and Tallante (Spain; 5.6±0.1 Ra) where recent subduction has occurred (Martelli et al., 2011; Faccini et al., 2019) (Figs. 44 and 45). Instead, the highest $^{3}He/^{4}He$ values generally are found in metasomatized Cpx and Opx, reflecting the composition of MORB-like astenospheric fluids (Rizzo et al., 2018; Faccini et al., 2019; present work) (Fig. 49B).

Regarding the origin of neon and argon, as discussed in Section 5.3.1.1 $^{20}Ne/^{22}Ne$ and $^{21}Ne/^{22}Ne$ as well as $^{40}Ar/^{36}Ar$ and $^{3}He/^{36}Ar$ reflect a contamination by atmosphere-derived fluids (Figs. 46 and 47). In fact, data from Eifel and Siebengebirge fall along the theoretical air-MORB mixing line defined for neon by Sarda et al. (1988) and Moreira et al. (1998) ($^{21}Ne/^{22}Ne = 0.06$ and $^{20}Ne/^{22}Ne = 12.5$) and for argon by Moreira et al. (1998) and Ballentine et al. (2005) ($^{40}Ar/^{36}Ar$ up to 44,000 and $^{3}He/^{36}Ar$~0.45) (Figs. 46 and 47). Similar indications were found by Gautheron et al. (2005) in other mantle xenoliths from Eifel and other European localities, although these authors inferred that the $^{3}He/^{36}Ar$ variability they found in Ol could be due to preferential loss of helium from the FI to the matrix of the mineral grains. We disagree with this interpretation, while we argue that the $^{3}He/^{36}Ar$ variability observed at constant $^{40}Ar/^{36}Ar$ depends on the distinct $^{4}He/^{40}Ar*$ and $^{3}He/^{4}He$

that characterized each xenolith and mineral phase. Our inference is based on the fact that we integrate the evidences from mineral chemistry with those from FI in Ol, Opx and Cpx in the same xenoliths, as well as similar considerations are made in other recent studies in European localities (Rizzo et al., 2018; Faccini et al., 2019). Moreover, a preferential loss of helium should induce an isotopic fractionation with a decrease of ^{3}He/^{4}He that we do not observe (see also Section 5.3.2.1 and Faccini et al., 2019). This implies that the original Ne and Ar isotopic signature of the mantle beneath Eifel and Siebengebirge can be considered as MORB-like.

5.3.4.2 Implications for the source of magmatism

The origin of Eifel and Siebengebirge as well as, more in general, of CEVP is currently a matter of debate. Most of the proposed models suggest the presence of single or multiple plumes under this portion of Europe, as well as the upwelling and melting of the lithospheric mantle. In detail, the presence of a mantle plume beneath the Rhenish Massif was originally inferred by analogy with the French Massif Central, where tomographic investigations indicated the presence of a low-velocity anomaly from 50-60 km down to 410-660 km depth (Granet et al., 1995; Sobolev et al., 1997; Ritter et al., 2001; Wilson and Patterson, 2001; Ritter, 2007 and references therein). A few geochemical studies of noble gases in mantle xenoliths or in surface gases from Eifel support the hypothesis of a plume beneath this area (Buikin et al., 2005; Trieloff and Altherr, 2007; Caracausi et al., 2016). However, more detailed geophysical and geodynamic observations as well as geochemical and petrological studies exclude the hypothesis of a mantle plume, while proponents of alternative models invoking passive upwelling of the asthenosphere or crustal extension and melting of the lithospheric mantle (Lustrino and Carminati, 2007 and references therein).

In fact, our evidences from noble gas isotopic systematics preclude the presence of a plume below the Eifel and Siebengebirge. This is because a plume-related signature should have ^{3}He/^{4}He values above the MORB range (>9 Ra), a lower ^{21}Ne/^{22}Ne ratio for a given ^{20}Ne/^{22}Ne than MORB melts, and ^{40}Ar/^{36}Ar of 5,000-10,000 (Allègre et al., 1987; Kurz et al., 2009; Mukhopadhyay, 2012; Moreira, 2013; Colin et al., 2015) (Figs. 44, 45, 46 and 47). Instead, the ranges of He, Ne, and Ar isotopic ratios measured in our mantle xenoliths are similar to those found in Ol from mantle xenoliths and in surface gases from Eifel as well as in other European regions where no plume was inferred, and compatible with a mixing between crustal- (for He isotopes) or atmosphere-derived (for Ne and Ar isotopes) and MORB-like fluids (Gautheron et al., 2005; Bräuer et al., 2013; Moreira et al., 2018; Rizzo et al., 2018; Bekaert et al., 2019; Faccini et al., 2019). Therefore, for the origin of European Cenozoic volcanism we argue that other models should be preferred (e.g., crustal extension and

melting of the lithospheric mantle, passive asthenosphere upwelling driven by decompression), as suggested by e.g. Lustrino and Carminati (2007 and references therein).

5.3.4.3 Comparison with gases emitted in the volcanic area of Eifel

The last volcanic activity at Eifel is dated at about 11 ka in the West Eifel (Zolitschka et al., 1995). However, since the volcanic activity alternated with long non-eruptive phases, this volcanism is considered dormant but not extinct (Schmincke, 2007). Effectively, the volcanic area is characterized by the occurrence of many CO_2-rich mineral springs and mofettes with significant contributions of mantle-derived helium that pointed to the existence of still active magmatic reservoir beneath the Eifel area (e.g., Giggenbach et al., 1991; Griesshaber et al., 1992; Aeschbach-Hertig et al., 1996; Bräuer et al., 2005, 2013; Bekaert et al., 2019). Most of these gas emissions and especially those showing the highest $^3He/^4He$ signature are nearly pure CO_2 and occur in the East Eifel, in an area of ~10 km^2 that is bordered by the Rieden, Wehr and Laacher See calderas (Giggenbach et al., 1991; Griesshaber et al., 1992; Aeschbach-Hertig et al., 1996; Bräuer et al., 2005, 2013). The highest $^3He/^4He$ are found in Wehr gases with ratios up to 5.7 Ra (Griesshaber et al., 1992; Bräuer et al., 2013), Ne-Ar isotopic ratios close to atmospheric values (i.e., $^{20}Ne/^{22}Ne$=9.7-10.1, $^{21}Ne/^{22}Ne$=0.027-0.030, and $^{40}Ar/^{36}Ar$=307-565), and $^4He/^{40}Ar*$ of 0.4-1.5 (Bräuer et al., 2013). However, the most famous and studied gas emissions are those from Laacher See, which is the result of the youngest volcanic eruption in the East Eifel about 12.9 Ka ago (van den Bogaard, 1995). Laacher See gases are discharged along the eastern shore and from the bottom of the maar lake (Giggenbach et al., 1991; Aeschbach-Hertig et al., 1996). The chemistry of these emissions is made of nearly pure CO_2, as in Wehr gases, with Ne-Ar isotopic ratios close to atmospheric values (i.e., $^{20}Ne/^{22}Ne$=9.7-10.0, $^{21}Ne/^{22}Ne$=0.027-0.030, and $^{40}Ar/^{36}Ar$=314-391), $^4He/^{40}Ar*$ of 1.1-3.0 and $^3He/^4He$ in the narrow range of 5.1-5.6 Ra that is almost constant since 1988 indicating a reduced magmatic activity (Giggenbach et al., 1991; Griesshaber et al., 1992; Aeschbach-Hertig et al., 1996; Bräuer et al., 2005, 2013). Bräuer et al., (2011, 2013) argue that this behaviour is in contrast with that of gases emitted from Bublák mofette (Cheb Basin) in the NW Bohemian Rift, where $^3He/^4He$ values are higher than in Eifel (up to 6.3 Ra) and varied significantly in the last decades in response to an inferred magmatic activity and an observed intra-crustal seismicity. Gas emissions from West Eifel are scarcer than in East Eifel and, although are equally made of nearly pure CO_2, are characterized by low $^3He/^4He$ (2.6 Ra at well Wallenborn) as well as a low air contamination (i.e., $^{20}Ne/^{22}Ne$ up to 11.2 and $^{40}Ar/^{36}Ar$=1,060) indicating that magmatic gases are contaminated by crustal fluids (Griesshaber et al., 1992). In the south of West Eifel, but outside the main volcanic area, gases made of almost pure CO_2 are emitted from two wells (Victoriaquelle and Schwefelquelle) that show $^3He/^4He$ of 4.2-4.5

Ra, $^{20}Ne/^{22}Ne$ up to 11.2, $^{21}Ne/^{22}Ne$ up to 0.046, $^{40}Ar/^{36}Ar$ up to 8,287, and $^{4}He/^{40}Ar*$ of 0.6-1.3 (Bräuer et al., 2013; Caracausi et al., 2016; Bekaert et al., 2019). Bräuer et al. (2013) argue that the differences in the $^{3}He/^{4}He$ values between East Eifel and South Eifel areas can be explained with the existence of at least two distinct magmatic reservoirs located in the lithospheric mantle beneath the Eifel area characterized by different melt composition, different gas/melt fractions and/or different age, whereas that of South Eifel would be suffering magma ageing. The location of these two reservoir in the lithospheric mantle is based on the fact that the highest $^{3}He/^{4}He$ values measured in gases from East Eifel (5.6-5.7 Ra) are comparable to those in FI from mantle xenoliths from West Eifel (5.7-6.3 Ra) carried out by Dunai and Baur (1995), Buikin et al. (2005) and Gautheron et al. (2005).

Our study add new $^{3}He/^{4}He$ and $^{4}He/^{40}Ar*$ data in FI from mantle xenoliths outcropping from West Eifel and, for the first time, from Siebengebirge by distinguishing different mineral phases, processes, and timing as well as xenoliths with cumulate origin. These new clues allow a more detailed comparison with the isotopic signature measured in surface gases. We recall that Ol, Opx, and Cpx from West Eifel show $^{3}He/^{4}He$ of 5.5-6.7 Ra, 5.5-6.5 Ra, and 5.6-6.7 Ra, respectively, while those from Siebengebirge show 6.02-6.80 in Ol and 6.03-6.80 in Opx (it was not possible to make measurements in Cpx). We do not report $^{4}He/^{40}Ar*$ values from mantle xenoliths because it makes no sense to make a comparison with that of surface gases, considering that this ratio is modified by partial melting and metasomatic or refertilization processes. Xenoliths of cumulate origin (MM1, GE1, and DBR2) were only found in West Eifel and show $^{3}He/^{4}He$ of 5.5-6.3 Ra and $^{4}He/^{40}Ar*$ of 0.5-4.0 (Table 5.6), with a clear trend of decreasing ratios with decreasing Mg# (Fig. 48). These new evidences suggest that gases emitted from East Eifel are not perfectly representative of the $^{3}He/^{4}He$ signature of the SCLM beneath this area, which has a higher isotopic signature and is comparable to that of Eger Rift (Bräuer et al., 2011; Rizzo et al., 2018 and references therein), while probably suffer a slight contamination by crustal fluids or due to magma ageing in the reservoir from which they are degassed. Instead, the range of $^{4}He/^{40}Ar*$ measured in cumulate xenoliths (0.5-4.0), which should be indicative of the degassing pressure and extent (e.g., Boudoire et al., 2018), perfectly matches that of surface gases (0.4-3.0) supporting the idea that the latter are degassed from a magma residing at SCLM depths, as inferred by Bräuer et al. (2013).

5.4 Summary and conclusions

We present the petrography and mineral chemistry study as well as the concentration and isotope composition of noble gases and CO_2 (only concentration) in FI trapped in Ol, Opx and Cpx separated from ultramafic xenoliths hosted in West Eifel and Siebengebirge volcanic fields (Germany) that erupted between ~0.5-0.01 and ~30-6 Ma, respectively. This multidisciplinary work allowed to define the mantle features beneath this sector of the European SCLM and reconstruct its temporal evolution.

The main results can be summarized as follows:

- The xenoliths from West Eifel (Meerfelder Maar, Dreis-Bruck, Gees) are generally lherzolitic, harzburgitic and wehrlitic in composition, with the occasional modal presence of both amphibole and phlogopite. Few ol-clinopyroxenites and one ol-websterite are also present. The xenoliths from Siebengebirge (Siebengebirge quarry and Eulenberg maar) are mostly harzburgitic apparently lacking hydrous mineral phases. Texture varies from protogranular, porphyroclastic and equigranular in most of the xenoliths, to cumulitic in some samples from West Eifel only.

- Olivine in West Eifel ultramafic xenoliths are characterized by a large compositional variation (Fo=83.4-91.6 and NiO=0.16-0.42 wt%), especially between the typical mantle lithologies (harzburgites and lherzolites) and those of different origin (reaction products and/or cumulates). On the other hand, olivine in Siebingebirge xenoliths have very restitic compositions, with Fo varying from 90.5 to 91.8 and NiO moving from 0.31 to 0.43, typical of depleted mantle lithologies.

- A wide compositional range can be also find in Opx, Cpx and Spinel. Partial melting modeling in opx allows to estimate that xenoliths from West Eifel vary from <5-10% in a few samples from Dreis-Bruck to ~25% in a few xenoliths from Gees, while those from Siebengebirge volcanic field show partial melting extents from ~15% up to more than 25-30% in some samples from Siebengebirge quarry. Instead, cpx record an anomalous enrichment in Al_2O_3 as well as path of LREE enrichment, which is more evident in some xenoliths from West Eifel. This behaviour is interpreted woth the occurrence of a refertilization process and a late metasomatic process by alkaline melts.

- The chemistry of FI is dominated by CO_2, with N_2 being the second-most-abundant species, and indicates that most of the Ol from xenoliths primarily represent a residual mantle depleted after various episodes of melt extractions, while the chemistry of Opx and Cpx suggests the overprinting of at least one metasomatic and one refertilization event postdating the partial melting. These events are mostly recorded in xenoliths from West Eifel, while the mantle beneath Siebengebirge appears strongly depleted (up to 30% or even more) and less modified by metasomatic processes.

- The $^3He/^4He$ ratio corrected for air contamination (Rc/Ra values) in Ol, Opx, and Cpx from West Eifel show $^3He/^4He$ of 5.5-6.7 Ra, while those from Siebengebirge show 6.0-6.8 Ra. This range of values is comparable to that found by Gautheron et al. (2005) in Ol only from Quaternary West Eifel (5.5-6.7 Ra) and that of other European localities (French Massif Central, Kapfenstein, Tallante and Calatrava, Lower Silesia, and Persani Mts.) that varies in

the range 5.5-6.9 Ra (Gautheron et al., 2005; Martelli et al., 2011; Rizzo et al., 2018; Faccini et al., 2019). This indicates that the ^{3}He/^{4}He signature beneath Eifel can be extended backward in time and is also representative of Tertiary magmatism.

- Some xenoliths from West Eifel show cumulate features as indicated by mineral chemistry as well as by ^{3}He/^{4}He and ^{4}He/^{40}Ar* values that tend toward the range of values measured in magmatic gases emitted at the surface.

- The systematics of Ne and Ar isotopes indicate that most of the data are consistent with mixing between air and a MORB-like mantle. This evidence, together with that from the measured ^{3}He/^{4}He ratios, excludes the presence of a classical plume of the lower mantle beneath the study area and the other localities belonging to CEVP. The geochemistry of FI results from a mixing of two endmembers: (1) the residual mantle, resulting from partial melting of European SCLM characterized by the recycling of crustal- and atmosphere-derived material from dehydration of fossil or recent slabs, and (2) an asthenosphere-derived metasomatic agent, which is variably CO_2-rich, and originally characterized by MORB-like ^{3}He/^{4}He ratios.

Figure S1. A) Photo of a neck made of columnar basalts located on the eastern side of Rheine River, within the Siebengebirge volcanic area. B) In this volcanic field, most of the xenoliths are hosted within lava, sills and/or necks (Siebengebirge). C) Instead, in West Eifel mantle xenoliths are found within scoria cone and/or pyroclastic deposits and/or within maars.

Table 5.1. Major oxides composition of minerals forming Meerfelder Maar xenoliths

Sample	MM-1_1	MM-1_1	MM-1_1	MM-1_1	MM-1_2	MM-1_2	MM-1_2	MM-1_2	MM-1_2	MM-1_2	MM-1_2	MM-1_2	MM-1_1	MM-1_1	MM-1_1	MM-1_1	MM-1_1	MM-1_1	MM-1_1
Rock type	Weh	Weh	Weh	Weh	Weh	Weh	Weh	Weh	Weh	Weh	Weh	Weh	Weh	Weh	Weh	Weh	Weh	Weh	Weh
phase	ol core	ol rim	ol core	ol core	ol core	ol core	ol rim	ol core	cpx core	cpx rim	cpx core	cpx core	cpx rim	sp core	sp core	sp core	phlog core	phlog core	phlog core
SiO_2	39.55	39.55	39.71	39.78	39.81	39.52	39.83	39.57	51.20	51.10	51.22	51.04	51.54	0.07	0.08	0.06	37.67	37.62	37.59
TiO_2	0.00	0.02	0.01	0.01	0.00	0.00	0.01	0.01	0.92	0.91	0.92	0.94	0.89	2.61	2.59	2.67	4.94	4.62	4.77
Al_2O_3	0.04	0.03	0.04	0.03	0.04	0.03	0.03	0.03	4.75	4.73	4.70	4.83	4.51	23.92	24.50	24.66	16.30	16.52	16.28
FeO	12.63	12.54	12.66	12.58	12.71	12.88	12.76	13.02	4.06	4.16	4.21	3.94	3.97	25.37	24.89	24.32	5.98	5.94	5.74
MnO	0.21	0.19	0.23	0.20	0.26	0.23	0.23	0.21	0.11	0.11	0.11	0.11	0.11	0.34	0.35	0.35	0.06	0.06	0.04
MgO	46.45	46.02	46.78	46.60	46.60	46.27	46.23	46.30	15.14	15.45	15.34	15.01	15.43	14.53	14.75	14.83	19.09	19.19	19.95
CaO	0.13	0.15	0.13	0.13	0.18	0.11	0.17	0.14	20.86	20.83	20.96	20.98	21.03	0.01	0.01	0.00	0.02	0.03	0.01
Na_2O	0.02	0.02	0.01	0.02	0.00	0.02	0.01	0.01	1.21	0.99	1.08	1.26	1.21				0.25	0.30	0.68
K_2O																	9.23	9.29	8.77
Cr_2O_3	0.02	0.03	0.03	0.03	0.03	0.03	0.03	0.02	1.12	1.19	1.24	1.39	1.14	31.69	31.86	31.49	1.59	1.55	1.60
NiO	0.31	0.31	0.29	0.32	0.26	0.31	0.31	0.28	0.01	0.09	0.05	0.01	0.00	0.27	0.30	0.25			
Tot	99.37	98.85	99.88	99.70	99.87	99.40	99.60	99.58	99.40	99.58	99.83	99.51	99.83	99.07	99.58	98.88	95.14	95.15	95.44
mg#	86.76	86.73	86.82	86.84	86.73	86.49	86.59	86.37	86.92	86.88	86.66	87.16	87.38	50.51	51.37	52.08	85.05	85.20	86.10
cr#														47.05	46.59	46.14			

Sample	MM-2R	MM-2R	MM-2R	MM-2R	MM-2R	MM-2R	MM-2R	MM-2R	MM-2R	MM-2R	MM-2R	MM-2R	MM-2R	MM-2R	MM-2R	MM-2R	MM-2R	MM-2R
Rock type	Lh	Lh	Lh	Lh	Lh	Lh	Lh	Lh	Lh	Lh	Lh	Lh	Lh	Lh	Lh	Lh	Lh	Lh
phase	ol1 core	ol1 core	ol1 core	ol1 core	cpx1 rim	cpx1 core	cpx1 core	cpx1 core	cpx1 rim	cpx1 core	opx rim	opx core	sp1 core	sp1 rim	sp1 core	amph rim	amph core	amph core
SiO_2	40.26	40.63	40.51	40.55	53.00	52.93	52.82	52.96	52.42	52.60	56.10	55.57	0.03	0.03	0.05	43.19	43.38	43.54
TiO_2	0.00	0.01	0.00	0.00	0.28	0.26	0.28	0.25	0.28	0.24	0.10	0.11	0.18	0.18	0.18	1.23	1.18	1.18
Al_2O_3	0.02	0.02	0.01	0.03	4.76	4.56	4.74	4.22	5.15	4.74	3.51	3.85	39.09	39.14	38.47	14.13	14.09	14.06
FeO	8.61	8.53	8.69	8.58	2.71	2.75	2.78	2.69	2.72	2.72	5.74	5.60	13.61	13.58	13.71	3.60	3.74	3.68
MnO	0.13	0.14	0.12	0.13	0.07	0.09	0.09	0.09	0.09	0.08	0.13	0.14	0.24	0.22	0.24	0.03	0.03	0.03
MgO	49.47	49.69	49.76	50.11	16.28	16.39	16.30	16.54	15.89	15.94	33.72	33.49	18.67	18.47	18.53	17.81	17.89	17.77
CaO	0.06	0.07	0.04	0.07	20.85	20.85	20.79	20.93	20.63	20.74	0.91	0.86	0.00	0.00	0.01	10.83	11.03	10.88
Na_2O	0.00	0.01	0.00	0.00	1.19	1.22	1.21	1.14	1.33	1.23	0.07	0.07				3.29	3.21	3.26
K_2O																0.66	0.67	0.59
Cr_2O_3	0.02	0.01	0.02	0.02	0.91	0.73	0.82	0.69	1.30	1.29	0.52	0.67	27.46	27.18	28.20	2.00	1.96	2.06
NiO	0.40	0.41	0.37	0.39	0.05	0.04	0.03	0.06	0.06	0.06	0.07	0.15	0.31	0.27	0.27			
Tot	98.98	99.51	99.54	99.88	100.11	99.82	99.86	99.56	99.87	99.64	100.87	100.52	99.84	99.23	99.85	96.8087	97.2213	97.0883
mg#	91.10	91.22	91.07	91.23	91.47	91.39	91.27	91.64	91.24	91.25	91.29	91.43	70.97	70.79	70.66	89.80	89.50	89.58
cr#													32.03	31.78	32.97			

Sample	MM-3	MM-3	MM-3	MM-3	MM-3	MM-3_a	MM-3_a	MM-3	MM-3	MM-3	MM-3	MM-3	MM-3_a	MM-3_a	MM-3_a
Rock type	Lh	Lh	Lh	Lh	Lh	Lh	Lh	Lh	Lh	Lh	Lh	Lh	Lh	Lh	Lh
phase	ol1 rim	ol1 core	ol1 core	cpx1 core	cpx1 rim	cpx1 core	cpx1 core	opx rim	opx core	opx core	sp1 core	sp1 rim	amph core	amph core	amph core
SiO_2	40.76	40.66	40.55	52.06	52.10	51.97	51.42	56.10	56.12	56.18	0.06	0.03	43.36	42.99	42.98
TiO_2	0.00	0.00	0.00	0.48	0.47	0.59	0.59	0.12	0.08	0.09	0.44	0.48	2.39	2.36	2.29
Al_2O_3	0.02	0.02	0.02	4.78	4.81	4.95	5.19	3.14	2.88	3.00	34.78	34.61	13.01	13.05	13.09
FeO	9.00	8.97	8.86	2.72	2.79	2.80	2.93	5.72	5.73	5.71	14.53	14.36	3.72	3.58	3.66
MnO	0.14	0.16	0.20	0.09	0.09	0.10	0.13	0.15	0.15	0.16	0.30	0.32	0.05	0.06	0.07
MgO	49.46	49.41	49.51	16.20	16.23	16.12	15.93	33.43	33.90	33.55	17.40	17.30	17.36	17.42	17.30
CaO	0.07	0.06	0.07	20.56	20.77	20.16	20.11	0.85	0.73	0.86	0.03	0.01	10.95	10.76	11.10
Na_2O	0.00	0.00	0.02	1.21	1.26	1.34	1.31	0.09	0.07	0.07			2.87	2.86	2.92
K_2O													1.17	1.20	1.13
Cr_2O_3	0.02	0.02	0.02	1.07	1.29	1.48	1.54	0.54	0.45	0.50	30.93	30.81	2.14	2.08	2.14
NiO	0.35	0.39	0.38	0.04	0.05	0.02	0.05	0.08	0.11	0.14	0.23	0.21			
Tot	99.82	99.71	99.62	99.21	99.85	99.52	99.21	100.22	100.22	100.25	98.87	98.35	97.06	96.39	96.71
mg#	90.73	90.75	90.87	91.39	91.22	91.13	90.65	91.24	91.33	91.28	68.10	68.22	89.27	89.66	89.39
cr#											37.36	37.39			

Sample	MM-4	MM-4	MM-4	MM-4	MM-4	MM-4	MM-4	MM-4	MM-4	MM-4	MM-4	MM-4	MM-4
Rock type	Lh	Lh	Lh	Lh	Lh	Lh	Lh	Lh	Lh	Lh	Lh	Lh	Lh
phase	oll core	oll core	oll core	oll core	cpx1 rim	cpx1 core	cpx1 core	opx rim	opx core	opx core	sp1 rim	sp1 core	sp1 core
SiO_2	40.88	40.51	40.52	40.75	52.19	52.03	51.66	54.23	54.24	55.10	0.09	0.07	0.09
TiO_2	0.00	0.00	0.00	-0.01	0.13	0.08	0.07	0.04	0.05	0.02	0.11	0.11	0.10
Al_2O_3	0.04	0.04	0.04	0.05	5.17	5.22	5.19	4.54	4.49	4.48	38.75	38.61	38.02
FeO	8.61	8.56	8.71	8.55	2.95	2.97	3.02	5.32	5.41	5.43	12.49	12.58	12.70
MnO	0.14	0.12	0.13	0.13	0.10	0.10	0.12	0.14	0.13	0.13	0.23	0.24	0.25
MgO	49.35	49.58	49.43	49.41	17.06	17.09	17.11	32.35	32.45	32.62	18.53	18.51	18.35
CaO	0.11	0.11	0.12	0.12	19.58	19.43	19.56	1.29	1.33	1.32	0.02	0.00	0.01
Na_2O	0.00	0.00	0.02	0.00	1.00	0.95	0.91	0.09	0.11	0.10			
K_2O													
Cr_2O_3	0.04	0.04	0.05	0.05	1.38	1.36	1.36	0.85	0.86	0.83	27.66	27.49	27.22
NiO	0.37	0.36	0.40	0.40	0.01	0.10	0.08	0.13	0.09	0.09	0.24	0.21	0.28
Tot	99.55	99.32	99.41	99.46	99.55	99.33	99.08	98.97	99.17	100.12	98.29	97.98	97.19
mg#	91.08	91.16	91.00	91.15	91.15	91.12	91.00	91.55	91.44	91.45	72.56	72.40	72.03
cr#											32.38	32.33	32.44

Sample	MM-5	MM-5	MM-5	MM-5	MM-5	MM-5	MM-5	MM-5	MM-5	MM-5	MM-5	MM-5	MM-5	MM-5	MM-5	MM-5	MM-5	MM-5
Rock type	Hz	Hz	Hz	Hz	Hz	Hz	Hz	Hz	Hz	Hz	Hz	Hz	Hz	Hz	Hz	Hz	Hz	Hz
phase	oll rim	oll core	oll core	oll core	oll core	oll core	cpx1 core	cpx1 core	cpx1 core	opx core	opx core	opx core	sp1 rim	sp1 core	sp1 core	amph core	amph core	amph core
SiO_2	40.72	40.67	40.36	40.95	40.83	40.62	53.28	52.86	52.67	55.81	55.80	55.90	0.03	0.03	0.02	43.16	43.45	43.28
TiO_2	-0.01	-0.01	0.00	-0.01	0.00	-0.01	0.03	0.08	0.04	0.02	0.00	0.02	0.05	0.04	0.04	0.33	0.30	0.31
Al_2O_3	0.01	0.01	0.01	0.01	0.01	0.01	3.12	3.18	3.19	2.41	2.36	2.41	30.74	30.54	30.85	14.25	14.27	14.28
FeO	8.60	8.62	8.57	8.66	8.74	8.81	2.57	2.69	2.61	5.60	5.46	5.57	16.65	16.85	16.76	3.97	3.94	4.06
MnO	0.12	0.12	0.13	0.11	0.13	0.12	0.10	0.09	0.09	0.14	0.15	0.14	0.29	0.30	0.33	0.08	0.06	0.07
MgO	49.46	49.76	49.51	49.70	49.45	49.64	16.68	16.70	16.70	34.02	34.02	33.86	16.01	16.00	16.00	17.45	17.62	17.67
CaO	0.08	0.05	0.07	0.04	0.05	0.04	21.61	21.75	21.87	0.64	0.65	0.65	0.01	0.02	0.01	11.26	11.06	11.30
Na_2O	-0.01	0.00	-0.01	0.01	0.00	0.01	0.94	0.98	0.95	0.05	0.03	0.05				2.67	2.64	2.72
K_2O																1.25	1.28	1.23
Cr_2O_3	0.03	0.00	0.01	0.02	0.01	0.01	0.66	0.72	0.72	0.37	0.33	0.34	33.85	33.48	34.03	1.72	1.76	1.73
NiO	0.33	0.39	0.36	0.38	0.37	0.39	0.07	0.07	0.07	0.12	0.07	0.12	0.22	0.19	0.19			
Tot	99.33	99.62	99.02	99.86	99.59	99.63	99.06	99.12	98.92	99.18	98.88	99.06	98.09	97.71	98.48	96.22	96.47	96.73
mg#	91.11	91.14	91.15	91.09	90.98	90.94	92.05	91.72	91.93	91.55	91.74	91.55	63.15	62.86	62.98	88.67	88.85	88.56
cr#													42.49	42.37	42.53			

Sample	MM-6	MM-6	MM-6	MM-6	MM-6	MM-6	MM-6	MM-6	MM-6	MM-6	MM-6	MM-6	MM-6	MM-6	MM-6	MM-6	MM-6
Rock type	Lh	Lh	Lh	Lh	Lh	Lh	Lh	Lh	Lh	Lh	Lh	Lh	Lh	Lh	Lh	Lh	Lh
phase	ol1 core	ol1 core	ol1 core	ol1 core	cpx1 rim	cpx1 core	cpx1 rim	cpx1 core	opx core	opx rim	opx core	opx not in photo	opx core	opx not in photo	sp1 core	sp1 core	sp1 rim
SiO_2	40.58	40.67	40.66	40.74	53.57	53.60	53.42	53.63	56.41	56.43	56.60	56.26	56.70	56.46	0.04	0.05	0.03
TiO_2	0.00	0.00	0.00	0.00	0.08	0.03	0.05	0.03	0.03	0.00	0.02	0.03	0.03	0.03	0.04	0.04	0.04
Al_2O_3	0.01	0.01	0.01	0.01	3.37	3.26	3.21	3.22	2.85	2.90	2.95	2.98	3.00	2.97	43.72	43.63	43.79
FeO	8.57	8.63	8.56	8.60	2.46	2.45	2.54	2.48	5.76	5.82	5.67	5.68	5.74	5.67	13.39	13.42	13.39
MnO	0.17	0.12	0.13	0.11	0.08	0.07	0.05	0.07	0.15	0.12	0.14	0.14	0.14	0.15	0.19	0.18	0.20
MgO	49.76	49.94	49.93	49.76	16.58	16.67	16.81	16.86	34.31	34.23	34.50	34.11	34.16	34.13	19.75	19.61	19.62
CaO	0.04	0.06	0.06	0.07	22.93	22.69	22.79	22.43	0.44	0.60	0.51	0.55	0.46	0.47	0.00	0.02	0.02
Na_2O	0.00	0.00	0.00	0.00	0.71	0.73	0.72	0.74	0.04	0.05	0.05	0.03	0.03	0.02			
K_2O																	
Cr_2O_3	0.01	0.01	0.00	0.01	0.70	0.62	0.60	0.59	0.33	0.33	0.32	0.33	0.37	0.35	22.00	21.89	21.97
NiO	0.37	0.40	0.39	0.38	0.02	0.04	0.10	0.03	0.09	0.10	0.13	0.07	0.08	0.08	0.34	0.27	0.34
Tot	99.52	99.84	99.74	99.69	100.49	100.15	100.30	100.07	100.44	100.58	100.89	100.18	100.72	100.32	99.67	99.29	99.54
mg#	91.18	91.16	91.22	91.16	92.32	92.38	92.19	92.36	91.39	91.29	91.56	91.45	91.39	91.47	72.44	72.25	72.31
cr#															25.24	25.18	25.18

Sample	MM-7	MM-7	MM-7	MM-7	MM-7	MM-7	MM-7	MM-7	MM-7	MM-7	MM-7	MM-7
Rock type	Lh	Lh	Lh	Lh	Lh	Lh	Lh	Lh	Lh	Lh	Lh	Lh
phase	ol1 core	ol1 core	cpx1 core	cpx1 core	cpx1 core	opx core	opx core	opx core	opx core	sp1 core	sp1 core	sp1 core
SiO_2	40.60	40.66	52.14	52.29	52.25	55.20	55.02	55.01	54.51	0.15	0.12	0.11
TiO_2	0.00	0.00	0.12	0.13	0.14	0.07	0.04	0.07	0.05	0.15	0.13	0.13
Al_2O_3	0.04	0.04	5.35	5.37	5.40	4.61	4.61	4.60	4.60	40.79	40.95	40.77
FeO	8.18	8.15	2.94	2.84	2.93	5.16	5.24	5.28	5.36	11.55	11.54	11.28
MnO	0.15	0.11	0.09	0.10	0.11	0.14	0.13	0.13	0.15	0.20	0.22	0.21
MgO	50.17	50.20	17.17	17.30	17.24	32.89	32.69	32.68	32.88	19.79	19.83	19.67
CaO	0.13	0.14	19.64	19.66	19.74	1.36	1.36	1.31	1.32	0.01	0.02	0.01
Na_2O	0.00	0.00	0.95	0.94	0.97	0.09	0.11	0.10	0.12			
K_2O												
Cr_2O_3	0.04	0.03	1.40	1.37	1.36	0.84	0.84	0.86	0.86	26.62	26.46	26.36
NiO	0.39	0.41	0.09	0.04	0.09	0.09	0.14	0.13	0.12	0.34	0.26	0.30
Tot	99.70	99.73	99.89	100.05	100.20	100.43	100.18	100.16	99.98	99.76	99.69	98.99
mg#	91.61	91.65	91.24	91.56	91.31	91.91	91.75	91.68	91.63	75.32	75.38	75.66
cr#										30.45	30.24	30.25

Sample	MM-8_1	MM-8_1	MM-8_1	MM-8_1	MM-8_1	MM-8_1	MM-8	MM-8_1	MM-8_1	MM-8_1	MM-8	MM-8_1	MM-8_1	MM-8 sp	MM-8 sp	MM-8 sp	MM-8_1	MM-8_1	MM-8_1	MM-8
Rock type	Lh	Lh	Lh	Lh	Lh	Lh	Lh	Lh	Lh	Lh	Lh	Lh	Lh	Lh	Lh	Lh	Lh	Lh	Lh	Lh
phase	ol1 rim	ol1 not in photo	ol1 not in photo	ol1 rim	ol1 rim	ol1 core	cpx1 core	cpx1 core	cpx1 core	cpx1 core	opx core, small	opx rim	opx core	sp1 core	sp1 core	sp1 core	amph core	amph core	amph rim	phlog core, small
SiO_2	40.46	40.55	40.66	40.34	40.79	40.43	53.16	52.64	52.71	52.52	55.94	56.18	56.25	0.04	0.04	0.05	44.01	43.68	43.76	37.85
TiO_2	0.00	0.00	0.00	0.00	0.00	0.00	0.07	0.18	0.19	0.17	0.02	0.01	0.03	0.09	0.10	0.10	0.59	0.59	0.61	1.03
Al_2O_3	0.01	0.01	0.01	0.01	0.01	0.01	4.04	5.13	5.16	5.02	3.36	3.02	2.99	31.84	31.93	32.47	13.58	13.64	13.70	17.77
FeO	8.97	8.84	8.77	8.83	8.88	8.89	2.80	2.87	2.96	2.90	5.85	5.77	5.74	15.63	15.83	15.68	3.70	3.70	3.74	3.75
MnO	0.12	0.14	0.16	0.12	0.11	0.16	0.08	0.10	0.10	0.08	0.14	0.16	0.14	0.28	0.30	0.30	0.03	0.05	0.04	0.01
MgO	49.85	49.73	49.91	49.86	50.01	49.65	16.56	16.00	15.97	15.90	33.44	33.69	33.56	16.63	16.56	16.73	18.19	17.98	18.05	22.15
CaO	0.05	0.07	0.06	0.05	0.06	0.05	20.94	20.38	20.27	20.71	0.80	0.83	0.84	0.02	0.02	0.00	11.17	10.91	10.97	0.12
Na_2O	0.01	0.00	0.00	0.02	0.01	0.01	1.18	1.39	1.41	1.36	0.08	0.08	0.07				3.00	3.10	3.12	1.12
K_2O																	1.09	1.07	1.10	8.44
Cr_2O_3	0.02	0.02	0.02	0.02	0.01	0.02	0.90	1.45	1.43	1.41	0.44	0.59	0.54	34.09	34.22	33.71	2.00	2.30	2.04	1.16
NiO	0.37	0.38	0.42	0.41	0.39	0.38	0.06	0.08	0.10	0.10	0.07	0.09	0.06	0.23	0.20	0.22				
Tot	99.87	99.73	100.01	99.65	100.27	99.59	99.79	100.18	100.26	100.12	100.13	100.41	100.21	99.07	99.34	99.52	97.42	97.08	97.17	93.47
mg#	90.83	90.93	91.02	90.96	90.94	90.87	91.34	90.85	90.58	90.73	91.06	91.23	91.25	65.47	65.09	65.54	89.75	89.66	89.58	91.33
cr#														41.81	41.82	41.05				

Sample	MM-9	MM-9	MM-9	MM-9	MM-9	MM-9	MM-9	MM-9	MM-9	MM-9	MM-9	MM-9	MM-9	MM-9	MM-9	MM-9	MM-9
Rock type	Lh	Lh	Lh	Lh	Lh	Lh	Lh	Lh	Lh	Lh	Lh	Lh	Lh	Lh	Lh	Lh	Lh
phase	oll core	oll core	oll core	oll core	oll core	oll core	oll core	cpx1 core	cpx1 core	cpx1 rim	opx rim	opx core	opx core	sp1 core	sp1 core	sp1 core	sp1 rim
SiO_2	40.57	40.42	40.22	40.46	40.17	40.41	40.34	51.05	51.13	51.33	53.92	53.72	53.78	0.12	0.13	0.09	0.12
TiO_2	0.00	0.00	0.00	0.00	0.00	0.00	0.00	0.23	0.19	0.21	0.07	0.08	0.07	0.15	0.15	0.14	0.16
Al_2O_3	0.04	0.04	0.04	0.04	0.04	0.03	0.03	5.00	4.99	5.00	4.55	4.60	4.51	48.89	48.83	48.79	49.01
FeO	9.69	9.55	9.60	9.46	9.49	9.49	9.43	3.45	3.44	3.38	6.13	6.15	6.18	12.42	12.41	12.46	12.20
MnO	0.13	0.14	0.14	0.11	0.14	0.13	0.14	0.11	0.12	0.11	0.15	0.15	0.14	0.17	0.19	0.18	0.17
MgO	49.30	49.41	48.98	49.09	49.09	48.99	49.32	17.06	16.91	17.10	32.20	32.23	32.10	20.36	20.32	20.31	20.72
CaO	0.13	0.11	0.13	0.15	0.14	0.12	0.14	20.16	20.15	20.25	1.37	1.38	1.34	0.00	0.00	0.01	0.00
Na_2O	0.00	0.00	0.01	0.00	0.00	0.01	0.00	0.66	0.62	0.69	0.08	0.07	0.07				
K_2O																	
Cr_2O_3	0.01	0.03	0.02	0.03	0.03	0.03	0.03	0.96	0.97	0.98	0.66	0.66	0.66	17.27	17.13	17.20	16.98
NiO	0.38	0.37	0.39	0.38	0.39	0.38	0.40	0.06	0.06	0.05	0.13	0.08	0.13	0.36	0.32	0.36	0.33
Tot	100.25	100.06	99.53	99.71	99.49	99.59	99.84	98.75	98.57	99.11	99.28	99.13	98.98	99.91	99.62	99.71	99.85
mg#	90.07	90.22	90.09	90.24	90.22	90.20	90.31	89.81	89.74	90.01	90.35	90.34	90.24	74.50	74.47	74.38	75.17
cr#														19.16	19.05	19.13	18.86

Sample	MM-10	MM-10	MM-10	MM-10	MM-10	MM-10	MM-10	MM-10	MM-10	MM-10	MM-10	MM-10	MM-10	MM-10	MM-10
Rock type	Lh	Lh	Lh	Lh	Lh	Lh	Lh	Lh	Lh	Lh	Lh	Lh	Lh	Lh	Lh
phase	oll core	oll core	oll core	oll core	cpx1 core	cpx1 core	cpx1 core	cpx1 core	cpx1 rim	cpx1 rim	opx core	opx core	sp1 core	sp1 core	sp1 rim
SiO_2	40.96	40.66	40.64	40.59	52.99	52.81	51.14	53.40	53.52	52.86	55.84	56.21	0.03	0.06	0.06
TiO_2	0.00	0.00	0.00	0.00	0.20	0.18	0.63	0.19	0.18	0.20	0.04	0.03	0.15	0.14	0.15
Al_2O_3	0.02	0.03	0.03	0.02	4.80	4.69	6.23	4.54	4.35	4.76	3.54	3.16	38.32	38.29	38.24
FeO	9.02	8.97	9.05	9.17	2.85	2.76	2.98	2.80	2.79	2.89	5.93	5.73	13.75	13.51	13.60
MnO	0.16	0.14	0.15	0.15	0.08	0.10	0.09	0.09	0.09	0.09	0.15	0.15	0.24	0.23	0.26
MgO	49.80	49.69	49.33	49.70	16.16	16.07	16.76	16.20	16.56	16.09	33.65	33.53	18.81	18.59	18.57
CaO	0.10	0.10	0.09	0.11	20.91	20.79	19.65	21.14	20.89	20.67	0.84	0.78	0.01	0.02	0.00
Na_2O	0.01	0.00	0.01	0.01	1.31	1.31	0.91	1.26	1.19	1.32	0.09	0.08			
K_2O															
Cr_2O_3	0.02	0.03	0.03	0.02	1.38	1.29	1.98	0.97	0.74	1.29	0.66	0.51	28.37	28.59	28.30
NiO	0.38	0.34	0.35	0.38	0.04	0.03	0.05	0.03	0.03	0.05	0.16	0.12	0.25	0.24	0.28
Tot	100.48	99.97	99.68	100.14	100.72	100.03	100.40	100.62	100.34	100.22	100.91	100.30	100.11	99.81	99.63
mg#	90.77	90.80	90.66	90.62	90.99	91.22	90.93	91.14	91.38	90.85	91.01	91.25	70.91	71.03	70.87
cr#													33.18	33.37	33.18

Table 5.2. Major oxides composition of minerals forming Dreis-Bruck (Dreiser Weiher) xenoliths

Sample	DBR-1B	DBR-1B	DBR-1B	DBR-1B	DBR-1B	DBR-1B	DBR-1B	DBR-1B	DBR-1B	DBR-1B	DBR-1B	DBR-1B	DBR-1B	DBR-1B	DBR-1B sp	DBR-1B sp	DBR-1B sp	DBR-1B sp
Rock type	Lh	Lh	Lh	Lh	Lh	Lh	Lh	Lh	Lh	Lh	Lh	Lh	Lh	Lh	Lh	Lh	Lh	Lh
phase	oll core	oll core	oll core	oll core	oll core	cpx1 core	cpx1 core	cpx1 rim	opx rim	opx core	opx core	opx core	opx core	opx core	sp1	sp1	sp1	sp1
SiO_2	40.20	40.18	39.78	39.82	39.76	50.72	50.80	50.58	53.70	53.69	53.65	53.53	53.81	53.28	0.10	0.12	0.13	0.13
TiO_2	0.00	0.01	0.01	0.01	0.01	0.73	0.60	0.65	0.29	0.22	0.22	0.27	0.24	0.23	0.59	0.59	0.58	0.56
Al_2O_3	0.05	0.05	0.07	0.04	0.06	6.56	6.58	6.62	5.35	5.39	5.32	5.37	5.45	5.41	46.16	45.93	46.36	45.73
FeO	10.80	10.87	10.75	10.80	10.79	4.08	4.24	4.13	6.91	6.87	6.93	6.95	6.95	6.85	14.93	15.09	15.16	14.77
MnO	0.18	0.16	0.15	0.16	0.16	0.12	0.12	0.13	0.16	0.15	0.15	0.15	0.16	0.16	0.20	0.22	0.19	0.19
MgO	48.83	48.44	48.36	48.49	48.54	16.58	16.56	16.63	31.45	31.38	31.54	31.40	31.69	31.09	19.57	19.29	19.35	19.63
CaO	0.12	0.13	0.12	0.14	0.15	18.99	18.62	18.86	1.40	1.43	1.38	1.37	1.39	1.41	0.01	0.00	-0.01	-0.01
Na_2O	0.00	-0.02	0.00	0.01	0.02	1.08	1.07	1.06	0.13	0.14	0.12	0.13	0.15	0.11	0.00	0.00	0.00	0.00
K_2O																		
Cr_2O_3	0.04	0.03	0.02	0.03	0.03	0.92	0.94	1.01	0.65	0.62	0.63	0.65	0.64	0.66	17.96	18.19	17.98	17.87
NiO	0.32	0.36	0.32	0.34	0.33	0.09	0.05	0.04	0.11	0.10	0.08	0.10	0.13	0.13	0.28	0.33	0.27	0.28
Tot	100.54	100.21	99.59	99.85	99.86	99.85	99.57	99.71	100.15	100.00	100.03	99.92	100.58	99.33	99.80	99.76	100.02	99.16
mg#	88.96	88.82	88.91	88.89	88.91	87.86	87.45	87.77	89.03	89.06	89.02	88.95	89.05	89.00	70.01	69.50	69.45	70.31
cr#															20.70	20.99	20.65	20.77

Sample	DBR-1B vein	DBR-1Bvein	DBR-1B vein	DBR-1B vein	DBR-1B vein	DBR-1B vein	DBR-1B vein	DBR-1B vein	DBR-1B vein	DBR-1B vein	DBR-1B vein	DBR-1B vein
Rock type	Ol-Cpxte	Ol-Cpxte	Ol-Cpxte	Ol-Cpxte	Ol-Cpxte	Ol-Cpxte	Ol-Cpxte	Ol-Cpxte	Ol-Cpxte	Ol-Cpxte	Ol-Cpxte	Ol-Cpxte
phase	ol rim	ol core	ol core	ol rim	ol core	ol rim	ol core	cpx core	cpx core	cpx rim	cpx core	cpx core
SiO_2	40.08	40.06	40.07	40.04	39.95	40.35	40.28	51.03	51.14	50.70	51.15	51.27	51.19
TiO_2	0.01	0.01	0.01	0.00	0.00	0.01	0.01	0.66	0.67	0.71	0.65	0.71	0.70
Al_2O_3	0.06	0.05	0.04	0.06	0.06	0.05	0.05	6.19	6.22	5.60	5.28	6.19	6.24
FeO	10.80	11.08	10.90	10.82	10.84	10.86	10.89	4.08	4.01	3.78	3.76	4.09	4.08
MnO	0.14	0.15	0.15	0.19	0.14	0.16	0.16	0.12	0.13	0.12	0.12	0.12	0.12
MgO	48.16	48.52	48.24	48.24	48.39	48.40	48.42	16.75	16.72	16.01	16.66	16.77	16.74
CaO	0.13	0.11	0.14	0.16	0.13	0.12	0.13	19.02	18.88	20.92	20.56	18.96	18.89
Na_2O	0.01	0.02	0.01	-0.01	0.01	0.00	0.00	1.03	1.02	0.81	0.73	1.08	1.05
K_2O													
Cr_2O_3	0.03	0.03	0.03	0.03	0.02	0.03	0.03	0.92	0.91	1.04	0.97	0.92	0.91
NiO	0.31	0.32	0.33	0.32	0.32	0.34	0.29	0.04	0.08	0.08	0.06	0.08	0.05
Tot	99.73	100.36	99.93	99.84	99.85	100.33	100.24	99.84	99.77	99.76	99.95	100.20	99.95
mg#	88.82	88.64	88.74	88.82	88.83	88.81	88.79	87.97	88.15	88.30	88.75	87.96	87.98
cr#													

Comment	DBR 2	DBR 2	DBR 2	DBR 2	DBR 2	DBR 2	DBR 2	DBR 2	DBR 2	DBR 2	DBR 2	DBR 2	DBR 2 sp	DBR 2 sp	DBR 2 sp	DBR 2 sp
Rock type	Lh	Lh	Lh	Lh	Lh	Lh	Lh	Lh	Lh	Lh	Lh	Lh	Lh	Lh	Lh	Lh
phase	ol rim	ol core	ol core	ol core	ol core	ol core	cpx core	cpx core	cpx core	cpx core	cpx core	cpx core	sp	sp	sp	sp
SiO2	40.01	39.58	40.06	39.83	39.77	39.88	51.31	51.29	51.26	51.24	51.32	51.30	0.10	0.11	0.13	0.10
TiO2	0.01	0.01	0.01	0.01	0.00	0.01	0.58	0.60	0.60	0.60	0.60	0.56	1.26	1.24	1.25	1.27
Al2O3	0.04	0.03	0.04	0.03	0.03	0.04	4.10	4.07	4.12	4.11	4.09	4.09	30.81	30.65	30.70	30.74
FeO	11.57	11.88	11.84	11.83	11.75	11.69	4.17	4.28	4.25	4.31	4.27	4.15	19.75	19.86	19.58	19.71
MnO	0.14	0.15	0.15	0.17	0.17	0.13	0.12	0.12	0.13	0.11	0.12	0.11	0.29	0.27	0.27	0.30
MgO	47.53	47.52	47.40	47.57	47.54	47.55	17.33	17.13	17.15	16.99	17.04	17.12	16.14	16.19	16.06	15.95
CaO	0.15	0.14	0.14	0.12	0.16	0.13	19.20	19.33	19.28	19.28	19.39	19.08	0.01	0.01	0.02	0.02
Na2O	0.00	0.01	0.00	0.00	-0.01	0.02	0.75	0.77	0.76	0.77	0.77	0.75				
K2O																
Cr2O3	0.05	0.04	0.04	0.04	0.03	0.04	1.29	1.30	1.29	1.31	1.30	1.30	31.02	31.09	30.80	30.76
NiO	0.28	0.31	0.30	0.31	0.32	0.32	0.02	0.06	0.05	0.03	0.10	0.07	0.28	0.27	0.16	0.24
Total	99.77	99.67	99.98	99.92	99.75	99.82	98.88	98.94	98.90	98.76	98.99	98.52	99.83	99.88	99.17	99.32
mg#	87.98	87.70	87.70	87.75	87.82	87.88	88.10	87.70	87.79	87.54	87.68	88.02	59.28	59.23	59.38	59.05
cr#													40.31	40.49	40.23	40.16

Comment	DBR-3	DBR-3	DBR-3	DBR-3	DBR-3	DBR-3	DBR-3	DBR-3	DBR-3	DBR-3	DBR-3	DBR-3	DBR-3	DBR-3	DBR-3	DBR-3	DBR-3
Rock type	Lh	Lh	Lh	Lh	Lh	Lh	Lh	Lh	Lh	Lh	Lh	Lh	Lh	Lh	Lh	Lh	Lh
phase	oll	oll	oll	oll	oll	oll	oll	cpx1	cpx1	cpx	opx	opx	opx	sp1	sp1	sp1	sp1
SiO2	40.00	39.97	39.96	40.14	40.07	40.06	39.76	50.99	51.17	50.80	53.85	54.11	53.93	0.10	0.14	0.12	0.12
TiO2	0.01	0.01	0.00	0.01	0.01	0.00	0.01	0.45	0.45	0.49	0.20	0.14	0.20	0.25	0.23	0.22	0.25
Al2O3	0.06	0.09	0.04	0.07	0.05	0.05	0.06	7.42	7.38	7.47	6.10	6.13	6.16	52.19	51.96	52.02	52.56
FeO	9.58	9.78	9.67	9.60	9.67	9.80	9.53	3.68	3.64	3.74	6.14	6.06	6.23	11.98	11.95	11.90	11.96
MnO	0.13	0.16	0.13	0.12	0.14	0.16	0.11	0.11	0.09	0.11	0.15	0.15	0.13	0.15	0.15	0.15	0.15
MgO	48.84	48.78	48.82	48.72	48.84	48.75	48.71	16.25	16.38	16.33	31.27	31.38	31.43	21.00	20.80	20.97	21.18
CaO	0.12	0.15	0.14	0.16	0.14	0.14	0.13	18.26	18.45	18.40	1.35	1.35	1.31	0.04	0.01	0.01	0.00
Na2O	0.03	0.03	0.02	0.00	0.01	0.00	0.01	1.30	1.26	1.32	0.15	0.15	0.15				
K2O																	
Cr2O3	0.03	0.03	0.03	0.03	0.03	0.02	0.03	0.93	0.95	0.94	0.60	0.62	0.61	13.08	13.19	13.19	13.25
NiO	0.36	0.39	0.40	0.37	0.36	0.37	0.39	0.05	0.05	0.06	0.08	0.11	0.06	0.33	0.33	0.33	0.38
Total	99.16	99.38	99.21	99.23	99.31	99.36	98.74	99.45	99.82	99.67	99.88	100.20	100.21	99.26	98.93	99.03	99.92
mg#	90.08	89.89	90.00	90.04	90.00	89.86	90.11	88.71	88.92	88.61	90.08	90.22	89.99	75.75	75.62	75.85	75.93
cr#														14.39	14.55	14.53	14.47

Comment	DBR 5	DBR 5	DBR 5	DBR 5	DBR 5	DBR 5	DBR 5	DBR 5	DBR 5	DBR 5	DBR 5	DBR 5	DBR 5	DBR 5	DBR 5	DBR 5	DBR 5	DBR 5
Rock type	Hz	Hz	Hz	Hz	Hz	Hz	Hz	Hz	Hz	Hz	Hz	Hz	Hz	Hz	Hz	Hz	Hz	Hz
phase	oll	oll	oll	oll	oll	cpx1	cpx1	cpx1	cpx1	cpx1	opx	opx	opx	opx	sp1	sp1	sp1	sp1
	rim	core	core	core	core	core	core	core	core	rim	rim	core	core	core	core	core	core	core
SiO2	40.25	40.31	40.35	40.18	40.23	50.48	50.72	50.57	50.59	50.47	53.24	53.02	53.22	53.34	0.12	0.12	0.14	0.12
TiO2	0.00	-0.01	0.01	0.00	0.00	0.57	0.63	0.61	0.56	0.60	0.18	0.17	0.22	0.17	0.24	0.24	0.26	0.23
Al2O3	0.05	0.06	0.04	0.05	0.06	6.81	6.71	6.81	6.79	6.82	5.38	5.45	5.45	5.35	56.51	56.19	56.65	56.29
FeO	10.40	10.09	10.18	10.34	10.39	3.87	3.78	3.86	3.87	3.94	6.56	6.55	6.51	6.59	11.75	11.53	11.80	11.66
MnO	0.13	0.15	0.12	0.16	0.19	0.12	0.11	0.11	0.12	0.12	0.15	0.15	0.15	0.14	0.13	0.13	0.14	0.14
MgO	48.91	48.70	48.86	48.83	48.79	15.90	16.10	16.06	16.11	16.09	31.53	31.29	31.40	31.33	21.70	21.38	21.54	21.31
CaO	0.11	0.13	0.13	0.13	0.11	17.66	17.98	18.10	17.55	17.66	1.32	1.35	1.29	1.25	-0.01	-0.01	0.00	-0.01
Na2O	0.01	0.01	0.01	0.01	0.02	1.42	1.43	1.48	1.41	1.40	0.18	0.17	0.19	0.18				
K2O																		
Cr2O3	0.02	0.02	0.02	0.02	0.02	0.74	0.74	0.75	0.76	0.76	0.47	0.47	0.47	0.48	8.88	9.15	9.02	9.01
NiO	0.38	0.38	0.36	0.36	0.35	0.07	0.02	0.06	0.07	0.06	0.06	0.11	0.13	0.15	0.43	0.38	0.40	0.36
Total	100.26	99.84	100.08	100.09	100.16	97.63	98.23	98.40	97.84	97.92	99.07	98.73	99.01	98.99	99.88	99.24	100.05	99.21
mg#	89.34	89.58	89.53	89.38	89.33	88.00	88.37	88.13	88.11	87.91	89.55	89.48	89.58	89.45	76.69	76.76	76.49	76.51
cr#															9.54	9.85	9.65	9.69

Comment	DBR-6	DBR-6	DBR-6	DBR-6	DBR-6	DBR-6	DBR-6	DBR-6	DBR-6	DBR-6	DBR-6	DBR-6	DBR-6	DBR-6	DBR-6	DBR-6	DBR-6	DBR-6	DBR-6	DBR-6	DBR-6
Rock type	Lh	Lh	Lh	Lh	Lh	Lh	Lh	Lh	Lh	Lh	Lh	Lh	Lh	Lh	Lh	Lh	Lh	Lh	Lh	Lh	Lh
phase	oll	oll	oll	oll	oll	cpx1	cpx1	cpx1	cpx1	cpx1	cpx1	cpx1	cpx1	opx	opx	opx	opx	opx	sp1	sp1	sp1
	core	core	core	core	core	core	core	core	core	core	rim	core	core	rim	rim	core	core	core	rim	core	core	core
SiO2	40.61	40.27	40.32	40.82	40.50	51.32	51.53	51.16	51.22	51.19	51.28	51.17	51.18	53.34	53.68	53.88	53.78	53.87	0.11	0.14	0.14	0.15
TiO2	0.00	0.00	0.01	0.00	0.00	0.26	0.23	0.25	0.22	0.26	0.21	0.22	0.28	0.08	0.10	0.06	0.08	0.09	0.17	0.17	0.18	0.17
Al2O3	0.07	0.06	0.05	0.06	0.06	6.57	6.57	6.68	6.63	6.64	6.64	6.57	6.56	5.56	5.55	5.54	5.53	5.43	47.69	47.68	47.42	47.30
FeO	9.35	9.45	9.48	9.48	9.43	3.68	3.62	3.65	3.62	3.72	3.63	3.60	3.72	6.06	6.03	6.01	5.99	6.03	12.93	12.73	12.88	12.60
MnO	0.14	0.15	0.14	0.14	0.16	0.11	0.11	0.11	0.10	0.11	0.11	0.10	0.10	0.14	0.14	0.14	0.13	0.16	0.18	0.17	0.18	0.19
MgO	49.56	49.30	49.67	49.54	49.60	17.12	17.10	17.19	17.10	17.33	17.13	17.06	17.10	31.78	31.86	31.78	32.00	31.86	20.46	20.35	20.39	20.73
CaO	0.15	0.14	0.14	0.16	0.16	18.70	18.57	18.49	18.67	18.60	18.61	18.57	18.50	1.53	1.51	1.47	1.47	1.46	-0.01	0.03	0.00	0.00
Na2O	0.01	-0.01	0.00	0.00	0.01	1.04	1.00	1.07	1.02	1.04	1.04	1.05	1.06	0.13	0.15	0.13	0.15	0.12	0.00	0.00	0.00	0.00
K2O																						
Cr2O3	0.04	0.04	0.04	0.04	0.03	1.19	1.20	1.16	1.19	1.18	1.17	1.18	1.20	0.75	0.75	0.74	0.76	0.76	18.19	18.18	18.29	18.25
NiO	0.38	0.38	0.38	0.40	0.37	0.08	0.04	0.05	0.06	0.08	0.04	0.07	0.03	0.10	0.14	0.11	0.10	0.12	0.40	0.38	0.37	0.30
Total	100.30	99.78	100.22	100.63	100.33	100.07	99.97	99.80	99.83	100.16	99.86	99.58	99.73	99.48	99.92	99.86	100.00	99.91	100.13	99.83	99.84	99.70
mg#	90.43	90.29	90.33	90.30	90.36	89.23	89.39	89.34	89.38	89.26	89.37	89.41	89.12	90.33	90.39	90.41	90.50	90.40	73.83	74.01	73.84	74.56
cr#																			20.38	20.37	20.55	20.56

Table 5.3. Major oxides composition of minerals forming Gees xenoliths

Sample	GE 1	GE 1	GE 1	GE 1	GE 1 wb_cpx1_c	GE 1_cpxsec1_c	GE 1_cpx theo	GE 1	GE 1	GE 1	GE 1	GE 1	GE 1	GE 1	GE 1	GE 1	GE 1	GE 1	GE 1 wb_opx1_r	GE 1 wb_opx1_c	GE 1 lh_opx2_c	GE 1 lh_opx2_r cl gl	GE 1 lh_opx3_c	GE 1 lh_opx3_r	GE 1 wb_opx4_c	GE 1 wb_opx4_r	GE 1 wb_opx5_c	GE 1 wb_opx5_r	GE1	GE1	GE1	GE1
Rock type	Ol-Wb	Ol-Wb	Ol-Wb	Ol-Wb	Ol-Wb?	Ol-Wb?	Ol-Wb?	Ol-Wb	Ol-Wb	Ol-Wb	Ol-Wb	Ol-Wb	Ol-Wb	Ol-Wb	Ol-Wb	Ol-Wb	Ol-Wb	Ol-Wb?	Ol-Wb?	Lh	Lh	Lh	Lh	Ol-Wb?	Ol-Wb?	Ol-Wb?	Ol-Wb?	Ol-Wb	Ol-Wb	Ol-Wb	Ol-Wb	Ol-Wb
phase	ol core	ol core	ol core	cpx core	cpx2 core	cpx2 core	cpx rim	cpx core	cpx core	cpx core	cpx core	cpx core	opx core	opx core	opx core	opx rim	opx core	opx core	opx rim	opx core	opx core	opx core	opx rim	opx core	opx rim	opx core	opx rim	opx core	sp core	sp core	sp core	sp core	
SiO$_2$	39.54	39.33	39.42	39.49	53.33	53.37	52.84	53.00	52.89	52.68	52.73	52.99	51.81	55.90	56.13	54.76	55.72	55.20	54.98	55.72	54.92	55.57	55.32	55.83	55.45	55.59	56.09	55.74	55.86	0.04	0.02	0.04	0.02
TiO$_2$	0.00	0.00	0.00	0.00	0.10	0.07	0.13	0.14	0.10	0.14	0.16	0.11	0.21	0.03	0.04	0.04	0.06	0.07	0.08	0.06	0.01	0.07	0.03	0.06	0.02	0.06	0.05	0.07	0.07	0.59	0.58	0.57	0.59
Al$_2$O$_3$	0.02	0.02	0.01	0.01	2.22	2.86	2.93	2.30	2.35	2.74	2.67	2.52	3.35	1.36	1.19	2.16	1.54	1.82	1.79	1.85	2.52	2.11	2.38	2.04	2.10	2.19	2.02	2.07	1.98	25.58	25.33	25.79	25.68
FeO	15.77	15.78	15.67	15.68	4.45	4.96	4.79	5.09	5.18	5.33	5.12	5.08	5.32	10.00	9.77	9.94	9.93	10.10	10.03	9.80	9.81	10.30	10.04	10.18	10.02	10.24	9.99	10.04	9.81	30.79	31.01	31.16	31.08
MnO	0.20	0.25	0.24	0.14	0.14	0.12	0.14	0.14	0.16	0.16	0.14	0.15	0.25	0.26	0.25	0.23	0.23	0.25	0.25	0.24	0.26	0.24	0.23	0.24	0.23	0.24	0.36	0.36	0.37	0.34			
MgO	44.41	44.50	44.43	44.45	16.65	16.43	16.41	16.85	16.75	16.52	16.48	16.71	16.19	31.67	31.86	30.60	31.96	31.50	31.05	31.55	30.50	31.13	30.44	31.13	30.64	31.06	31.64	31.12	30.72	11.91	12.02	11.90	11.65
CaO	0.11	0.09	0.10	0.09	21.91	21.10	21.39	21.20	21.02	20.96	21.21	21.25	20.79	0.85	0.79	1.13	0.40	0.48	0.61	0.62	0.95	0.50	1.11	0.48	1.04	0.45	0.41	0.55	1.04	-0.02	-0.01	0.02	0.00
Na$_2$O	0.00	0.00	0.02	0.01	0.56	0.68	0.67	0.62	0.63	0.65	0.65	0.65	0.73	0.05	0.04	0.07	0.03	0.02	0.00	0.06	0.06	0.00	0.07	0.04	0.05	0.02	0.00	0.05	0.06				
K$_2$O	0.00				0.00		0.01											0.00				0.00		0.01									
Cr$_2$O$_3$	0.01	0.00	0.00	0.02	0.52	0.46	0.46	0.27	0.24	0.32	0.34	0.34	0.60	0.10	0.11	0.22	0.19	0.29	0.29	0.27	0.29	0.27	0.19	0.26	0.21	0.27	0.25	0.27	0.18	27.57	27.76	27.50	27.36
NiO	0.20	0.19	0.18	0.17	0.03	0.05	0.02	0.03	0.01	0.04	0.02	0.01	0.07	0.03	0.00	0.05	0.00	0.03	0.05	0.05	0.06	0.03	0.05	0.02	0.03	0.05	0.03	0.02	0.04	0.18	0.13	0.15	0.18
Tot	100.27	100.17	100.09	100.17	99.90	100.13	99.78	99.64	99.32	99.57	99.54	99.80	99.16	100.27	100.24	100.07	99.78	99.16	100.07	99.78	99.39	100.23	99.88	100.31	99.81	100.12	100.74	100.18	100.01	97.41	97.61	97.85	97.33
mg#	83.38	83.40	83.48	83.48	86.97	85.52	85.92	85.51	85.21	84.66	85.16	85.42	84.44	84.95	85.32	84.59	85.15	84.75	84.66	85.16	84.71	84.35	84.39	84.50	84.50	84.39	84.95	84.66	84.80	40.81	40.85	40.49	40.05
cr#																														41.96	42.38	41.70	41.68

Sample	GE-3	GE-3	GE-3	GE-3	GE-3	GE-3	GE-3	GE-3	GE-3	GE-3	GE-3	GE-3	GE-3	GE-3
Rock type	Hz	Hz	Hz	Hz	Hz	Hz	Hz	Hz	Hz	Hz	Hz	Hz	Hz	Hz
phase	ol1 core	ol1 core	ol1 core	ol1 core	cpx small	cpx small	cpx small	cpx small	opx rim	opx core	opx core	opx core	sp1 not in photo	sp1 not in photo
SiO$_2$	40.60	40.69	40.57	40.80	51.38	51.22	49.41	53.42	56.51	56.47	56.61	56.58	0.03	0.03
TiO$_2$	0.00	0.00	0.00	-0.01	0.22	0.20	0.26	0.15	0.05	0.02	0.03	0.05	0.05	0.06
Al$_2$O$_3$	0.00	0.00	0.01	0.00	4.43	4.51	6.44	2.38	2.01	2.16	2.02	1.88	39.12	39.29
FeO	8.46	8.36	8.52	8.56	2.64	2.64	2.84	2.67	5.77	5.74	5.58	5.71	16.01	15.83
MnO	0.14	0.14	0.14	0.13	0.06	0.04	0.08	0.07	0.16	0.15	0.15	0.15	0.24	0.23
MgO	49.72	49.72	49.46	49.91	16.06	16.61	14.94	17.58	34.43	34.17	34.43	34.30	17.52	17.76
CaO	0.03	0.02	0.02	0.02	21.98	21.30	19.84	22.20	0.34	0.34	0.31	0.32	0.00	0.02
Na$_2$O	-0.01	0.00	0.01	0.02	0.73	0.72	1.11	0.53	0.01	0.02	0.00	0.01		
K$_2$O														
Cr$_2$O$_3$	0.01	0.00	0.00	0.01	1.60	2.11	4.64	0.80	0.29	0.32	0.32	0.28	24.26	24.78
NiO	0.35	0.39	0.37	0.39	0.06	0.01	0.08	0.06	0.07	0.07	0.04	0.11	0.32	0.25
Tot	99.28	99.32	99.09	99.82	99.15	99.36	99.65	99.88	99.65	99.46	99.50	99.39	97.85	98.52
mg#	91.28	91.37	91.18	91.22	91.56	91.82	90.36	92.14	91.41	91.38	91.67	91.46	66.09	66.66
cr#													29.38	29.74

Sample	GE-4	GE-4	GE-4	GE-4	GE-4	GE-4	GE-4	GE-4	GE-4	GE-4	GE-4	GE-4	GE-4 sp	GE-4 sp	GE-4 sp
Rock type	Hz?	Hz?	Hz?	Hz?	Hz?	Hz?	Hz?	Hz?	Hz?	Hz?	Hz?	Hz?	Hz?	Hz?	Hz?
phase	ol1 core	ol1 core	ol1 core	ol1 core	cpx1 core	cpx1 core	cpx1 core	cpx1 core	cpx1 rim	opx core	opx core	opx core	sp1 core	sp1 core	sp1 core
SiO$_2$	40.53	40.44	40.48	40.67	52.45	52.64	53.38	52.50	52.45	56.20	55.44	55.52	0.04	0.02	0.03
TiO$_2$	-0.01	-0.01	0.00	0.00	0.05	0.04	0.03	0.10	0.07	0.00	0.04	0.04	0.00	0.01	0.01
Al$_2$O$_3$	0.01	0.01	0.01	0.00	4.07	4.02	3.40	4.25	3.57	2.35	2.82	3.34	47.86	47.69	47.62
FeO	8.41	8.67	8.47	8.53	2.48	2.45	2.64	2.61	2.40	5.75	5.82	5.80	12.80	12.83	12.69
MnO	0.16	0.13	0.10	0.15	0.09	0.07	0.08	0.06	0.08	0.14	0.16	0.14	0.19	0.18	0.18
MgO	49.69	49.54	49.47	49.66	15.82	15.87	16.31	15.70	16.07	34.02	33.79	33.77	19.89	19.99	19.65
CaO	0.06	0.06	0.06	0.05	22.72	23.00	21.72	22.62	23.10	0.36	0.39	0.32	0.00	0.00	0.01
Na$_2$O	0.00	0.00	0.00	0.00	0.94	1.00	1.11	1.01	0.85	0.05	0.06	0.04			
K$_2$O															
Cr$_2$O$_3$	0.01	0.01	0.01	0.00	0.77	0.71	0.60	0.74	0.61	0.20	0.29	0.37	17.14	17.04	16.98
NiO	0.34	0.37	0.38	0.33	0.02	0.06	0.04	0.03	0.06	0.06	0.08	0.11	0.32	0.30	0.37
Tot	99.20	99.21	98.99	99.40	99.41	99.87	99.33	99.65	99.28	99.14	98.89	99.44	98.41	98.21	97.72
mg#	91.33	91.06	91.24	91.21	91.93	92.02	91.66	91.47	92.26	91.34	91.19	91.21	73.47	73.52	73.40
cr#													19.38	19.33	19.31

Sample	GE-5_1	GE-5_1	GE-5_1	GE-5_1	GE-5_1	GE-5	GE-5	GE-5	GE-5_1	GE-5_1	GE-5_1	GE-5_1	GE-5_1	GE-5_1	GE5_sp1_c	GE5_sp1_r	GE5_sp2_c	GE5_sp2_r	GE5_sp2_c	GE5_sp3_c	GE5_sp4_c	GE-5	GE-5	GE-5	GE-5	GE-5_1	GE-5_1	GE-5_1	GE-5_1
Rock type	Weh	Weh	Weh	Weh	Weh	Weh	Weh	Weh	Weh	Weh	Weh	Weh	Weh	Weh	Weh	Weh	Weh	Weh	Weh	Weh	Weh	Weh	Weh	Weh	Weh	Weh	Weh	Weh	Weh
phase	ol	ol	ol	ol	ol	cpx	cpx	cpx	cpx	cpx	cpx	cpx	cpx	cpx	sp1	sp1	sp1	sp1	sp1	sp1	sp1	phlog	phlog	phlog	phlog	phlog	phlog	phlog	phlog
	core	core	core	core	core	core	core	core	core	rim	in sp	in sp	core	core	core	rim	core	rim	core	core	core	core	core	core	small	small	core	rim	rim
SiO_2	39.69	39.51	39.98	39.90	40.01	50.22	50.51	51.13	50.87	49.80	51.86	52.57	50.81	50.95	0.04	0.06	0.07	0.05	0.03	0.06	0.08	37.57	37.48	37.09	37.12	37.35	37.28	37.39	37.17
TiO_2	0.01	0.01	0.00	0.01	0.01	0.79	0.86	0.76	0.88	1.15	0.49	0.40	0.82	0.80	1.86	2.69	1.64	2.68	1.92	2.60	3.27	3.96	3.94	3.91	3.90	3.97	3.85	3.82	3.95
Al_2O_3	0.03	0.02	0.04	0.02	0.02	4.33	4.07	4.08	4.22	5.04	2.96	2.71	4.16	4.06	16.90	24.39	15.52	24.00	17.00	21.32	22.77	16.43	16.70	16.50	16.62	16.74	16.45	16.49	16.43
FeO	12.18	12.24	12.25	12.27	12.49	3.98	3.95	3.82	3.64	3.93	3.39	3.39	3.61	3.58	27.54	29.26	26.46	29.21	27.67	29.10	32.55	6.15	5.96	5.99	5.83	5.95	5.80	5.73	5.65
MnO	0.24	0.24	0.23	0.25	0.22	0.09	0.08	0.11	0.07	0.07	0.10	0.10	0.11	0.09	0.25	0.23	0.22	0.25	0.22	0.24		0.05	0.03	0.08	0.04	0.05	0.02	0.08	0.04
MgO	47.22	47.18	47.16	47.41	47.10	15.46	15.52	15.79	15.48	15.01	16.24	16.38	15.44	15.73	12.42	14.04	12.20	14.22	12.37	13.60	13.19	20.48	20.42	20.28	20.31	20.29	20.49	20.58	20.45
CaO	0.26	0.26	0.25	0.26	0.26	23.84	23.71	23.15	23.78	23.58	23.01	22.86	23.26	23.34	0.02	0.09	0.04	0.00	0.00	0.01	0.27	0.03	0.03	0.01	0.06	0.08	0.02	0.00	0.00
Na_2O	0.00	0.00	-0.01	0.00	-0.02	0.47	0.43	0.60	0.48	0.43	0.68	0.70	0.61	0.57								0.34	0.32	0.28	0.28	0.26	0.34	0.37	0.33
K_2O																						10.03	10.09	9.99	10.11	10.05	10.10	9.94	9.95
Cr_2O_3	0.01	0.01	0.03	0.01	0.02	0.90	0.74	0.76	1.05	0.93	1.48	1.73	1.18	0.86	38.62	27.08	42.15	27.94	38.67	31.50	24.69	0.00	0.00	0.00	0.00	0.00	0.00	0.00	0.00
NiO	0.32	0.31	0.31	0.32	0.31	0.02	0.06	0.08	0.06	0.00	0.04	0.05	0.03	0.00	0.22	0.27	0.19	0.28	0.21	0.27	0.31						0.04	0.04	0.05
Tot	99.97	99.78	100.23	100.47	100.42	100.10	99.92	100.27	100.55	99.95	100.25	100.90	100.03	99.98	98.15	98.42	98.75	98.89	98.37	98.96	97.86	85.01	84.88	84.16	84.17	84.69	84.26	84.45	84.02
mg#	87.35	87.29	87.27	87.32	87.05	87.38	87.51	88.04	88.34	87.18	89.51	89.59	88.39	88.66	44.56	46.10	45.10	46.45	44.33	45.43	41.93	85.58	85.93	85.78	86.11	85.86	86.29	86.49	86.58
cr#															60.52	42.69	64.56	43.85	60.41	49.78	42.10								

Sample	GE-9	GE-9	GE-9	GE-9	GE-9	GE-9	GE-9	GE-9	GE-9	GE-9	GE-9	GE-9
Rock type	Weh	Weh	Weh	Weh	Weh	Weh	Weh	Weh	Weh	Weh	Weh	Weh
phase	ol	ol	ol	ol	ol	ol	cpx	cpx	cpx	sp	sp	sp
	core	core	rim	core	core	core	core	core	core	core	core	core
SiO_2	40.38	40.55	40.38	40.46	40.46	40.32	52.94	52.49	51.75	0.08	0.12	0.09
TiO_2	0.01	0.01	0.02	0.00	0.01	0.01	0.57	0.67	0.82	1.42	1.46	1.46
Al_2O_3	0.02	0.02	0.02	0.03	0.03	0.02	2.65	3.22	3.86	21.10	24.13	23.15
FeO	9.83	9.88	9.93	10.11	10.12	9.91	3.08	3.21	3.25	16.69	18.70	18.04
MnO	0.20	0.16	0.18	0.19	0.18	0.17	0.11	0.10	0.07	0.40	0.37	0.36
MgO	48.65	48.66	48.67	48.73	48.98	48.88	16.99	16.62	15.85	15.07	14.45	15.06
CaO	0.20	0.26	0.15	0.12	0.12	0.12	22.13	22.64	22.72	0.16	0.20	0.19
Na_2O	0.01	0.00	0.04	0.00	0.02	0.01	0.62	0.59	0.70			
K_2O												
Cr_2O_3	0.03	0.04	0.04	0.03	0.03	0.03	1.15	1.01	1.22	42.05	37.93	39.16
NiO	0.30	0.32	0.37	0.36	0.40	0.37	0.07	0.08	0.02	0.22	0.26	0.28
Tot	99.63	99.91	99.79	100.03	100.34	99.84	100.30	100.63	100.27	97.50	97.92	98.09
mg#	89.82	89.77	89.73	89.57	89.61	89.78	90.76	90.23	89.68	61.67	57.93	59.79
cr#												

Sample	GE-10	GE-10	GE-10	GE-10	GE-10	GE-10	GE-10	GE-10	GE-10	GE-10	GE-10	GE-10	GE-10	GE-10	GE-10
Rock type	Hz	Hz	Hz	Hz	Hz	Hz	Hz	Hz	Hz	Hz	Hz	Hz	Hz	Hz	Hz
phase	oll	oll	oll	oll	cpx1	cpx1	cpx1	cpx1	opx	opx	opx	opx	sp1	sp1	sp1
	core	core	core	core	core	core	core	rim	rim	core	core	core	core	core	core
SiO_2	40.36	40.33	40.37	40.50	53.04	53.21	53.67	53.24	56.98	56.89	56.87	56.55	0.03	0.01	0.00
TiO_2	0.01	-0.01	-0.01	0.00	0.05	0.05	0.06	0.06	-0.03	-0.04	0.04	0.02	0.01	0.01	0.01
Al_2O_3	0.00	0.01	0.00	0.00	3.23	3.20	3.29	3.20	1.47	1.56	1.81	2.18	32.72	32.86	32.80
FeO	8.19	8.38	8.18	8.15	2.23	2.35	2.26	2.26	5.28	5.37	5.47	5.45	16.78	16.12	16.25
MnO	0.10	0.10	0.14	0.14	0.05	0.07	0.07	0.07	0.14	0.15	0.14	0.15	0.29	0.30	0.30
MgO	49.69	49.94	49.77	50.11	15.94	15.93	15.89	15.81	35.08	34.95	34.73	34.67	16.38	16.35	16.33
CaO	0.01	0.03	0.03	0.03	22.56	22.44	22.29	22.38	0.32	0.32	0.35	0.38	-0.02	-0.02	0.01
Na_2O	0.00	-0.01	0.00	-0.02	1.28	1.20	1.28	1.25	0.00	0.03	0.03	0.02			
K_2O															
Cr_2O_3	0.01	0.00	0.00	0.01	0.95	0.91	0.92	0.93	0.30	0.33	0.31	0.39	31.80	31.89	32.04
NiO	0.36	0.36	0.36	0.34	0.04	0.01	0.02	0.02	0.09	0.05	0.08	0.08	0.24	0.16	0.22
Tot	98.72	99.13	98.84	99.27	99.38	99.37	99.75	99.23	99.65	99.61	99.82	99.89	98.54	97.96	98.22
mg#	91.53	91.40	91.55	91.64	92.71	92.37	92.59	92.57	92.21	92.06	91.88	91.89	63.50	64.39	64.17
cr#													39.47	39.44	39.58

Table 5.4. Major oxides composition of minerals forming Siebengebirge xenoliths

Sample	SB-1 ol	SB-1 ol	SB-1 ol	SB-1 ol	SB-1 ol	SB-1 cpx inlc of glass and olivine	SB-1 cpx inlc of glass and olivine	SB-1 cpx inlc of glass and olivine	SB-1 opx not in photo	SB-1 opx not in photo	SB-1 opx not in photo	SB-1 opx not in photo	SB-1 sp not in photo	SB-1 sp not in photo	SB-1 sp not in photo
Rock type	Dn	Dn	Dn	Dn	Dn	Dn	Dn	Dn	Dn	Dn	Dn	Dn	Dn	Dn	Dn
phase	ol	ol	ol	ol	ol	cpx	cpx	cpx	opx	opx	opx	opx	sp	sp	sp
SiO_2	40.33	40.47	40.33	40.49	40.17	54.38	53.49	51.94	56.64	56.43	56.45	56.55	0.01	0.00	0.04
TiO_2	0.00	0.00	0.00	0.00	0.00	0.05	0.09	0.23	0.02	0.07	0.04	0.02	0.17	0.16	0.38
Al_2O_3	0.01	0.00	-0.01	0.00	0.00	0.78	1.77	3.17	1.25	1.69	1.63	1.85	18.80	18.80	18.67
FeO	9.31	9.11	9.05	9.25	9.13	2.04	2.47	2.82	6.17	6.27	6.12	6.17	20.16	20.42	18.70
MnO	0.13	0.12	0.18	0.15	0.15	0.07	0.09	0.08	0.16	0.16	0.15	0.15	0.38	0.35	0.37
MgO	49.31	49.31	49.21	49.07	49.47	17.68	17.27	16.73	34.61	34.21	34.44	34.13	13.44	13.49	13.55
CaO	0.11	0.16	0.15	0.15	0.11	23.98	23.25	21.50	0.36	0.30	0.29	0.30	0.07	0.07	0.06
Na_2O	0.00	0.01	-0.01	0.00	0.01	0.37	0.45	0.70	0.01	0.02	0.02	0.03			
K_2O															
Cr_2O_3	0.03	0.02	0.02	0.03	0.04	0.42	0.77	2.01	0.19	0.23	0.22	0.22	45.51	45.21	46.69
NiO	0.31	0.31	0.36	0.31	0.36	0.04	0.07	0.05	0.05	0.09	0.07	0.07	0.19	0.19	0.12
Tot	99.54	99.50	99.28	99.44	99.44	99.82	99.72	99.22	99.46	99.47	99.43	99.50	99.01	99.04	98.90
mg#	90.42	90.61	90.64	90.43	90.62	93.91	92.57	91.37	90.91	90.68	90.93	90.79	54.30	54.06	56.35
cr#													61.88	61.73	62.66

Sample	SB-2	SB-2	SB-2	SB-2	SB-2	SB-2	SB-2	SB-2	SB-2	SB-2	SB-2	SB-2	SB-2	SB-2	SB2_SP1_C	SB2_SP1_R	SB2_sp2_c	SB2_sp2_r	SB2_sp3_c	SB2_sp3_r	SB2_sp4_c	SB2_sp4_r
Rock type	Hz	Hz	Hz	Hz	Hz	Hz	Hz	Hz	Hz	Hz	Hz	Hz	Hz	Hz	Hz	Hz	Hz	Hz	Hz	Hz	Hz	Hz
phase	oll	oll	oll	oll	oll	cpx1	cpx1	cpx1	cpx1	opx	opx	opx	opx	opx	sp1 core	sp1 rim	sp1 core	sp1 rim	sp1 core	sp1 rim	sp1 core	sp1 rim
SiO_2	40.59	40.52	40.71	40.35	40.37	51.45	51.81	51.89	52.20	56.06	56.38	55.67	55.70	55.45	0.03	0.01	0.01	0.04	0.02	0.04	0.03	0.03
TiO_2	0.00	0.00	-0.01	0.00	0.00	0.50	0.40	0.40	0.26	0.02	0.02	0.08	0.10	0.12	0.04	0.14	0.04	0.16	0.03	0.14	0.04	0.07
Al_2O_3	0.00	0.01	0.00	0.00	0.00	3.80	4.04	3.92	3.37	2.04	2.09	2.81	2.75	2.89	51.72	52.78	50.90	51.35	49.96	50.15	50.73	50.93
FeO	8.80	8.80	8.73	8.65	8.68	2.90	2.37	2.35	2.26	5.78	5.72	5.81	5.85	5.86	11.87	10.96	12.22	10.66	12.33	10.70	12.21	10.48
MnO	0.15	0.12	0.13	0.13	0.11	0.08	0.07	0.08	0.07	0.15	0.15	0.15	0.13	0.12	0.09	0.07	0.09	0.07	0.08	0.08	0.08	0.07
MgO	50.01	50.04	49.89	49.73	49.80	16.31	15.56	15.73	16.03	34.62	34.35	33.94	34.22	33.87	20.06	20.39	19.61	19.98	19.57	19.71	19.48	20.02
CaO	0.04	0.04	0.06	0.03	0.03	22.58	22.75	22.91	22.88	0.45	0.44	0.41	0.42	0.39	0.00	0.01	0.01	0.04	0.00	0.01	0.02	0.00
Na_2O	0.01	0.00	0.01	-0.01	-0.01	0.69	0.87	0.86	0.75	0.03	0.03	0.02	0.03	0.04								
K_2O																						
Cr_2O_3	0.02	0.00	0.00	0.00	-0.01	0.73	0.92	0.95	0.85	0.26	0.26	0.37	0.39	0.40	15.52	15.50	16.67	16.79	16.93	17.93	16.55	17.85
NiO	0.39	0.41	0.36	0.39	0.37	0.03	0.04	0.06	0.04	0.06	0.09	0.08	0.09	0.07	0.33	0.27	0.35	0.29	0.29	0.26	0.32	0.26
Tot	100.01	99.95	99.88	99.27	99.33	99.07	98.83	99.15	98.71	99.46	99.53	99.34	99.68	99.21	99.88	100.36	100.15	99.60	99.40	99.21	99.67	99.89
mg#	91.01	91.02	91.06	91.11	91.09	90.92	92.13	92.28	92.66	91.44	91.46	91.24	91.25	91.15	75.07	76.82	74.09	76.96	73.87	76.65	73.97	77.30
cr#															16.76	16.45	18.02	17.99	18.52	19.34	17.95	19.04

Sample	SB 3	SB 3	SB 3	SB 3	SB 3	SB 3 cpx with sp incl and Na-rich glass with bubles	SB 3 cpx with sp incl and Na-rich glass with bubles	SB 3 cpx with sp incl and Na-rich glass with bubles	SB 3 cpx with sp incl and Na-rich glass with bubles	SB 3	SB 3	SB 3	SB 3	SB 3	SB 3	SB 3	SB 3	SB 3	SB 3
Rock type	Hz	Hz	Hz	Hz	Hz	Hz	Hz	Hz	Hz	Hz	Hz	Hz	Hz	Hz	Hz	Hz	Hz	Hz	Hz
phase	oll	oll	oll	oll	oll	cpx1	cpx1	cpx1	cpx1	opx	opx	opx	opx	opx	sp1	sp1	sp1	sp1	sp1
SiO_2	40.53	40.75	40.50	40.33	40.37	52.56	52.96	53.10	52.85	55.79	56.26	55.97	55.98	56.30	0.01	0.03	0.02	0.04	0.01
TiO_2	0.00	0.00	-0.01	0.00	0.01	0.09	0.11	0.07	0.10	0.02	0.01	0.02	0.02	0.03	0.06	0.06	0.05	0.04	0.05
Al_2O_3	0.01	0.00	0.01	0.01	0.01	2.28	2.05	2.12	2.13	2.16	2.17	2.14	2.09	2.10	44.60	44.85	45.04	45.63	45.65
FeO	8.59	8.56	8.35	8.59	8.45	2.44	2.15	2.18	2.17	5.74	5.78	5.65	5.66	5.69	14.39	14.34	14.42	14.39	14.48
MnO	0.10	0.13	0.09	0.14	0.14	0.08	0.07	0.08	0.07	0.14	0.15	0.14	0.15	0.14	0.18	0.20	0.21	0.21	0.21
MgO	50.34	50.64	50.46	50.43	50.23	17.32	17.10	17.32	17.37	34.69	34.63	34.52	34.41	34.87	18.87	19.17	19.25	19.01	19.06
CaO	0.03	0.08	0.03	0.04	0.04	23.56	23.47	23.77	23.70	0.43	0.42	0.45	0.43	0.43	-0.02	-0.01	0.00	0.00	-0.01
Na_2O	0.00	0.00	0.01	-0.01	-0.01	0.36	0.36	0.34	0.35	0.00	0.00	0.00	0.01	0.02					
K_2O																			
Cr_2O_3	0.01	0.00	0.00	0.00	0.00	0.43	0.44	0.45	0.46	0.29	0.27	0.28	0.27	0.27	20.33	20.09	19.66	19.56	19.75
NiO	0.43	0.40	0.41	0.39	0.37	0.03	0.04	0.03	0.08	0.09	0.05	0.08	0.10	0.08	0.28	0.23	0.32	0.28	0.29
Tot	100.04	100.57	99.85	99.94	99.62	99.15	98.75	99.45	99.27	99.36	99.75	99.25	99.12	99.72	98.96	99.19	99.38	99.31	
mg#	91.26	91.33	91.50	91.27	91.37	92.66	93.40	93.42	93.45	91.50	91.43	91.59	91.54	91.56	70.04	70.42	70.39	70.19	69.66
cr#															23.42	23.11	22.65	22.34	22.50

Sample	SB4_oll1_c	SB4_oll1_r	SB4_ol2_c	SB4_ol2_r	SB4_ol3_c	SB4_ol3_r	SB4_cpx1_c	SB4_cpx1_r	SB4_cpx2sec_c	SB4_cpx2sec_bis	SB4_opx1_c	SB4_opx1_r	SB4_opx2_c	SB4_opx2_r	SB4_opx3_c	SB4_opx3_r	SB4_sp1_c	SB4_sp1_r	SB4_sp2_c	SB4_sp2_r	SB4_sp3
Rock type	Hz	Hz	Hz	Hz	Hz	Hz	Hz	Hz	Hz	Hz	Hz	Hz	Hz	Hz	Hz	Hz	Hz	Hz	Hz	Hz	Hz
phase	oll core	oll rim	oll core	oll rim	oll core	oll rim	cpx1 core	cpx1 rim	cpx2 core	cpx2 core bis	opx core	opx rim	opx core	opx rim	opx core	opx rim	sp1 core	sp1 rim	sp1 core	sp1 rim	sp1
SiO_2	40.91	41.13	40.97	40.96	41.01	40.89	55.02	54.72	54.83	54.95	41.45	57.62	57.20	57.92	56.88	58.15	0.03	0.00	0.02	0.05	0.00
TiO_2	0.00	0.00	0.00	0.00	0.00	0.00	0.01	0.02	0.00	0.02	0.02	0.01	0.02	0.00	0.03	0.02	0.05	0.05	0.04	0.01	0.08
Al_2O_3	0.01	0.01	0.00	0.00	0.00	0.00	1.57	1.59	1.65	1.61	0.00	1.70	1.87	1.17	2.08	1.10	25.83	21.75	18.88	18.93	18.32
FeO	8.52	8.43	8.55	8.65	8.57	8.50	2.26	2.37	2.32	2.36	8.43	5.56	5.76	5.67	5.66	5.56	18.17	17.94	16.79	17.43	18.16
MnO	0.15	0.10	0.15	0.14	0.15	0.13	0.07	0.07	0.07	0.07	0.17	0.13	0.14	0.15	0.15	0.15	0.11	0.13	0.12	0.14	0.15
MgO	49.93	49.99	50.02	49.97	49.96	49.71	17.01	17.06	17.03	17.16	49.98	34.48	34.56	34.88	34.56	35.00	15.76	14.84	14.72	14.46	14.65
CaO	0.04	0.04	0.03	0.03	0.04	0.15	22.84	22.84	22.76	23.20	0.10	0.47	0.41	0.47	0.43	0.45	0.00	0.01	0.02	0.03	0.00
Na_2O	0.00	0.01	0.00	0.00	0.01	0.00	0.84	0.92	0.85	0.72	0.00	0.07	0.05	0.06	0.06	0.05					
K_2O							0.01	0.01	0.01	0.01	0.02	0.00	0.00	0.01	0.01						
Cr_2O_3	0.01	0.00	0.01	0.00	0.00	0.00	0.84	0.85	0.67	0.35	0.05	0.33	0.34	0.31	0.37	0.22	39.42	44.23	48.14	48.27	47.69
NiO	0.42	0.38	0.35	0.41	0.42	0.41	0.02	0.00	0.06	0.05	0.18	0.08	0.07	0.09	0.05	0.07	0.18	0.16	0.12	0.15	0.14
Tot	100.00	100.10	100.08	100.16	100.16	99.81	100.49	100.30	100.23	100.50	100.40	100.45	100.42	100.71	100.28	100.76	99.79	99.39	99.21	99.90	99.37
mg#	91.26	91.35	91.25	91.15	91.22	91.24	93.06	92.72	92.90	92.85	91.36	91.71	91.44	91.64	91.58	91.82	60.73	59.57	60.97	59.66	58.98
cr#																	50.59	57.71	63.10	63.11	63.59

Sample	SB5_oll_c	SB5_oll_r	SB5_oll_r2	SB5_ol2_c	SB5_ol2_r	SB5_ol3_c	SB5_ol3_r	SB5_ol4_c	SB5_ol4_r	SB5_cpxsec1_c	SB5_cpxsec1_r	SB5_cpxsec2_c	SB5_cpxsec2_r	SB5_cpxsec3_c	SB5_cpxsec4_c	SB5_cpxsec5_c	SB5_opx1_c smesc	SB5_opx1_r smesc	SB5_opx2_c smesc	SB5_opx2_r smesc	SB5_opx3_c smesc	SB5_opx3_r smesc	SB5_opx4_c_r smesc	SB5_opx4_r smesc	SB5_sp1_c	SB5_sp1_r	SB5_sp2_c	SB5_sp2_r
Rock type	Hz	Hz	Hz	Hz	Hz	Hz	Hz	Hz	Hz	Hz	Hz	Hz	Hz	Hz	Hz	Hz	Hz	Hz	Hz	Hz	Hz	Hz	Hz	Hz	Hz	Hz	Hz	Hz
phase	oll core	oll rim	oll rim	oll core	oll rim	oll core	oll rim	oll core	oll rim	cpx2	cpx2	cpx2	cpx2	cpx2	cpx2	cpx2	opx core smesc	opx rim smesc	opx core smesc	opx rim smesc	opx core smesc	opx rim smesc	opx core smesc	opx rim smesc	sp1 core	sp1 rim	sp1 core	sp1 rim
SiO_2	40.90	40.72	41.07	40.74	40.83	40.77	41.07	40.51	41.04	51.83	54.05	52.62	53.88	54.95	52.96	54.56	58.04	57.98	58.21	58.10	58.26	58.14	58.60	57.80	0.00	0.02	0.05	0.06
TiO_2	0.00	0.00	0.00	0.00	0.00	0.00	0.00	0.00	0.00	0.31	0.16	0.32	0.19	0.07	0.30	0.09	0.01	0.04	0.01	0.02	0.00	0.06	0.06	0.05	0.04	0.01	0.16	0.34
Al_2O_3	0.01	0.00	0.00	0.00	0.00	0.00	0.00	0.01	0.00	3.59	1.45	3.00	2.24	0.66	2.88	1.55	0.60	0.53	0.55	0.53	0.57	0.57	0.54	0.56	9.14	9.95	9.89	9.78
FeO	8.84	8.81	8.78	8.89	8.96	8.74	8.77	8.83	8.85	2.13	1.89	2.40	2.74	2.44	2.54	2.62	5.43	5.61	5.59	5.61	5.58	5.54	5.50	5.49	18.37	18.19	17.91	17.59
MnO	0.14	0.14	0.15	0.12	0.11	0.13	0.13	0.15	0.15	0.06	0.07	0.05	0.07	0.07	0.07	0.07	0.14	0.15	0.15	0.15	0.16	0.14	0.17	0.15	0.14	0.15	0.16	0.17
MgO	49.95	49.94	49.65	49.63	49.62	49.64	49.46	49.37	49.46	15.70	17.02	15.58	16.36	17.59	16.44	18.63	35.05	35.08	34.91	34.96	35.22	34.99	35.02	35.08	15.02	12.88	12.71	12.88
CaO	0.03	0.03	0.02	0.03	0.05	0.02	0.03	0.04	0.03	19.91	22.92	19.42	17.83	21.10	18.57	17.64	0.47	0.39	0.33	0.30	0.38	0.34	0.37	0.37	0.01	0.00	0.02	0.06
Na_2O	0.00	0.00	0.00	0.00	0.00	0.00	0.02	0.00	0.00	1.54	0.60	1.94	2.15	1.06	1.88	1.38	0.08	0.07	0.07	0.07	0.08	0.07	0.07	0.07				
K_2O										0.02	0.07	0.00	0.00	0.00	0.00	0.00												
Cr_2O_3	0.01	0.02	0.05	0.01	0.00	0.01	0.00	0.01	0.00	4.21	1.36	4.04	4.04	0.06	1.86	3.99	0.32	0.25	0.27	0.20	0.28	0.29	0.31	0.29	57.39	58.18	57.88	57.52
NiO	0.35	0.35	0.35	0.34	0.35	0.34	0.37	0.35	0.33	0.07	0.04	0.06	0.04	0.05	0.08	0.06	0.07	0.03	0.07	0.07	0.07	0.07	0.07	0.07	0.35	0.37	0.37	0.36
Tot	100.22	99.82	100.02	99.93	99.93	99.66	99.87	99.24	99.48	99.72	99.48	99.67	100.11	99.79	99.68	100.36	100.31	100.05	100.05	100.08	100.57	100.18	100.66	99.89	100.06	99.89	99.17	99.75
mg#	90.96	90.93	90.97	90.90	90.80	91.01	90.95	90.88	90.84	92.94	94.13	92.08	91.41	92.77	92.03	92.17	92.00	91.76	91.76	91.73	91.83	91.84	91.90	91.92	55.54	55.47	56.16	56.78
cr#																									80.81	79.69	79.71	79.79

Sample	SB6_oll1_c	SB6_oll1_r	SB6_ol2_c	SB6_ol2_r	SB6_ol3_c	SB6_ol3_r	SB6_cpx1_c	SB6_cpx1_r	SB6_cpx2_c	SB6_cpx2_r	SB6_cpx3_c	SB6_cpx3_r	SB6_cpx4_c	SB6_cpx4_r	SB6_opx1_c	SB6_opx1_r	SB6_opx2_c	SB6_opx2_r	SB6_opx3_c	SB6_opx3_r	SB6_smescinopx	SB6_sp1_c	SB6_sp1_r	SB6_sp2_c	SB6_sp2_r
Rock type	Lh	Lh	Lh	Lh	Lh	Lh	Lh	Lh	Lh	Lh	Lh	Lh	Lh	Lh	Lh	Lh	Lh	Lh	Lh	Lh	Lh	Lh	Lh	Lh	Lh
phase	oll core	oll rim	oll core	oll rim	oll core	oll rim	cpx1 core	cpx1 rim	cpx1 core	cpx1 rim	cpx1 core	cpx1 rim	cpx1 core	cpx1 rim	opx core	opx rim	opx core	opx rim	opx core	opx rim	opx smesc	sp1 core	sp1 rim	sp1 core	sp1 rim
SiO_2	41.28	40.81	40.90	40.69	41.04	41.09	52.75	52.79	51.78	52.89	53.11	52.48	51.81	53.06	56.09	56.81	56.50	56.62	56.40	56.92	55.21	0.02	0.04	0.02	0.09
TiO_2	0.00	0.00	0.00	0.00	0.00	0.00	0.40	0.36	0.44	0.41	0.32	0.30	0.41	0.06	0.11	0.06	0.08	0.07	0.07	0.06	0.23	0.06	0.06	0.09	0.09
Al_2O_3	0.01	0.01	0.01	0.01	0.00	0.00	4.12	4.51	5.11	3.92	3.77	2.28	5.24	3.95	3.14	2.63	3.03	2.88	3.12	2.57	3.36	49.52	48.52	49.38	50.71
FeO	9.20	9.34	9.16	9.20	9.09	9.34	2.52	2.91	2.41	3.10	2.38	2.63	2.46	2.46	6.05	6.09	6.04	6.12	6.17	6.09	5.55	12.63	13.11	13.02	11.98
MnO	0.13	0.15	0.14	0.12	0.15	0.09	0.11	0.07	0.09	0.11	0.07	0.09	0.08	0.15	0.16	0.15	0.15	0.14	0.16	0.14	0.12	0.07	0.09	0.09	0.06
MgO	49.85	49.06	49.46	49.48	49.03	49.36	17.00	17.13	15.40	17.39	16.16	17.08	15.39	15.84	33.87	34.26	33.81	33.91	33.85	34.06	30.10	19.39	19.22	19.53	19.36
CaO	0.04	0.11	0.03	0.03	0.02	0.09	22.01	21.04	22.64	21.68	23.07	22.28	22.64	22.99	0.43	0.44	0.43	0.42	0.37	0.41	4.61	0.00	0.01	0.00	0.00
Na_2O	0.00	0.01	0.00	0.01	0.00	0.01	0.93	0.67	0.99	0.57	0.81	0.56	0.94	0.75	0.02	0.02	0.01	0.00	0.00	0.10					
K_2O																									
Cr_2O_3	0.01	0.00	0.00	0.01	0.00	0.01	0.84	0.90	1.25	0.53	0.76	1.34	1.11	0.70	0.37	0.27	0.38	0.37	0.40	0.27	0.49	17.89	18.69	18.30	17.95
NiO	0.35	0.37	0.38	0.40	0.39	0.37	0.04	0.06	0.01	0.05	0.05	0.06	0.05	0.01	0.04	0.07	0.05	0.07	0.07	0.07	0.07	0.30	0.29	0.31	0.30
Tot	100.88	99.85	100.08	99.93	99.69	100.42	100.70	100.49	100.09	100.60	100.45	99.98	100.30	100.22	100.27	100.84	100.50	100.56	100.66	101.61	99.85	100.09	100.28	100.99	100.77
mg#	90.62	90.35	90.58	90.55	90.58	90.40	92.31	91.29	91.92	90.92	92.37	92.04	91.77	91.98	90.89	90.93	90.89	90.81	90.72	90.89	90.62	73.24	72.31	72.78	74.22
cr#																						19.51	20.54	19.91	19.19

Sample	SB7_ol1_c	SB7_ol1_r	SB7_ol2_c	SB7_ol3_c	SB7_ol3_r	SB7_ol4_c	SB7_ol4_r	SB7_cpxsec1_c	SB7_cpxsec1_r	SB7_cpxsec2_c	SB7_cpxsec2_r	SB7_sp1_c	SB7_sp1_r	SB7_sp2_c
Rock type	Dn	Dn	Dn	Dn	Dn	Dn	Dn	Dn	Dn	Dn	Dn	Dn	Dn	Dn
phase	ol1 core	ol1 rim	ol1 core	ol1 core	ol1 rim	ol1 core	ol1 rim	cpx2 core	cpx2 rim	cpx2 core	cpx2 rim	sp1 core	sp1 rim	sp1 core
SiO_2	40.76	40.65	40.68	41.14	41.18	41.05	40.85	52.17	51.34	50.80	50.77	0.00	0.01	0.00
TiO_2	0.00	0.00	0.00	0.01	0.00	0.00	0.00	0.41	0.84	0.62	1.05	0.55	0.58	0.59
Al_2O_3	0.00	0.00	0.00	0.00	0.00	0.00	0.00	3.42	3.41	4.65	4.37	8.13	9.48	9.32
FeO	9.25	9.03	9.16	9.05	9.22	9.09	8.98	2.10	3.26	2.15	3.48	22.44	20.85	21.74
MnO	0.22	0.17	0.21	0.22	0.23	0.22	0.22	0.03	0.06	0.05	0.05	0.21	0.25	0.25
MgO	49.04	49.09	49.52	49.63	49.41	49.33	49.59	16.29	15.92	15.11	15.23	12.41	12.32	12.02
CaO	0.06	0.12	0.07	0.07	0.06	0.06	0.15	23.16	24.13	22.61	24.40	0.00	0.00	0.01
Na_2O	0.00	0.00	0.00	0.01	0.00	0.00	0.00	0.70	0.34	1.05	0.40			
K_2O								0.00	0.00	0.01	0.02			
Cr_2O_3	0.01	0.02	0.01	0.02	0.01	0.02	0.02	2.02	0.32	3.06	0.27	54.29	54.84	54.31
NiO	0.39	0.38	0.38	0.39	0.39	0.39	0.41	0.04	0.08	0.02	0.06	0.17	0.16	0.18
Tot	99.71	99.45	100.02	100.52	100.50	100.16	100.22	100.35	99.70	100.12	100.09	98.49	98.76	98.67
mg#	90.43	90.64	90.60	90.72	90.52	90.63	90.78	93.24	89.71	92.62	88.64	49.64	51.29	49.64
cr#												81.75	79.51	79.63

Table 5. Major oxides composition of minerals forming Eulenberg xenoliths

Sample	EUL-1	EUL-1	EUL-1	EUL-1	EUL-1	EUL-1	EUL-1	EUL-1	EUL-1	EUL-1	EUL-1	EUL-1	EUL-1
Rock type	Hz	Hz	Hz	Hz	Hz	Hz	Hz	Hz	Hz	Hz	Hz	Hz	Hz
phase	ol1	ol1	ol1	ol1	cpx1	cpx1	cpx1	opx	opx	opx	sp1	sp1	sp1
SiO_2	40.54	40.42	40.20	40.76	52.75	52.34	52.37	56.50	56.17	56.25	0.04	0.03	0.00
TiO_2	-0.01	0.00	0.00	0.00	0.17	0.21	0.22	0.02	0.03	0.03	0.05	0.04	0.02
Al_2O_3	0.01	0.00	0.02	0.01	2.50	2.80	2.64	1.99	2.16	2.32	51.57	51.17	51.32
FeO	9.16	9.25	9.37	9.36	2.32	2.33	2.26	6.14	6.28	6.14	12.57	12.39	12.45
MnO	0.14	0.11	0.12	0.12	0.07	0.07	0.07	0.15	0.15	0.16	0.14	0.16	0.15
MgO	49.42	49.59	49.83	49.78	17.41	16.71	16.77	34.77	34.44	34.30	20.36	20.68	20.75
CaO	0.08	0.05	0.03	0.03	23.64	24.29	24.24	0.36	0.32	0.29	-0.01	0.01	0.00
Na_2O	0.00	0.00	0.00	0.01	0.28	0.28	0.26	0.01	0.00	0.01			
K_2O													
Cr_2O_3	0.01	0.00	0.00	0.01	0.44	0.56	0.62	0.19	0.23	0.25	14.26	14.47	14.31
NiO	0.42	0.37	0.39	0.36	0.06	0.03	0.06	0.04	0.10	0.07	0.35	0.33	0.35
Tot	99.77	99.80	99.96	100.44	99.65	99.62	99.52	100.15	99.88	99.83	99.48	99.46	99.57
mg#	90.58	90.52	90.46	90.46	93.03	92.75	92.96	90.99	90.72	90.86	74.26	74.83	74.81
cr#											15.65	15.94	15.76

Sample	ELU-2	ELU-2	ELU-2	ELU-2	ELU-2	ELU-2	ELU-2	ELU-2	ELU-2	ELU-2	ELU-2	ELU-2	ELU-2	ELU-2	ELU-2
Rock type	Hz	Hz	Hz	Hz	Hz	Hz	Hz	Hz	Hz	Hz	Hz	Hz	Hz	Hz	Hz
phase	ol	ol	ol	ol	cpx	cpx	cpx	cpx	opx	opx	opx	opx	sp	sp	sp
SiO_2	40.64	38.79	40.42	40.42	53.50	53.37	53.66	53.52	56.15	56.36	56.52	56.51	0.05	0.03	0.04
TiO_2	-0.01	-0.01	0.00	-0.01	0.07	0.13	0.07	0.05	0.04	0.03	0.03	0.02	0.15	0.18	0.22
Al_2O_3	0.00	0.00	0.00	0.00	2.05	1.75	1.56	1.59	2.41	2.16	2.02	2.00	44.22	44.37	44.11
FeO	8.99	8.72	8.93	8.96	2.39	2.03	2.00	2.10	6.21	6.16	6.13	6.05	13.77	13.66	13.67
MnO	0.13	0.15	0.15	0.12	0.08	0.05	0.06	0.08	0.14	0.15	0.15	0.14	0.24	0.23	0.22
MgO	49.63	47.42	49.55	50.06	17.34	17.12	17.39	17.36	34.10	34.35	34.57	34.42	18.71	18.95	18.92
CaO	0.06	0.07	0.06	0.12	23.33	24.62	24.65	24.63	0.31	0.31	0.28	0.34	0.04	0.03	0.03
Na_2O	0.01	0.01	0.01	-0.02	0.44	0.23	0.19	0.17	0.00	0.01	0.01	0.01			
K_2O															
Cr_2O_3	0.02	0.00	0.01	0.02	0.28	0.45	0.38	0.33	0.29	0.27	0.24	0.22	21.71	21.42	21.55
NiO	0.37	0.36	0.35	0.30	0.05	0.04	0.01	0.03	0.06	0.06	0.08	0.09	0.26	0.25	0.28
Tot	99.84	95.51	99.48	99.99	99.52	99.78	99.98	99.85	99.71	99.87	100.04	99.81	99.38	99.39	99.28
mg#	90.77	90.64	90.81	90.87	92.82	93.77	93.92	93.64	90.73	90.86	90.94	91.02	70.77	71.20	71.15
cr#													24.77	24.46	24.68

Sample	EUL4_ol1_c	EUL4_ol1_r	SB5_ol2_c	SB5_ol3_c	SB5_ol3_r	SB5_cpx1_c	SB5_cpx1_r	SB5_cpx2_c	SB5_cpx2_r	SB5_cpx3_c	SB5_cpx3_r	SB5_opx1_c	SB5_opx1_r	SB5_opx2_c	SB5_opx2_r	SB5_opx3_c	SB5_opx3_r	SB5_sp1_c	SB5_sp1_r	SB5_sp2_c	SB5_sp2_r	SB5_sp3_c	SB5_sp3_r
Rock type	Hz	Hz	Hz	Hz	Hz	Hz	Hz	Hz	Hz	Hz	Hz	Hz	Hz	Hz	Hz	Hz	Hz	Hz	Hz	Hz	Hz	Hz	Hz
phase	ol1	ol1	ol1	ol1	ol1	cpx1	cpx1	cpx1	cpx1	cpx1	cpx1	opx	opx	opx	opx	opx	opx	sp1	sp1	sp1	sp1	sp1	sp1
	core	rim	core	core	rim	core	rim	core	rim	core	rim	core	rim	core	rim	core	rim	core	rim	core	rim	core	rim
SiO_2	40.98	40.70	40.64	41.02	40.92	54.14	54.13	54.25	54.47	53.29	54.82	56.76	57.38	56.51	57.78	56.45	57.40	0.02	0.04	0.02	0.03	0.01	0.06
TiO_2	0.00	0.00	0.00	0.01	0.00	0.03	0.04	0.06	0.05	0.04	0.03	0.02	0.01	0.02	0.01	0.03	0.04	0.02	0.01	0.02	0.04	0.00	0.02
Al_2O_3	0.01	0.00	0.01	0.00	0.01	1.81	1.63	1.85	1.68	2.52	1.43	2.91	1.52	3.12	1.52	2.64	2.00	43.41	43.45	43.94	44.01	44.09	42.89
FeO	8.87	8.84	8.68	8.70	9.16	1.94	2.02	2.00	1.95	2.34	2.21	5.95	5.73	5.94	5.84	6.02	6.06	13.93	13.66	13.71	12.16	13.65	13.18
MnO	0.12	0.14	0.13	0.17	0.13	0.05	0.05	0.05	0.04	0.05	0.07	0.13	0.14	0.14	0.16	0.14	0.14	0.08	0.09	0.09	0.10	0.11	0.09
MgO	49.46	49.30	49.98	49.81	49.69	17.24	17.13	17.28	17.24	17.29	17.80	34.12	34.42	33.92	34.87	34.31	34.64	18.87	18.17	19.24	18.24	19.14	18.47
CaO	0.02	0.02	0.01	0.02	0.13	24.33	24.21	24.00	24.27	23.55	24.12	0.31	0.34	0.40	0.30	0.30	0.30	0.01	0.04	0.00	0.00	0.00	0.02
Na_2O	0.00	0.00	0.00	0.00	0.00	0.28	0.29	0.32	0.28	0.46	0.27	0.00	0.02	0.02	0.00	0.01	0.00						
K_2O						0.00	0.01	0.00	0.00	0.00	0.01	0.01	0.00	0.00	0.00	0.00							
Cr_2O_3	0.01	0.01	0.01	0.01	0.04	0.48	0.46	0.49	0.52	0.50	0.25	0.49	0.25	0.56	0.17	0.42	0.40	23.54	24.20	22.85	25.13	22.85	24.88
NiO	0.43	0.40	0.40	0.40	0.34	0.04	0.04	0.03	0.06	0.04	0.04	0.07	0.08	0.07	0.13	0.07	0.10	0.27	0.29	0.26	0.25	0.31	0.28
Tot	99.90	99.40	99.86	100.12	100.41	100.33	100.00	100.31	100.55	100.07	101.05	100.76	100.16	100.71	100.78	100.39	101.05	100.40	100.16	100.35	100.21	100.39	100.14
mg#	90.86	90.85	91.12	91.08	90.62	94.07	93.81	93.91	94.03	92.96	93.48	91.09	91.46	91.05	91.41	91.04	91.06	70.70	70.34	71.44	72.78	71.42	71.41
cr#																		26.67	27.20	25.86	27.69	25.80	28.01

Sample	EUL5_ol1_c	EUL5_ol1_r	EUL5_ol2_c	EUL5_ol2_r	EUL5_ol3_c	EUL5_ol3_r	EUL5_cpxsec1_c	EUL5_cpxsec1_r	EUL5_cpx2_c	EUL5_cpx2_r	EUL5_cpx3_c	EUL5_opx1_c	EUL5_opx1_r	EUL5_opx2_c	EUL5_opx2_r	EUL5_opx3_c	EUL5_opx3_r	EUL5_sp1_c	EUL5_sp1_r	EUL5_sp2_c	EUL5_sp2_r	EUL5_sp3_c	EUL5_sp3_r	EUL5_sp4_c
Rock type	Hz	Hz	Hz	Hz	Hz	Hz	Hz	Hz	Hz	Hz	Hz	Hz	Hz	Hz	Hz	Hz	Hz	Hz	Hz	Hz	Hz	Hz	Hz	Hz
phase	oll core	oll rim	oll core	oll rim	oll core	oll rim	cpx2 core	cpx2 rim	cpx1 core	cpx1 rim	cpx1 core	opx core	opx rim	opx core	opx rim	opx core	opx rim	spl core	spl rim	spl core	spl rim	spl core	spl rim	spl core
SiO_2	41.22	41.13	40.93	40.99	40.87	40.79	53.74	54.54	52.91	54.69	54.12	56.73	57.63	56.78	57.64	56.85	57.17	0.04	0.02	0.03	0.07	0.02	0.02	0.02
TiO_2	0.00	0.00	0.00	0.00	0.00	0.00	0.12	0.01	0.04	0.01	0.04	0.00	0.03	0.01	0.03	0.02	0.00	0.00	0.00	0.00	0.02	0.00	0.02	0.02
Al_2O_3	0.00	0.01	0.00	0.00	0.00	0.03	3.23	2.06	3.98	1.83	2.21	2.66	1.77	2.52	1.94	2.85	2.20	42.95	41.68	40.84	36.52	43.87	39.92	43.91
FeO	8.13	8.33	8.25	8.09	8.26	8.03	2.45	2.16	2.50	2.03	2.04	5.52	5.47	5.31	5.36	5.42	5.48	12.40	12.63	12.47	13.16	12.46	13.31	12.92
MnO	0.13	0.11	0.13	0.09	0.10	0.11	0.07	0.07	0.05	0.06	0.07	0.14	0.12	0.15	0.13	0.12	0.12	0.08	0.09	0.10	0.08	0.09	0.09	0.08
MgO	50.08	50.15	50.13	50.18	50.12	50.24	18.46	17.21	17.47	17.36	17.06	34.40	35.05	34.12	34.80	34.31	34.54	19.16	18.80	19.09	17.90	19.27	18.25	18.79
CaO	0.03	0.02	0.03	0.05	0.05	0.21	20.37	23.45	20.75	23.49	23.54	0.45	0.49	0.46	0.54	0.45	0.49	0.00	0.01	0.00	0.04	0.01	0.03	0.00
Na_2O	0.00	0.00	0.00	0.01	0.00	0.00	0.79	0.70	0.74	0.47	0.61	0.04	0.03	0.05	0.03	0.03	0.03							
K_2O							0.00	0.01	0.01	0.00	0.00	0.02	0.00	0.00	0.00	0.00	0.01							
Cr_2O_3	0.01	0.01	0.00	0.01	0.01	0.02	1.03	0.48	1.55	0.38	0.45	0.37	0.24	0.33	0.31	0.41	0.32	25.12	26.79	27.19	31.10	24.10	27.81	23.85
NiO	0.41	0.39	0.41	0.39	0.41	0.36	0.06	0.06	0.02	0.05	0.07	0.05	0.10	0.08	0.10	0.10	0.10	0.25	0.20	0.22	0.23	0.27	0.21	0.27
Tot	100.00	100.14	99.86	99.80	99.81	99.77	100.32	100.76	100.02	100.38	100.21	100.37	100.91	99.81	100.87	100.56	100.45	100.18	100.44	100.17	99.35	100.30	99.88	100.08
mg#	91.65	91.47	91.55	91.70	91.54	91.77	93.06	93.41	92.57	93.84	93.71	91.74	91.95	91.97	92.04	91.86	91.83	73.36	72.63	73.17	70.79	73.39	70.96	72.16
cr#																		28.18	30.13	30.87	36.35	26.92	31.85	26.71

Table 5.6 - Geochemistry of noble gas in fluid inclusions hosted in minerals of mantle xenoliths from Eifel and Siebengebirge (Germany). Oliv stands for olivine, Opx for orthopyroxene, and Cpx for clinopyroxene.

Sample	Mineral	weight (g)	^{4}He mol/g	^{3}He	^{20}Ne mol/g	^{21}Ne mol/g	^{22}Ne mol/g	CO_2	N_2*	Air mol/g	^{40}Ar mol/g	^{36}Ar mol/g	^{40}Ar* mol/g
MM1	Oliv	0.67	1.9E-12	1.6E-17	6.0E-15	1.7E-17	6.1E-16	1.6E-10	2.0E-09	3.1E-10	3.3E-12	9.6E-15	4.8E-13
MM2	Oliv	0.74	9.6E-13	8.9E-18	1.6E-15	4.5E-18	1.6E-16	3.7E-10	3.1E-09	1.2E-10	4.4E-12	3.6E-15	3.3E-12
MM3	Oliv	0.63	8.9E-13	8.3E-18	1.9E-15	5.9E-18	2.0E-16	2.3E-10	2.9E-09	3.0E-10	3.3E-12	9.3E-15	5.4E-13
MM4	Oliv	0.69	1.7E-12	1.4E-17	8.2E-15	2.4E-17	8.3E-16	4.1E-10	7.0E-09	3.8E-10	7.2E-12	1.2E-14	3.7E-12
MM5	Oliv	0.64	6.1E-13	5.2E-18	2.0E-15	5.3E-18	2.0E-16	1.2E-10	7.4E-10	9.0E-11	1.4E-12	2.8E-15	5.5E-13
MM6	Oliv	0.67	9.1E-13	7.8E-18	1.4E-15	4.2E-18	1.4E-16	1.2E-10	1.9E-09	6.2E-11	2.3E-12	2.0E-15	1.8E-12
MM7	Oliv	0.70	2.5E-12	1.9E-17	4.8E-15	1.5E-17	4.9E-16	3.4E-10	2.3E-09	3.3E-10	6.4E-12	1.0E-14	3.3E-12
MM8	Oliv	0.66	4.3E-12	3.8E-17	6.1E-15	1.8E-17	6.2E-16	2.0E-09	1.6E-09	3.3E-10	6.3E-12	1.0E-14	3.2E-12
MM9	Oliv	0.70	2.2E-12	1.9E-17	7.3E-15	2.2E-17	7.4E-16	5.5E-10	3.3E-09	3.5E-10	7.3E-12	1.1E-14	4.0E-12
DBR2	Oliv	0.73	7.6E-12	6.3E-17	1.8E-14	5.3E-17	1.8E-15	9.2E-11	4.0E-09	8.6E-10	2.1E-11	2.7E-14	1.3E-11
DBR5	Oliv	0.69	3.0E-13	2.4E-18	4.4E-16	1.3E-18	4.4E-17	2.9E-10	4.2E-10	2.3E-11	5.0E-13	7.2E-16	2.9E-13
DBR6	Oliv	0.69	2.7E-12	2.3E-17	2.5E-15	7.5E-18	2.5E-16	5.5E-11	1.1E-09	1.5E-10	5.4E-12	4.8E-15	4.0E-12
DBR9	Oliv	0.68	9.1E-13	7.5E-18	1.0E-15	3.2E-18	1.0E-16	1.4E-10	9.0E-11	5.9E-11	2.3E-12	1.9E-15	1.8E-12
GE1	Oliv	0.34	2.0E-12	1.5E-17	8.5E-15	2.5E-17	8.6E-16	1.1E-08	1.5E-09	1.5E-10	2.8E-12	4.7E-15	1.4E-12
EUL2	Oliv	0.15	5.9E-13	4.9E-18	5.5E-16	2.0E-18	5.5E-17	1.8E-08	1.6E-09	9.0E-11	4.1E-12	2.8E-15	3.2E-12
EUL5	Oliv	0.68	8.7E-13	8.2E-18	4.9E-16	1.2E-18	5.0E-17	3.6E-09	8.9E-10	8.1E-11	2.5E-12	2.6E-15	1.7E-12
SB3	Oliv	0.69	1.0E-13	8.5E-19	4.8E-16	1.5E-18	4.6E-17	1.0E-09	5.2E-10	1.5E-11	1.1E-12	4.8E-16	9.7E-13
SB5	Oliv	0.64	1.3E-13	1.1E-18	6.9E-16	2.1E-18	6.9E-17	1.1E-09	2.8E-10	4.7E-11	2.3E-12	1.5E-15	1.8E-12
MM2	Opx	0.53	5.9E-13	5.2E-18	1.3E-15	4.1E-18	1.3E-16	2.9E-10	1.3E-09	9.6E-11	2.7E-12	3.0E-15	1.8E-12
MM3	Opx	0.51	1.1E-12	9.4E-18	2.8E-15	9.0E-18	2.9E-16	6.7E-09	3.0E-09	1.7E-10	2.3E-12	5.2E-15	7.8E-13
MM4	Opx	0.22	6.7E-12	5.5E-17	1.7E-14	5.2E-17	1.7E-15	2.6E-07	4.8E-09	5.2E-10	2.9E-11	1.6E-14	2.4E-11
MM5	Opx	0.71	5.5E-13	5.0E-18	7.3E-15	2.0E-17	7.4E-16	8.6E-11	1.0E-09	1.1E-10	2.7E-12	3.4E-15	1.7E-12
MM6	Opx	0.51	4.7E-13	4.0E-18	2.7E-15	7.9E-18	2.7E-16	1.3E-08	1.2E-09	6.6E-11	2.7E-12	2.1E-15	2.1E-12
MM7	Opx	0.42	5.0E-12	3.9E-17	3.3E-15	1.1E-17	3.3E-16	5.8E-08	1.5E-09	1.4E-10	1.1E-11	4.5E-15	9.6E-12
MM8	Opx	0.32	5.0E-12	4.4E-17	1.7E-14	5.1E-17	1.7E-15	9.6E-08	4.9E-09	4.2E-10	1.6E-11	1.3E-14	1.2E-11
MM9	Opx	0.54	5.4E-12	4.6E-17	2.2E-14	6.7E-17	2.2E-15	2.0E-07	2.8E-09	5.1E-10	2.3E-11	1.6E-14	1.8E-11
DBR5	Opx	0.80	7.9E-12	7.0E-17	2.9E-15	1.0E-17	2.7E-16	1.9E-07	2.1E-09	1.1E-10	2.0E-11	3.5E-15	1.9E-11
DBR6	Opx	0.42	1.5E-11	1.3E-16	9.4E-15	3.0E-17	8.9E-16	5.1E-07	3.7E-09	2.2E-10	5.0E-11	6.9E-15	4.8E-11
DBR9	Opx	0.40	6.3E-12	5.5E-17	6.2E-15	1.8E-17	6.1E-16	1.5E-07	2.5E-09	1.8E-10	1.9E-11	5.8E-15	1.7E-11
GE1	Opx	0.41	1.3E-11	9.9E-17	3.9E-14	1.1E-16	4.0E-15	4.7E-07	6.4E-09	2.2E-10	1.1E-11	6.9E-15	9.2E-12
EUL2	Opx	0.52	2.6E-13	2.4E-18	9.7E-16	2.9E-18	9.7E-17	2.4E-09	6.6E-10	4.7E-10	5.7E-12	1.5E-14	1.3E-12
EUL5	Opx	0.50	7.7E-13	7.4E-18	3.9E-15	1.1E-17	3.9E-16	5.7E-09	6.0E-10	2.8E-10	4.0E-12	8.8E-15	1.4E-12
SB3	Opx	0.48	5.3E-13	4.4E-18	1.1E-15	3.4E-18	1.1E-16	6.7E-09	1.5E-09	1.3E-10	2.5E-12	4.1E-15	1.3E-12
SB5	Opx	0.86	3.1E-13	1.4E-18	1.6E-14	4.6E-17	1.6E-15	8.8E-10	8.3E-10	5.8E-10	5.9E-12	1.8E-14	5.9E-13
SB5	Opx	0.53	1.7E-13	7.5E-19	4.3E-15	1.3E-17	4.4E-16	2.5E-11	5.7E-10	1.5E-10	1.8E-12	4.8E-15	3.6E-13
MM1	Cpx	0.12	3.2E-11	2.7E-16	6.5E-15	2.0E-17	6.3E-16	1.2E-06	4.1E-09	2.2E-10	1.0E-11	6.9E-15	7.9E-12
MM4	Cpx	0.10	1.4E-11	1.2E-16	5.3E-15	1.9E-17	4.9E-16	6.0E-07	6.0E-09	1.9E-10	5.7E-11	5.9E-15	5.6E-11
MM6	Cpx	0.30	4.0E-12	3.4E-17	3.5E-15	1.1E-17	3.5E-16	1.6E-08	3.8E-09	1.9E-10	1.5E-11	6.0E-15	1.4E-11
MM7	Cpx	0.21	8.4E-12	6.5E-17	2.3E-15	8.0E-18	2.1E-16	1.1E-07	2.0E-09	7.9E-11	1.7E-11	2.5E-15	1.7E-11
MM8	Cpx	0.22	2.4E-11	2.3E-16	9.3E-15	3.0E-17	9.1E-16	1.0E-06	4.5E-09	4.4E-10	2.5E-11	1.4E-14	2.1E-11
MM9	Cpx	0.14	9.5E-12	8.4E-17	6.4E-15	2.4E-17	6.2E-16	2.8E-07	6.8E-09	2.8E-10	3.7E-11	8.8E-15	3.5E-11
DBR2	Cpx	0.10	2.0E-11	1.6E-16	5.4E-15	2.0E-17	5.0E-16	3.3E-07	5.2E-09	2.5E-10	3.8E-11	8.0E-15	3.5E-11
DBR5	Cpx	0.13	1.4E-11	1.2E-16	3.5E-15	1.3E-17	3.2E-16	2.7E-07	3.9E-09	1.5E-10	3.7E-11	4.6E-15	3.5E-11
DBR6	Cpx	0.11	2.2E-11	1.8E-16	9.2E-15	3.3E-17	8.6E-16	7.2E-07	7.5E-09	4.1E-10	6.9E-11	1.3E-14	6.6E-11
DBR9	Cpx	0.23	1.2E-11	1.0E-16	7.0E-15	2.3E-17	6.7E-16	2.7E-07	3.6E-09	2.2E-10	3.1E-11	6.8E-15	2.9E-11
GE1	Cpx	0.12	4.1E-11	3.3E-16	6.9E-14	2.1E-16	6.9E-15	1.3E-06	1.1E-08	8.7E-10	3.2E-11	2.7E-14	2.4E-11

Sample	Mineral	^{4}He/^{20}Ne	^{4}He/^{40}Ar*	R/Ra	Rc/Ra	Err Rc/Ra +/-	^{40}Ar/^{36}Ar	Err (%)	^{38}Ar/^{36}Ar	Err (%)	^{20}Ne/^{22}Ne	Err 20/22 +/-	^{21}Ne/^{22}Ne	Err 21/22 +/-	Mg#	CO$_2$/^{3}He	^{3}He/^{36}Ar
MM1	Oliv	310.1	3.91	6.28	6.28	0.07	344.8	0.1	0.18664	0.184	9.90	0.02	0.0289	0.0004	86.7	1.02E+07	1.69E-03
MM2	Oliv	599.2	0.29	6.66	6.66	0.08	1209.6	0.1	0.18400	0.181	9.90	0.06			91.2	4.12E+07	2.46E-03
MM3	Oliv	459.7	1.65	6.68	6.68	0.07	353.7	0.1	0.18662	0.184	9.88	0.04	0.0301	0.0005	90.8	2.83E+07	8.91E-04
MM4	Oliv	212.3	0.47	5.74	5.75	0.11	600.3	0.0	0.18634	0.184	9.92	0.02	0.0295	0.0004	91.1	2.93E+07	1.15E-03
MM5	Oliv	310.0	1.11	6.15	6.15	0.08	490.3	0.1	0.18599	0.183	9.82	0.06			91.1	2.38E+07	1.84E-03
MM6	Oliv	648.2	0.51	6.21	6.21	0.08	1199.2	0.2	0.18675	0.184	10.11	0.08	0.0306	0.0008	91.2	1.53E+07	4.01E-03
MM7	Oliv	521.9	0.77	5.45	5.46	0.06	607.8	0.0	0.18597	0.186	9.89	0.02	0.0298	0.0005	91.6	1.77E+07	1.82E-03
MM8	Oliv	702.9	1.32	6.31	6.31	0.06	607.3	0.1	0.18570	0.185	9.98	0.03	0.0295	0.0005	90.9	5.40E+07	3.61E-03
MM9	Oliv	303.6	0.56	6.02	6.03	0.08	652.3	0.0	0.18538	0.185	9.97	0.02	0.0300	0.0005	90.2	2.94E+07	1.68E-03
DBR2	Oliv	423.8	0.57	5.93	5.93	0.05	784.0	0.0	0.18564	0.185	10.06	0.02	0.0299	0.0003	87.8	1.47E+06	2.31E-03
DBR5	Oliv	670.4	1.03	5.74	5.74	0.11	699.3	0.4	0.19238	0.192	10.05	0.17	0.0303	0.0012	89.4	1.21E+08	3.31E-03
DBR6	Oliv	1095.4	0.68	6.04	6.04	0.07	1121.5	0.1	0.18734	0.187	10.08	0.05	0.0308	0.0007	90.3	2.44E+06	4.72E-03
DBR9	Oliv	892.9	0.51	5.94	5.94	0.07	1256.0	0.1	0.18486	0.184	10.02	0.07	0.0315	0.0012	89.7	1.85E+07	4.05E-03
GE1	Oliv	232.3	1.37	5.49	5.49	0.06	597.5	0.1	0.18611	0.186	9.91	0.03	0.0288	0.0005	83.4	7.41E+08	3.16E-03
EUL2	Oliv	1070.0	0.18	6.01	6.02	0.11	1427.6	0.3	0.19043	0.190	11.02	0.40	0.0372	0.0034	90.8	3.71E+09	1.73E-03
EUL5	Oliv	1760.6	0.50	6.79	6.79	0.09	971.8	0.0	0.18865	0.188	10.24	0.14			91.6	4.35E+08	3.20E-03
SB3	Oliv	208.4	0.10	6.09	6.10	0.15	2344.4	0.5	0.19209	0.192	10.32	0.12	0.0323	0.0014	91.3	1.19E+09	1.78E-03
SB5	Oliv	182.2	0.07	6.13	6.14	0.15	1522.2	0.2	0.18682	0.186	10.10	0.09	0.0306	0.0016	90.9	1.02E+09	7.26E-04
MM2	Opx	463.1	0.33	6.38	6.38	0.09	876.8	0.1	0.18590	0.185	10.19	0.10	0.0325	0.0009	91.4	5.56E+07	1.72E-03
MM3	Opx	384.2	1.39	6.26	6.26	0.08	444.2	0.1	0.18477	0.184	9.98	0.05	0.0321	0.0007	91.3	7.16E+08	1.80E-03
MM4	Opx	389.3	0.28	5.94	5.94	0.08	1777.9	0.0	0.18689	0.186	10.04	0.03	0.0307	0.0006	91.5	4.71E+09	3.37E-03
MM5	Opx	75.7	0.32	6.52	6.55	0.09	792.0	0.1	0.18647	0.186	9.87	0.02			91.6	1.72E+07	1.47E-03
MM6	Opx	174.6	0.22	6.17	6.18	0.09	1328.4	0.2	0.18612	0.186	9.84	0.05	0.0294	0.0008	91.4	3.28E+09	1.96E-03
MM7	Opx	1535.0	0.53	5.56	5.56	0.08	2419.7	0.0	0.18746	0.187	10.16	0.06	0.0334	0.0005	91.7	1.50E+09	8.64E-03
MM8	Opx	301.8	0.41	6.34	6.34	0.09	1235.9	0.0	0.18578	0.185	9.98	0.02	0.0306	0.0004	91.2	2.18E+09	3.37E-03
MM9	Opx	245.4	0.30	6.15	6.16	0.09	1402.0	0.0	0.18755	0.187	10.04	0.02	0.0306	0.0004	90.3	4.27E+09	2.87E-03
DBR5	Opx	2754.0	0.41	6.38	6.38	0.07	5682.6	0.0	0.19687	0.197	10.86	0.05	0.0386	0.0006	89.5	2.71E+09	1.98E-02
DBR6	Opx	1571.7	0.31	6.43	6.43	0.07	7192.1	0.0	0.19898	0.199	10.54	0.04	0.0342	0.0007	90.4	3.88E+09	1.89E-02
DBR9	Opx	1008.9	0.36	6.26	6.26	0.07	3304.8	0.0	0.18748	0.188	10.32	0.04	0.0303	0.0008	90.3	2.68E+09	9.45E-03
GE1	Opx	321.0	1.36	5.65	5.66	0.06	1625.3	0.1	0.18432	0.185	9.89	0.01	0.0291	0.0003	84.9	4.72E+09	1.42E-02
EUL2	Opx	269.9	0.20	6.72	6.73	0.12	383.2	0.1	0.18589	0.186	10.01	0.11	0.0307	0.0020	91.3	9.80E+08	1.64E-04
EUL5	Opx	200.3	0.55	6.83	6.84	0.09	456.0	0.1	0.18633	0.187	9.95	0.06	0.0294	0.0009	91.9	7.69E+08	8.34E-04
SB3	Opx	470.2	0.41	6.03	6.03	0.09	605.4	0.1	0.18868	0.189	10.07	0.13	0.0308	0.0026	91.5	1.52E+09	1.07E-03
SB5	Opx	19.6	0.52	3.23	3.27	0.05	327.9	0.1	0.18576	0.186	9.83	0.02	0.0290	0.0003	91.8	6.26E+08	7.73E-05
SB5	Opx	40.4	0.48	3.08	3.10	0.07	369.9	0.1	0.18759	0.187	9.86	0.04	0.0290	0.0007	91.8	3.38E+07	1.55E-04
MM1	Cpx	4928.7	4.04	6.19	6.19	0.07	1444.6	0.2	0.18348	0.184	10.52	0.07	0.0325	0.0015	87.0	4.47E+09	3.99E-02
MM4	Cpx	2665.2	0.25	6.26	6.26	0.07	9797.2	0.2	0.19609	0.196	11.03	0.04	0.0395	0.0011	91.1	4.83E+09	2.10E-02
MM6	Cpx	1129.2	0.29	6.14	6.14	0.07	2561.6	0.1	0.18519	0.185	10.06	0.06	0.0316	0.0009	92.3	4.59E+08	5.70E-03
MM7	Cpx	3650.3	0.50	5.64	5.64	0.06	6987.0	0.2	0.19402	0.194	10.95	0.13	0.0383	0.0020	91.4	1.63E+09	2.63E-02
MM8	Cpx	2634.3	1.15	6.75	6.76	0.07	1815.4	0.1	0.18667	0.187	10.26	0.04	0.0328	0.0008	90.9	4.56E+09	1.64E-02
MM9	Cpx	1490.3	0.27	6.37	6.37	0.07	4258.3	0.1	0.18803	0.188	10.44	0.07	0.0397	0.0015	89.9	3.37E+09	9.63E-03
DBR2	Cpx	3672.3	0.56	5.89	5.89	0.05	4721.4	0.0	0.19337	0.193	10.90	0.12	0.0403	0.0016	87.8	2.04E+09	2.04E-02
DBR5	Cpx	3983.9	0.39	6.40	6.40	0.07	7947.0	0.1	0.19404	0.194	10.89	0.11	0.0417	0.0022	88.1	2.22E+09	2.67E-02
DBR6	Cpx	2372.9	0.33	6.06	6.06	0.05	5425.0	0.0	0.18911	0.189	10.77	0.09	0.0385	0.0012	89.3	3.92E+09	1.44E-02
DBR9	Cpx	1676.6	0.41	6.35	6.35	0.07	4519.7	0.0	0.19157	0.192	10.46	0.04	0.0347	0.0014	88.5	2.58E+09	1.53E-02
GE1	Cpx	596.0	1.70	5.80	5.80	0.07	1169.8	0.1	0.18524	0.186	9.85	0.02	0.0298	0.0004	85.1	4.08E+09	1.20E-02

Table 5.7 - Representative trace element analyses of clinopyroxene (cpx) and orthopyroxene (opx) in West Eifel and Siebengebirge mantle xenoliths.

Sample	MM1				MM2							
Rock type												
phase	cpx	cpx	cpx	cpx	cpx	cpx	cpx	cpx	opx	opx	opx	opx
Li	1.17	1.38	0.78	0.82	1407.00	1465.00	1467.00	1463.00	1528.00	1530.00	1418.00	1370.00
Cs	<0.041	<0.038	<0.038	<0.039	<0.042	<0.042	<0.040	<0.039	<0.042	<0.041	<0.042	<0.043
Rb	<0.074	0.27	<0.075	<0.070	<0.081	<0.081	<0.075	<0.072	<0.082	0.13	<0.076	<0.077
Ba	0.34	1.78	0.07	0.31	<0.033	0.06	0.04	0.03	<0.0236	0.81	<0.043	<0.040
Th	0.18	0.15	0.34	0.30	0.79	0.90	0.57	0.55	0.00	0.03	0.01	<0.0046
U	0.02	0.01	0.05	0.05	0.16	0.16	0.10	0.10	0.00	0.01	<0.0048	<0.0039
Nb	0.71	0.64	1.05	1.10	0.57	0.66	0.44	0.33	0.03	0.18	0.03	0.04
Ta	0.20	0.20	0.25	0.24	0.16	0.14	0.13	0.10	<0.0040	0.01	0.00	0.00
La	8.51	7.60	9.35	9.14	19.12	19.21	16.81	16.88	0.04	0.13	0.03	0.04
Ce	29.54	26.37	32.11	31.65	56.15	57.44	50.82	50.95	0.18	0.31	0.18	0.17
Pb	0.10	0.11	0.13	0.15	0.28	0.28	0.22	0.21	<0.0088	0.02	<0.0100	<0.0080
Pr	5.04	4.52	5.33	5.42	7.43	7.55	6.62	6.69	0.03	0.05	0.03	0.03
Sr	189.5	183.1	189.9	191.2	263.1	250.2	264.6	255.9	0.9	1996.0	0.6	0.5
Nd	26.48	24.60	27.88	27.82	29.28	30.62	26.08	26.32	0.17	0.19	0.18	0.18
Zr	160.6	145.8	175.6	170.7	43.6	56.5	34.7	35.5	3.0	2.7	2.9	3.2
Hf	5.42	5.23	5.93	5.77	1030.00	1587.00	0.85	0.86	0.06	0.05	0.08	0.09
Sm	6.51	6.17	6.93	6.52	4.60	5.03	3.96	4.19	0.07	0.08	0.07	0.07
Eu	1.98	1.89	2.06	2.14	1.35	1.40	1.15	1.18	0.02	0.03	0.02	0.02
Ti**	6474	6405	7032	6905	1912	2191	1507	1546	519	450	520	583
Gd	5.79	5.47	6.02	5.72	3.57	3.85	2.93	3.09	0.06	0.09	0.07	0.09
Tb	0.78	0.72	0.79	0.81	0.49	0.52	0.37	0.40	0.02	0.02	0.02	0.02
Dy	4.34	4.18	4.52	4.54	2.80	3.01	2.32	2.47	0.14	0.15	0.12	0.13
Y	18.3	17.1	19.1	18.8	13.2	14.6	11.3	11.6	1.0	0.9	0.9	0.9
Ho	0.74	0.71	0.79	0.76	0.51	0.59	0.43	0.44	0.03	0.03	0.03	0.03
Er	1.91	1.62	1.94	1.92	1.39	1.62	1.24	1.22	0.14	0.11	0.14	0.13
Tm	0.23	0.22	0.25	0.24	0.20	0.19	0.17	0.16	0.02	0.02	0.02	0.03
Yb	1.39	1.30	1.56	1.55	1.29	1.40	1.08	1.20	0.22	0.21	0.18	0.19
Lu	0.19	0.17	0.21	0.18	0.18	0.18	0.14	0.16	0.04	0.03	0.03	0.03

Sample	MM3								MM4				
Rock type													
phase	cpx	cpx	cpx	cpx	opx	opx	opx	opx	cpx	cpx	opx	opx	opx
Li	1467.00	1371.00	1516.00	1375.00	1443.00	1354.00	1390.00	1410.00	1.39	1.27	1.03	1.18	1.19
Cs	<0.039	<0.040	<0.040	<0.038	<0.038	<0.037	<0.037	<0.037	<0.042	<0.043	<0.045	<0.042	<0.042
Rb	<0.068	0.18	<0.073	<0.069	<0.070	<0.068	<0.070	<0.067	<0.079	<0.079	<0.083	<0.077	<0.083
Ba	0.06	1274.00	0.08	0.08	<0.043	<0.0260	<0.038	<0.031	0.43	0.30	0.04	<0.028	0.03
Th	0.59	0.75	0.67	0.64	0.01	0.01	0.01	0.00	0.10	0.08	<0.0036	<0.0030	<0.0027
U	0.12	0.16	0.14	0.13	<0.0036	0.00	0.01	0.00	0.03	0.02	<0.0029	<0.0030	0.00
Nb	0.58	0.70	0.71	0.70	0.04	0.03	0.04	0.03	0.46	0.43	0.05	0.05	0.06
Ta	0.10	0.12	0.17	0.15	<0.0036	<0.0032	<0.0044	<0.0043	0.03	0.04	<0.0028	0.00	0.00
La	14.00	15.00	14.22	13.81	0.03	0.02	0.03	0.03	1.36	1.59	0.01	0.01	0.01
Ce	43.52	45.35	43.66	42.75	0.12	0.12	0.14	0.13	2.35	2.86	0.04	0.03	0.03
Pb	0.18	0.30	0.19	0.17	<0.0081	<0.0080	<0.0068	<0.0082	0.02	0.02	<0.0050	<0.0058	<0.0077
Pr	6.41	6.70	6.60	6.43	0.03	0.03	0.03	0.03	0.24	0.28	0.01	<0.0035	0.00
Sr	224.4	225.9	237.6	231.2	0.4	0.4	0.5	0.4	9.7	16.9	0.1	0.1	0.1
Nd	30.67	31.43	31.05	29.81	0.16	0.18	0.18	0.17	0.99	0.99	0.02	0.03	<0.0172
Zr	66.1	72.8	69.5	66.7	3.4	3.4	3.8	4.1	1.1	1.1	0.2	0.1	0.1
Hf	1580.00	1760.00	1540.00	1485.00	0.05	0.06	0.10	0.12	0.04	0.03	<0.0122	<0.0073	0.01
Sm	6.34	6.64	6.34	6.29	0.06	0.09	0.10	0.06	0.21	0.27	0.02	<0.0199	<0.0235
Eu	1.88	1.91	1.95	1.79	0.03	0.03	0.04	0.03	0.06	0.09	<0.0082	<0.0077	<0.0087
Ti**	2514	2783	2523	2557	738	516	816	1037	480	478	194	191	190
Gd	5.30	5.45	5.07	5.06	0.08	0.10	0.11	0.11	0.30	0.27	<0.0216	<0.0176	<0.0209
Tb	0.67	0.74	0.65	0.68	0.02	0.03	0.02	0.02	0.07	0.07	<0.0048	<0.0051	<0.0033
Dy	4.11	4.21	3.95	3.84	0.19	0.17	0.15	0.15	0.65	0.64	0.05	0.05	0.04
Y	18.1	18.7	17.5	17.3	1125.0	1151.0	1151.0	1132.0	4.2	4.1	0.4	0.4	0.4
Ho	0.72	0.74	0.67	0.68	0.04	0.04	0.04	0.04	0.16	0.16	0.02	0.01	0.02
Er	1.80	1.91	1.83	1.72	0.14	0.15	0.16	0.15	0.53	0.52	0.07	0.08	0.06
Tm	0.24	0.24	0.24	0.24	0.02	0.03	0.03	0.03	0.09	0.08	0.02	0.01	0.01
Yb	1.57	1.55	1.51	1.45	0.22	0.21	0.26	0.26	0.64	0.60	0.15	0.13	0.12
Lu	0.20	0.21	0.19	0.19	0.04	0.04	0.04	0.04	0.10	0.10	0.03	0.02	0.02

Sample	MM5								MM6									
Rock type																		
phase	cpx	cpx	cpx	cpx	opx	opx	opx	opx	cpx	cpx	cpx	cpx	cpx	cpx	opx	opx	opx	opx
Li	1.24	1.25	1.34	1.33	1.42	1.38	1.42	1.46	0.59	0.42	0.51	0.47	0.86	0.79	0.81	0.75	0.79	0.75
Cs	<0.042	<0.039	<0.042	<0.040	<0.041	<0.040	<0.044	<0.040	<0.040	<0.031	<0.046	<0.043	<0.045	<0.043	<0.038	<0.042	<0.043	<0.041
Rb	<0.076	<0.074	<0.080	<0.075	<0.081	<0.079	<0.080	<0.077	<0.078	<0.084	<0.088	<0.079	<0.086	<0.079	<0.073	<0.073	<0.083	<0.074
Ba	0.04	0.07	<0.042	0.06	<0.0265	<0.026	<0.038	0.03	<0.041	<0.031	0.05	0.16	0.06	0.04	<0.026	<0.030	<0.0237	<0.034
Th	1.85	1.91	1.97	1.98	0.04	0.02	0.02	0.06	2.62	1.95	2.77	2.83	2.86	2.54	0.01	0.02	0.02	0.02
U	0.31	0.33	0.33	0.32	0.01	0.07	0.01	0.01	0.54	0.43	0.59	0.56	0.66	0.59	0.01	0.01	0.01	0.01
Nb	0.12	0.12	0.11	0.10	0.01	<0.0040	0.01	0.01	0.52	0.35	0.51	0.59	0.58	0.48	0.02	0.01	0.01	0.01
Ta	0.02	0.01	0.02	0.02	<0.00176	0.02	<0.00179	<0.00171	0.07	0.05	0.08	0.08	0.09	0.08	<0.0024	<0.00213	0.00	<0.0033
La	16.79	19.28	18.14	18.72	0.03	0.03	0.02	0.03	20.37	15.61	20.97	21.15	20.45	19.83	0.02	0.02	0.02	0.02
Ce	39.63	44.08	41.89	43.28	0.09	0.09	0.10	0.09	30.90	23.50	31.52	32.75	31.55	30.32	0.03	0.05	0.06	0.05
Pb	0.87	0.95	0.90	0.97	<0.0072	0.01	<0.0086	<0.0076	1.16	0.89	1.13	1.09	1.21	1.18	<0.0082	<0.0071	<0.0086	0.01
Pr	4.16	4.52	4.26	4.43	0.01	0.01	0.02	0.02	2.61	2.01	2.61	2.71	2.77	2.58	0.01	0.01	0.01	0.01
Sr	268.6	285.6	276.5	281.2	0.4	0.2	0.3	0.4	199.1	151.0	199.3	200.8	198.7	197.6	0.1	0.2	0.2	0.1
Nd	14.06	15.55	14.57	14.98	0.06	0.05	0.06	0.07	8.00	6.20	8.34	8.83	8.68	8.29	0.02	0.03	0.02	0.02
Zr	21.7	18.9	20.3	20.0	0.9	1.0	0.9	0.9	4.3	3.3	4.3	4.2	4.9	4.7	0.2	0.2	0.2	0.1
Hf	0.45	0.43	0.46	0.46	0.01	0.02	0.02	0.02	0.08	0.06	0.09	0.06	0.06	0.07	0.01	<0.0068	<0.0119	<0.0069
Sm	1.88	2.11	1.93	2.11	0.03	<0.026	<0.0222	<0.0184	0.92	0.76	0.89	0.99	1.06	0.96	<0.0280	<0.0187	<0.0169	0.01
Eu	0.57	0.62	0.55	0.58	<0.0066	0.01	0.01	0.01	0.31	0.24	0.28	0.29	0.29	0.31	<0.0045	<0.0073	<0.0088	0.01
Ti**	258	217	247	244	76	76	79	77	316	247	334	328	366	340	100	95	101	99
Gd	1.27	1.39	1.27	1.23	<0.029	0.03	0.03	0.04	0.75	0.57	0.77	0.78	0.96	0.85	<0.0187	0.02	<0.0212	<0.0167
Tb	0.18	0.20	0.17	0.19	0.00	0.00	<0.0027	0.01	0.13	0.11	0.14	0.13	0.15	0.15	<0.0033	0.00	0.00	<0.0030
Dy	1.12	1.18	1.10	1.07	0.05	0.06	0.04	0.03	0.96	0.75	0.98	1.01	1.16	1.05	0.03	0.04	0.02	0.03
Y	5.5	5.9	5.4	5.6	0.3	0.4	0.4	0.3	5.8	4.5	5.8	5.7	6.8	6.3	0.3	0.3	0.3	0.3
Ho	0.22	0.22	0.21	0.23	0.01	0.01	0.01	0.01	0.22	0.17	0.23	0.23	0.27	0.27	0.01	0.01	0.01	0.01
Er	0.60	0.65	0.60	0.61	0.05	0.05	0.04	0.04	0.68	0.55	0.69	0.71	0.83	0.72	0.06	0.06	0.05	0.05
Tm	0.09	0.09	0.09	0.10	0.01	0.01	0.01	0.01	0.11	0.08	0.11	0.10	0.12	0.11	0.01	0.01	0.01	0.01
Yb	0.70	0.68	0.69	0.64	0.09	0.11	0.11	0.10	0.83	0.63	0.81	0.73	0.90	0.91	0.08	0.11	0.12	0.13
Lu	0.10	0.10	0.09	0.10	0.02	0.02	0.02	0.02	0.12	0.08	0.12	0.11	0.14	0.12	0.02	0.02	0.03	0.02

Sample MM7 / MM8

Sample	MM7								MM8										
Rock type																			
phase	cpx	cpx	cpx	cpx	opx	opx	opx	opx	cpx	cpx	cpx	cpx	cpx	cpx	cpx	opx	opx	opx	opx
Li	0.87	0.85	0.79	0.86	0.92	0.84	0.93	0.84	1.35	1.48	1.60	1.76	1.54	1.67	1.61	1.36	1.31	1.36	1.37
Cs	<0.048	<0.046	<0.046	<0.048	<0.049	<0.047	<0.046	<0.044	<0.041	<0.045	<0.043	<0.046	<0.041	<0.045	<0.042	<0.040	<0.042	<0.043	<0.043
Rb	<0.090	<0.083	<0.085	<0.091	<0.086	<0.087	<0.085	<0.083	<0.080	<0.087	<0.081	<0.089	<0.079	<0.081	0.08	<0.081	<0.075	<0.078	<0.079
Ba	0.27	0.22	0.39	0.23	<0.048	<0.039	0.02	<0.037	0.09	0.06	0.07	0.15	3.52	0.10	0.61	<0.0227	0.02	<0.023	<0.046
Th	0.29	0.28	0.30	0.27	0.01	0.01	0.00	0.00	0.64	0.95	1.02	1.00	1.27	1.66	1.69	0.00	0.01	0.01	0.00
U	0.10	0.08	0.08	0.08	<0.0037	<0.0033	<0.0033	<0.0032	0.11	0.18	0.22	0.22	0.27	0.35	0.37	0.00	0.00	0.00	0.00
Nb	2.32	2.26	2.42	2.30	0.26	0.23	0.23	0.23	0.69	0.83	0.93	0.96	1.15	1.07	1.01	0.03	0.02	0.04	0.03
Ta	0.17	0.16	0.18	0.16	0.01	0.02	0.01	0.01	0.06	0.10	0.08	0.09	0.09	0.10	0.10	<0.00184	<0.0023	<0.0026	<0.0026
La	3.90	3.82	3.85	3.82	0.02	0.03	0.02	0.02	18.81	21.43	21.15	21.03	22.50	18.91	21.29	0.03	0.03	0.04	0.03
Ce	10.00	10.09	10.26	10.18	0.10	0.15	0.09	0.09	53.57	61.04	60.63	60.92	64.01	54.26	58.35	0.13	0.16	0.16	0.16
Pb	0.05	0.02	0.02	0.03	<0.0093	<0.0082	<0.0063	0.01	0.38	0.43	0.40	0.36	0.45	0.42	0.44	<0.0107	<0.0083	<0.0102	0.01
Pr	1.47	1.46	1.49	1.48	0.02	0.02	0.02	0.02	6.82	8.07	8.08	8.12	8.32	7.56	7.82	0.03	0.03	0.02	0.03
Sr	97.6	97.6	100.1	99.4	0.7	1.1	0.6	0.6	292.5	312.1	299.8	294.9	304.9	261.9	278.1	0.5	0.5	0.5	0.6
Nd	7.61	7.69	7.97	7.72	0.13	0.15	0.08	0.09	29.05	34.84	36.07	35.97	36.52	36.21	36.79	0.16	0.16	0.20	0.18
Zr	4.5	4.7	4.7	4.7	0.6	0.6	0.6	0.6	23.7	29.4	27.9	28.3	31.0	23.1	24.6	1.3	1.3	1.4	1.5
Hf	0.22	0.21	0.22	0.23	0.04	0.03	0.03	0.02	0.87	0.96	0.84	0.88	0.88	0.76	0.84	0.03	0.03	0.04	0.04
Sm	1.72	1.71	1.69	1.61	0.03	0.05	0.05	0.05	5.12	6.51	6.97	7.02	6.89	7.74	7.53	0.07	0.06	0.08	0.07
Eu	0.40	0.40	0.41	0.37	0.02	0.02	0.02	0.01	1.46	1.89	2.00	2.07	2.06	2.25	2.22	0.03	0.02	0.03	0.03
Ti**	679	687	683	684	273	272	259	266	453	539	607	650	617	1018	988	141	152	167	167
Gd	0.73	0.75	0.74	0.82	<0.030	0.04	0.04	0.03	3.52	4.53	4.84	5.00	4.97	5.83	5.63	0.08	0.10	0.10	0.07
Tb	0.15	0.14	0.14	0.14	0.01	0.00	0.01	0.01	0.47	0.61	0.71	0.69	0.68	0.76	0.80	0.02	0.02	0.02	0.02
Dy	1.23	1.14	1.22	1.21	0.10	0.10	0.10	0.09	2.51	3.26	3.51	3.61	3.66	4.14	4.15	0.15	0.15	0.13	0.13
Y	7.1	7.1	7.1	7.1	0.8	0.7	0.7	0.7	10.7	14.2	15.1	15.1	15.8	17.2	17.1	0.9	0.9	0.9	0.9
Ho	0.29	0.29	0.29	0.29	0.02	0.03	0.02	0.02	0.43	0.59	0.62	0.67	0.63	0.71	0.71	0.04	0.03	0.04	0.04
Er	0.85	0.87	0.89	0.87	0.11	0.11	0.11	0.10	1.11	1.44	1.57	1.53	1.57	1.73	1.68	0.12	0.11	0.11	0.13
Tm	0.13	0.13	0.13	0.13	0.02	0.02	0.02	0.02	0.14	0.17	0.19	0.20	0.21	0.21	0.24	0.02	0.02	0.02	0.02
Yb	0.81	0.93	0.92	0.92	0.19	0.18	0.17	0.20	0.94	1.14	1.24	1.27	1.36	1.42	1.44	0.18	0.18	0.21	0.19
Lu	0.13	0.14	0.13	0.13	0.03	0.04	0.03	0.03	0.12	0.17	0.18	0.17	0.17	0.17	0.18	0.03	0.03	0.03	0.03

Sample MM9 / DBR5

Sample	MM9								DBR5							
Rock type																
phase	cpx	cpx	cpx	cpx	opx	opx	opx	opx	cpx	cpx	cpx	cpx	opx	opx	opx	opx
Li	1.53	1.47	1.38	1.35	1.24	1.32	1.18	1.20	1.50	1.44	1.46	1.42	1.41	1.40	1.42	1.46
Cs	<0.048	<0.045	<0.048	<0.049	<0.053	0.05	<0.052	<0.049	<0.039	<0.040	<0.041	<0.040	<0.044	<0.042	<0.042	<0.040
Rb	<0.088	<0.092	<0.092	<0.091	<0.095	0.15	<0.097	<0.089	<0.073	<0.071	<0.078	<0.073	<0.081	<0.080	<0.078	<0.075
Ba	0.07	0.12	0.14	0.09	<0.049	1.39	0.14	<0.031	0.39	0.17	0.08	<0.043	0.07	<0.029	0.03	<0.037
Th	0.04	0.04	0.04	0.04	<0.0045	0.02	<0.0045	<0.00168	0.02	0.01	0.02	0.02	<0.0037	<0.0036	0.00	<0.0042
U	0.01	0.01	0.01	0.01	<0.0024	0.01	0.00	<0.0043	0.00	0.00	0.01	0.01	<0.0043	<0.0053	<0.0031	<0.0029
Nb	0.26	0.27	0.27	0.26	0.03	0.17	0.03	0.04	0.22	0.21	0.25	0.25	0.02	0.02	0.02	0.02
Ta	0.02	0.02	0.03	0.02	0.00	0.01	<0.00229	<0.0025	0.03	0.02	0.03	0.03	<0.0036	0.00	<0.0031	<0.0024
La	1.18	1.18	1.23	1.17	0.01	0.13	<0.0058	0.01	1.06	1.04	1.12	1.17	0.01	0.01	0.01	0.01
Ce	2.74	2.71	2.73	2.66	0.03	0.22	0.03	0.03	4.03	4.03	4.05	4.10	0.04	0.04	0.04	0.04
Pb	0.02	0.03	0.02	0.02	<0.0103	<0.0093	0.01	<0.0094	0.02	0.02	0.01	<0.0111	<0.0091	<0.0063	<0.0075	<0.0100
Pr	0.33	0.34	0.33	0.33	<0.0048	0.02	<0.0048	0.00	0.76	0.74	0.74	0.75	0.01	0.01	0.01	0.01
Sr	21.4	21.5	21.1	20.9	0.2	1.5	0.2	0.1	74.0	73.1	72.5	72.9	0.6	0.6	0.6	0.6
Nd	1.57	1.50	1.50	1.45	<0.029	0.08	0.03	0.03	4.53	4.38	4.22	4.51	0.07	0.08	0.09	0.08
Zr	5.6	5.5	5.4	5.5	0.9	1.1	0.9	0.8	30.4	30.5	29.6	30.2	3.7	3.7	3.6	3.8
Hf	0.21	0.21	0.21	0.21	0.03	0.04	0.03	0.03	0.93	0.95	0.97	0.98	0.12	0.11	0.11	0.12
Sm	0.64	0.50	0.58	0.57	0.03	0.04	<0.032	<0.022	1.73	1.76	1.68	1.67	0.05	0.05	0.04	0.07
Eu	0.23	0.26	0.25	0.24	0.01	<0.0067	0.01	0.01	0.69	0.68	0.71	0.68	0.02	0.02	0.03	0.03
Ti**	1100	1092	1083	1097	454	458	429	419	3972	3972	3907	3977	1325	1313	1324	1332
Gd	1.06	0.95	1.02	1.07	0.05	0.04	0.05	0.04	2.49	2.48	2.41	2.41	0.09	0.10	0.09	0.10
Tb	0.23	0.21	0.23	0.22	0.01	0.01	0.02	0.01	0.45	0.44	0.42	0.43	0.03	0.02	0.03	0.02
Dy	1.69	1.77	1.68	1.67	0.15	0.14	0.13	0.14	3.12	3.10	3.19	3.21	0.24	0.24	0.24	0.23
Y	9.9	9.7	9.9	9.8	1.1	1.1	1.1	1.1	17.3	17.4	16.8	17.0	1.7	1.7	1.7	1.7
Ho	0.40	0.38	0.39	0.41	0.04	0.04	0.04	0.05	0.65	0.67	0.65	0.67	0.06	0.06	0.05	0.07
Er	1.13	1.13	1.14	1.16	0.16	0.14	0.14	0.14	1.97	1.94	1.92	1.90	0.25	0.23	0.23	0.21
Tm	0.18	0.15	0.17	0.16	0.03	0.03	0.04	0.03	0.26	0.28	0.25	0.26	0.04	0.04	0.04	0.04
Yb	1.21	1.13	1.24	1.09	0.22	0.24	0.25	0.23	1.89	1.78	1.80	1.79	0.34	0.34	0.34	0.38
Lu	0.17	0.16	0.15	0.16	0.05	0.05	0.05	0.04	0.27	0.27	0.24	0.24	0.06	0.06	0.06	0.06

Sample DBR6 / DBR9

	cpx	cpx	cpx	cpx	opx	opx		cpx	cpx	cpx	cpx	cpx	opx	opx	opx	opx
Sample	DBR6							DBR9								
phase	cpx	cpx	cpx	cpx	opx	opx		cpx	cpx	cpx	cpx	cpx	opx	opx	opx	opx
Li	1.21	1.22	1.21	1.15	1.25	2.10		1.45	1.43	1.50	1.48	1.46	1.48	1.38	1.50	1.12
Cs	<0.039	<0.040	0.04	<0.040	<0.044	0.07		<0.042	0.26	<0.044	<0.043	<0.046	<0.046	<0.042	<0.047	<0.034
Rb	<0.073	<0.073	<0.074	<0.076	<0.081	3.90		<0.081	<0.49	<0.081	<0.082	<0.088	<0.085	<0.078	<0.089	<0.060
Ba	0.09	0.14	0.14	0.13	<0.030	50.48		0.04	<0.17	<0.026	0.06	<0.034	<0.037	<0.033	<0.038	0.05
Th	0.05	0.06	0.06	0.06	0.00	0.61		0.01	0.03	0.01	0.01	0.01	<0.0051	<0.0022	<0.0032	<0.0036
U	0.01	0.01	0.01	0.01	<0.0031	0.25		0.00	<0.0177	<0.0040	0.01	0.00	<0.0037	<0.0036	<0.0029	<0.00259
Nb	0.35	0.36	0.39	0.40	0.03	5.95		0.14	0.22	0.15	0.16	0.14	0.01	0.02	0.01	0.01
Ta	0.04	0.04	0.04	0.04	<0.0032	0.30		0.02	<0.023	0.02	0.02	0.02	<0.0039	<0.00241	<0.0040	<0.0030
La	0.51	0.61	0.53	0.63	0.01	4.46		0.95	1.05	0.95	0.98	1.05	0.01	0.01	0.01	0.01
Ce	1.12	1.18	1.09	1.23	0.02	8.15		3.76	3.94	3.83	3.88	3.99	0.05	0.04	0.04	0.04
Pb	0.01	0.01	<0.0113	<0.0093	<0.0113	0.23		0.01	<0.073	0.01	<0.0102	<0.0134	<0.0139	<0.0094	<0.0131	<0.0063
Pr	0.20	0.18	0.19	0.17	0.01	0.79		0.73	0.80	0.71	0.72	0.77	0.01	0.01	0.01	0.01
Sr	15.5	16.8	15.3	17.3	0.2	48.1		70.2	76.4	71.3	71.7	74.9	0.6	0.6	0.6	0.5
Nd	1.29	1.24	1.27	1.23	0.03	2.87		4.21	4.42	4.53	4.54	4.55	0.06	0.08	0.08	0.07
Zr	4.3	4.3	4.4	4.5	0.6	8.5		31.2	35.9	31.6	31.6	33.5	3.9	3.9	3.6	2.7
Hf	0.28	0.26	0.26	0.26	0.03	0.19		0.99	0.85	1.01	1.04	1.06	0.10	0.12	0.11	0.09
Sm	0.69	0.69	0.74	0.75	0.03	0.33		1.82	1.57	1.73	1.72	1.76	0.03	0.06	0.05	0.04
Eu	0.31	0.34	0.29	0.31	0.01	0.13		0.68	0.63	0.70	0.71	0.72	0.03	0.03	0.02	0.02
Ti**	1630	1590	1564	1569	611	921		4111	4301	4132	4094	4262	1349	1338	1309	994
Gd	1.31	1.38	1.30	1.25	0.04	0.37		2.47	2.58	2.64	2.72	2.61	0.15	0.11	0.13	0.08
Tb	0.25	0.24	0.23	0.25	0.01	0.05		0.46	0.61	0.46	0.44	0.46	0.02	0.03	0.03	0.02
Dy	1.84	1.82	1.86	1.83	0.13	0.35		3.39	3.43	3.32	3.39	3.48	0.23	0.24	0.26	0.17
Y	10.5	10.5	10.1	10.2	1.2	1.7		18.4	20.7	18.5	18.4	19.2	1.8	1.7	1.7	1.3
Ho	0.40	0.41	0.38	0.39	0.04	0.06		0.72	0.73	0.75	0.71	0.74	0.07	0.06	0.07	0.05
Er	1.11	1.21	1.14	1.16	0.17	0.21		2.14	2.23	2.10	2.06	2.05	0.27	0.24	0.22	0.16
Tm	0.17	0.17	0.16	0.17	0.03	0.03		0.29	0.27	0.30	0.29	0.29	0.05	0.05	0.03	0.03
Yb	1.22	1.13	1.16	1.13	0.22	0.29		1.91	2.40	1.95	1.93	2.06	0.33	0.35	0.35	0.26
Lu	0.15	0.15	0.16	0.16	0.05	0.05		0.27	0.26	0.29	0.28	0.28	0.06	0.06	0.06	0.05

Sample GE1 / SB3

	cpx	cpx	cpx	cpx	opx	opx	opx	opx		cpx	cpx	ol	opx	opx	opx	opx
Sample	GE1									SB3						
phase	cpx	cpx	cpx	cpx	opx	opx	opx	opx		cpx	cpx	ol	opx	opx	opx	opx
Li	1.51	1.12	1.93	1.87	2.51	2.61	2.05	1.59		1.30	7.25	2.66	8.50	7.18	11.30	9.07
Cs	<0.035	<0.036	<0.037	<0.037	<0.040	<0.038	<0.038	<0.037		<0.047	<0.038	<0.038	<0.048	<0.046	<0.048	<0.044
Rb	<0.066	0.08	0.14	<0.067	<0.073	<0.071	<0.073	<0.070		0.10	<0.072	0.10	<0.094	<0.086	<0.094	<0.086
Ba	0.91	4.07	6.33	0.10	<0.022	<0.025	0.02	<0.0213		3.56	0.05	<0.032	0.21	0.24	2.44	1.38
Th	0.16	0.15	0.24	0.20	0.01	0.01	0.01	0.01		0.05	0.44	0.00	0.14	0.16	0.32	0.29
U	0.02	0.02	0.03	0.02	0.00	<0.0029	0.00	<0.0027		0.01	0.20	0.00	0.05	0.05	0.08	0.07
Nb	0.60	0.45	0.84	0.57	0.01	<0.0051	0.01	0.01		0.42	0.01	0.00	0.01	<0.0063	0.01	<0.0056
Ta	0.08	0.03	0.13	0.13	<0.0038	0.00	<0.0028	<0.0023		0.02	<0.00256	<0.00256	<0.0029	<0.0028	<0.0036	<0.00198
La	9.72	4.15	11.78	15.22	0.01	0.01	0.03	0.02		0.57	7.64	0.05	0.21	0.26	0.67	0.54
Ce	21.79	7.73	27.81	42.02	0.02	0.02	0.05	0.05		1.10	6.03	0.03	0.11	0.17	0.42	0.37
Pb	0.33	0.41	0.32	0.33	<0.0069	<0.0105	<0.0059	<0.0087		0.02	0.81	0.03	0.02	0.02	0.08	0.05
Pr	2.25	0.72	3.08	5.20	<0.00226	<0.00206	0.00	<0.0030		0.18	0.45	<0.00196	0.01	0.01	0.03	0.02
Sr	102.3	49.2	132.3	198.5	0.1	0.1	0.1	0.1		16.1	86.8	0.2	1.6	2.4	7.4	5.9
Nd	7.35	2.59	10.74	19.45	0.01	0.02	<0.0183	<0.0154		1.21	2.13	<0.0191	0.03	0.06	0.13	0.10
Zr	14.8	6.1	24.5	51.0	0.5	0.5	0.4	0.4		4.3	7.1	0.0	0.8	0.8	1.1	1.1
Hf	0.25	0.20	0.50	1.25	0.02	<0.0126	0.01	0.02		0.28	0.23	<0.0119	0.03	0.03	0.02	0.04
Sm	0.97	0.45	1.58	2.93	<0.0189	<0.0199	0.02	<0.0179		0.75	0.54	<0.0203	<0.0260	0.028	<0.032	<0.028
Eu	0.25	0.10	0.40	0.79	<0.0045	<0.0041	<0.01	0.01		0.30	0.20	<0.0053	<0.0078	0.01	0.01	0.01
Ti**	826	821	887	749	379	375	363	360		1263	474	11	285	282	281	278
Gd	0.70	0.34	1.09	1.90	<0.0146	<0.0209	<0.027	0.02		1.27	0.58	0.01	0.03	0.02	<0.023	0.02
Tb	0.08	0.05	0.11	0.23	0.00	<0.0027	<0.0026	<0.00202		0.25	0.11	<0.0031	<0.0040	0.01	0.01	0.01
Dy	0.43	0.27	0.73	1.35	<0.0182	<0.0131	0.02	0.02		1.91	0.81	<0.0099	0.04	0.04	0.10	0.08
Y	2.1	1.1	3.3	6.1	0.1	0.1	0.1	0.2		10.7	4.5	0.1	0.4	0.4	0.6	0.6
Ho	0.08	0.05	0.13	0.23	0.00	0.00	0.00	0.00		0.43	0.19	0.00	0.01	0.02	0.02	0.02
Er	0.21	0.13	0.33	0.64	<0.0094	0.01	0.01	0.02		1.22	0.57	0.01	0.07	0.07	0.09	0.07
Tm	0.03	0.02	0.04	0.08	0.00	0.00	<0.0037	0.00		0.19	0.08	0.00	0.01	0.01	0.01	0.02
Yb	0.20	0.14	0.32	0.57	0.03	0.03	0.04	0.05		1.29	0.59	0.02	0.15	0.33	0.16	0.15
Lu	0.03	0.02	0.04	0.08	0.00	0.01	0.01	0.01		0.18	0.08	0.01	0.03	0.02	0.03	0.03

Sample SB5 / EUL2 / EUL5

	opx	opx	opx	opx		opx	opx	opx	opx	opx		opx	opx	opx	opx
Sample	SB5					EUL2						EUL5			
phase	opx	opx	opx	opx		opx	opx	opx	opx	opx		opx	opx	opx	opx
Li	4.27	3.11	2.65	2.77		2.64	0.66	0.58	2.15	0.56		8.32	6.44	14.90	4.57
Cs	0.04	<0.058	<0.029	0.04		<0.048	<0.038	<0.037	<0.035	<0.035		<0.038	<0.036	<0.036	<0.038
Rb	16.37	11.48	0.53	1.34		<0.097	<0.068	0.08	0.15	<0.060		<0.070	<0.069	<0.074	<0.067
Ba	104.09	55.90	21.03	66.66		<0.028	<0.036	0.04	12.41	<0.0188		1.73	0.05	0.63	0.08
Th	1.55	0.64	0.08	0.13		<0.0034	0.07	0.06	0.02	<0.0026		0.55	0.05	0.32	0.06
U	0.43	0.12	0.03	0.07		<0.00	0.01	0.02	0.02	0.01		0.43	0.07	0.27	0.08
Nb	15.73	10.43	0.61	3.19		<0.0078	<0.0052	0.02	0.14	0.00		0.01	<0.0061	0.01	<0.0044
Ta	0.13	0.06	0.01	0.02		<0.0029	<0.0044	<0.0034	<0.0030	<0.00		0.00	<0.0034	<0.0023	<0.00152
La	29.75	15.51	0.93	1.24		<0.0042	0.01	0.03	0.33	<0.0046		0.75	0.04	0.36	0.04
Ce	56.28	26.35	1.69	2.37		<0.00	0.02	0.04	0.22	0.00		0.47	0.03	0.20	0.03
Pb	0.09	<0.083	0.03	0.03		<0.0122	<0.0056	<0.0077	0.09	0.01		0.03	<0.0070	0.02	<0.0063
Pr	4.88	2.15	0.15	0.20		<0.0020	<0.0030	0.01	0.01	<0.0035		0.03	<0.0035	0.01	<0.0029
Sr	80.8	31.8	5.5	12.0		0.0	0.0	0.3	3.3	0.0		15.5	0.5	7.3	0.6
Nd	13.82	5.33	0.56	0.59		<0.0166	<0.0213	0.01	<0.0170	0.01		0.07	<0.0146	0.03	0.01
Zr	3.6	2.0	0.2	0.3		0.1	0.0	0.0	0.2	0.0		0.3	0.2	0.3	0.2
Hf	0.07	0.03	0.00	<0.0080		<0.0061	<0.0101	<0.0117	<0.0044	<0.0099		<0.0091	<0.0116	<0.0105	0.01
Sm	1.43	0.44	0.11	0.11		<0.030	<0.0101	<0.0173	<0.0099	<0.0223		0.01	<0.0197	<0.0106	<0.0100
Eu	0.44	0.15	0.04	0.03		<0.0088	<0.0051	<0.0041	<0.0029	<0.0037		<0.0059	<0.0080	<0.0080	<0.0041
Ti**	616	454	159	195		81	157	199	194	239		114	112	107	115
Gd	0.95	0.38	0.07	0.08		<0.029	<0.0096	<0.0094	<0.0132	0.02		<0.023	<0.0131	<0.0222	<0.030
Tb	0.11	0.04	0.01	0.02		<0.0033	<0.0031	0.00	0.00	0.00		<0.0028	0.00	<0.0033	0.00
Dy	0.62	0.31	0.09	0.11		<0.0227	0.01	<0.0144	0.02	<0.0161		<0.0104	0.01	0.02	0.01
Y	3.4	1.9	0.9	0.9		0.1	0.2	0.2	0.2	0.2		0.1	0.1	0.1	0.1
Ho	0.11	0.05	0.02	0.03		<0.0040	0.00	0.01	0.01	0.01		0.01	0.00	0.01	0.00
Er	0.30	0.20	0.12	0.08		0.02	0.04	0.04	0.03	0.03		0.03	0.02	<0.0030	0.02
Tm	0.04	0.03	0.02	0.01		0.00	0.01	0.01	0.01	0.01		0.01	0.01	<0.0026	0.01
Yb	0.29	0.21	0.14	0.13		0.05	0.09	0.10	0.09	0.09		0.04	0.06	0.06	0.07
Lu	0.03	0.02	0.02	0.02		0.01	0.02	0.02	0.02	0.02		0.02	0.01	0.02	0.01

Chapter – 6 –

Concluding remarks

6. Concluding remarks

In this PhD thesis, I investigated European ultramafic xenoliths from Lower Silesia (Eger Rift), Persani Mts. (Transylvania), West Eifel and Siebengebirge (Germany), while those from French Massif Central are still under study. The xenoliths are spinel-bearing lherzolites and harzburgites sometime containing amphibole and phlogopite. Cumulate samples are also present.

The main outcomes are summarized as follows:

- The chemistry of FI in mantle xenoliths from the studied areas revealed is dominated by CO_2, with N_2 as second major species. Ne and Ar concentration and isotopic ratios indicate variable extents of contamination by atmosphere-derived fluids. Most of this contamination likely derives from the recycling of atmospheric-derived material inherited by local/recent or fossil subduction. This is evident in the mantle xenoliths from Persani Mts., where recent subduction occurred and in which has introduced the highest degree of air contamination.

- Olivine are systematically gas-poor respect to Px from the same xenoliths, as also observed in SCLM xenoliths from other localities on Earth. Among Oliv from European xenoliths, those from Lower Silesia display the highest CO_2 concentrations suggesting carbonated-like metasomatism, as also inferred from trace elements in cpx.

- The mineral chemistry and He/Ar* in FI indicate that Oliv and Px result from variable extents of partial melting, while Px also indicate the occurrence of metasomatism/refertilization. The highest degrees of melting (~30%) are found in harzburgite samples from Lower Silesia and Siebengebirge volcanic area, which are also among the oldest within our suite of samples (>6 Ma). Instead, evidences of low degrees of melting and/or refertilization are found in Persani Mts. and West Eifel, which are Quaternary and underwent refertilization processes, which are probably Quaternary and postponed mantle melting feeding Lower Silesia and Siebengebirge magmatism.

- In this thesis, I had the opportunity to deepen the knowledge on the variations observed in some noble gas tracers as He/Ar*. This ratio revealed a powerful indicator of partial melting (especially in oliv) and a tracer to distinguish cumulate from mantle xenoliths as well as to recognize the entrapment of secondary (magmatic) fluid inclusions.

- The $^3He/^4He$ corrected for air contamination (Rc/Ra) is within European SCLM range (6±1 Ra) that is lower than MORB (8±1 Ra). This indicates a widespread recycling of crustal material below Europe if compared to other continental rifts (e.g., WARS). However, the careful investigation of olivine, cpx, and opx in single localities allowed distinguishing small but significative variations of $^3He/^4He$ that are related to distinct histories among the various portions of the European SCLM. In detail, Persani Mts. show the lowest $^3He/^4He$ values that

indicate highest degree of crustal recycling due to the recent subduction that plays an important role in contaminating the mantle. Instead, metasomatism involving asthenospheric MORB-like fluids well explains the highest $^{3}He/^{4}He$ values (up to the lower limit of MORB range) recognized in all the studied localities.

- Ne-Ar-He isotopic systematics indicates that most of the data fall along a mixing between air and a MORB-like mantle.

- I presented the first data of carbon isotope composition of CO_2 ($\delta^{13}C$ V-PDB) in the Lower Silesia mantle xenoliths, which experienced metasomatism by carbonated-rich fluids. This revealed $\delta^{13}C$ values of ~ -3.9 ‰ that are within MORB range with <0.1% limestone contamination.

- The comparison of $^{3}He/^{4}He$ signature measured in mantle xenoliths from the three target areas with that of CO_2-dominated gas emissions located within or nearby shows that only gases emitted along Eger Rift are representative of the local mantle signature, suggesting an active magmatic activity below this area. Instead, gases emitted in East Eifel and nearby Persani Mts. are variably contaminated by crustal fluids during their passage toward the surface or are released from a cooling and ageing magma residing within the crust.

- This Thesis leads to improve the understanding of the European SCLM composition and its evolution, indicating the lack of evidences in support of a single or multiple plume, as previously hypothesized for some portions of European continental Rift system.

References

Aiuppa, A., Fischer, T. P., Plank, T., Robidoux, P., and Di Napoli, R. (2017). Along-arc, inter-arc and arc-to-arc variations in volcanic gas CO2/STratios reveal dual source of carbon in arc volcanism. Earth-Science Rev. 168, 24–47. doi:10.1016/j.earscirev.2017.03.005.

Abe, N., Arai, S., Yurimoto, H., 1998. Geochemical characteristics of the uppermost mantle beneath the Japan island arcs; implications for upper mantle evolution. Physics of the Earth and Planetary Interiors 107, 233–48.

Aeschbach-Hertig, W., Kipfer, R., Hofer, M., Imboden, D.M., Wieler, R., Signer, P., 1996. Quantification of gas fluxes from the subcontinental mantle: the example of Laacher See, a maar lake in Germany. Geochim. Cosmochim. Acta 60, 31–41.

Allègre, J. C., Staudacher, T., and Sarda, P. (1987). Rare gas systematics: formation of the atmosphere, evolution and structure of the Earth's mantle. Earth Planet. Sci. Lett. 81, 127–150. doi:10.1016/0012-821X(87)90151-8.

Althaus, T., Niedermann, S., Erzinger, J., 1998. Noble gases in ultramafic mantle xenoliths of the Persani Mountains, Transylvaninan Basin, Romania. Goldschmidt Conference Toulouse 1998 Abstract book, Mineralogical Magazine 62A.

Althaus, T., Niedermann, S., Erzinger, J., 2000. Noble gas studies of fluids and gas exhalations in the East Carpathians, Romania. Chemie der Erde 60, 189–207.

Amhed, A.H., Moghazi, A.K.M., Moufti, M.R., Dawoo, Y.H., Ali, K.A., 2016. Nature of the lithospheric mantle beneath the Arabian Shield and genesis of Al-spinel micropods: Evidence from the mantle xenoliths of Harrat Kishb, Western Saudi Arabia. Lithos 240–243, 119–139.

Anderson, D.L., 1998. A model to explain the various paradoxes associated with mantle noble gas geochemistry. Proceedings of the National Academy of Sciences USA 95, 9087-9092.

Andreani, L., Stanek, K. P., Gloaguen, R., Krentz, O., & Domínguez-González, L. (2014). DEM-based analysis of interactions between tectonics and landscapes in the Ore Mountains and Eger Rift (East Germany and NW Czech Republic). Remote Sensing, 6(9), 7971–8001. https://doi.org/10.3390/rs6097971

Arai, S., Ishimaru, S., 2008. Insights into petrological characteristics of the lithosphere of mantle wedge beneath arcs through peridotite xenoliths: a review. Journal of Petrology 49, 665–695.

Arai, S., Ishimaru, S., Okrugin, V.M., 2003. Metasomatized harzburgite xenoliths from Avacha volcano as fragments of mantle wedge of the Kamchatka arc: Implication for the metasomatic

agent. The Island Arc 12, 233-246.

Arai, S., Takada, S., Michibayashi, K., Kida, M., 2004. Petrology of peridotite xenoliths from Iraya Volcano, Philippines, and its implication for dynamic mantle-wedge processes. Journal of Petrology 45, 369-389.

Babuska,V.&Plomerova, J. (2001): Subcrustal lithosphere around the Saxothuringian – Moldanubian Suture Zone – a model derived from anisotropy of seismic wave velocities. Tectonophysics, 332, 185–199.

Bali, E., Szabó, C., Vaselli, O., Török, K., 2002. Significance of silicate melt pockets in upper mantle xenoliths from the Bakony–Balaton Highland Volcanic Field, Western Hungary. Lithos 61, 79–102.

Ballentine, C.J., 1997. Resolving the mantle He/Ne and crustal 21Ne/ 22Ne in well gases. Earth and Planetary Science Letters 152, 233–249.

Ballentine, C.J., Marty, B., Sherwood Lollar, B., Cassidy, M., 2005. Neon isotopes constrain convection and volatile origin in the Earth's mantle. Nature 433, 33–38.

Ballhaus, C., Berry, R.F., Green, D.H., 1991. High pressure experimental calibration of the olivine-orthopyroxene-spinel oxygen barometer: implications for the oxidation state of the mantle. Contribution to Mineralogy and Petrology 107, 27-40.

Barry, P. H., Hilton, D. R., Füri, E., Halldórsson, S. A., and Grönvold, K. (2014). Carbon isotope and abundance systematics of Icelandic geothermal gases, fluids and subglacial basalts with implications for mantle plume-related CO_2 fluxes. Geochim. Cosmochim. Acta 134, 74–99. doi:10.1016/j.gca.2014.02.038.

Battaglia, A., Bitetto, M., Aiuppa, A., Rizzo, A. L., Chigna, G., Watson, I. M., D'Aleo, R., Juárez Cacao, F. J., and de Moor, M. J. (2018). The Magmatic gas Signature of Pacaya Volcano, With Implications for the Volcanic CO_2 Flux From Guatemala. Geochemistry, Geophys. Geosystems, 667–692. doi:10.1002/2017GC007238.

Beard, A.D., Downes, H., Mason, P.R.D., Vetrin, V.R., 2007. Depletion and enrichment processes in the lithospheric mantle beneath the Kola Peninsula (Russia): Evidence from spinel lherzolite and wehrlite xenoliths. Lithos 94, 1-24.

Bénard, A., Woodland, A.B., Arculus, R.J., Nebel, O., McAlpine, S.R.B., 2018. Variation in sub-arc mantle oxygen fugacity during partial melting recorded in refractory peridotite xenoliths from the West Bismarck Arc. Chemical Geology 486, 16-30.

Bernstein, S., Kelemen, P.B., Hanghøj, K., 2007. Consistent olivine Mg# in cratonic mantle refl ects Archean mantle melting to the exhaustion of orthopyroxene. Geology 35, 459-462.

Białek, D., Raczyński, P., Sztajner, P. & Zawadzki, D. (2007). Archeocjaty wapieni wojcieszowskich. Przegląd Geologiczny 55, 1112-1116.

Bianchini, G., Beccaluva, L., Nowell, G.M., Pearson, D.G., Siena, F., 2011. Mantle xenoliths from Tallante (Betic Cordillera): Insights into the multi-stage evolution of the south Iberian lithosphere. Lithos 124, 308-318.

Birkenmajer, K., Pécskay, Z., Grabowski, J., Lorenc,M.W., Zagożdżon, P. (2007). Radiometric dating of the Tertiary volcanics in Lower Silesia, Poland. V. K–Ar and palaeomagnetic data from late Oligocene to early Miocene basaltic rocks of theNorth-SudeticDepression. Annales Societatis Geologorum Poloniae 77, 1–16.

Bonadiman, C., Beccaluva, L., Coltorti, M., Siena, F., 2005. Kimberlite-like metasomatism and 'garnet signature' in spinelperidotite xenoliths from Sal, Cape Verde Archipelago: relics of a subcontinental mantle domain within the Atlantic Oceanic lithosphere? Journal of Petrology 46, 2465-2493.

Bonadiman, C., Coltorti, M., 2011. Numerical modelling for peridotite phase melting trends in the SiO2-Al2O3-FeO-MgO-CaO system at 2 GPa. 21° Goldschmidt Conf., August 14-19, 2011, Prague. Mineralogical Magazine, 75(3), 548.

Bonadiman, C., Coltorti, M., 2018. Mantle subsolidus and melting behavior as modelled in the system CMASFe. 3rd European Mantle Workshop, Pavia, June 26-28, 2018, Abstract Book.

Bonadiman, C., Nazzareni, S., Coltorti, M., Comodi, P., Giuli, G., Faccini, B., 2014. Crystal chemistry of amphiboles: implications for oxygen fugacity and water activity in lithospheric mantle beneath Victoria Land, Antarctica. Contribution to Mineralogy and Petrology 167: 984, DOI 10.1007/s00410-014-0984-8.

Bonatti, E., Peyve, A., Kepezhinskas, P., Kurentsova, N., Seyler, M., Skolotnev, S., Udintsev, G., 1992. Upper mantle heterogeneity below the Mid-Atlantic Ridge, 0–15N. Journal of Geophysical Research 97, 4461–4476.

Bonatti, E., Seyler, M., Sushevskaya, N., 1993. A cold suboceanic mantle belt at the Earth's equator. Science 261, 315–320.

Boudoire, G., Rizzo, A.L., Di Muro, A., Grassa, F., Liuzzo, M. 2018. Extensive CO2 degassing in the upper mantle beneath oceanic basaltic volcanoes: First insights from Piton de la Fournaise

volcano (La Reunion Island). Geochimica et Cosmochimica Acta, 235, 376-401.

Brandl, P. A., Genske, F. S., Beier, C., Haase, K. M., Sprung, P., and Krumm, S. H. (2015). Magmatic evidence for carbonate metasomatism in the lithospheric mantle underneath the Ohře (Eger) Rift. J. Petrol. 56, 1743–1774. doi:10.1093/petrology/egv052.

Brandon, A.D., Draper, D.S., 1996. Constraints on the origin of the oxidation state of mantle overlying subduction zones: an example from Simcoe, Washington, USA. Geochimica et Cosmochimica Acta 60, 1739–1749.

Bräuer, K., Kämpf, H., Koch, U., and Strauch, G. (2011). Monthly monitoring of gas and isotope compositions in the free gas phase at degassing locations close to the Nový Kostel focal zone in the western Eger Rifţ Czech Republic. Chem. Geol. 290, 163–176. doi:10.1016/j.chemgeo.2011.09.012.

Bräuer, K., Kämpf, H., Koch, U., Strauch, G., 2005. Monthly monitoring of gas and isotope compositions in the free gas phase at degassing locations close to the Nový Kostel focal zone in the western Eger Rift, Czech Republic. Geophys. Res. Lett. 32, L08303. http://dx.doi.org/10.1029/2004GL022205

Bräuer, K., Kämpf, H., Niedermann, S., Strauch, G., 2013. Indications for the ex-istence of different magmatic reservoirs beneath the Eifel area (Germany): a multi-isotope (C, N, He, Ne, Ar) approach. Chem. Geol.356, 193–208.

Bräuer, K., Kämpf, H., Niedermann, S., Strauch, G., and Tesař, J. (2008). Natural laboratory NW Bohemia: Comprehensive fluid studies between 1992 and 2005 used to trace geodynamic processes. Geochemistry, Geophys. Geosystems 9. doi:10.1029/2007GC001921.

Bräuer, K., Kämpf, H., Niedermann, S., Strauch, G., and Weise, S. M. (2004). Evidence for a nitrogen flux directly derived from the European subcontinental mantle in the Western Eger Rift, Central Europe. Geochim. Cosmochim. Acta 68, 4935–4947. doi:10.1016/j.gca.2004.05.032.

Brey, G.P., Köhler, T., 1990. Geothermobarometry in the four-phase lherzolites II. New Thermobarometers and practical assessment of existing thermobarometers. Journal of Petrology 31, 1353-1378.

Bryant, J.A., Yogodzinsky, G.M., Churikova, T.G., 2007. Melt-mantle interactions beneath the Kamchatka arc: evidence from ultramafic xenoliths from Shiveluch volcano. Geochemistry Geophysics Geosystems 8, Q04007, doi:10.1029/2006GC001443, ISSN: 1525-2027.

Buikin, A., Trieloff, M., Hopp, J., Althaus, T., Korochantseva, E., Schwarz, W. H., and Altherr, R.

(2005). Noble gas isotopes suggest deep mantle plume source of late Cenozoic mafic alkaline volcanism in Europe. Earth Planet. Sci. Lett. 230, 143–162. doi:10.1016/j.epsl.2004.11.001.

Burnard, P. (2004). Diffusive fractionation of noble gases and helium isotopes during mantle melting. Earth Planet. Sci. Lett. 220, 287–295. doi:10.1016/S0012-821X(04)00060-3.

Burnard, P. G., Farley, K. a., and Turner, G. (1998). Multiple fluid pulses in a Samoan harzburgite. Chem. Geol. 147, 99–114. doi:10.1016/S0009-2541(97)00175-7.

Burnard, P., Graham, D., and Turner, G. (1997). Vesicle-specific noble gas analyses of "popping rock": Implications for primordial noble gases in earth. Science (80). 276, 568–571. doi:10.1126/science.276.5312.568.

Buzek C., Holy F., and Kvacek Z. (1996) Early Miocene flora of the Cypris shale (Western Bohemia). Acta Musei Nat. Prague, B, Hist. Naturalis 52, 1–72.

Caracausi, A., Avice, G., Burnard, P. G., Füri, E., and Marty, B. (2016). Chondritic xenon in the Earth's mantle. Nature 533, 82–85. doi:10.1038/nature17434.

Chalot-Prat, F., Bouillier, A-M., 1997. Metasomatism in the subcontinental mantle beneath the Eastern Carpathians (Romania): new evidence from trace element geochemistry. Contribution to Mineralogy and Petrology 129, 284-307.

Chazot, G., Menzies, M., Harte, B., 1996. Silicate glasses in spinel lherzolites from Yemen: origin and chemical composition. Chemical Geology 134, 159-179.

Colin, A., Moreira, M., Gautheron, C., Burnard, P., 2015. Constraints on the noble gas composition of the deep mantle by bubble-by-bubble analysis of a volcanic glass sample from Iceland. Chem. Geol.417, 173–183.

Coltorti M., Downes H., Gregoire M. & O'Reilly S.Y. (eds). 2010. Petrological evolution of the European Lithospheric Mantle. Journal Geological Society of London Sp.Is. 377, 246pp (ISSN 0016-7649 Geosciences Multidisciplinary 20/129; I.F. 2.097, 2005).

Coltorti M., Downes H., Grégoire M., O'Reilly S.Y. (eds.) 2009. Petrological evolution of the European Lithospheric Mantle: from Archean to present day. J.Petrol. 50, 7, 223pp.

Coltorti, M., Beccaluva L., Bonadiman, C., Faccini, B., Ntaflos T., Siena F., 2004. Amphibole genesis via metasomatic reaction with clinopyroxene in mantle xenoliths from Victoria Land, Antarctica. Lithos 75, 115-139.

Coltorti, M., Bonadiman, C., Faccini, B., Ntaflos, T., Siena, F., 2007a. Slab melt and intraplate metasomatism in Kapfenstein mantle xenoliths (Styrian Basin, Austria). Lithos 94, 66-89.

Coltorti, M., Bonadiman, C., Faccini, B., Grégoire, M., O'Reilly, S.Y., Powell, W., 2007b. Amphiboles from suprasubduction and intraplate lithospheric mantle. Lithos 99, 68-84.

Correale, A., Martelli, M., Paonita, A., Rizzo, A., Brusca, L., and Scribano, V. (2012). New evidence of mantle heterogeneity beneath the Hyblean Plateau (southeast Sicily, Italy) as inferred from noble gases and geochemistry of ultramafic xenoliths. Lithos 132–133, 70–81. doi:10.1016/j.lithos.2011.11.007.

Correale, A., Paonita, A., Rizzo, A., Grassa, F., and Martelli, M. (2015). The carbon-isotope signature of ultramafic xenoliths from the Hyblean Plateau (southeast Sicily, Italy): Evidence of mantle heterogeneity. Geochemistry, Geophys. Geosystems 16, 600–611. doi:10.1002/2014GC005656.

Correale, A., Rizzo, A. L., Barry, P. H., Lu, J., and Zheng, J. (2016). Refertilization of lithospheric mantle beneath the Yangtze craton in south-east China: Evidence from noble gases geochemistry. Gondwana Res. 38. doi:10.1016/j.gr.2016.01.003.

Correale, A., Pelorosso, B., Rizzo, A.L., Coltorti, M., Italiano, F., Bonadiman, C., Giacomoni, P.P. (2019). The nature of the West Antarctic Rift System as revealed by noble gases in mantle minerals, Chemical Geology, 524, 104-118.

Créon, L., Rouchon, V., Youssef, S., Rosenberg, E., Delpech, G., Szabó, C., Remusat, L., Mostefaoui, S., Asimow, P. D., Antoshechkina, P. M., et al. (2017). Highly CO_2-supersaturated melts in the Pannonian lithospheric mantle – A transient carbon reservoir? Lithos 286–287, 519–533. doi:10.1016/j.lithos.2016.12.009.

Ćwiek, M., Matusiak-Małek, M., Puziewicz, J., Ntaflos, T., (2018) Lithospheric mantle beneath NE part of Bohemian Massif and its rekation to overlying crust: new insights from Pilchowice xenolith suite, Sudetes, SW Poland. International Journal of Earth Sciences, 107,1731-1753

Day, J. M. D., Barry, P. H., Hilton, D. R., Burgess, R., Pearson, D. G., and Taylor, L. A. (2015). The helium flux from the continents and ubiquity of low-3He/4He recycled crust and lithosphere. Geochim. Cosmochim. Acta 153, 116–133. doi:10.1016/j.gca.2015.01.008.

Deines, P. (2002). The carbon isotope geochemistry of mantle xenoliths. Earth-Science Rev. 58, 247–278.

Demény, A., Harangi, S., Vennemann, T.W., Casillas, R., Horvát, P., Milton, A.J., Mason, P.R.D., Ulianov, A., 2012. Amphiboles as indicators of mantle source contamination: Combined evaluation of stable H and O isotope compositions and trace element ratios. Lithos 152, 141-156.

Demény, A., Vennemann, T.W., Homonnay, Z., Milton, A., Embey-Isztin, A., Nagy, G., 2005. Origin of amphibole megacrysts in the Pliocene-Pleistocene basalts of the Carpathian-Pannonian region. Geologica Carpathica 56, 179-189.

Dèzes, P., Schmid, S. M., and Ziegler, P. A. (2004). Evolution of the European Cenozoic Rift System: Interaction of the Alpine and Pyrenean orogens with their foreland lithosphere. Tectonophysics 389, 1–33. doi:10.1016/j.tecto.2004.06.011.

Di Piazza, A., Rizzo, A. L., Barberi, F., Carapezza, M. L., De Astis, G., Romano, C., and Sortino, F. (2015). Geochemistry of the mantle source and magma feeding system beneath Turrialba volcano, Costa Rica. Lithos 232, 319–335. doi:10.1016/j.lithos.2015.07.012.

Dick, H.J.B., Natland, J.H., 1996. Late stage melt evolution and transport in the shallow mantle beneath the East Pacific Rise, in: Gillis, K., Mevel, C. and Allan, J. (Eds), Proceedings of the Ocean Drilling Program, Scientific Results, v. 147, Texas A&M University, Ocean Drilling Program, College Station, TX.

Downes, H., 2001. Formation and modification of the shallow sub-continental lithospheric mantle: a review of geochemical evidence from ultramafic xenolith suites and tectonically emplaced ultramafic massifs of Western and Central Europe. Journal of Petrology 42, 233-250.

Downes, H., Seghedi, I., Szakács, A., Dobosi, G., James, D.E., Vaselli, O., Rigby, I.J., Ingram, G.A., Rex, D., Pécskay, Z., 1995. Petrology and geochemistry of the late Tertiary/Quaternary mafic alkaline volcanism in Romania. Lithos 35, 65–81.

Downes, H., Thirlwall, M. F., and Trayhorn, S. C. (2001). Miocene subduction-related magmatism in southern Sardinia : Sr ± Nd- and oxygen isotopic evidence for mantle source enrichment. J. Volcanol. Geotherm. Res. 106. doi:10.1016/S0377-0273(00)00269-9.

Dunai T. J. and Porcelli D. (2002) Storage and transport of noble gases in the subcontinental lithosphere. Rev. Mineral. Geochem. 47, 371–409.

Dunai, T. J., and Baur, H. (1995). Helium, neon, and argon systematics of the European subcontinental mantle: Implications for its geochemical evolution. Geochim. Cosmochim. Acta 59, 2767–2783. doi:10.1016/0016-7037(95)00172-V.

Edwards, M.A., Grasemann, B., 2009. Mediterranean snapshots of accelerated slab retreat: subduction instability in stalled continental collision. Geological Society, London, Special Publication 311, 155-192.

Embey-Isztin, A., Dobosi, G., Altherr, R., Meyer, H.-P., 2001. Thermal evolution of the lithosphere

beneath the western Pannonian Basin: evidence from deep seated xenoliths. Tectonophysics 331, 285-306.

Ernst, A., Bohaty, J. (2009). Schischcatella (Fenestrata, Bryozoa) from the Devonian of the Rhenish Massif, Germany. Palaeontology, Vol. 52, Part 6, 2009, pp. 1291–1310.

Faccenna, C., Becker, T.W., Lallemand, S., Lagabrielle, Y., Funiciello, F., Piromallo, C., 2010. Subduction-triggered magmatic pulses: a new class of plumes? Earth and Planetary Science Letters 299, 54–68.

Faccini, B., Bonadiman, C., Coltorti, M., Grégoire, M., Siena, F., 2013. Oceanic material recycled within the sub-Patagonian lithospheric mantle (Cerro del Fraile, Argentina). Journal of Petrology 54, 1211-1258.

Faccini, B., Rizzo, A.L., Bonadiman, C., Ntaflos, T., Seghedi, I., Grégoire, M., Ferretti, G., Coltorti, M. (2020). Subduction-related refertilization and alkaline metasomatism in the Eastern Transylvanian Basin lithospheric mantle: evidence from mineral chemistry and noble gases in fluid inclusions. Lithos, under revisions.

Falus, G., Szabó, C., Vaselli, O., 2000. Mantle upwelling within the Pannonian Basin: evidence from xenolith lithology and mineral chemistry. Terra Nova 12, 295-302.

Falus, G., Tommasi, A., Ingrin, J., Szabó, C., 2008. Deformation and seismic anisotropy of the lithospheric mantle in the southeastern Carpathians inferred from the study of mantle xenoliths. Earth and Planetary Science Letters 272, 50–64.

Falus, G., Tommasi, A., Soustelle, V., 2011. The effect of dynamic recrystallization on olivine crystal preferred orientations in mantle xenoliths deformed under varied stress conditions. Journal of Structural Geology 33, 1528-1540.

Foley, S.F., 2011. A reappraisal of redox melting in the Earth's Mantle as a function of tectonic setting and time. Journal of Petrology 52, 1363-1391.

Forshaw, J.B., Waters, D.J., Pattison, D.R.M., Palin, R.M., Gopon, P., 2019. A comparison of observed and thermodynamically predicted phase equilibria and mineral compositions in mafic granulites. Journal of Metamorphic Geology 37, 153-179.

Francis, D.M., 1976. The origin of amphibole in lherzolite xenoliths from Nunivak island Alaska. Journal of Petrology 17, 357–378.

Franz, L., Becker, K.P., Kramer, W., Herzig, P.M., 2002. Metasomatic mantle xenoliths from the Bismarck microplate (Papua New Guinea) – Thermal evolution, geochemistry and extent of

slab-induced metasomatism. Journal of Petrology 43, 315-343.

Frechen, J. & Vieten, K. (1970). Petrographie der Vulkanite des Siebengebirges. Die peralkalische Gesteinsreihe Alkalitrachyt-Sanidinbasanit. Decheniana 122, 357-377.

Füri, E., Hilton, D. R., Halldórsson, S. A., Barry, P. H., Hahm, D., Fischer, T. P., and Grönvold, K. (2010). Apparent decoupling of the He and Ne isotope systematics of the Icelandic mantle: The role of He depletion, melt mixing, degassing fractionation and air interaction. Geochim. Cosmochim. Acta 74, 3307–3332. doi:10.1016/j.gca.2010.03.023.

Füri, E., Hilton, D. R., Murton, B. J., Hémond, C., Dyment, J., and Day, J. M. D. (2011). Helium isotope variations between Réunion Island and the Central Indian Ridge (17°-21°S): New evidence for ridge-hot spot interaction. J. Geophys. Res. Solid Earth 116, 1–17. doi:10.1029/2010JB007609.

Gautheron, C. and Moreira, M. (2002). Helium signature of the subcontinental lithospheric mantle. Earth Planet. Sci. Lett. 199, 39–47. doi:10.1016/S0012-821X(02)00563-0.

Gautheron, C., Moreira, M., and Allègre, C. (2005). He, Ne and Ar composition of the European lithospheric mantle. Chem. Geol. 217, 97–112. doi:10.1016/j.chemgeo.2004.12.009.

Gennaro, M. E., Grassa, F., Martelli, M., Renzulli, A., and Rizzo, A. L. (2017). Carbon isotope composition of CO_2-rich inclusions in cumulate-forming mantle minerals from Stromboli volcano (Italy). J. Volcanol. Geotherm. Res. 346. doi:10.1016/j.jvolgeores.2017.04.001.

Giggenbach, W.F., Sano, Y., Schmincke, H.U., 1991. CO_2-rich gases from Lakes Nyos and Monoun, Cameroon; Laacher See, Germany; Dieng, Indonesia, and Mt. Gambier, Australia — variations on a common theme. J. Volcanol. Geotherm. Res. 45, 311–323.

Gîrbacea, R., Frisch, W., Linzer, H.-G., 1998. Post-orogenic uplift induced extension: a kinematic model for the Pliocene to recent tectonic evolution of the Eastern Carpathians (Romania). Geologica Carpathica 49, 315–327.

Graham (2002). Noble Gas Isotope Geochemistry of Mid-Ocean Ridge and Ocean Island Basalts: Characterization of Mantle Source Reservoirs. Rev. Mineral. Geochemistry 47, 247–317. doi:10.2138/rmg.2002.47.8.

Grégoire, M., McInnes, B.I.A., O'Reilly, S.Y., 2001. Hydrous metasomatism of oceanic sub-arc mantle, Lihir, Papua New Guinea — part 2. Trace element characteristics of slab-derived fluids. Lithos 59, 91–108.

Griesshaber, E., Niedermann, S., Schulte, U., Möller, P., Dulski, P., 2002. Geochemical

characteristics of the mantle plume at the Eifel. Geochim. Cosmochim. Acta 66, Goldschmidt A291.

Griesshaber, E., O'Nions, R.K., Oxburgh, E.R., 1992. Helium and carbon isotope systematics in crustal fluids from the Eifel, the Rhine Graben and Black Forest, F.R.G. Chem. Geol. 99, 213–235.

Guillot, B., and Sator, N. (2011). Carbon dioxide in silicate melts: A molecular dynamics simulation study. Geochim. Cosmochim. Acta 75, 1829–1857. doi:10.1016/j.gca.2011.01.004.

Gurenko, A. A., Hoernle, K. A., Hauff, F., Schmincke, H. U., Han, D., Miura, Y. N., and Kaneoka, I. (2006). Major, trace element and Nd-Sr-Pb-O-He-Ar isotope signatures of shield stage lavas from the central and western Canary Islands: Insights into mantle and crustal processes. Chem. Geol. 233, 75–112. doi:10.1016/j.chemgeo.2006.02.016.

Harangi, S., 2001. Neogene to Quarternary volcanism of the Carpathian-Pannonian Region – a review. Acta Geologica Hungarica 44, 223-258.

Harangi, S., Lenkey, L., 2007. Genesis of the Neogene to Quaternary volcanism in the Carpathian-Pannonian region: Role of subduction, extension, and mantle plume. Geological Society of America Special Paper 418, 67-92.

Harangi, S., Sági, T., Seghedi, I., Ntaflos, T., 2013. A combined whole-rock and mineral-scale investigation to reveal the origin of the basaltic magmas of the Perşani monogenetic volcanic field, Romania, eastern-central Europe. Lithos 180–181, 43-57.

Harangi, S., Jankovics, M. É., Sági, T., Kiss B., Lukács R., Soós I., 2014. Origin and geodynamic relationships of the Late Miocene to Quaternary alkaline basalt volcanism in the Pannonian basin, eastern–central Europe. International Journal of Earth Sciences (Geol Rundsch) 104, 2007-2032.

Harrison, D., Barry, T., and Turner, G. (2004). Possible diffusive fractionation of helium isotopes in olivine and clinopyroxene phenocrysts. Eur. J. Mineral. 16, 213–220. doi:10.1127/0935-1221/2004/0016-0213.

Hawthorne, F.C., Oberti, R., 2007. Amphiboles: crystal chemistry. Reviews in Mineralogy and Geochemistry 67, 1–54.

Heber, V. S., Brooker, R. A., Kelley, S. P., and Wood, B. J. (2007). Crystal-melt partitioning of noble gases (helium, neon, argon, krypton, and xenon) for olivine and clinopyroxene. Geochim. Cosmochim. Acta 71, 1041–1061. doi:10.1016/j.gca.2006.11.010.

Heber, V.S., Wieler, R., Baur, H., Olinger, C., Friedmann, A., Burnett, D.S. (2009) Noble gas composition of the solar wind as collected by the Genesis mission. Geochimica et Cosmochimica Acta 73, 7414–7432.

Hellebrand, E., Snow, J.E., Dick, H.J.B., Hofmann, A.W., 2001. Coupled major and trace elements as indicators of the extent of melting in mid-ocean-ridge peridotites. Nature 410, 677-681.

Herzberg, C., Vidito, C., Starkey, N.A., 2016. Nickel–cobalt contents of olivine record origins of mantle peridotite and related rocks. American Mineralogist 101,1952–1966.

Hilton, D. R., Hammerschmidt, K., Teufel, S., and Friedrichsen, H. (1993). Helium isotope characteristics of Andean geothermal fluids and lavas. Earth Planet. Sci. Lett. 120, 265–282. doi:10.1016/0012-821X(93)90244-4.

Hilton, D.R., McMurty, G.M., Kreulen, R. (1997). Evidence for extensive degassing of the Hawaiian mantle plume from helium-carbon relationship at Kilauea volcano. Geophys. Res. Lett. 24, 3065-3068.

Hilton, D. R., Fischer, T. P., and Marty, B. (2002). Noble Gases and Volatile Recycling at Subduction Zones. Rev. Mineral. Geochemistry 47, 319–370. doi:10.2138/rmg.2002.47.9.

Hilton, D. R., Ramírez, C. J., Mora-Amador, R., Fischer, T. P., Füri, E., Barry, P. H., and Shaw, A. M. (2010). Monitoring of temporal and spatial variations in fumarole helium and carbon dioxide characteristics at Poás and Turrialba Volcanoes, Costa Rica (2001-2009). Geochem. J. 44, 431–440.

Hoefs, J. (2015). Stable isotope geochemistry. Springer Edition.

Holness, M.B., Vukmanovic, Z., Mariani, E., 2017. Assessing the role of compaction in the formation of adcumulates: a microstructural perspective. Journal of Petrology 58, 643-674.

Hrubcová, P., Geissler, W. H., Bräuer, K., Vavryčuk, V., Tomek, Č., and Kämpf, H. (2017). Active Magmatic Underplating in Western Eger Rift, Central Europe. Tectonics 36, 2846–2862. doi:10.1002/2017TC004710.

Ionov, D.A., 2010. Petrology of mantle wedge lithosphere: new data on supra-subduction zone peridotite xenoliths from the andesitic Avacha volcano, Kamchatka. Journal of Petrology 51, 327-361.

Ionov, D.A., Hofmann, A.W., 1995. Nb-Ta-rich mantle amphiboles and micas: implications for subduction-related metasomatic trace element fractionations. Earth and Planetary Science Letters 131, 341-356.

Ionov, D.A., Griffin, W.L., O'Reilly, S.Y., 1997. Volatile-bearing minerals and lithophile trace elements in the upper mantle. Chemical Geology 141, 153-184.

Ionov, D.A., Bodinier, J-L., Mukasa, S. B., Zanetti, A., 2002. Mechanism and sources of mantle metasomatism: major and trace element compositions of peridotite xenoliths from Spitsbergen in the context of numerical modelling. Journal of Petrology 43, 2219-2259.

Ionov, D.A., and Hofmann, A.W. (2007). Depth of formation of sub-continental off-craton peridotites: Earth and Planetary Science Letters, v. 261, p. 620–634, doi:10.1016/j.epsl.2007.07.036.

Ionov, D.A., Bénard, A., Plechov, P.Yu., Shcherbakov, V.D., 2013. Along-arc variations in lithospheric mantle compositions in Kamchatka, Russia: First trace element data on mantle xenoliths from the Klyuchevskoy Group volcanoes. Journal of Volcanology and Geothermal Research 263, 122–131.

Ishimaru, S., Arai, S., 2008. Calcic amphiboles in peridotite xenoliths from Avacha volcano, Kamchatka, and their implications for metasomatic conditions in the mantle wedge. Geological Society Special Publications 293, 35-55.

Ishimaru, S., Arai, S., Ishida, Y., Mirasaka, M., Okrugin, V.M., 2007. Melting and Multi-stage Metasomatism in the MantleWedge beneath a Frontal Arc Inferred from Highly Depleted Peridotite Xenoliths from the AvachaVolcano, Southern Kamchatka. Journal of Petrology 48, 395-433.

Ismail-Zadeh, A., Matenco, L., Radulian, M., Cloetingh, S., Panza, G., 2012. Geodynamics and intermediate-depth seismicity in Vrancea (the south-eastern Carpathians): current state-of-the art. Tectonophysics 530–531, 50–79.

Jambon, A., Weber, H., Braun, O. (1986). Solubility of He, Ne, Ar, Kr and Xe in a basalt melt in the rauge 1250-1600°C. Geochemical implicactions. Geochim. Cosmochim. Acta 50, 401-408.

Jamieson, H.E., Roeder, P.L., 1984. The distribution of Mg and Fe2+ between olivine and spinel at 1300°C. American Mineralogist 69, 283-291.

Javoy, M., and Pineau, F. (1991). The volatiles record of a " popping " rock from the Mid-Atlantic Ridge at 14 ° N : chemical and isotopic composition of gas trapped in the vesicles. 107, 598–611.

Johnson, K.T.M., Dick, H.J.B., Shimizu, N., 1990. Melting in the oceanic upper mantle: an Ion Microprobe study of diopsides in abyssal peridotites. Journal of Geophysical Research 95, 2661-

2678.

Jones, A. P., Genge, M., and Carmody, L. (2013). Carbonate Melts and Carbonatites. Rev. Mineral. Geochemistry 75, 289–322. doi:10.2138/rmg.2013.75.10.

Kaneoka, I. (1983). Noble gas constraints on the layered structure of the mantle. Nature 302, 698-700.

Kennedy, B.M., Hiyagon, H., and Reynolds, J.H., 1990. Crustal neon: a striking uniformity. Earth and Planetary Science Letters 98, 277-286.

Kepezhinskas, P., Defant, M.J., Drummond, M.S., 1996. Progressive enrichment of island arc mantle by metl-peridotite interaction inferred from Kamchatka xenoliths. Geochimica et Cosmochimica Acta, 60, 1217-1229.

Keyser, M., Ritter, J.R.R., Jordan, M., 2002. 3D shear-wave velocity structure of the Eifel plume, Germany. Earth Planet. Sci. Lett. 203, 59-82.

Kis, B.M., Ionescu, A., Cardellini, A., Harangi, S., Baciu, C., Caracausi, A., Viveiros, F. 2017. Quantification of carbon dioxide emissions of Ciomadul, the youngest volcano of the Carpathian-Pannonian Region (Eastern-Central Europe, Romania). Journal of Volcanology and Geothermal Research 341, 119–130.

Kis, B.M., Caracausi, Palcsu, L., Baciu, C., A., Ionescu, A., Futó, I., Sciarra, A., Harangi, S. 2019. Noble gas and carbon isotope systematics at the seemingly inactive Ciomadul volcano (Eastern-Central Europe, Romania): evidence for volcanic degassing. Geochemistry, Geophysics, Geosystems, https://doi.org/10.1029/2018GC008153.

Klemme, S., 2007. The influence of Cr on the garnet–spinel transition in the Earth's mantle: experiments in the system MgO–Cr2O3–SiO2 and thermodynamic modeling. Lithos 77, 639-646.

Kolb, M., Paulick, H., Kirchenbaur, M., Münker, C., 2012. Petrogenesis of mafic to felsic lavas from the Oligocene Siebengebirge volcanic field (Germany): implications for the origin of intracontinental volcanism in Central Europe. Journal of Petrology 53, 2349–2379.

Koněčný, V., Kováč, M., Lexa, J., Šefara, J., 2002. Neogene evolution of the Carpatho-Pannonian region: an interplay of subduction and back-arc diapiric uprise in the mantle. EGU Stephan Mueller Special Publication Series 1, 105-123.

Kovács, I., Patkó, L., Falus, G., Aradi, L.E., Szanyi, G., Gráczer, Z., Szabó, C., 2018. Upper mantle xenoliths as sources of geophysical information: the Perşani Mts. area as a case study. Acta

Geodaetica et Geophysica, https://doi.org/10.1007/s40328-018-0231-2.

Kryza, R., Willner, A. P., Massonne, H. J., Muszyński, A. & Schertl, H. P. (2011). Blueschist-facies metamorphism in the Kaczawa Mountains (Sudetes, SW Poland) of the Central-European Variscides: P-T constraints from a jadeite-bearing metatrachyte. Mineralogical Magazine 75, 241-263.

Kurz, M.K. (1986). Cosmogenic helium in a terrestrial igneous rock. Nature 320, 435-439.

Kurz, M. D., Curtice, J., Fornari, D., Geist, D., and Moreira, M. (2009). Primitive neon from the center of the Galápagos hotspot. Earth Planet. Sci. Lett. 286, 23–34. doi:10.1016/j.epsl.2009.06.008.

Ladenberger, A., Lazor, P., and Michalik, M. (2009). CO2 fluid inclusions in mantle xenoliths from Lower Silesia (SW Poland): formation conditions and decompression history. Eur. J. Mineral. 21, 751–761. doi:10.1127/0935-1221/2009/0021-1930.

Lee, C.T., Rudnick, R.L., McDonough, W.F., Horn, I., 2000. Petrologic and geochemical investigation of carbonates in peridotite xenoliths from northeastern Tanzania. Contribution to Mineralogy and Petrology 139, 470-484.

Lehmann, J., 1983. Diffusion between olivine and spinel: Application to geothermometry Earth and Planetary Science Letters, 64,123-138.

Lustrino, M., and Carminati, E. (2007). Phantom plumes in Europe and the circum-Mediterranean region. Geol. Soc. Am. Spec. Pap. 430, 723–745. doi:10.1130/2007.2430(33).

Lustrino, M., and Wilson, M. (2007). The circum-Mediterranean anorogenic Cenozoic igneous province. Earth-Science Rev. 81, 1–65. doi:10.1016/j.earscirev.2006.09.002.

Macpherson, C., Mattey, D. (1994). Carbon isotope variations of CO2 in Central Lau Basin basalats and ferrobasalts. Earth Planet. Sci. Lett. 121, 263–276.

Majdanski, M., Grad, M., Guterch, A., SUDETES 2003 Working Group (2006): 2-D seismic tomographic and ray tracing modelling of the crustal structure across the Sudetes Mountains basing on SUDETES 2003 experiment data. Tectonophysics, 413, 249–269.

Mandler, B.E., Grove, T.L., 2016. Controls on the stability and composition of amphibole in the Earth's mantle. Contribution to Mineralogy and Petrology 171:68.

Martelli, M., Bianchini, G., Beccaluva, L., and Rizzo, A. (2011). Helium and argon isotopic compositions of mantle xenoliths from Tallante and Calatrava, Spain. J. Volcanol. Geotherm. Res. 200, 18–26. doi:10.1016/j.jvolgeores.2010.11.015.

Martelli, M., Rizzo, A. L., Renzulli, A., Ridolfi, F., Arienzo, I., and Rosciglione, A. (2014). Noble-gas signature of magmas from a heterogeneous mantle wedge: The case of Stromboli volcano (Aeolian Islands, Italy). Chem. Geol. 368, 39–53. doi:10.1016/j.chemgeo.2014.01.003.

Martin, M., Wenzel, F., CALIXTO Working Group, 2006. High-resolution teleseismic body wave tomography beneath SE Romania: II. Imaging of a slab detachment scenario. Geophysical Journal International 164, 579–595.

Marty, B., 2012. The origins and concentrations of water, carbon, nitrogen and noble gases on Earth. Earth and Planetary Science Letters 313–314, 56–66.

Marty, B., and Jambon, A. (1987). C3He in volatile fluxes from the solid Earth: implications for carbon geodynamics. Earth Planet. Sci. Lett. 83, 16–26. doi:10.1016/0012-821X(87)90047-1.

Mason, P.R.D., Downes, H., Thirlwall, M. F., Seghedi, I., Szakács, A., Lowry, D., Mattey, D., 1996. Crustal assimilation as a major petrogenetic process in the East Carpathian Neogene and Quaternary continental margin arc, Romania. Journal of Petrology 37, 927-959.

Mason, P.R.D., Seghedi, I., Szákacs, A., Downes, H., 1998. Magmatic constraints on geodynamic models of subduction in the East Carpathians, Romania. Tectonophysics 297, 157–176.

Matenco, L., Bertotti, G., Leever, K., Cloetingh, S., Schmid, S.M., Tărăpoancă, M., Dinu, C., 2007. Large-scale deformation in a locked collisional boundary: Interplay between subsidence and uplift, intraplate stress, and inherited lithospheric structure in the late stage of the SE Carpathians evolution. Tectonics 26, TC4011, doi:10.1029/2006TC001951.

Matsumoto, T., Honda, M., McDougall, I., and O'Reilly, S. Y. (1998). Noble gases in anhydrous lherzolites from the Newer Volcanics, southeastern Australia: A MORB-like reservoir in the subcontinental mantle. Geochim. Cosmochim. Acta 62, 2521–2533. doi:10.1016/S0016-7037(98)00173-2.

Matsumoto T., Honda, M., McDougall, I., O'Really, S.Y., Norman, M., Yaxley, G. (2000). Noble gases in pyroxenites and metasomatised peridotites from the Newer Volcanics, southeastern Australia: Implications for mantle metasomatism. Chem. Geol. 168, 49–73. doi:10.1016/S0009-2541(00)00181-9.

Matsumoto, T., Chen, Y., and Matsuda, J. (2001). Concomitant occurrence of primordial and recycled noble gases in the Earth's mantle. Earth Planet. Sci. Lett. 185, 35–47. doi:10.1016/S0012-821X(00)00375-7.

Matsumoto, T., Pinti, D. L., Matsuda, J. I., and Umino, S. (2002). Recycled noble gas and nitrogen

in the subcontinental lithospheric mantle: Implications from N-He-Ar in fluid inclusions of SE Australian xenoliths. Geochem. J. 36, 209–217. doi:10.2343/geochemj.36.209.

Mattey, D. P. (1991). Carbon dioxide solubility and carbon isotope fractionation in basaltic melt. Geochim. Cosmochim. Acta 55, 3467–3473. doi:10.1016/0016-7037(91)90508-3.

Mattioli, G.S., Wood, B., 1988. Magnetite activities across the MgAl2O4–Fe3O4 spinel join, with application to thermobarometric estimates of upper mantle oxygen fugacity. Contribution to Mineralogy and Petrology 98, 148–162.

Matusiak-Malek, M., Puziewicz, J., Ntaflos, T., GréGoire, M., Benoit, M., and KlüGel, A. (2014). Two contrasting lithologies in off-rift subcontinental lithospheric mantle beneath central Europec-the Krzeniów (SW Poland) case study. J. Petrol. 55, 1799–1828. doi:10.1093/petrology/egu042.

Matusiak-Małek, M., Puziewicz, J., Ntaflos, T., Grégoire, M., Kukuła, A., and Wojtulek, P. M. (2017). Origin and evolution of rare amphibole-bearing mantle peridotites from Wilcza Góra (SW Poland), Central Europe. Lithos 286–287, 302–323. doi:10.1016/j.lithos.2017.06.017.

Mazur, S., Aleksandrowski, P., Kryza, R. & Oberc-Dziedzic, T. (2006). The Variscan orogen in Poland. Geological Quarterly 50, 89-118.

McDonough, W.F., and Sun, S.-s., 1995, The composition of the Earth: Chemical Geology, v. 120, p. 223–253, doi:10.1016/0009-2541(94)00140-4.

McInnes, B.I.A., Grégoire, M., Binns, R.A., Herzig, P.M., Hannington, M.D., 2001. Hydrous metasomatism of oceanic sub-arc mantle, Lihir, Papua New Guinea: petrology and geochemistry of fuid-metasomatised mantle wedge xenoliths. Earth and Planetary Science Letters 188, 169-183.

Mercier, J.-C.C., Nicolas, A., 1975. Textures and fabrics of upper mantle peridotites as illustrated by xenoliths from basalts. Journal of Petrology 16, 454-487.

Mertes H, Schmincke HU (1985) Mafic potassic lavas of the Quaternary West Eifel field (Western Germany) I. Major and trace elements. Contrib Mineral Petrol 89:330-345

Merten, S., Matenco, L., Foeken, J.P.T., Stuart, F.M., Andriessen, P.A.M., 2010. From nappe stacking to out-of-sequence post-collisional deformations: Cretaceous to Quaternary exhumation history of the SE Carpathians assessed by low-temperature thermochronology. Tectonics 29, TC3013.

Moine, B.N., Grégoire, M., O'Reilly, S.Y., Sheppard, S.M.F., Cottin, J.Y., 2001. High field strength element fractionation in the upper mantle: evidence from amphibole-rich composite mantle

xenoliths from the Kerguelen Islands (Indian Ocean). Journal of Petrology 42, 2145-2167.

Molnár, K., Harangi, S., Lukács, R., Dunkl, I., Schmitt, A.K., Kiss, B., Garamhegyi, T., Seghedi, I., 2018. The onset of the volcanismin the Ciomadul Volcanic Dome Complex (Eastern Carpathians): eruption chronology and magma type variation. Journal of Volcanology and Geothermal Research 354, 39–56.

Moreira, M. (2013). Noble Gas Constraints on the Origin and Evolution of Earth's Volatiles. Geochemical Perspectives (2013) 2 (2): 229-230.

Moreira, M., Kunz, J., and Allègre, C. (1998). Rare gas systematics in popping rock: Isotopic and elemental compositions in the upper mantle. Science (80-.). 279, 1178–1181. doi:10.1126/science.279.5354.1178.

Moreira, M., Rouchon, V., Muller, E., and Noirez, S. (2018). The xenon isotopic signature of the mantle beneath Massif Central. Geochemical Perspect. Lett. 6, 28–32. doi:10.7185/geochemlet.1805.

Mukhopadhyay, S., 2012. Early differentiation and volatile accretion recorded in deep-mantle neon and xenon. Nature 486 (7401), 101.

Niu, Y., 2004. Bulk-rock major and trace element compositions of abyssal peridotites: implications for mantle melting, melt extraction and post-melting processes beneath mid-ocean ridges. Journal of Petrology 45, 2423-2458.

Niu, Y., Langmuir, C.H., Kinzler, R.J., 1997. The origin of abyssal peridotites: a new perspective. Earth and Planetary Science Letters 152, 251-265.

Nowell, D.A., Jones, M.C., Pyle, D.M., 2006. Episodic Quaternary volcanism in France and Germany. Journal of Quaternary Science 21, 645–675.

Ntaflos, T., Bizimis, M., Abart, R., 2017. Mantle xenoliths from Szentbékálla, Balaton: Geochemical and petrological constraints on the evolution of the lithospheric mantle underneath Pannonian Basin, Hungary. Lithos 276, 30-44.

Nuccio, P. M., Paonita, A., Rizzo, A., and Rosciglione, A. (2008). Elemental and isotope covariation of noble gases in mineral phases from Etnean volcanics erupted during 2001-2005, and genetic relation with peripheral gas discharges. Earth Planet. Sci. Lett. 272, 683–690. doi:10.1016/j.epsl.2008.06.007.

Oncescu, M.C., Burlacu, V., Anghel, M., Smalberger, V., 1984. Three-dimensional P-wave velocity image under the Carpathian arc. Tectonophysics 106, 305–319.

O'Neill, H. St.C., 1981. The transition between spinel lherzolite and garnet lherzolite and its use as a geobarometer. Contrib Mineral Petrol 77, 185 194.

O'Neill, H.S.C., Wall, V.J., 1987. The olivine–orthopyroxene–spinel oxygen geobarometer, the nickel precipitation curve, and the oxygen fugacity of the Earth's upper mantle. Journal of Petrology 28, 1169–1191.

Ozima, M., Podosek, F.A. (1983). Noble Gas Geochemistry. Cambridge University Press, New York.

Ozima, M., Podosek, A.P., 2002. Noble Gas Geochemistry, second ed. Cambridge University Press, Cambridge 10–15.

Panaiotu, C.G., Pécskay, Z., Hambach, U., Seghedi, I., Panaiotu, C.C., Itaya, C.E.T., Orleanu, M., Szakács, A., 2004. Short-lived Quaternary volcanism in the Persani Mountains (Romania) revealed by combined K–Ar and paleomagnetic data. Geologica Carpathica 55, 333–339.

Parkinson, I.J., Arculus, R.J., Eggins, S.M., 2003. Peridotite xenoliths from Grenada, Lesser Antilles Island Arc. Contribution to Mineralogy and Petrology 146, 241–262.

Pécskay, Z., Edelstein, O., Seghedi, I., Szakács, A., Crihan, M., Bernad, A., 1995a. K-Ar dating of Neogene-Quaternary calc-alkaline volcanic rocks in Romania. Acta Vulcanologica 7, 53-61.

Pécskay, Z., Lexa, J., Szakács, A., Balogh, K., Seghedi, I., Konečný, V., Kovács, M., Márton, E., Kaličiak, M., Széky-Fux, V., Póka, T., Gyarmati, P., Edelstein, O., Rosu, E., Žec, B., 1995b. Space and time distribution of Neogene-Quaternary volcanism in the Carpatho-Pannonian Region. Acta Vulcanologica 7, 15-28.

Pécskay, Z., Birkenmajer, K. (2013). Insight into the geochronology of Cenozoic alkaline basaltic volcanic activity in Lower Silesia (SW Poland) and adjacent areas. In: Büchner, J., Rapprich, V., Tietz, O. (Eds.), Basalt 2013 – Cenozoic Magmatism in Central Europe, Abstract and Excursion Guides. Czech Geological Survey. Prague and Seckneberg Museum of Natural History Görlitz, pp. 66–67.

Pilet, S., Ulmer, P., Villiger, S., 2010. Liquid line of descent of a basanitic liquid at 1.5 GPa: constraints on the formation of metasomatic veins. Contributions to Mineralogy and Petrology 159, 621–643.

Plomerová, J., Achauer, U., Babuška, V., Vecsey, L., the BOHEMA working group (2007). Upper mantle beneath the Eger Rift (Central Europe): plume or asthenosphere upwelling? Geophysical Journal International 169, 675–682.

Popa, M., Radulian, M., Szakács, A., Seghedi, I., Zaharia, B., 2012. New seismic and tomography

data in the southern part of the Harghita Mountains (Romania, Southeastern Carpathians): connection with recent volcanic activity. Pure and Applied Geophysics 169, 1557–1573.

Pouchou, J.L., Pichoir, F., 1991. Quantitative analysis of homogeneous or stratified microvolumes applied the model "PAP", in: Heinrich, K.F.J., Newbury, D.E. (Eds.), Electron Probe Quantification. Plenum, New York, London, pp. 31–35.

Powell, W., Zhang, M., O'Reilly, S.Y., Tiepolo, M., 2004. Mantle amphibole trace-element and isotopic signatures trace multiple metasomatic episodes in lithospheric mantle, western Victoria, Australia. Lithos 75, 141-171.

Prodehl, C., Mueller, S., & Haak, V. (1995). The European Cenozoic Rift System. In K. H. Olsen (Ed.), Continental rifts: Evolution, Structure, Tectonics. Developments in Geotectonics (Vol. 25, pp. 133–212). New York: Elsevier.

Rison, W., and Craig, H. (1983). Helium isotopes and mantle volatiles in Loihi Seamount and Hawaiian Island basalts and xenoliths. Earth Planet. Sci. Lett. 66, 407–426. doi:10.1016/0012-821X(83)90155-3.

Ritter, J.R.R., Jordan, M., Christensen, U.R., Achauer, U., 2001. A mantle plume below the Eifel volcanic fields, Germany. Earth Planet. Sci. Lett. 186, 7–14.

Ritter, J.R.R., 2007. The seismic signature of the Eifel Plume. In: Ritter, J.R.R., Christensen, U.R. (Eds.), Mantle Plumes: A Multidisciplinary Approach. Springer-Verlag, Berlin Heidelberg, pp. 379–404.

Rizzo, A. L., Barberi, F., Carapezza, M. L., Di Piazza, A., Francalanci, L., Sortino, F., and D'Alessandro, W. (2015). New mafic magma refilling a quiescent volcano: Evidence from He-Ne-Ar isotopes during the 2011-2012 unrest at Santorini, Greece. Geochemistry, Geophys. Geosystems 16. doi:10.1002/2014GC005653.

Rizzo, A.L., Pelorosso, B., Coltorti, M., Ntaflos, T., Bonadiman, C., Matusiak-Małek, M., Italiano, F., Bergonzoni, G., 2018. Geochemistry of noble gases and CO2 in fluid inclusions from lithospheric mantle beneath Wilcza Góra (Lower Silesia, Southwest Poland). Frontiers in Earth Sciences 6:215. doi: 10.3389/feart.2018.00215.

Robidoux, P., Aiuppa, A., Rotolo, S. G., Rizzo, A. L., Hauri, E. H., and Frezzotti, M. L. (2017). Volatile contents of mafic-to-intermediate magmas at San Cristóbal volcano in Nicaragua. Lithos 272–273. doi:10.1016/j.lithos.2016.12.002.

Roedder, E., 1984. Fluid inclusions reviews in mineralogy. Mineralogical Society of America 12, 644

doi: 10.1515/9781501508271.

Sano, Y., Marty, B. (1995). Origin of carbon in fumarolic gas from island arcs. Chem. Geol. 119, 265–274.

Sapienza, G., Hilton, D. R., and Scribano, V. (2005). Helium isotopes in peridotite mineral phases from Hyblean Plateau xenoliths (south-eastern Sicily , Italy). Chem. Geol. 219, 115–129. doi:10.1016/j.chemgeo.2005.02.012.

Sarda, P., 2004. Surface noble gas recycling to the terrestrial mantle. Earth and Planetary Science Letters 228, 49–63.

Sarda, P., Staudacher, T., and Allègre, C. J. (1988). Neon isotopes in submarine basalts. Earth Planet. Sci. Lett. 91, 73–88. doi:10.1016/0012-821X(88)90152-5.

Sawicki, L. (1995). Geological Map of Lower Silesia With Adjacent Czech and German Territories (Without Quaternary Deposits). Polish Geological Institute, Warszawa.

Schmädicke, E., Gose, J., Will, T.M., 2011. Heterogeneous mantle underneath the North Atlantic: Evidence from water in orthopyroxene, mineral composition and equilibrium conditions of spinel peridotite from different locations at the Mid-Atlantic Ridge. Lithos 125, 308–320.

Schmincke H-U, Lorenz V, Seck HA (1983) The Quaternary Eifel volcanic fields. In: Fuchs K et al (eds) Plateau Uplift - The Rhenish Shield - A Case History. Springer (Heidelberg), pp 139-151

Schmincke, H.-U., 2007. The Quaternary volcanic fields of the East and the West Eifel (Germany). In: Ritter, J.R.R., Christensen,U.R. (Eds.),Mantle Plumes:AMultidisciplinary Approach. Springer-Verlag, Berlin Heidelberg, pp. 241–322.

Scott, J.M., Liu, J., Pearson, D.G., Waight T.E., 2016. Mantle depletion and metasomatism recorded in orthopyroxene in highly depleted peridotites. Chemical Geology 441, 280-291.

Seghedi, I., Downes, H., 2011. Geochemistry and tectonic development of Cenozoic magmatism in the Carpathian–Pannonian region. Gondwana Research, 20, 655–672.

Seghedi, I., Downes, H., Szakács, A., Mason, P.R.D., Thirlwall, M.F., Roşu, E., Pécskay, Z., Marton, E., Panaiotu, C., 2004. Neogene-Quaternary magmatism and geodynamics in the Carpathian–Pannonian region: a synthesis. Lithos 72, 117–146.

Seghedi, I., Matenco, L., Downes, H., Mason, P.R.D., Szakács, A., Pécskay, Z., 2011. Tectonic significance of changes in post-subduction Pliocene-Quaternary magmatism in the south east part of the Carpathian–Pannonian region. Tectonophysics 502, 146–157.

Seghedi, I., Popa R-G., Panaiotu, C.G., Szakács, A., Pécskay, Z., 2016. Short-lived eruptive episodes during the construction of a Na-alkalic basaltic field (Perşani Mountains, SE Transylvania, Romania). Bullettin of Volcanology 78:69, DOI 10.1007/s00445-016-1063-y.

Seyler, M., Cannat, M.C., Mével, C., 2003. Evidence for major-element heterogeneity in the mantle source of abyssal peridotites from the Southwest Indian Ridge (52° to 68°E). Geochemistry Geophysics Geosystems 4, 9101, DOI:10.1029/2002GC000305.

Shibata, T., Thompson, G., 1986. Peridotites from the Mid-Atlantic Ridge at 43° N and their petrogenetic relation to abyssal tholeiites. Contributions to Mineralogy and Petrology 93,144-159.

Smulikowski, K., Kozłowska-Koch, M. (1984). Bazaltoidy Wilczej Góry koło Złotoryi (Dolny Śląsk) i ich enklawy. Archiwum Mineralogiczne 40, 53–104 (in Polish).

Sorbadere F., Laurenz V., Frost D.J., Wenz M., Rosenthal A., McCammon C., Rivard C., 2018. The behaviour of ferric iron during partial melting of peridotite. Geochimica et Cosmochimica Acta 239, 235–254.

Špaček, P., Sýkorová, Z., Pazdírková, J., Švancara, J., and Havíř, J. (2006). Present-day seismicity of the south-eastern Elbe Fault System (NE Bohemian Massif). Stud. Geophys. Geod. 50, 233–258. doi:10.1007/s11200-006-0014-z.

Straub, S. M., Gomez-Tuena, A., Stuart, F.M., Zellmer, G.F., Espinasa-Perena, R., Cai, Y., Iizuka, Y., 2011. Formation of hybrid arc andesites beneath thick continental crust. Earth and Planetary Science Letters 303, 337-347.

Stuart, F. M., Lass-Evans, S., Fitton, J. G., and Ellam, R. M. (2003). High 3He/4He ratios in picritic basalts from Baffin Island and the role of a mixed reservoir in mantle plumes. Nature 424, 57–59. doi:10.1038/nature01711.

Szabó, Cs., Vaselli, O., Vanucci, R., Bottazzi, P., Ottolini, L., Coradossi, N., Kubovics, I., 1995a. Ultramafic xenoliths from the Little Hungarian Plain (Western Hungary): a petrologic and geochemical study. Acta Vulcanologica 7, 249–263.

Szabó, C., Harangi, S., Vaselli, O., Downes, H., 1995b. Temperature and oxygen fugacity in peridotite xenoliths from the Carpathian-Pannonian Region. Acta Vulcanologica 7, 231-239.

Szakács, A., Seghedi, I., Pécskay, Z. 1993. Pecularities of South Harghita Mts. as terminal segment of the Carpathian Neogene to Quaternary volcanic chain. Revue Roumaine de Géologie 37, 21–36.

Szakács, A., Seghedi, I., 1995. The Călimani-Ghiurghiu-Harghita volcanic chain, East Carpathians, Romania: volcanological features. Acta Vulcanologica 7, 145-153.

Takazawa, E., Frey, F.A., Shimizu, N., Obata, M., 2000. Whole rock compositional variation in an upper mantle peridotite (Horoman, Hokkaido, Japan): are they consistent with a partial melting process. Geochimica et Cosmochimica Acta 64, 695–716.

Taylor, W.R. 1998. An experimental test of some geothermometer and geobarometer formulations for upper mantle peridotites with application to the thermobarometry of fertile lherzolite and garnet websterite. Neues Jahrbuch für Mineralogie Abhandlungen 172, 381-408.

Tiepolo, M., Bottazzi, P., Palenzona, M., Vannucci, R., 2003. A Laser probe coupled with ICP double-focusing sector-field mass spectrometer for in situ analysis of geological samples and U–Pb dating of zircon. The Canadian Mineralogist 41, 259–272.

Todt,W. & Lippolt, H. J. (1980). K-Ar age determination on tertiary volcanic rocks: V. Siebengebirge, Siebengebirge-Graben. Journal of Geophysics 48, 18-27.

Touron, S., Renac, C., O'Reilly, S.Y., Cottin, J.-Y., Griffin, W.L., 2008. Characterization of the metasomatic agent in mantle xenoliths from Devès, Massif Central (France) using coupled in situ trace-element and O, Sr and Nd isotopic compositions, in: Coltorti M., Grégoire M. (Eds) "Metasomatism in Oceanic and Continental Lithospheric Mantle". Geological Society, London, Special Publication 293, pp 177-196.

Trieloff, M., Altherr, R., 2007. He–Ne–Ar isotope systematics of Eifel and Pannonian Basin mantle xenoliths trace deep mantle plume-lithosphere interaction beneath the European continent. In: Ritter, J.R.R., Christensen, U.R. (Eds.), Mantle Plumes: A Multidisciplinary Approach. Springer-Verlag, Berlin Heidelberg, pp. 339–367.

Trull, T. W., and Kurz, M. D. (1993). Experimental measurements of 3He and 4He mobility in olivine and clinopyroxene at magmatic temperatures. Geochim. Cosmochim. Acta 57, 1313–1324. doi:10.1016/0016-7037(93)90068-8.

Ulrych, J., Dostal, J., Adamović, J., Jelínek, E., Špaček, P., Hegner, E., and Balogh, K. (2011). Recurrent Cenozoic volcanic activity in the Bohemian Massif (Czech Republic). Lithos 123, 133–144. doi:10.1016/j.lithos.2010.12.008.

Ulrych, J., Krmíček, L., Tomek, Č., Lloyd, F. E., Ladenberger, A., Ackerman, L., and Balogh, K. (2016). Petrogenesis of Miocene alkaline volcanic suites from western Bohemia: Whole rock geochemistry and Sr-Nd-Pb isotopic signatures. Chemie der Erde - Geochemistry 76, 77–93.

doi:10.1016/j.chemer.2015.11.003.

Upton, B.G.J., Downes, H., Bonadiman, C., Kirstein, L.A., Hill, P.G., Ntaflos, T., 2011. The lithospheric mantle and lower crust-mantle relationships under Scotland: a xenolithic perspective. Journal of the Geological Society, London 168, 873-885.

Valbracht, P. J., Honda, M., Matsumoto, T., Mattielli, N., McDougall, I., Ragettli, R., and Weis, D. (1996). Helium, neon and argon isotope systematics in Kerguelen ultramafic xenoliths: implications for mantle source signatures. Earth Planet. Sci. Lett. 138, 29–38. doi:10.1016/0012-821X(95)00226-3.

Vaselli, O., Downes, H., Thirlwall, M.F., Dobosi, G., Coradossi, N., Seghedi, I., Szakács, A., Vannucci, R., 1995. Ultramafic xenoliths in Plio-Pleistocene alkali basalts from the Eastern Transylvanian basin: depleted mantle enriched by vein metasomatism. Journal of Petrology 36, p.23-55.

Vaselli, O., Minissale, A., Tassi, F., Magro, G., Seghedi, I., Ioane, D., Szakács, A., 2002. A geochemical traverse across the Eastern Carpathians (Romania): constraints on the origin and evolution of the mineral waters and gas discharge. Chemical Geology 182, 637–654.

Vieten, K., Hamm, H. M. & Grimmeisen, W. (1988). Tertiarer Vulkanismus des Siebengebirges. Fortschritte der Mineralogie, Beihefte 66, 1-42.

Weinlich, F. H., Bräuer, K., Kämpf, H., Strauch, G., Tesař, J., & Weise, S. M. (1999). An active subcontinental mantle volatile system in the western Eger rift, Central Europe: Gas flux, isotopic (He, C, and N) and compositional fingerprints. Geochimica et Cosmochimica Acta, 63(21), 3653–3671. https://doi.org/10.1016/S0016-7037(99)00187-8

Wilson M, Downes H (1991) Tertiary–Quaternary Extension-Related Alkaline Magmatism in Western and Central Europe. J Petrology 32:811-849

Wilson M, Patterson R (2001) Intraplate magmatism related to short-wavelength convective instabilities in the upper mantle: evidence from tertiary-Quaternary volcanic province of western and central Europe. Geological Society of America, Special Papers 352:37-58.

Wilson, M., and Downes, H. (2006). Tertiary-Quaternary Intra-Plate Magmatism and Mantle Dynamics in Europe. Cent. Eur., 147–166.

Witt-Eickschen, G., Harte, B., 1994. Distribution of trace elements between amphibole and clinopyroxene from mantle peridotites of the Eifel (western Germany): An ion-microprobe study. Chemical Geology 117, 235-250.

Witt-Eickschen, G., Kaminsky, W., Kramm, U. & Harte, B. (1998). The nature of young vein metasomatism in the lithosphere of the West Eifel (Germany): geochemical and isotopic constraints from composite mantle xenoliths from the Meerfelder Maar. Journal of Petrology 39, 155-185.

Witt-Eickschen, G., Seck, H. A., Mezger, K., Eggins, S. M. & Altherr, R. (2003). Lithospheric mantle evolution beneath the Eifel (Germany): Constraints from Sr-Nd-Pb isotopes and trace element abundances in spinel peridotite and pyroxenite veins. Journal of Petrology 44, 1077-1095.

Wood, B.J., Virgo, D., 1989. Upper mantle oxidation state: ferric iron contents of lherzolite spinels by 57Fe Mössbauer spectroscopy and resultant oxygen fugacities. Geochimica et Cosmochimica Acta 53, 1227–1291.

Workman, R.K., Hart, S.R., 2005. Major and trace element composition of the depleted MORB mantle (DMM). Earth and Planetary Science Letters 231, 53-72.

Xu, Y.G., Bodinier, J.-L., 2004. Contrasting enrichments in high- and low-temperature mantle xenoliths from Nushan, Eastern China: results of a single metasomatic event during lithospheric accretion? Journal of Petrology 45, 321-341.

Yamamoto, J., Kaneoka, I., Nakai, S., Kagi, H., Prikhod'ko, V. S., and Arai, S. (2004). Evidence for subduction-related components in the subcontinental mantle from low 3He/4He and 40Ar/36Ar ratio in mantle xenoliths from Far Eastern Russia. Chem. Geol. 207, 237–259. doi:10.1016/j.chemgeo.2004.03.007.

Yamamoto, J., Nishimura, K., Sugimoto, T., Takemura, K., Takahata, N., and Sano, Y. (2009). Diffusive fractionation of noble gases in mantle with magma channels: Origin of low He/Ar in mantle-derived rocks. Earth Planet. Sci. Lett. 280, 167–174. doi:10.1016/j.epsl.2009.01.029.

Yoshikawa, M., Tamura, A., Arai, S., Kawamoto, T., Payot, B.D., Rivera, D.J., Bariso, E.B., Mirabueno, M.H.T., Okuno, M., Kobayashi, T., 2016. Aqueous fluids and sedimentary melts as agents for mantle wedge metasomatism, as inferred from peridotite xenoliths at Pinatubo and Iraya volcanoes, Luzon arc, Philippines. Lithos 262, 355-368.

Zanetti, A., Vannucci, R., Oberti, R., Dobosi, G., 1995. Trace-element composition and crystal-chemistry of mantle amphiboles from the Carpatho-Pannonian region. Acta Vulcanologica 7, 265-276.

Ziberna, L., Klemme, S., Nimis, P., 2013. Garnet and spinel in fertile and depleted mantle: insights from thermodynamic modelling. Contribution to Mineralogy and Petrology 166, 411–421.

Ziegler P (1992) European Cenozoic rift system. Tectonophysics 208:91-111.

Zolitschka B, Negendank JFW, Lottermoser B G (1995) Sedimentological proof and dating of the early Holocene volcanic eruption of Ulmener Maar (Vulkaneifel, Germany). Geol Rdsch 84:213-219.

Sezioni

Dottorati di ricerca

Il tuo indirizzo e-mail

rzznrl@unife.it

Oggetto:

Dichiarazione di conformità della tesi di Dottorato

Io sottoscritto Dott. (Cognome e Nome)

Rizzo Andrea Luca

Nato a:

Milano

Provincia:

MI

Il giorno:

30/01/1974

Avendo frequentato il Dottorato di Ricerca in:

SCIENZE DELLA TERRA E DEL MARE

Ciclo di Dottorato

32

Titolo della tesi:

The composition of noble gas and CO2 in the European subcontinental lithospheric mantle

Titolo della tesi (traduzione):

La composizione di gas nobili e CO2 nel mantello litosferico sub-continentale Europeo

Tutore: Prof. (Cognome e Nome)

Coltorti Massimo

Settore Scientifico Disciplinare (S.S.D.)

GEO/07-08

Parole chiave della tesi (max 10):

Gas nobili (Noble gas), CO2, Inclusioni fluide (Fluid Inclusions), Mantello Europeo (European mantle), Xenoliti di mantello (Mantle xenoliths), Rifusione parziale (Partial melting), Metasomatismo (Metasomatism), Rifertilizzazione (Refertilization), SCLM, MORB

Consapevole, dichiara

CONSAPEVOLE: (1) del fatto che in caso di dichiarazioni mendaci, oltre alle sanzioni previste dal codice penale e dalle Leggi speciali per l'ipotesi di falsità in atti ed uso di atti falsi, decade fin dall'inizio e senza necessità di alcuna formalità dai benefici conseguenti al provvedimento emanato sulla base di tali dichiarazioni; (2) dell'obbligo per l'Università di provvedere al deposito di legge delle tesi di dottorato al fine di assicurarne la conservazione e la consultabilità da parte di terzi; (3) della procedura adottata dall'Università di Ferrara ove si richiede che la tesi sia consegnata dal dottorando in 2 copie, di cui una in formato cartaceo e una in formato pdf non modificabile su idonei supporti (CD-ROM, DVD) secondo le istruzioni pubblicate sul sito : http://www.unife.it/studenti/dottorato alla voce ESAME FINALE – disposizioni e modulistica; (4) del fatto che l'Università, sulla base dei dati forniti, archivierà e renderà consultabile in rete il testo completo della tesi di dottorato di cui alla presente dichiarazione attraverso l'Archivio istituzionale ad accesso aperto "EPRINTS.unife.it" oltre che attraverso i Cataloghi

delle Biblioteche Nazionali Centrali di Roma e Firenze. DICHIARO SOTTO LA MIA RESPONSABILITA': (1) che la copia della tesi depositata presso l'Università di Ferrara in formato cartaceo è del tutto identica a quella presentata in formato elettronico (CD-ROM, DVD), a quelle da inviare ai Commissari di esame finale e alla copia che produrrà in seduta d'esame finale. Di conseguenza va esclusa qualsiasi responsabilità dell'Ateneo stesso per quanto riguarda eventuali errori, imprecisioni o omissioni nei contenuti della tesi; (2) di prendere atto che la tesi in formato cartaceo è l'unica alla quale farà riferimento l'Università per rilasciare, a mia richiesta, la dichiarazione di conformità di eventuali copie. PER ACCETTAZIONE DI QUANTO SOPRA RIPORTATO

Dichiarazione per embargo

12 mesi

Richiesta motivata embargo

1. Tesi in corso di pubblicazione

Liberatoria consultazione dati Eprints

Consapevole del fatto che attraverso l'Archivio istituzionale ad accesso aperto "EPRINTS.unife.it" saranno comunque accessibili i metadati relativi alla tesi (titolo, autore, abstract, ecc.)

Firma del dottorando

Ferrara, li ___25-02-2020_____ (data) Firma del Dottorando
_____

Firma del Tutore

Visto: Il Tutore Si approva Firma del Tutore _____